Universidade de Aveiro
2022

Américo Soares Ribeiro

Resiliência e utilização sustentável das infraestruturas portuárias da costa oeste Ibérica: desafios climáticos

Resilience and sustainable use of Iberian west coast port infrastructures under climate challenges

Universidade de Aveiro
2022

Américo Soares Ribeiro

Resiliência e utilização sustentável das infraestruturas portuárias da costa oeste Ibérica: desafios climáticos

Resilience and sustainable use of Iberian west coast port infrastructures under climate challenges

Tese apresentada à Universidade de Aveiro para cumprimento dos requisitos necessários à obtenção do grau de Doutor em Ciência, Tecnologia e Gestão do Mar, realizada sob a orientação científica do Doutor João Miguel Dias, Professor Catedrático do Departamento de Física da Universidade de Aveiro, e do Doutor Ramon Gómez-Gesteira, Professor Catedrático da Faculdade de Ciências de Ourense da Universidade de Vigo

O autor foi financiado pela Fundação para a Ciência e Tecnologia (FCT), através da bolsa de Doutoramento com a referência SFRH/BD/114919/2016, no âmbito do Quadro de Referência Estratégico Nacional (QREN) e do Programa Operacional de Potencial Humano (POPH), comparticipado pelo Fundo Europeu e por fundos nacionais do Ministério da Educação e Ciência (MEC). Este trabalho foi também desenvolvido no âmbito do Projecto “WECAnet: A pan-European network for Marine Renewable Energy” (CA17105), co-financiado pela Cooperação Europeia em Ciência e Tecnologia (COST) e União Europeia através do Programa HORIZON2020; e do projeto MarRisk (0262_MARRISK_1_E), financiado pelo Programa Operativo de Cooperação Transfronteiriço Portugal-Espanha (POCTEP INTERREG V A 2015 – 2019).

o júri

Presidente	Doutor Armando José Formoso de Pinho professor catedrático da Universidade de Aveiro
vogais	Doutora Liliana Celia Rusu professora catedrática da Universidade de Galati
	Doutor Vicente Perez Muñuzut professor catedrático da Universidade de Santiago de Compostela
	Doutor João Miguel Sequeira Silva Dias professor catedrático da Universidade de Aveiro
	Doutor Ramiro Joaquim de Jesus Neves professor associado com agregação da Universidade de Lisboa
	Doutora Magda Catarina Ferreira de Sousa Investigadora da Universidade de Aveiro

Acknowledgement

There are a number of people that I would like to thank for their guidance, help and support while doing this thesis. Firstly I would like to thank my parents as they always supported me in my studies and endeavours. Secondly, I would like to thank my supervisors for the opportunity to work with them on a fascinating project. I enjoyed working with João Dias and Moncho Gómez Gesteira, who helped me overcome the many obstacles I encountered. Your guidance, the discussions and the “trips” are much appreciated. You steered me in the right direction whenever I thought I needed it. Thank you for that. Special thanks also go to Maite deCastro, of whom I am gratefully indebted for your accessibility, knowledge and enthusiasm during our meetings.

I would like to acknowledge all members of the NMEC and EPhysLab groups for their insights and knowledge on the topic of this thesis. Individually, I would like to thank Magda Sousa for being a friend and mentor throughout my academic journey. Xurxo Costoya and Marisela Des Villanueva for their support and humour during the months in Ourense.

Special thanks go to my friends André Pinto, Filipe Tártaro, Rui Leitão, Helena Correia and Cláudia Simões for their support and encouragement.

palavras-chave Alterações climáticas; Estruturas portuárias; Recursos energéticos renováveis; Avaliação de inundações

resumo

Os portos têm um forte impacto na atividade económica das regiões costeiras onde estão inseridos, constituindo também fontes locais de poluição associados a várias fontes de emissões. As projeções de alterações no sistema climático indicam que a frequência e a intensidade nos níveis extremos do mar (ESL), compostos pela combinação do nível médio do mar, da maré astronómica e da maré meteorológica, juntamente com a agitação marítima e os caudais fluviais irão aumentar, afetando a fiabilidade e operabilidade dos portos. Nas últimas décadas, vários esforços têm sido feitos de forma a serem tomadas ações para contrariar as alterações climáticas, através do uso de energias limpas e viáveis para os portos de forma a contrariar o elevado uso de energias fósseis. As atividades e estruturas portuárias tornam os portos um desafio para serem inclusivos e promoverem um desenvolvimento sustentável através de infraestruturas resilientes e inovação. A costa Noroeste Ibérica (NWIC) é atravessada por uma das rotas marítimas mais importantes e movimentadas do Oceano Atlântico, tendo vários portos que constituem uma porta de entrada essencial para a Europa. Os portos de Lisboa, Aveiro, Vigo e o Porto Exterior da Corunha são analisados neste trabalho devido a estarem localizados em diferentes ambientes costeiros, nomeadamente a Ria de Aveiro, o Estuário do Tejo, a Ria de Vigo e a Costa da Corunha, respetivamente, o que traz desafios distintos relacionados com o impacto local das alterações climáticas. Com base no exposto, este estudo assenta na análise conceptual do clima histórico, presente e futuro, com o objetivo de avaliar o impacto das alterações climáticas nas estruturas portuárias da Costa Oeste Ibérica e a viabilidade de novos recursos energéticos para reduzir a pegada de carbono dos portos.

Neste âmbito foram desenvolvidos modelos hidrodinâmicos de elevada resolução para a NWIC e para cada zona portuária em estudo, baseados no DELFT3D model suite, visando analisar o impacto das alterações climáticas nas estruturas portuárias e avaliar os recursos de energia marinha disponíveis na NWIC, de forma a promover atividades portuárias com emissões de carbono baixas ou nulas. Esta avaliação foi realizada através da aplicação do método Delphi, que se baseia em índices de parâmetros físicos, de forma a facilitar a classificação da viabilidade de exploração da energia das ondas e da energia híbrida eólica-ondas na NWIC. Foi ainda analisada a eficiência e o custo da energia no ciclo de vida de dois dispositivos que usam a energia das ondas (WEC) de forma a exemplificar um parque de energia das ondas. Os modelos locais foram utilizados para avaliar o risco de inundação nas instalações portuárias para o clima atual e futuro, em cenários de alterações climáticas para períodos de retorno de 10, 25 e 100 anos. No caso do Porto Exterior da Corunha foi ainda estudado o galgamento em condições climáticas extremas através da aplicação do modelo não hidrostático XBeach. Com base nesta implementação foi desenvolvido um modelo operacional local, que constitui uma ferramenta de análise do risco para previsão do galgamento de infraestruturas em condições de regime de ondas muito energéticas, e consequentemente, para prevenir e suprir danos humanos e materiais.

Os resultados obtidos permitiram a identificação das zonas marinhas com maior potencial energético nas regiões circundantes dos portos, mostrando a variabilidade dos WECs na exploração da energia das ondas. De uma forma geral, as condições de exploração da energia das ondas e do recurso híbrido eólica-ondas irão diminuir até ao final do século devido ao aumento da variabilidade da disponibilidade do recurso. O risco de exploração irá aumentar devido à maior frequência de ocorrência das ondas extremas. Apesar destas condições, o recurso energético é classificado como excelente na NWIC onde se situam os portos de Aveiro e Lisboa, e como excecional nas proximidades do Porto Exterior da Corunha e do porto de Vigo, no extremo noroeste da NWIC. Adicionalmente, os portos podem usar WECs para explorar a energia das ondas perto das suas instalações, mesmo quando o recurso disponível é baixo. Relativamente aos padrões de inundação, verifica-se que variam significativamente de acordo com a localização dos portos. De facto, as lagunas e os estuários são mais propensos a inundações pelo ESL devido à sua topografia plana e com cotas baixas. A Ria de Vigo, que apresenta uma topografia irregular e é protegida pelas ilhas Cíes, propicia condições naturais para que o porto de Vigo seja resiliente a inundações. Esta resiliência é ainda mais evidente no Porto Exterior da Corunha, onde não ocorrem inundações devido à existência de um dique de proteção contra tempestades. No entanto, podem ocorrer inundações causadas por galgamentos quando ocorrem ondas caracterizadas por elevada energia. Os resultados do modelo XBeach revelam que o galgamento poderá aumentar no futuro perante ondas mais energéticas.

keywords Climate change; Port structures; Marine renewable energy; Flood assessment

abstract

Ports have a significant impact on the economic activity in coastal areas and are linked with several port-related emissions sources of local pollution. Future climate change projections indicate that the frequency and intensity of extreme sea levels (ESL), a combination of the mean sea level, astronomical tide, and storm surge, as well as waves and river discharges, will increase with impacts on the port's reliability and operability. In the last decades, various efforts have been made to take climate action by pursuing affordable and clean energy to ports to counter the high demands on fossil energies. The port activities and structures make the ports challenging to be inclusive and promote sustainable development with resilient infrastructure and innovation. The Northwest Iberian Coast (NWIC) is crossed by one of the most important and busiest shipping lanes of the Atlantic Ocean and features several ports that provide an essential gateway for Europe. The ports of Aveiro, Lisbon, Vigo and A Coruña Outer Port are considered in this work due to their location in different environments, namely the Aveiro lagoon, Tagus estuary, Ria de Vigo and the A Coruña coast, respectively, which brings distinct challenges related to climate change local impact. Drawing on the above, this study is based on the conceptual analysis of historical, present and future climate, aiming to assess the climate change impact on West Iberian Coast port structures and the feasibility of new energy resources to reduce the ports carbon footprint.

In this context, high-resolution hydrodynamic models were developed for the northwest Iberian coast (NWIC) and for each port area under study, based on the DELFT3D model suite, in order to accurately research the impact of climate change in the ports' structures and assess the marine energy resources available in the NWIC to promote the low- or zero-carbon port activities. The energy resource assessment was performed by applying a Delphi method based on physical point of view indices to facilitate the classification of the viability of exploiting the hybrid wind-wave energy and wave energy resource along with the NWIC. A study of the efficiency and cost of energy over the life-cycle of two wave energy devices (WEC) to exemplify a planned wave energy farm was also performed. This approach allowed the identification of the offshore areas with the highest energy surrounding a port and showed the variability between WECs to exploit the wave energy resource available. The local models were used to assess the risk of flooding at the port facilities for the current and future climate, under climate change scenarios for return periods of 10, 25 and 100 years. In the case of the Outer Port of A Coruña, overtopping in extreme weather conditions was also studied through the application of the non-hydrostatic XBeach model. Based on this implementation, a local operational model was developed, which constitutes a risk analysis tool for predicting infrastructure overtopping in conditions of high energetic waves, and consequently, to prevent and overcome losses of property and human safety.

In general, conditions for the exploitation of wave and hybrid wind-wave energy will decrease by the end of the century due to the increase in energy variability. The risk factor will also increase due to the major frequency of extreme ocean waves. Despite this, the energy resource is classified as excellent along the NWIC where Aveiro and Lisbon Ports are located, and as outstanding in the NW extreme of the NWIC, close to Vigo and A Coruña Outer Ports. In addition, the ports can use WECs to exploit wave energy close to their facilities, even when the available resource is low. The flood pattern varies significantly according to the location of the ports. Lagoons and estuaries are more prone to floods by the ESL due to the low and flat topography. Ria de Vigo, with irregular topography and sheltered by the Cíes Islands, makes the Vigo port resilient to floods by the climate drivers. This resilience is more evident for the A Coruña Outer port, where no floods occurred. However, this port relies on a breakwater to protect the facilities from hazardous weather, which may cause overtopping under high energetic waves.

CONTENTS

LIST OF FIGURES

LIST OF TABLES

LIST OF SYMBOLS

C_v	Variability index
DC	Distance to coast
Dm	Direction from which the waves are coming
Downtime	The measure of time in which a Wave energy device operates efficiently
DWNT	Total time with useful wind speed occurrence
EWH	Extreme wave height
g	Gravitational acceleration
H_s	Significant wave height
H_{max}	Maximum wave height
I_{wave}	Wave energy resource index
I_{wind}	Wind energy resource index
M_v	Monthly variability index
n_m	Number of GCMs used to force WWIII
R^k	Random number with an equal probability between ±1
Risk	Risk of extreme wind speeds or extremely large wave heights
RLO	Rich level occurrence, frequency of WPD higher than 200 Wm^{-2}
RMSE	Root-mean-square error
S_m	Directional spreading
T_p	Peak wave period
Tr^{10}	10-year return period
Tr^{25}	25-year return period
Tr^{100}	100-year return period
W	Mean weight of each index
W_{ann}	Annual average wind speed
WD	Water depth
WP	Power transmitted by a regular wave per unit crest width (Wm^{-1})

WDP	Wind Density Power
ρ	Seawater density
σ	Standard deviation

LIST OF ACRONYMS

BCC-CSM1.1	Beijing Climate Center - Climate System Model version 1.1
CFSR	Climate Forecast System Reanalysis
CMIP5	Coupled Model Intercomparison Project Phase 5
CSIRO	Commonwealth Scientific and Industrial Research Organisation
ESL	Extreme sea level
GCM	Global Climate Model
IEC	International Electrotechnical Commission
IPCC	Intergovernmental Panel on Climate Change
LCOE	Levelized Cost of Energy
MHWS	Mean High Water Springs
MIROC5	Model for Interdisciplinary Research on Climate
MRI-CGCM3	Meteorological Research Institute - Coupled Global Climate Model version 3
MSL	Mean Seal Level
NWIC	Northwest Iberian Coast
OP	Overlap percentage
PDF	Probability distribution function
RCM	Regional Climate Model
RCP	Representative Concentration Pathway
SSE	Sea Surface Elevation
SIMAR	Model points from the Spanish Port Authority
SMHI	Swedish Meteorological and Hydrological Institute
SWAN	Simulating Waves Nearshore
WEC	Wave energy device
WWIII	WAVEWATCH III

PUBLICATIONS AND COMMUNICATIONS IN THE CONTEXT OF THIS THESIS

A number of publications in peer-reviewed journals and presentations at international and national conferences resulted from the research developed in the scope of this dissertation. Some publications were used as a basis for several chapters of this thesis (marked in bold in the list below).

Papers in international journals indexed in Web of Science:

- Ribeiro A. S., Lopes C. L., Sousa M. C., Gomez-Gesteira M., Dias J. M. (2021). Flooding Conditions at Aveiro Port (Portugal) within the Framework of Projected Climate Change. Journal of Marine Science and Engineering; 9(6):595. **(Chapter 4)**
- Ribeiro A. S., Costoya X., de Castro M., Carvalho D., Dias J. M., Rocha A., Gomez-Gesteira M. (2020). Assessment of Hybrid Wind-Wave Energy Resource for the NW Coast of Iberian Peninsula in a Climate Change Context. Applied Sciences; 10(21):7395. **(Chapter 3)**
- Ribeiro A.S., deCastro M., Rusu L., Bernardino M., Dias J.M., Gomez-Gesteira M. (2020). Evaluating the Future Efficiency of Wave Energy Converters along the NW Coast of the Iberian Peninsula. Energies; 13(14). **(Chapter 3)**
- Ribeiro A. S., DeCastro M., Costoya X., Rusu L., Dias J. M., Gomez-Gesteira M. (2021). A Delphi Method to Classify Wave Energy Resource for the 21st century: Application to the NW Iberian Peninsula. Energy; 235:121396. **(Chapter 3)**
- Castro-Santos, L., DeCastro, M., Costoya, X., Filgueira-Vizoso, A., Lamas-Galdo, I., Ribeiro, A.S., Dias, J. M., Gómez-Gesteira, M. (2021). Economic Feasibility of Floating Offshore Wind Farms Considering Near Future Wind Resources: Case Study of Iberian Coast and Bay of Biscay. International Journal of Environmental Research and Public Health, 18(5), 2553. **(Chapter 3)**

Papers in international journals indexed in Web of Science that have minor contributions but related with the aim of this thesis:

- Fernández-Fernández, S., Silva, P. A., Ferreira, C., Ribeiro, A. S., Abreu, T., Romão, S., Baptista, P., Fontán-Bouzas, Á., Dias, J. M., Coelho, C., & Bernardes, C. (2018). Assessment of Dredging/Dumping Scenarios for Figueira da Foz Coastal Region (W Portugal). Journal of Coastal Research, 85, 1266–1270

- Sousa, M. C., DeCastro, M., Gago, J., Ribeiro, A. S., Des, M., Gómez-Gesteira, J. L., Dias, J. M., & Gomez-Gesteira, M. (2021). Modelling the Distribution of Microplastics Released by Wastewater Treatment Plants in Ria de Vigo (NW Iberian Peninsula). Marine Pollution Bulletin, 166, 112227.

- Sousa, M. C., Ribeiro, A., Des, M., Gomez-Gesteira, M., deCastro, M., Dias, J. M. (2020). NW Iberian Peninsula Coastal Upwelling Future Weakening: Competition between Wind Intensification and Surface Heating. Science of The Total Environment, 703, 134808.

- Sousa, M. C., Ribeiro, A. S., Des, M., Mendes, R., Alvarez, I., Gomez-Gesteira, M., Dias, J. M. (2018). Integrated High-resolution Numerical Model for the NW Iberian Peninsula Coast and Main Estuarine Systems. Journal of Coastal Research, 85, 66–70.

- Mendes J., Ruela R., Picado A., Pinheiro J. P., Ribeiro A. S., Pereira H., Dias J. M. (2021). Modeling Dynamic Processes of Mondego Estuary and Óbidos Lagoon Using Delft3D. Journal of Marine Science and Engineering; 9(1):91.

- Oliveira, V. H., Sousa, M. C., Picado, A., Mendes, R., Ribeiro, A. S., Morgado, F., Dias, J. M. (2021). Coupled Modelling of the Interaction between Dissolved Substances Emitted by Minho and Lima Estuarine Outflows (Portugal). Journal of Marine Systems, 103601

- Ouni, H., Sousa, M. C., Ribeiro, A. S., Pinheiro, J., Ben M’Barek, N., Tarhouni, J., Tlatli-Hariga, N., & Dias, J. M. (2020). Numerical Modeling of Hydrodynamic Circulation in Ichkeul Lake-Tunisia. Energy Reports, 6, 208–213.

- Pinheiro, P., Lopes, C. L., Ribeiro, S., & Sousa, M. C. (2020). Tide-surge Interaction in Ria de Aveiro Lagoon and its Influence in Local Inundation Patterns. Continental Shelf Research, 200 (October 2019).

Other communications:

- Ribeiro A. S., Gomez-Gesteira M., Dias J. M. (2020). Climate Change Impact on West Iberian Coast Port Defenses and Maritime Traffic. Ciência 2020 - Science and Technology in Portugal Summit. 3-4 November, Lisbon, Portugal

Chapter 1

GENERAL INTRODUCTION

This chapter presents a brief review of the research scope to contextualise the problem under study, followed by a systematisation of the major motivations and aims that drove this work and a synthesis of the structure of this thesis.

1.1 INTRODUCTION

Maritime transport is essential to the world's economy as over 90% of the world's trade is carried by sea, and it is the most cost-effective way to move bulk goods and materials worldwide [1]. Shipping is an international service industry, and all ports operate in the global economy and are subject to economic cycles [2]. Port facilities are generally designed to protect against extreme weather events that occur at least every 50 years [3]. The recent series of storms highlighted the need to investigate the capability and effectiveness of port structures. In addition, future climate projections indicate that the frequency and intensity of extreme sea levels [4–8] will increase with impacts on ports operation [9]. Demand for a port is strongly correlated to climatic conditions and will be affected by climate change, and it can also be affected by its vulnerability to disruption from extreme weather events, affecting the port's reliability and operability, which may lead to a shift to alternative ports [10]. The directive 2009/18/EC of the European Parliament and the Council recognizes the importance of reducing the risk of future marine casualties by heavy weather damage. Therefore, it is crucial to improve knowledge about port structures.

Climate change evidences the mean sea level rise, intensification of severe storm-surges and changes in wind and wave patterns [11,12] will modify the extreme weather events [5,13–16] and hydrodynamic circulation at the vicinity and inside the ports [17–21] and will impact the maritime traffic, berthing [3, 7, 8], infrastructure, equipment, port operations and consequently threaten the economic growth [9, 10].

In the last decades, efforts have been made to tackle the effects of climate change by reducing carbon emissions, implementing strategies and regulations to private and public sectors aiming to protect public health and the environment and contributing to the fight against climate change. The United Nations, through the 2030 Agenda for Sustainable Development (https://www.un.org/sustainabledevelopment/) seeks a global action to promote actions to end poverty, protect the planet and improve lives and prospects around the globe. This call pledge to strengthen institutions to achieve these goals. Following these guidelines, the International Maritime Organization, a global network of maritime technology cooperation, take climate action by pursuing affordable and clean energy to ships and ports to counter the high demands on fossil energies [26]. The European Council and the European Parliament also endorsed long-term climate neutrality for the European Union to redress climate change through strategic priorities that rely on the adaptation and mitigation of crucial sectors [27,28]. The growing energy demands of the maritime transport sector are one of the top priorities. The strategy lies on improving energy security, reducing the dependence on imported fossil energies and supporting sustainable jobs and growth in the "blue" and "green" economy in order to create a new internal market capable of exporting products and services and reducing carbon emission from burning fossil fuels, improving the air quality [29,30].

Maritime ports are hubs of economic activity with several port-related emissions sources, such as domestic vessels, cargo handling equipment, heavy-duty vehicles, locomotives and the electrical grid. These activities and structures make the ports challenging to be inclusive and promote sustainable development with resilient infrastructure and innovation. The ports features and their location facilitate the use of marine renewable energy sources, from wave-wind farms to the test and implement energy converters in their infrastructures [31].

The Northwest Iberian Coast (NWIC) is crossed by one of the most important and busiest shipping lanes of the Atlantic Ocean, with hundreds of ships circulating daily from the Mediterranean (and Asia through the Suez channel and Africa to North Europe vice-versa). Due to the intensive maritime traffic, this area has vital sea lanes and traffic separation schemes [32] in the territorial sea of Portugal [33] and Spain [34]. This fact confers great responsibility in maritime security, assuring the navigation on the respective coastal waters, and aiding the vessels in avoiding accidents like the well-known Prestige [35].

The NWIC features several ports that provide an essential gateway for Europe and Asia for trading and are vital for Portugal and Spain's national economies [36]. This coast is characterised by highly variable coastal systems (estuaries, Rias and lagoons), namely the Rias Altas and Baixas (Galicia, Spain), Aveiro lagoon and Tagus estuary (Portugal). These systems have characteristics of natural harbours and led to the establishment of the ports of Vigo (Rias Baixas), Aveiro (Aveiro lagoon), Lisbon (Tagus estuary) and more recently, the A Coruña Outer Port (northern coast of the Galicia) (Figure 1.1). These ports are located in different environments, which brings them distinct challenges related to climate change drivers (depicted characteristics of the ports are listed in Chapter 4).

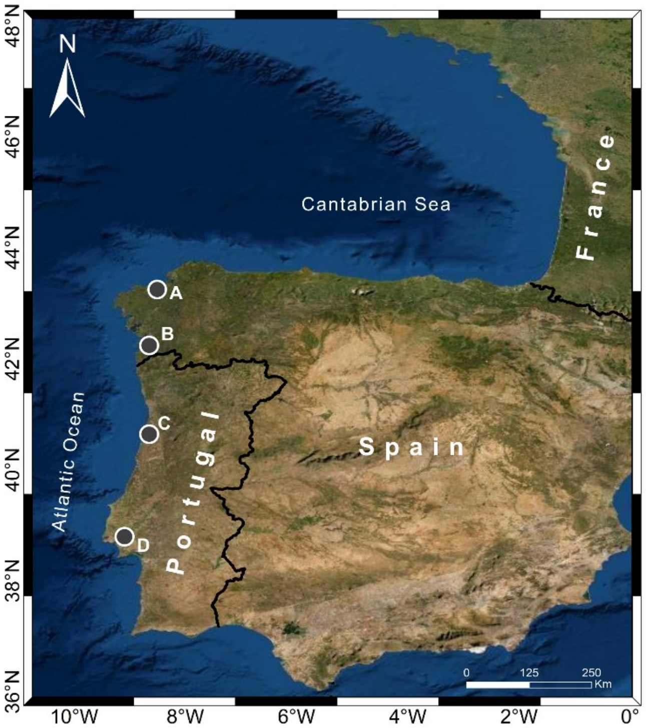

Figure 1.1 – Area under study. White circles are the locations of the harbours considered for this study. **A** A Coruña Outer Port (43.35°N, 8.51°W), **B** Vigo (42.23°N, 8.74°W), **C** Aveiro (40.64°N, 8.75°W), and **D** Lisbon (38.70°N, 9.17°W). Adapted from [37].

The series of storms during winter 2013-14 highlighted the need to investigate the capability and efficiency in ports across the Atlantic Area and particularly in NWIC. At the international level, PIANC (Association for Waterborne Transport Infrastructure) is preparing technical guidance to help the port owners, operators and users to adapt to climate change. The knowledge is somewhat limited about the risks that the NWIC ports face from climate change and how those risks can be mitigated [24,38].

The principal resource for global climate change predictions is the reports published by the Intergovernmental Panel on Climate Change (IPCC), through the IPCC fifth assessment report (AR5) [13] and the upcoming AR6 (https://www.ipcc.ch/report/ar6/wg1) due for release in 2022. The IPCC scenarios are based on possible evolutions of the climate throughout the 21st century as a function of greenhouse gas emissions (GHG) and the evolution of human societies and their implications for the climate. The AR5 divided these scenarios into four categories of Representative Concentration Pathway (RCP), which can be listed considering the numerical values of the RCPs (2.6, 4.5, 6.0 and 8.5), refer to the concentrations by 2100. The high warming scenario (RCP8.5) leads to more significant impacts and costs, and consequently, to adapt to these changes will also cost more. This GHG scenario is considered the most realistic today due to the lack of effective actions to reduce GHG emissions worldwide [39–43], exposing the area under study to extreme sea levels (ESL) higher than 4.5 m in 2100 [18].

Numerical models have become irreplaceable tools to link climate change, operational oceanography and marine affairs since they continuously provide state estimates and forecasts of coastal ocean state [44] under present [45,46] and climate change [47] conditions. Some studies analysed the impact of climate change in the NWIC using regional numerical models focusing only on the adjacent shelf [48–52] or local areas [19–21].

Some operational models are capable of forecasting the regional and local NWIC circulation, wave and atmospheric data. However, those are working at a regional scale in the NWIC (http://www.hidrografico.pt/agitacao-maritima-forecast.php) or in a regional to local scale in the north and south Spanish coast (http://www.puertos.es/es-es/proyectos/Paginas/SAPOS.aspx). These model applications present severe limitations if used to evaluate climate change impacts in the ports since they were typically implemented for large areas with coarse resolution or to a limited place, not including all the physical drivers of the local dynamics simultaneously, and not focusing on the effects on the port structures. The ability to accurately predict the impact of future climate on the coastal environment is critical to assess the safety of the operating conditions of the ports and pursue low- or zero-carbon activities.

Hereupon, this proposal is a state-of-the-art challenge, which aims to give a step forward, with a high-resolution model application comprising simultaneously selected ports of the NWIC based on the different geomorphological environments that characterize the NWIC, which bestow them distinct challenges related to climate change impacts under RCP8.5. With this methodology, it will be accurately researched the impact of climate change in the structures of the ports, as well as the assessment of the marine energy resources available in the NWIC to eliminate, reduce and/or limit the damage to people and property, economic activities, employment, environment and infrastructures.

1.2 RESEARCH QUESTIONS

The main goal of this thesis is twofold: assess the climate change impact on West Iberian Coast port structures and evaluate the feasibility of new energy resources to reduce the ports carbon footprint. The goals will focus on anticipating and limiting damage to people and property and reducing economic losses towards the use of green energies and carbon emissions.

State-of-the-art realistic present and future climate change scenarios will be determined to force high-resolution model applications designed with SWAN, DELFT3D and XBeach suitable for the NWIC and small-scale areas. Specific objectives of this proposal are to:

- Perform an inventory and assessment of port infrastructures as well as of the local infrastructures resistance;
- Analyse atmospheric and oceanic data predicted from different Global Climate Models (GCM) and Regional Climate Models (RCM) for future climate change and assess their changes from the present climate;
- Characterize met-ocean-land parameters under present and future climate change scenarios;
- Develop numerical model applications using SWAN and XBeach models to reproduce and forecast wave regime for the West Iberian Peninsula coast and local port scales, respectively;

- Develop integrated numerical model applications using the model DELFT3D to reproduce and forecast hydrodynamics at the NWIC, including the ports;
- Evaluate future climate change effects in wave regime, sea level and hydrodynamics patterns for the Western Iberian Peninsula coast, focusing the different ports under research for the present and future climate using model applications designed with DELFT3D, SWAN and Xbeach, forced with atmospheric, ocean and river discharge data;
- Assess how changes in wave regime, sea level, and hydrodynamics pattern will impact port structures;
- Assess ocean energy resources and how they will be impacted by climate change;
- Analyse the effects of local hydrodynamic and wave regime changes on ports operations;
- Map the offshore and shoreside energy source potential to support the supply of low-carbon and zero-carbon fuels to ports and further to promote the long-term climate neutrality in climate change scenarios;
- Map the potential port flood areas induced by climate change;

These goals will be achieved using RCM's and GCM's projections based on the RCP8.5 scenario. Thus, this proposal aims to answer the following questions:

1. What will be the consequences of climate change on port structures and, consequently, port activities over selected ports located in the NWIC?
2. How can ports seek renewable energy supplies to tackle the actual high demand for fossil fuels?
3. How to mitigate these consequences to assure the resilience under climate change of these ports in the future?

1.3 STRUCTURE OF THIS WORK

Ports adaptation to future climate relies on strategic plans to follow the EU directives for the Blue Economy and Blue growth. The main pillars of the strategic plan are supported by smart, sustainable and integrated growth, which focus on innovation, inclusive and green port activities by promoting responsible use of the natural resources in the Port's activities. Recent hazardous weather created favourable conditions for floods in coastal areas, testing the resilience of the present port infrastructures, where climate change can diminish their ability to cope with future challenging weather and environmental conditions. Thus, the research questions related to these concerns are addressed throughout several chapters, fulfilling the thesis objectives and answering the problem definition. Each chapter starts with a general background on the features and importance of the topic under discussion by presenting a short literature review, converging to the study objectives. The current chapter presents a brief introduction to contextualize the problem under study. Chapter two lists the data and methods used to assess the subsequent chapters.

Chapter three is dedicated to assessing the marine renewable energy in the study area by applying a Delphi method based on physical factors capable of classifying the energy resource. The Delphi method is applied to wave and hybrid wave-wind energies, followed by evaluating the efficiency of two wave energy converters (WEC) in the study area. This approach allows identifying the offshore areas with the highest energy surrounding a port and to study the efficiency and cost of energy over the life-cycle of two WECs, to exemplify a planned wave energy farm in the study area. The fourth chapter focuses on the resilience of the port infrastructures to climate change by addressing the flooding conditions of the selected ports under forcing drivers for 10-, 25- and 100-year return periods. The preparation of flood maps makes possible to identify the most vulnerable port areas. Chapter five aims to study the flooding resulting from overtopping events in the Outer Port of A Coruña, presenting the background, data and methodology necessary to configure the operational model developed. This is used to identify historical and future events of overtopping, as well as make forecasts up to 24 hours. Chapter six presents the main conclusions of this thesis and suggestions for further research.

Chapter 2

DATA AND METHODS

This chapter presents the methodology used in this thesis to collect and analyse the historical and climate data required to perform the energy (Chapter 3) and flood (Chapter 4) assessment. The resulting dataset is used in forthcoming chapters for the implementation of the numerical models.

2.1 RATIONALE

Ocean circulation is a crucial climate regulator through complex and diverse mechanisms that interact to produce this circulation. Wind-driven combined with density-driven circulation defines ocean circulation from global to regional scale. This circulation is still poorly understood due to its volatility to climate drivers and their spatial variability, which are predicted to change during the following decades. Such processes have consequences on society by affecting artificial structures. Thus, it is vital to increase the knowledge about the interactions between ocean circulation and climate through observations when they are available and attainable and numerical models for larger space and time scales. As subsequently listed, this section focuses on the data collection regarding meteo-ocean drivers and the statistical analysis best suited to identify the most accurate and reliable drivers to be used as forcing conditions in the numerical models.

The methodology developed to achieve the objectives of this thesis is depicted in the sketch provided in Figure 2.1.

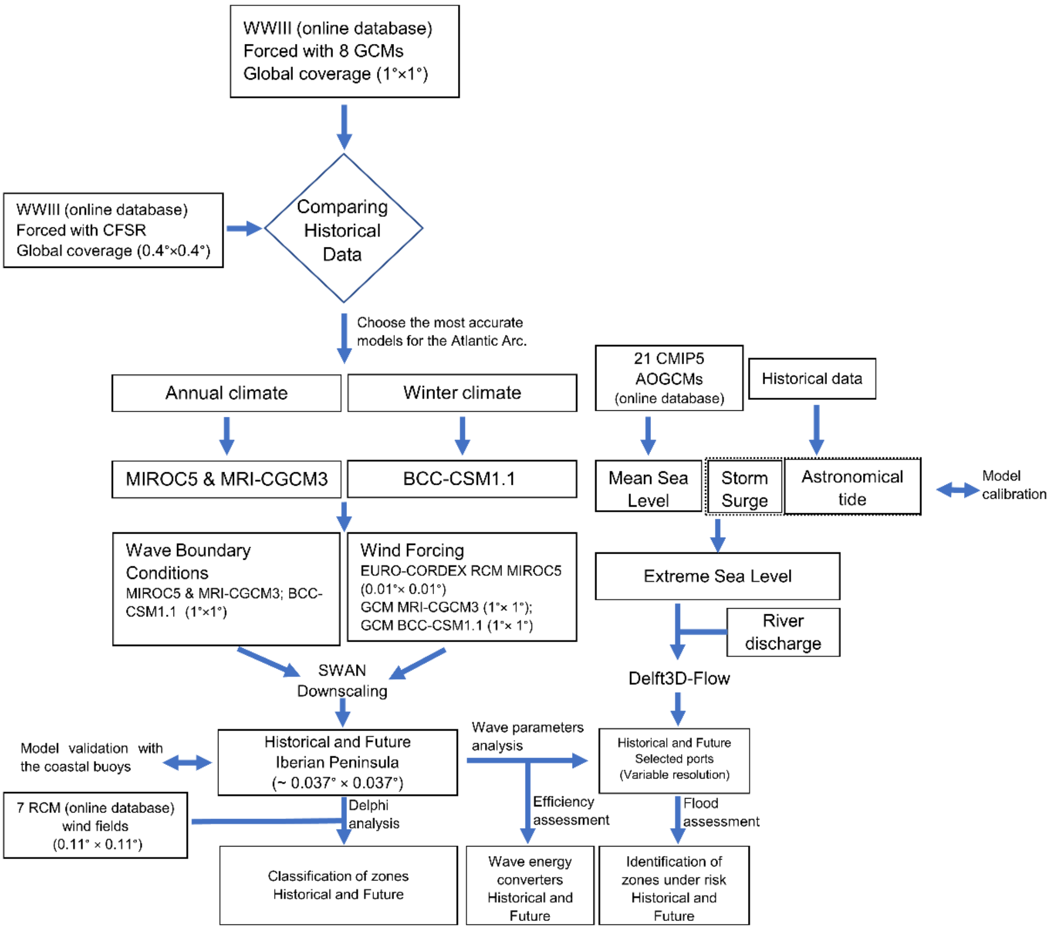

Figure 2.1 - Methodological sketch.

2.2 DATA

The following section describes the collection of data from several online databases or provided by institutions that are used to perform the energy and flood assessment. These assessments are achieved through numerical modelling that allows an effective dynamic downscaling. To this end, wave and wind GCMs are collected to analyse the most suitable GCMs to be imposed in the boundary conditions (atmospheric and ocean) of the wave model and assess the energy resource at the regional level. In addition, numerical models also require additional inputs to simulate water level under different future climate conditions. Thus, tidal data, river discharge and bathymetry are also collected, as well as tidal and wave *in-situ* data, which are used to validate the numerical models.

2.2.1 Wave model

Wave model and wave energy assessment require wave fields of significant wave height (H_s) and peak period (T_p). Thus, historical and future H_s and T_p data obtained from the WAVEWATCH III (WWIII) simulations available on the online database of the Commonwealth Scientific and Industrial Research Organisation (CSIRO) will be used as the starting point [56]. These simulations were carried out by the CSIRO and the Bureau of Meteorology datasets developed under the Pacific-Australia Climate Change Science and Adaptation Planning Programme (PACCSAP). WWIII was forced with 8 different GCMs (Table 2.1) [56], providing outputs with global coverage although with a coarse spatial resolution (1°×1°).

Table 2.1 Global Climate Models (GCMs) from the Coupled Model Intercomparison Project - Phase 5 (CMIP5).

GCM	Institute
ACCESS1.0	CSIRO (Commonwealth Scientific and Industrial Research Organisation), and BOM (Bureau of Meteorology), Australia
CNRM-CM3	Centre National de Recherches Météorologiques / Centre Européen de Recherche et Formation Avancées en Calcul Scientifique, France
BCC-CSM1.1	Beijing Climate Centre, China Meteorological Administration
GFDL-CM3	Geophysical Fluid Dynamics Laboratory, National Oceanic and Atmospheric Administration (NOAA), United States of America
HadGEM2-ES	Met Office Hadley Centre (additional HadGEM2-ES realisations contributed by Instituto Nacional de Pesquisas Espaciais, Spain), UK
INMCM4	Russian Institute for Numerical Mathematics, Russia
MIROC5	Atmosphere and Ocean Research Institute (The University of Tokyo), National Institute for Environmental Studies, and Japan Agency for Marine-Earth Science and Technology
MRI-CGCM3	Meteorological Research Institute, Japan Meteorological Agency

Wave simulations were carried out using the third generation spectral wind-wave WWIII model [57]. The outputs of the simulations for the wave hindcast [58] and the wave climate projection [56] can be described as follows:

1. Global ocean wave hindcast [58] was performed forcing the WWIII model version 4.08 with CFSR hourly winds and daily sea-ice concentration. All grids were forced with Climate Forecast System Reanalysis (CFSR) surface winds at 0.3º spatial resolution. The model was run on a 0.4º × 0.4º global grid from 1979 to 2010.
2. Wind-wave climate projections for the 21st century [56,59] were performed using a 1º global implementation of the WWIII model version 3.14 forced with 3 hourly surface wind and linearly interpolated monthly sea-ice concentration fields taken from the CMIP5 (Coupled Model Intercomparison Project Phase 5) GCMs. GCMs (Table 2.1) were used to drive the WWIII model under the RCP8.5 greenhouse gas emission scenario. Historical global wave projections span from 1979 to 2005 (historical), mid-century from 2026 to 2045 (near future) and end-of-century from 2081 to 2099 (far future), with a coarse resolution of 1°×1°.

2.2.2 Atmospheric model

The wave model and the hybrid energy assessment requires wind fields, and thereby historical, and future wind fields were retrieved from the regional climate simulations within the EURO-CORDEX branch [60] (Table 2.2) under the RCP8.5 greenhouse emission scenario. GCMs and RCMs at a spatial resolution of 1° and 0.11°, respectively. Two sets of periods were obtained given the twofold objectives:

1. Considering the comparison described in section 2.3.2, the climate models selected to provide the regional atmosphere forcing for the annual and winter climates are identified with an asterisk (Table 2.2), namely MIROC5-CCLM4-8-17 RCM and MRI-CGCM3 GCM, and BCC-CSM1.1 GCM, respectively. The choice of the MRI-CGCM3 and BCC-CSM1.1 GCMs was due to the non-existent RCM using these GCMs for this region. These wind fields are characterised by a 6-hourly time step (10 m above sea level) with a spatial resolution of 12.5 km, for the climate periods from 1979 to 2005 (historical), 2026 to 2045 (near future) and from 2081 to 2099 (far future).
2. For the assessment of hybrid wind-wave energy resources, 7 different RCMs (Table 2.2) were used to perform a multi-model ensemble [37,61] (described later in section 2.3.2). Daily wind speed at 10 m height was retrieved for the climate period from 2026 to 2045 (near future).

Table 2.2 Regional climate models (RCMs) from the Coordinated Regional Climate Downscaling Experiment (CORDEX) project (http://www.cordex.org/).

GCM	RCM	INSTITUTE
*MIROC5	CCLM4-8-17	Climate Limited-area Modeling Community, European Consortium
*MRI-CGCM3	-	Meteorological Research Institute, Japan Meteorological Agency
*BCC-CSM1.1	-	Beijing Climate Center, China Meteorological Administration
CNRM-CM5	RCA4	Swedish Meteorological and Hydrological Institute
CNRM-CM5	CCLM4-8-17	Climate Limited-area Modeling Community, European Consortium
CNRM-CM5	RCA4	Swedish Meteorological and Hydrological Institute
IPSL-CM5A-MR	RCA4	Swedish Meteorological and Hydrological Institute
IPSL-CM5A-MR	WRF331F	Institut Pierre-Simon Laplace, Guyancourt, France
MPI-ESM-LR	CCLM4-8-17	Climate Limited-area Modeling Community, European Consortium
MPI-ESM-LR	REMO2009	Helmholtz-Zentrum Geesthacht, Climate Service Center, Max Planck Institute for Meteorology

2.2.3 Buoy data

The wave model validation is performed using the Spanish Port Authority online database (http://www.puertos.es/en-us/oceanografia/Pages/portus.aspx), which have an hourly output of historical and real-time data for waves (other variables are also available). These buoys are divided into two types: *in-situ* stations and model points (SIMAR). The *in-situ* buoys are geographically placed along the coast and close to the shore, while SIMAR points have a broader dispersion in the area. The SIMAR points use the Iberian-Biscay-Ireland operational grid [62]. *In-situ* stations along the Portuguese coast were also obtained by the Portuguese Hydrographic Institute (https://www.hidrografico.pt/index/en). The buoys used in this study are identified in Table 2.3.

Table 2.3 Buoys in the Northwest Iberian Peninsula coast.

Buoy name	Latitude (°N)	Longitude (°W)	Validation period
Cádiz	36.49	6.96	1996-2005
Figueira da Foz	40.20	9.13	1990-1996
Leixões	41.32	8.98	1996-2005
Cape Silleiro	42.12	9.43	1998-2005
Villano Sisargas	43.50	9.21	1998-2005
Estaca de Bares	44.12	7.67	1996-2005
Cape Peñas	43.75	6.16	1990-2005
Bilbao-Vizcaya	43.63	3.04	1996-2005
SIMAR 1042054	38.50	9.50	1979-2005
SIMAR 1068084	46.00	3.00	1979-2005

2.2.4 Tidal data

The data set available for this study is a combination of observations recorded in tidal gauges and field surveys in the different domains in study. This sea surface elevation (SSE) data is used to perform the hydrodynamic model calibration for the Aveiro, Tagus, Vigo and A Coruña Outer Port (Table 2.4) and for further analysis to determine ESL (marked with an asterisk). Aveiro and Tagus time series were obtained through field surveys recorded in July of 2019 and between 2002 and 2003 for Aveiro, whereas Tagus data was observed in 1972, 1981 and in 1986. Vigo and A Coruña Outer Port data are obtained through the Spanish Port Authority online database (http://www.puertos.es/en-us/oceanografia/Pages/portus.aspx). Data sampling was provided with an hourly time step for all tide gauges.

Table 2.4 Tidal gauges used for the calibration and the validation periods, and for the ESL analysis (gauges identified with asterisk).

Domain	Gauge	Latitude (°N)	Longitude (°W)	Available period
Aveiro	Barra*	40.644	-8.748	1976-2013
	Carregal	40.852	-8.656	2002-2003
	Cacia	40.693	-8.598	2002-2003
	Cais do Bico	40.728	-8.648	2002-2003
	Cires	40.658	-8.709	2002-2003
	Costa Nova	40.619	-8.748	2002-2003
	Cais da Pedra	40.548	-8.673	2019
	Lota	40.641	-8.674	2002-2003
	Ponte Cais	40.636	-8.690	2002-2003
	Puxadouro	40.814	-8.645	2019
	Rio Novo	40.695	-8.635	2002-2003
	São Jacinto	40.666	-8.725	2002-2003
	Torreira	40.764	-8.696	2002-2003
	Vista Alegre	40.583	-8.684	2019
	Vagueira	40.562	-8.757	2019
Tagus	Cascais*	38.691	-9.417	1986-2021
	Paço de Arcos	38.690	-9.294	26-01-1972 31-12-1972
	Pedrouços	38.693	-9.225	28-09-1971 27-09-1972
	Trafaria	38.675	-9.236	1972
	Lisboa	38.700	-9.163	1972
	Cacilhas	38.688	-9.148	1972
	Seixal	38.651	-9.077	1972
	Alfeite	38.668	-9.034	09-04-1981 14-05-1981
	Montijo	38.701	-8.977	1972
	Cabo Ruivo	38.766	-9.093	1972
	Alcochete	38.757	-8.966	05-01-1972 31-12-1972
	Ponta da Erva	38.826	-8.969	1972
	Póvoa de Santa Iria	38.856	-9.061	04-08-1972 16-10-1972
	Vila Franca de Xira	38.954	-8.986	1972
Vigo	Vigo port*	42.24	8.73	1992-2021
A Coruña Outer Port	Punta Langosteira*	43.35	8.53	2012-2021

2.2.5 Tidal forcing

The open ocean boundary for the hydrodynamic model implementations are prescribed by applying two different tidal forcing:

1. Astronomic constituents were obtained from Oregon State University (OSU) TOPEX/Poseidon Global Inverse Solution 8.0 (TPX08-atlas). A global model of ocean tides [63] with 1/6 resolution in the global ocean, and higher resolution in specific coastal regions, such as the Iberian Peninsula coast. The constituents are M_2, S_2, N_2, K_2, K_1, O_1, P_1, Q_1, M_F, MM, M_4, MS_4 and MN_4, and are used to propagate the tidal signal in the simulations concerned the hydrodynamic model calibration for the different local domains, which are described in detail later.
2. Water level, obtained from the nearest tidal gauge to the open ocean boundary of each domain (Table 2.4– marked with an asterisk). This type of boundary is intended to determine the ESL applied to the flooding scenarios, described later.

2.2.6 Mean Sea level

Mean Sea level (MSL) data for the Portuguese coast was obtained for the RCP8.5 by analysing sea level variations for 2026–2045 and 2081–2099 [53]. Sea level data correspond to an ensemble mean of 21 CMIP5 AOGCMs (Atmosphere-Ocean General Circulation Models) that support the global estimates of the fifth IPCC report. These data are accessible through the LAS (Live Access Server) interface of the Integrated Climate Data Center (ICDC) of the University of Hamburg (https://icdc.cen.uni-hamburg.de/1/daten/ocean/ar5-slr.html, accessed on 27 February 2021). As mentioned before, the AR6 contains a refinement of the AR5 scenarios by considering new processes, however the MSL predicted to the study region is similar to the one assessed under the AR5 (https://sealevel.nasa.gov/ipcc-ar6-sea-level-projection-tool). Thus, the mean sea-level rise expected for the upcoming decades on the west coast of the Iberian Peninsula is shown in Table 2.5.

Table 2.5 The additional rise in mean sea level for historical, near- and far future periods.

Period	Mean sea-level rise (m)
Historical (1979-2005)	0
Near Future (2026-2045)	0.19
Far Future (2081-2100)	0.68

2.2.7 River discharge

Difficulties in accessing *in-situ* river discharge and continuous monitoring data of the various discharges located in Aveiro, Tagus and Vigo domains led to the use of results of watershed models. Therefore, for the Aveiro lagoon tributaries are used the outputs from the SWAT model [64]. This model was previous calibrated and validated by [65], containing daily values between 1931 and 2010. Regarding Tagus and Vigo tributaries, data from the Hydrological Predictions for the Environment (E-hype) model online database [66] (https://hypeweb.smhi.se/explore-water/historical-data/europe-time-series/) from the Swedish Meteorological and Hydrological Institute (SMHI) is used. SMHI has an extensive repository of simulated long-term series of several variables for the different basins in Europe, such as river discharges. Through the HYPE v 2.1 were obtained time series of 30 years (01-01-1980 to 31-12-2010) for the Tagus and Vigo tributaries. Following the thesis objectives, higher discharges are observed during winter and will be used to assess the climate change impacts during these months (December, January, and February).

Climate change impacts can also be accessed in the SMHI database by selecting a temporal period and its corresponding emission scenario (RCP8.5), which allows observing the prediction of river discharge for each river basin and estimate the future climate discharges (Table 2.6).

Table 2.6 Historical average winter river discharge and prediction (%) for the study regions for the mid and end-century.

Domain	Tributaries	Discharge (m^3s^{-1})	2026-2045	2081-2100
Aveiro	Vouga	136	-11	-21
	Antuã	11	-11	-21
	Cáster	12	-11	-21
	Boco	4	-11	-21
	Ribeira dos Moínhos	13	-11	-21
Tagus	Tagus	994	-8	-23
	Sorraia	85	-8	-23
	Trancão	12	-12	-26
	Vale Michões	3	-8	-23
Vigo	Oitavén-Verdugo	61	-10	-17

2.2.8 Bathymetry

High resolution and reliable bathymetry and topography are critical inputs for numerical modelling to produce accurate results, especially regarding flooding analysis. Given the study's spatial variability and physical constraints, which ranges from a significant fraction of the west coast of the Iberian Peninsula to a small port, a large set of bathymetric and topographic data was considered. The coastal region bathymetry was constructed based on the General Bathymetric Chart of the Oceans (GEBCO) [67]. Concerning the local domains, the data collection will be listed in the sections corresponding to each port due to the diversified environments where the ports are located.

2.3 METHODS

The historical climate data from the different GCMs (section 2.2.1) was first compared with hindcast data with reanalysis winds from the CFSR [56,68]. The comparison identified the GCMs that provide the wavefield closest to the reanalysis data for the annual and winter climates. A dynamical downscaling is then carried out with the SWAN model forced at open boundaries with the coarse wave field provided by WWIII CSIRO data and wind fields obtained from the EURO-CORDEX branch (section 2.2.2). This approach generates relatively fine resolution wave fields both for the historical period, which will be compared with in-situ data provided by coastal buoys, and for the future period. In addition, wind and wave fields are used to classify the wave energy resource and hybrid wave-wind resources by means of a Delphi method, which allows the estimation of the best locations for wave and hybrid wave-wind energy exploitation for the historical and future periods. The assessment of the efficiency of WECs is also performed to determine the most suitable WEC for each location.

The flood assessment resort to these wave fields as inputs for Delft3D WAVE, and later, simultaneously with Delft3D FLOW, in order to simulate the flow and short-wave propagation in ports under extreme events. As mean sea-level rise and storms become more intense, the prediction of these drivers becomes essential to address the climate change impacts in ports, which are susceptible to being flooded due to their location. The flood risk is correlated to the intensity and periodicity of the drivers (relative sea level, storm surge, riverine flows, and wave-induced currents), showing higher risk when the combination of several drivers reaches their highest values.

2.3.1 Wave Power

The wave power is the metric used in this work to quantify the amount of wave energy resource and identify hazardous weather, since higher wave power is linked to winter climate, where higher and energetic waves occur. Thus, the power transmitted by an irregular wave per unit crest width (WP in Wm^{-1}) in deep- water is determined in this study by

$$WP = \frac{\rho g^2}{64\pi} H_s^2 T_e \tag{1}$$

where H_s is the significant wave height, ρ is seawater density (1025 kgm^{-3}), g is the gravitational acceleration, and T_e is the wave energy period. T_e was estimated based on the peak wave period (T_p) [69] as

$$T_e = \alpha T_p \tag{2}$$

where α depends on the shape of the wave spectrum, and an $\alpha = 0.9$ was adopted for this study [70,71].

2.3.2 Wave GCMs statistical analysis

As mentioned before, it is essential to identify the best GCMs that characterize the wave climate of the study area. For this purpose, historical and future *Hs* and *Tp* data obtained from the simulations available on the CSIRO online database are used as the starting point [56]. Each wave variable's statistical analysis must be conducted to determine the most accurate model for reproducing the historical climatic conditions. The skill of these CMIP5 GCMs was evaluated in previous studies [61,72,73] for the Atlantic Arc and the NWIC. This performance metric of GCMs has been applied [74–79] to explore the frequency and severity of climate extremes and has been useful to evaluate the climate models. Other indicators, such as Root Mean Square Error (*RMSE*) and *Bias* were also used to assess the performance of various climate parameters [80–85]. These studies suggested that the model's performance was region and season-specific and some climate models perform better for some variables than others.

Following this approach, the skill of the CMIP5 GCMs [56] was statistically analysed in terms of the overlap percentage (OP) between hindcast [58] and historical probability distribution functions (PDFs) for H_s, T_p and WP. This procedure, previously used in other studies [52,75,86], is more robust than statistics like means and standard deviations and enables the evaluation of how well climate models simulate the data distribution of a variable [75]. OP equal to 100% indicates that both PDFs (numerical and measured *in-situ*) are identical in such a way that the WWIII model under analysis accurately reproduces the observations. In order to compare the historical simulations forced with GCMs with the control simulation forced with CFSR data, H_s, T_p

and *WP* from WWIII simulations were 6-hourly-averaged and spatially interpolated from 0.4º×0.4º (available when forcing with reanalysis data) to 1º×1º (available when forcing with GCMs) by means of a scattered data interpolation method [87].

To analyse future changes in *WP*, a multi-model approach, which minimises the bias and errors of every single model, was considered with $\Delta WP_{MM} = <WP^{F} - WP^{H}>n_{m}$, where n_m is the number of GCMs used to force WWIII and the subscripts *F* and *H* refer to future (*NF* for near future and *FF* for far future) and historical data, respectively. In addition, a consensus criterion [88] was considered to provide significance to ΔWP_{MM} determining the agreement among the different models that make up the multi-model ensemble. The consensus criterion is based on two conditions:

1. Firstly, ΔWP^{n} were calculated both for each *n* model separately and for the multi-model ensemble. The first condition states that for every pixel, at least 60% of all models show the same parity as the multi-model mean.
2. The Mann-Whitney (or Wilcoxon rank-sum test) nonparametric test was imposed for every pixel, on each model and multi-model ensemble [89]. In each grid point was considered a 5% significance. The latter condition consists that at least 60% of the models that fulfilled the first condition passed the Mann-Whitney-Wilcoxon test.

The H_s, T_p and *WP* are the most important variables to describe the wave climate and energy resource. Thus, the evaluation of the skill of WWIII simulations forced with CMIP5 GCMs to simulate the wave propagation along the Atlantic Arc for the 21st century was analysed by means of the OP between hindcast and historical PDFs for H_s, T_p and *WP* (Table 2.7).

Table 2.7 Overlap percentage between hindcast and historical PDFs for H_s, T_p and *WP* from 1980 to 2005 for the Atlantic Arc.

GCM	OP H_S (%)	OP T_p (%)	OP *WP* (%)
ACCESS1.0	77	86	86
BCC-CSM1.1	81	87	88
CNRM-CM3	74	74	76
GFDL-CM3	83	90	88
HadGEM2-ES	73	84	84
INMCM4	80	83	86
MIROC5	87	90	93
MRI-CGCM3	86	85	95

GCMs show an OP greater than 70% for all variables, being the MIROC5 GCM and MRI-CGCM3 models the ones that show the greatest OP for H_s, T_p and *WP*. The same pattern can also be observed in Figure 2.2, where these two models distinguish from the others with higher OP observed along the coast of the Iberian Peninsula. MIROC5 GCM stands with the highest OP along the west coast (>90%) and the lowest ones along the French coast (Figure 2.2g), whereas for MRI-CGCM3 GCM the highest OP is observed in the Bay of Biscay (>90%), slightly decreasing towards the south on the west coast of the Iberian Peninsula (Figure 2.2h). The remaining climate models can be considered satisfactory when compared with previous research in the area. In particular, [52] calculated the OP of winds between all coastal buoys moored around the Iberian Peninsula and data provided by GCMs at the same locations, obtaining a mean OP of 69%.

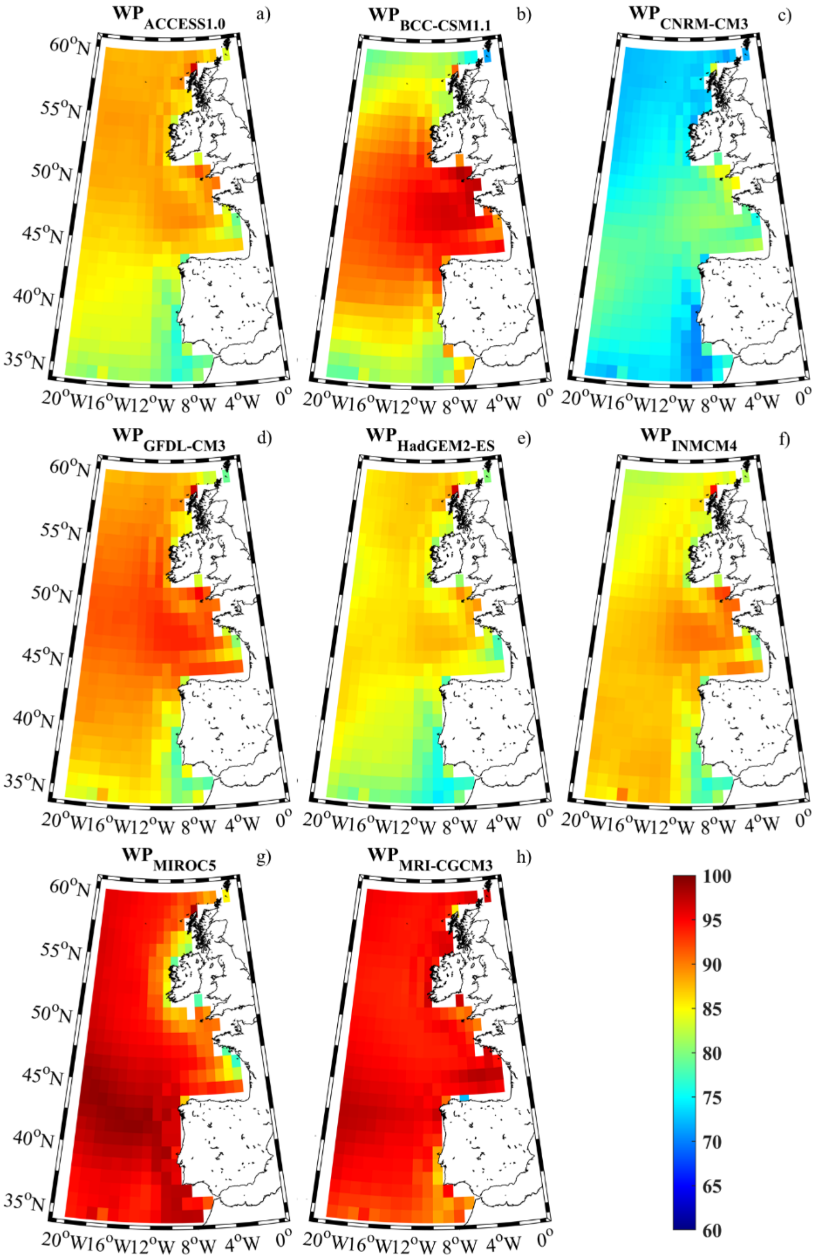

Figure 2.2 - Overlap percentage for wave power in the Atlantic Arc for the models shown in Table 2.7.

Notwithstanding the above considerations, the identified GCMs represent the annual wave climate and are not representative of the extreme weather observed during the winter months. Thus, it is required to identify the best GCM that describe the wave climate in these months. In this regard, the *RMSE* and *Bias* (Equations (3) and (4)) were determined to the 8 GCMS (Table 2.1), taking into account the extreme wave climate (maximum H_s), that is observed during the winter months in the study area (December, January and February) [90] for the return periods of Tr^{10}, Tr^{25} and Tr^{100} (Table 2.8).

$$RMSE = \left(\sqrt{\frac{1}{\mathrm{N}}\sum_{\mathrm{i=1}}^{\mathrm{N}}(\mathrm{M_i}-\mathrm{O_i})^2}\right) \quad (3)$$

$$Bias = \left(\frac{1}{\mathrm{N}}\sum_{\mathrm{i=1}}^{\mathrm{N}}(\mathrm{M_i}-\mathrm{O_i})\right) \quad (4)$$

where M_i and O_i are the GCMs simulations with historical climate and the reanalysis, respectively, and *N* the number of observation pairs. The high resemblance between the wave reanalysis and historical wave climate is represented by a *RMSE* around 0, and *Bias* with positive (negative) values indicate that the historical climate shows lower (higher) values than the reanalysis.

Table 2.8 - Wave height (H_s), *RMSE* (meters) and *Bias* for the winter months considering the 10-, 25- and 100-years return periods.

GCM	***Tr^{10}***		***Tr^{25}***		***Tr^{100}***	
	RMSE	***Bias***	***RMSE***	***Bias***	***RMSE***	***Bias***
ACESS1.0	1.4	1.2	1.5	1.3	1.7	1.4
BCC-CSM1.1	0.7	0.1	0.8	0.1	1.0	0.0
CNRM-CM5	3.7	3.7	4.3	4.2	5.1	4.9
GFDL-CM3	1.5	1.2	1.6	1.2	1.8	1.2
HadGEM2-ES	1.1	0.7	1.3	0.7	1.7	0.7
INMCM4	1.2	0.7	1.3	0.7	1.6	0.5
MIROC5	1.0	0.0	1.4	-0.1	1.9	-0.2
MRI-CGCM3	2.5	-1.9	2.9	-2.2	3.5	-2.6

The *RMSE* and *Bias* indicators show that the BCC-CSM1.1 GCM represents the best climate model to reproduce the IP west coast's extreme wave climate. These results show that the models performance can be seasonal specific, where MIROC5 and MRI-CGCM3 GCM were the best models to reproduce the area's annual mean wave conditions [61,72,73], and BCC-CSM1.1 GCM the extreme wave conditions during winter [91].

2.3.3 Wind Power

Wind power is the metric used to quantify the amount of wind energy. Thus, the wind power density (*WPD* in watts m^{-2}) was determined by:

$$WPD = \frac{1}{2}\rho_a {W_H}^3 \quad (5)$$

where ρ_a is the air density (1.225 kgm^{-3} at 15°C and 1000 hPa) and W_H is the wind speed at the selected hub height (120 m). *WPD* is the power available to be converted by a wind turbine at a specific location. When investigating wind energy changes due to global warming, an important detail is related to changes in the air density due to temperature increases. However, these are not relevant since a 5°C temperature increase represents only a 1% decrease of the *WPD* (for the same wind speed). Since *WPD* is independent of the turbine power curve, it is a suitable wind energy metric.

2.3.4 Wind GCMs statistical analysis

Similar to the statistical analysis performed in section 2.3.2, the wind GCMs performance was also performed. To evaluate the performance of the wind GCMS, a multi-model ensemble approach was applied using a consensus criterion [86,92] to reduce the biases of each model that make up the multi-model. This consensus criterion determines the concordance of the multi-model ensemble wind speed difference (future minus past) with the different models by imposing two conditions to evaluate the statistical significance of the pixels, similar to the one used for the wave statistical analysis (section 2.3.2). The first condition states that at least 75% of all models present the same sign of the multi-model mean in every pixel. The second condition imposes that at least 80% of the models that met the first condition pass the Mann-Whitney-Wilcoxon test [89] (a 5% significant level was considered at each pixel). For further information on the consensus criterion, the reader is referred to [86,92].

The accuracy of this ensemble of RCMs was previously analysed by [51,52,61] in the area under analysis. The error percentage between RCM projected winds and *in-situ* buoys shows values around 10% for the whole Iberian Peninsula and around 8% in the area under study. Additionally, the overlap percentage between the distributions of winds measured by buoys and estimated by RCMs shows values higher than 83% ± 3% for the whole Iberian Peninsula and higher than 85% ± 3% for the area under study.

2.3.5 Extreme sea level

The flood assessment proposed in the thesis objectives is conducted by considering the ESL as input at the oceanic open boundary of the hydrodynamic models. Coastal flooding is linked to storm surge events, that generate an abnormal sea level rise above the predicted astronomical tide. When storm surge and high tides coincide, it can cause extreme flooding in these regions [53,93]. Climate change can worsen these events due to the predicted mean sea-level rise in the upcoming years [5,38,94–96].

By following this line of reasoning, ESL was analysed considering the SSE data recorded at the nearest oceanic tidal gauge of each domain (Table 2.4 – marked with an asterisk). The observed SSE was decomposed into astronomic and residual series and analysed independently to determine the probability of tidal and storm surge levels [53,93]. The tide signal was determined by the astronomic constituents, which were used to obtain the residuals by subtracting the tide to the recorded SSE. The occurrence probability of tidal levels was determined through the analysis of a reconstructed tidal signal of 18.6 years, which corresponds to the 5th component of the lunar nodal cycle [97], considering the constituents obtained by the most uninterrupted time series of SSE.

According to [98], the extreme sea level occurs when the tidal level is higher than the mean high water springs (MHWS) at the present mean sea level. However, MHWS vary geographically, showing different values at each tidal gauge (Table 2.9). Taking into consideration this variability, the probability of occurrence was computed for each tide gauge considered for the ESL analysis (Figure 2.3).

Table 2.9 - Mean high water springs (MHWS) and storm surge for each return periods referred to the mean sea level at each tide gauge.

		Storm Surge (m)		
Tide Gauge	**MHWS (m)**	Tr^{10}	Tr^{25}	Tr^{100}
Barra	3.30	0.95	1.08	1.25
Cascais	3.30	0.92	1.02	1.15
Vigo	3.79	0.68	0.78	0.88
Punta Langosteira	4.49	0.72	0.81	0.89

The residuals filtered from the SSE were used to determine the probability of occurrence of storm surge height by analysing the peaks over a threshold value [53]. The empirical cumulative distribution function (CDF) was computed following [99], and the parameters of the most probable generalised Pareto distribution (GPD) were computed considering a lower and the upper limits at a confidence level of 95 % to investigate the adjustment between empirical and GPD distribution (Figure 2.3 b, d, f).

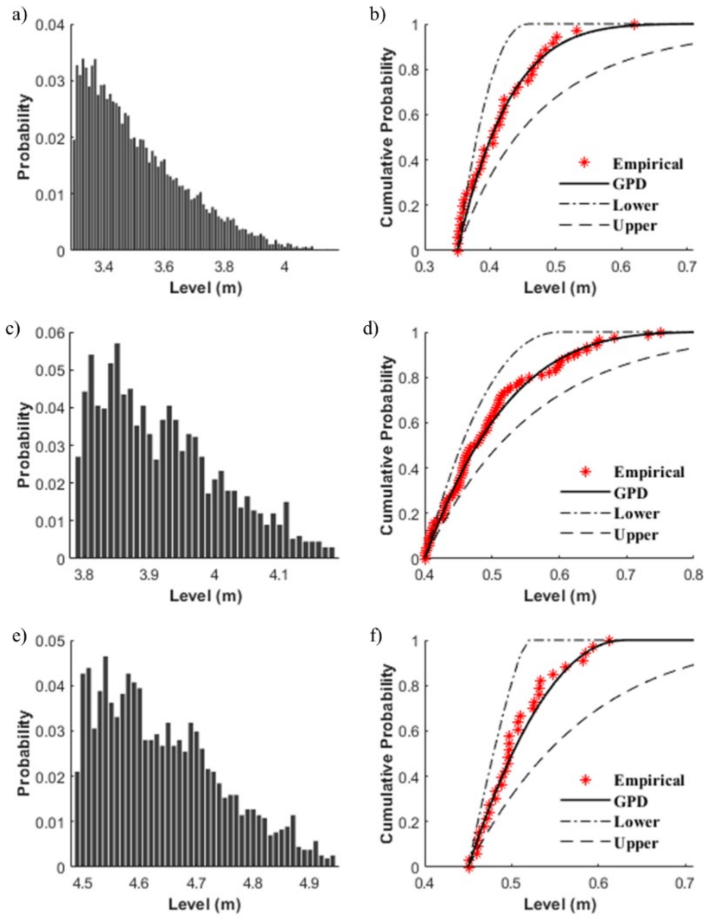

Figure 2.3 - Probability of tidal astronomic levels (a, c, e). Empirical and theoretical cumulative distribution functions (GPD, 5 and 95%) for storm surge levels (b, d, f) for Cascais (a, b), Vigo (c, d) and Punta Langosteira (e, f) locations. For Barra, the reader is referred to [53].

Following this approach, the ESL was determined for the historical and future periods considering that mean sea-level rise dominates the increase in floods, whereas changes in storm surge heights and tides are expected to be minimal in the future [100–102] (Table 2.10). The values for Near Future and Far Future horizons consider MSL rise of 0.19 m and 0.68 m, respectively, that were obtained for the RCP8.5.

Table 2.10 - The return period of 10-, 25- and 100- year with the extreme sea level (in meters) considering a simultaneously high tide and storm surge.

	Domain	**Historical**	**Near Future**	**Far Future**
Tr^{10}	Aveiro	4.25	4.44	4.93
	Tagus	4.22	4.41	4.90
	Vigo	4.47	4.66	5.15
	A Coruña Outer Port	5.21	5.40	5.89
Tr^{25}	Aveiro	4.38	4.57	5.06
	Tagus	4.32	4.51	5.00
	Vigo	4.57	4.76	5.25
	A Coruña Outer Port	5.30	5.49	5.98
Tr^{100}	Aveiro	4.55	4.74	5.23
	Tagus	4.45	4.64	5.13
	Vigo	4.67	4.86	5.35
	A Coruña Outer Port	5.38	5.57	6.06

These inputs are used to feed the hydrodynamic model in order to simulate several climate change scenarios under RCP8.5, including a reference scenario representing the present climate.

2.3.6 River discharge analysis

The flood assessment proposed in the thesis objectives also considers the influence of river discharge, which is imposed as input at the fluvial open boundary of the hydrodynamic models. The daily values (section 2.2.7) obtained were used to calculate the peak discharge for the Tr^{10}, Tr^{25} and Tr^{100} by following an approach similar to that used to determine ESL (Table 2.10). The climate period's return values were calculated by fitting the generalised Pareto distribution (GPD) to identify each driver's extreme values by assuming stationary signals. The future extreme river discharge at daily scale under the RCP8.5 can be estimated (section 2.2.7 – Table 2.6) for the mid and end-century for each region (Table 2.11). Hence, this reduction was considered for the near and far future periods, following an approach similar to previous studies [91,103,104].

Table 2.11 - River discharges ($m^3 s^{-1}$) for 10-, 25- and 100-years return periods.

		Historical			Near Future			Far Future		
Domain	**Tributaries**	Tr^{10}	Tr^{25}	Tr^{100}	Tr^{10}	Tr^{25}	Tr^{100}	Tr^{10}	Tr^{25}	Tr^{100}
Aveiro	Vouga	1302	1559	1943	1158	1387	1729	1028	1232	1535
	Antuã	173	203	245	154	181	218	137	160	194
	Caster	78	94	118	69	84	105	62	74	93
	Boco	63	81	108	56	72	96	50	64	85
	Ribeira dos Moínhos	221	283	381	196	252	339	175	223	301
Tagus	Tagus	5318	6906	9256	4892	6354	8515	4095	5318	7127
	Sorraia	691	895	1196	636	823	1100	532	689	921
	Trancão	101	129	170	89	113	150	74	95	126
	Vale Michões	51	66	88	47	60	81	39	51	68
Vigo	Verdugo	511	606	747	460	546	673	424	503	620

2.2.7 Assessment of the wave energy resource

The wave energy resource assessment was performed by the classification of the historical and future wave energy resource [73] along the northwest coast of the Iberian Peninsula following a method similar to that applied to assess offshore wind energy in previous studies [61,105,106]. The approach, which is based on a Delphi method technique [107], relies on an anonymous participatory method used to gather information based on scientists and engineers' expertise in a structured way, reaching a common consensus. This technique is a process where a panel of experts participate in several rounds of surveys, and the responses are aggregated and subsequently receive feedback in the form of a statistical representation of the collective decision. Experts from the steering committee and participants in the COST Action WECANet: A pan-European Network for Marine Renewable Energy (https://www.wecanet.eu) participated in a three-step process [61] that can be resumed as follows: in the first step, experts were surveyed on common factors that they considered to be influential for WECs, regardless of the particular features and type of WEC. The experts proposed and agreed upon the factors that covered a wide range of aspects, including the physical component that depends on the resource (wave energy and variability), the environmental risks, and the cost. The second step consisted of a normalisation method in order to compare factors with different scales and units. In the latter, experts were consulted again to assign a weight to each factor, following the protocol described later.

The following describes the factors that experts considered essential for WECs.

The wave power (*WP* previously defined) accounts for the wave energy resource. It is well known that a converter device only converts a fraction of the energy due to wave propagation, being that usable fraction dependent on the converter device. Here, it will only be referred to as the available potential (the resource), no matter the converter's features.

The temporal variability of wave energy is an important factor for wave energy resource exploitation. Sites with moderate or stable wave energy potential will be more attractive for any wave energy extraction project than sites with a more energetic but unstable resource. In this context, the Variability index (C_v) [108] is defined as:

$$C_v = \frac{\sigma}{\overline{WP}} \tag{6}$$

where $\overline{WP}$ and σ are the mean and standard deviation of the *WP,* respectively.

Additionally, the Monthly variability index (M_v) [108] was also considered to capture the monthly variability of the wave energy resource. This index was defined as:

$$M_v = \frac{WP_{M1} - WP_{M12}}{\overline{WP}} \tag{7}$$

where $\overline{WP}$ is the annual mean of the *WP*, and WP_{M1} and WP_{M12} represent the *WP* for the most and least energetic months, respectively.

The effectiveness in the exploitation of wave energy resource is also an important factor because some WECs work correctly and efficiently in a particular range of periods and heights. In this context, the *Downtime* index was considered. The upper and lower threshold of the *Downtime* index were H_s = 8 m and H_s = 1 m, respectively. Following [109], the upper- threshold of the downtime indicates the WEC interruption due to extreme waves conditions, and the lower threshold indicates the length of time of calms, a minimal wave power generation. This index provides a measure of the time in which a WEC is operating efficiently and safely.

The *Risk* index considers extremely large waves that can also highly impact ocean engineering safety. This index was calculated in terms of the annual extreme wave heights (*EWH*) using the Gumbel distribution, a widely used method. The extreme wave height was then calculated for a 50-year return period based on the Gumbel curve method [61,86,92].

Finally, water depth (*WD*) and distance to coast (*DC*) indices were also determined for every grid pixel to account for cost factors related to grid connection and marine engineering. The *WD* index calculation was obtained from the ETOPO bathymetry [110], and the *DC* index considered the Global Self-consistent, Hierarchical, High-resolution Geography (GSHHG) coastline database [111].

As previously mentioned, each index has its own magnitude and units, which makes it necessary to perform a normalisation before integrating all indices into a single one that characterises the wave energy resource for every grid pixel. Following a procedure similar to the one described in [86], all factors were normalised considering 10 categories within the limit values provided by [61], except *WD* and *DC,* which were normalised considering five categories as in [86]. Note that the last two factors remain unchanged in time since they only depend on topographic constraints. As previously mentioned, normalised values were calculated [86,92] so that both positive and negative indices render positive factors allowing the data to be displayed in a best-worst (best = 1, worst =0) scale. The partitions of the interval [0 , 1] were calculated considering a 1/(*n*-1) step, where *n* is the number of categories (10 or 5, depending on the index). Table 2.12 and Table 2.13 show the range of values for each parameter.

Table 2.12 - Normalized criterion for *WP*, *Cv*, *Mv*, *Downtime* and *Risk* indices, considering 10 categories within the limits provided by [3]. The partitions of the [0 - 1] interval were calculated considering a 1/(*n*-1) step, where *n*=10 is the number of categories. Optimal indices values correspond to 1 and the worst to 0.

Normalized value	***WP*** **(Wm^{-1})**	***Cv***	***Mv***	***Downtime*** **(%)**	***Risk*** **(m)**
0.0	< 10	> 1.9	> 2.5	> 90	> 21
0.1	10-20	1.7-1.9	2.25-2.5	90-80	20-21
0.2	20-30	1.5-1.7	2.0-2.25	80-70	19-20
0.3	30-40	1.3-1.5	1.75-2.0	70-60	18-19
0.4	40-50	1.1-1.3	1.5-1.75	60-50	17-18
0.5	50-60	0.9-1.1	1.25-1.5	50-40	16-17
0.7	60-70	0.7-0.9	1.0-1.25	40-30	15-16
0.8	70-80	0.5-0.7	0.75-1.0	30-20	14-15
0.9	80-90	0.3-0.5	0.5-0.75	20-10	13-14
1.0	> 90	< 0.3	< 0.5	< 10	< 13

Table 2.13 - Normalized criterion for *WD* and *DC* indices. The partitions of the [0 - 1] interval were calculated considering a 1/(*n*-1) step, where *n*=5 is the number of categories. Optimal values correspond to 1 and the worst to 0.

Normalized value	***WD*** **(m)**	***DC*** **(º)**
0.00	>500	>4.0
0.25	100-500	3.0-4.0
0.50	50-100	2.0-3.0
0.75	25-50	0.5-2.0
1.00	0-25	<0.5

As previously mentioned, fifteen experts in wave energy and engineers were consulted to give each normalised factor a weight coefficient to perform a Delphi method for the offshore hybrid wind-wave energy resource [61]. The weight coefficients and corresponding standard deviation for the wave energy factors evaluated are described in Table 2.14. The standard deviation was calculated as:

$$\sigma = \sqrt{\frac{\sum_{i=1}^{N} |A_i - \bar{A}|^2}{N_E - 1}} \tag{8}$$

where A is the weight coefficient, $\bar{A}$ is the mean value of A and N_E is the number of experts (15).

The final wave energy resource index (I_{wave}) was obtained by adding the weighted indices, which can be expressed as:

$$I_{wave}^{k} = \sum_{i=1}^{N} \langle W_i^k \rangle \, I_i^k \tag{9}$$

where N is the number of indices, I_i^k is the normalised value of each index (Table 2.12 and Table 2.13), $\langle W_i^k \rangle$ is the mean weight of each index (Table 2.14, where weights are described as a mean and standard deviation) to each grid point *k*.

Table 2.14 - Weight coefficient and standard deviation of wave energy factors, environmental risk factors and cost factors averaged to the fifteen wave energy experts and engineers consulted.

Coefficient	Weight ± σ
WP	0.44 ± 0.05
C_v	0.10 ± 0.01
M_v	0.05 ± 0.01
Downtime (%)	0.10 ± 0.02
Risk (m)	0.14 ± 0.01
WD	0.07 ± 0.02
DC	0.10 ± 0.01

As a result of the Delphi method, the wave energy resource classification is similar to [86] according to the criteria specified in Table 2.15.

Table 2.15 - Classification of the wave energy resource (w_{er}).

Class	Categorization value	Resource Potential
1	$w_{er} \leq 0.2$	Poor
2	$0.2 < w_{er} \leq 0.3$	Marginal
3	$0.3 < w_{er} \leq 0.4$	Fair
4	$0.4 < w_{er} \leq 0.5$	Good
5	$0.5 < w_{er} \leq 0.6$	Excellent
6	$0.6 < w_{er} \leq 0.7$	Outstanding
7	$w_{er} > 0.7$	Superb

2.3.8 Assessment of the wind energy resource

The assessment of wind energy resource was carried out by applying a method similar to that used for the wave resource, as both wind and wave resources share the same characteristics and constraints. In this context, the wind energy resource assessment can be performed considering eight indices, following the methodology applied by [71,86,92] to assess the richness of the wind resource, the variability, the environmental risk and cost parameters. These indices are: Annual average wind speed (W_{ann}), rich level occurrence (*RLO*), downtime (*DWNT*), coefficient of variation index (C_v), monthly variability index (M_v), risk of extreme wind speeds (*Risk*), water depth (*WD*) and distance to coast (*DC*).

The richness of the wind resource parameter accounts for the potential wind energy resource available, which is also independent of the converter device. The W_{ann} index is divided into seven partitions following the NREL classification scheme [112]. The rich level occurrence measured by means of the *RLO* index is defined as the frequency of *WPD* higher than 200 Wm^{-2}.

The effectiveness in the exploitation of the wind energy resource is also a key factor because wind turbines only operate in a particular range that allows energy production. The upper (cut-off speed) and lower (cut-in speed) thresholds of this range are usually around 4 and 25 ms^{-1}, respectively [86,92]. In this sense, the *DWNT* index measures the total time with useful wind speed occurrence (EWSO) in which a wind turbine is producing electricity.

The temporal variability of the wind energy was also considered for the wind energy exploitation by means of the C_v and M_v indices that were calculated as for the wave resource, but changing *WP* by *WPD*.

Similar to *EWH*, a risk factor that considers extreme wind speeds (*EWS*) was also determined by means of the *EWS* over a 50-year period calculated based on the Gumbel curve method.

The calculation of the cost factors (*WD* and *DC*) was performed for every grid pixel, using the same method applied for the wind resource and the same normalization process described in Table 2.13.

The other indices were also subjected to the same normalization process applied in the wind energy classification. The normalization criterion is described in Table 2.16.

Table 2.16 - Normalization criterion used for *RLO*, *DWNT*, *Cv*, *Mv* and *EWS* indices related to richness factors, variability factors and environmental risk factors.

Normalized	***RLO* (%)**	***DWNT* (%)**	**C_v**	**M_v**	***EWS* (ms^{-1})**
0/9	< 10	< 10	> 1.9	> 2.5	> 27
1/9	10-20	10-20	1.7-1.9	2.25-2.5	25.5–27.0
2/9	20-30	20-30	1.5-1.7	2.0-2.25	24.0–25.5
3/9	30-40	30-40	1.3-1.5	1.75-2.0	22.5–24.0
4/9	40-50	40-50	1.1-1.3	1.5-1.75	21.0-22.5
5/9	50-60	50-60	0.9-1.1	1.25-1.5	19.5-21.0
6/9	60-70	60-70	0.7-0.9	1.0-1.25	18.0-19.5
7/9	70-80	70-80	0.5-0.7	0.75-1.0	16.5-18.0
8/9	80-90	80-90	0.3-0.5	0.5-0.75	15.0-16.5
9/9	> 90	> 90	< 0.3	< 0.5	< 15.0

The weight coefficients for wind energy indices based on the Delphi method classification are described in Table 2.17.

Table 2.17 - Weight coefficient in the wind energy classification. The standard deviation was calculated (Equation (8)) where A is the weight coefficient, $\bar{\boldsymbol{A}}$ is the mean value of A and $\boldsymbol{N_E}$ is the number of experts (10) consulted in [106].

Richness			**Variability**		**Risk**	**Cost**	
W_{ann}	***RLO***	***DWNT***	**C_v**	*M_v*	***EWS***	***WD***	***DC***
0.22 ± 0.02	*0.10 ± 0.01*	*0.22 ± 0.02*	0.10 ± 0.01	0.05 ± 0.01	0.14 ± 0.01	0.07 ± 0.01	0.10 ± 0.02

The final wind energy resource index (I_{wind}) was obtained by adding the weighted indices, which can be expressed as:

$$I_{wind}^{k} = \sum_{i=1}^{N} \langle W_i^k \rangle \ I_i^k \tag{10}$$

where *N* is the number of indices, I_i^k is the normalised value of each index (Table 2.16 and Table 2.13), $\langle W_i^k \rangle$ is the mean weight of each index (Table 2.17, where weights are described as a mean and standard deviation) to each grid point *k*.

2.3.9 Classification of the hybrid energy resources

The classification of the hybrid wind-wave energy resource was also determined by taking into account the final wave (Equation (9)) and wind (Equation (10)) energy resource by the combined index (*CI*) of wind and wave energy resources, which can be defined as:

$$\text{Combined Index} = \frac{I_{\text{wave}} + I_{\text{wind}}}{2} \tag{11}$$

2.3.10 Sensitivity analysis of the energy resources

A sensitivity analysis was also applied to the factors used for the wave and wind classification to analyse the final index's dependence on the variability of the weight coefficients. The sensitivity test followed a Monte Carlo approach applied to each grid point, and can be depicted in the following steps:

1. Random variation of each index, allowing each weight to vary randomly:

$$W_i^k = \langle W_i^k \rangle + R^k \ \sigma(W_i^k) \tag{12}$$

   where R^k is a random number with an equal probability between ±1 and σ is the standard deviation. Note that random number was used for each grid point *k*.

2. Renormalisation of each Index. Weights were normalised before random variation in such a way that

$$\sum_{i=1}^{N} W_i^k = 1 \tag{13}$$

   This procedure cannot guarantee the normalisation after the random variation. Thus it is necessary to renormalise the weights by

$$W_i^k = \frac{W_i^k}{\sum_{i=1}^{N} \langle W_i^k \rangle} \tag{14}$$

3. The wave energy resource index was recomputed considering the new weights

$$I_j^k = \sum_{i=1}^{N} W_i^k I_i^k \tag{15}$$

   where *j* refers to the different realisations of the Monte Carlo approach, similar to [61], with a total of 100,000 realisations.

4. The root-mean-square error (*RMSE*) of each grid point *k* was calculated between the reference index I^k and the different realisations I_j^k

$$RMSE^k = \sqrt{\frac{\sum_{j=1}^{J} \left(I^k - I_j^k\right)^2}{J}} \tag{16}$$

5. Finally, the $RMSE_j$ associated to each realisation was calculated as

$$RMSE_j = \sqrt{\frac{\sum_{k=1}^{N_p} \left(I^k - I_j^k\right)^2}{N_p}} \tag{17}$$

   where N_p is the number of grid points.

6. The mean value of the classification index was calculated as the average of all realizations by using the following expression

$$\langle I_j^k \rangle = \frac{1}{J} \sum_{j=1}^{J} I_j^k \tag{18}$$

2.3.11 Parameters to assess the efficiency of the WECs

The assessment of the efficiency and cost of energy over the life cycle of WECs along the study area is also analysed. Comparing the efficiency of different WECs is not straightforward due to the wide variety of technologies (point absorber, terminator or attenuator) for harvesting wave energy. Each WEC has a characteristic nominal power and a power matrix representing the maximum energy that the WEC could harvest. This confers a range of power that each WEC can efficiently capture from the wave energy flux for different sea states. These sea states can be characterised by the H_s and T_p parameters obtained from the numerical modelling for the past and only through numerical modelling for future projections [72].

Two parameters have been widely used in the literature to assess and compare the efficiency of different devices for specific sites, namely the load factor and the capture width [113,114].

The power load factor (ε) for a specific WEC can be expressed in % by:

$$\varepsilon = 100 \times \frac{P_E}{P_{max}} \tag{19}$$

where P_{max} represents the maximum electric power, provided by the manufacturer [115], that can be harvested with a specific WEC, and P_E the average electric power that can be extracted with a certain device.

$$P_E = \frac{1}{100} \sum_{i=1}^{n_T} \sum_{j=1}^{n_H} p_{ij} P_{ij} \tag{20}$$

where p_{ij} is the percentage of occurrence of a given sea state bined in terms of H_s and T_p, and P_{ij} is the electric power for the same bin obtained from the power matrix provided by the manufacturer for that specific WEC [113,114].

The capture width (C_w, in meters) represents the width of the wavefront from which the energy is extracted, and it can be defined as the ratio of the WEC electric power (P_E) to the wave power resource (P) defined above:

$$C_w = \frac{P_E}{P} \tag{21}$$

According to [116] these indices are the most appropriate to compare the efficiency of different WECs. Actually, they have been used to evaluate the performance of the different technologies along the Portuguese continental coastal environment [113].

The amount of electricity generated (E_P, in MWh) [117] during the WEC lifetime can be expressed by:

$$E_P = \frac{P_E \times Lifetime}{1000} \tag{22}$$

where *Lifetime* represents the total service life of the WEC (25 years). The cost of energy (C_E, in EUR/MWh) [118] is the total cost involved during the lifespan use of the WEC, including the capital, operation, and maintenance cost, divided by E_P:

$$C_E = \frac{\sum C_A + C_{OM}}{E_P} \tag{23}$$

where C_A is the capital cost and C_{OM} is the operation and maintenance cost of a specific WEC. Two types of WECs are studied, a point absorber (Aqua Buoy [119]) and an attenuator (Pelamis [118]), whose sum of capital, operation, and maintenance costs can be estimated to be around 8.9 and 2.2 million euros, respectively, for a 25-year lifetime (see [118,120]).

The difference between the future and the historical period for all the variables (P, ε, P_E, C_w, and C_E) will be calculated as $\Delta X = X^F - X^H$, where X is the variable under study and the subscripts F and H refer to the future and historical data, respectively.

2.4 NUMERICAL MODELLING

The assessment of the energy resource and flood is only viable through numerical modelling due to the large spatial and temporal scales involved. Several numerical models are suitable for modelling the hydrodynamics in deep, coastal and shallow waters. The selection of the model should consider the knowledge of the model's limitations, the processes under study and the available data. Considering these criteria, it was decided to use a package of numerical models developed by Delft University of Technology in the Netherlands in this study. The choice relies on the institution's expertise on free-surface waves and flood risk that led to the development of the following models listed below.

Simulations from regional to local were carried out using the Delft3D model. Delft3D suite is composed of several modules capable of interacting with each another. Delft3D was used to simulate the hydrodynamics of the study area due to the available features comprising tide and wind-driven flows, river flow, and wave-driven currents.

The wind-generated waves (wave-averaged type) are modelled by the WAVE module [121], which uses the third-generation spectral wave model SWAN (an acronym for Simulating Waves Nearshore) [122], herein referred to as WAVE. SWAN computes the evolution of random, shorted-crested wind-generated waves in coastal regions with deep, intermediate and shallow water. Similar to Delft3D, it is developed at the Delft University of Technology in the Netherlands, although with an independent team apart from Delft3D. However, it can be coupled with the Delft3D suite through WAVE.

The hydrodynamic conditions are modelled with the Delft3D-FLOW module [123], a multi-dimensional hydrodynamic model that simulates non-steady flow resulting from tidal and meteorological forcing a rectilinear or a curvilinear grid, herein referred to as FLOW. This model can predict the flow in shallow seas, coastal areas, estuaries, lagoons, rivers and lakes. It aims to model flow phenomena in which the horizontal length and time scales are significantly larger than the vertical scales. The hydrodynamic of local ports are modelled with FLOW and is used in WAVE, which is executed in a combination between the modules allowing a two-way wave-current interaction.

Simulations used a compiled Delft3D version 4.04, which was updated on a monthly basis. The Delft3D source code is open source (svn.oss.deltares.nl), and the work developed in this thesis were used windows machines. FLOW and WAVE (through SWAN) is parallelised using MPI, which attaches good scalability of the machines' physical resources and allows faster and reliable simulations.

The spatial and temporal variability of the simulations led to a careful setting of the coupling interval between WAVE and FLOW, which is a compromise between computational accuracy (in theory, more frequent coupling is better) and computational efficiency (less frequent coupling is better). Locations with tidal dominance (range or rapidly changing wave and current conditions) require an hourly coupling for a practical and useful interval.

The application developed consists of an integrated setup of WAVE and FLOW. Two lower resolution grids will match the NWIC and the coastal region of the NWIC, respectively, while the highest resolution grids were designed to cover each port location. The results from the wave database supplied WAVE following a nested-grid approach designed specifically for the selected ports. The FLOW consists of an integrated high-resolution numerical model that uses sub-domains dedicated to the selected ports, simulating the wave-current considering reflection and refraction.

The implementation of each model is based on bathymetric and topographic data available and listed in this chapter and comprises the current port structures identified later for each port, which can be adaptable for future climate simulations. This approach provides the tool to give a step forward in the integrating modelling of separated coastal/port systems and gives conditions for a holistic view of the selected ports comprising each port individually.

Hydrodynamic and wave models are implemented and calibrated, comparing model predictions with *in-situ* data and determining the best-fit calibration parameters. Afterwards, the model accuracy is determined by quantifying the adjustment between model results and observations. Finally, the models are validated with independent data. Detailed model setup and implementations for energy and flood assessment are described in the forthcoming chapters.

Chapter 3

RESOURCE ASSESSMENT

This chapter provides an assessment of the wave and hybrid wave-wind energy resources in the study area by applying a Delphi method based on physical factors capable of classifying the energy resource. The Delphi method is applied to wave and hybrid wave-wind energies, followed by evaluating the efficiency of two wave energy converters (WEC) in the study area. This approach allows identifying the offshore areas with the highest energy surrounding a port and a study of efficiency and cost of energy over the life-cycle of two WECs to exemplify a planned wave energy farm in the study area.

3.1 INTRODUCTION

The development of renewable sources of energy has become essential to mitigate the human influence on climate change. Ocean energy is one of the five strategic priorities of Europe to meet growing energy demand; to significantly improve energy security, reducing the dependence on energy imported from outside Europe; to support sustainable jobs and growth in the "blue economy"; to create a new internal market capable of exporting marine renewable energy products and services; and to reduce carbon emission from burning fossil fuels, also improving the air quality.

Wave energy emerges as a renewable energy with high potential for exploitation, presenting many positive aspects such as i) the ocean covers around 71% of the Earth, making it very accessible; ii) waves contain a considerable amount of potential energy (they are generated and transmit energy across the ocean for thousands of miles); iii) wave energy has a higher density and predictability than solar and wind energy [47,124].

For the reasons above mentioned, a strenuous effort is underway to assess the wave energy resource (a complete summary in [108,125–129]) and to develop technologies allowing a sustainable extraction and exploitation of the wave energy [113,130–133] at global [113,125,134,135] and regional [130,136–143] scales for wave power resource, and their combined exploitation with wind resources [144] in Europe [45,46,61,145,146] and worldwide [147,148]. These studies determined the most suitable locations for wind exploitation and the specific wave energy conversion (WEC) devices for those locations. Hybrid wind-wave farms can reduce installation and maintenance costs [145,149] and increase the energy availability of a location by compensating the intermittent wind nature with good wave conditions. In addition, the technology readiness level and the Levelized cost of energy (LCOE) of wind technologies are one step ahead of wave technologies. Furthermore, the wave farms can protect the wind farms, and the combined wind-wave farms can provide coastal protection [150–152]. Moreover, the wave energy harvest viability relies on the rate between the energy cost and the capital required for the projects, which may vary depending on the targeted market and the revenue [117,118,153–155] predicted at the present currency. Current wind and wave energy technology are intended to have a useful life of at least 20 years [118,156]. Therefore, when using this combined energy resource, it is vital to take into account not only current climatic conditions, but also the effect of climate change on wind and wave energy resources in the near future [72].

Climatic simulations based on the scenarios defined by the Intergovernmental Panel on Climate Change (IPCC) [157] are used to analyse the climate change impact on wave energy production both at global and regional scales [47,70,109,158,159]. The GMCs accuracy is highly dependent on the model performance and climate sensitivity, which decreases for long term projections [13]. However, to carry out a reliable analysis of the future wave energy resource, it is necessary to characterise not only the regional wave regime, but also several factors related to environmental risks and costs [71,106,158], which include the proximity to technical and logistic hubs, such as the ports, that allow for more affordable maintenance and serve as aggregators of products and services. These aspects must be analysed at a smaller spatial scale to find the optimal location for the installation of energy farms through numerical modelling.

For this reason, aligned with the urgent need to reduce the carbon footprint for the industries and sectors related to oceans, seas and coasts, ports can use renewable energy sources to enhance energy efficiency. This effort to tackle the climate crises requires healthy seas and sustainable use of their resources to create alternatives to fossil fuels. Transitioning to a sustainable blue economy requires investment in innovative technologies, such as wave energy which will create new green jobs and businesses in the blue economy.

Following this strategy, this chapter evaluates the wave resource in the study area aiming to identify the offshore areas around the ports under analysis with the highest energy potential, using a Delphi method that considers the estimation of the wave power resource and other factors such as stability, risk, and installation and maintenance costs. This Delphi method provides insights and an assessment of the applicability of future wave resource harvest potential. An additional assessment of the hybrid wave and wind energy resource is also applied in the near future due to the brevity of the EU and ONU energy goals, followed by an evaluation of the future efficiency and cost of energy of two WECs along the northwest coast of the Iberian Peninsula for the near future.

To fulfil these assessments, the need to use numerical models is a must, such as SWAN model, through DELFT3D-WAVE, which is applied to the northwest coast of the Iberian Peninsula, considering the best GCMs previously identified: MIROC5 and MRI-CGCM3 GCMs, the best climate models to reproduce the annual and winter wave conditions in this area.

3.2 GCMS MULTI-MODEL ANALYSIS

The *WP* is the most important variable to assess the wave resource and is also a valuable indicator for coastal risk considering that higher *WP* is linked to more energetic waves and consequently greater damage to coastal structures. Thus, *WP* was calculated employing a multi-model mean of the WWIII simulations driven by MIROC5 and MRI-CGCM3 GCMs and is represented in Figure 3.1 for the historical period (1979-2005, Figure 3.1a) and the near (2026-2045, Figure 3.1b) and far (2081-2100, Figure 3.1c) future.

Macroscopically, the *WP* pattern is similar for all periods, although it tends to decrease in most of the Atlantic Arc along the 21st century. During the historical period, *WP* values greater than 60 kWm^{-1} were obtained in front of the Scottish and Irish coasts and at ocean locations north of 43 ºN (Figure 3.1a), which is in agreement with previous studies [134,143]. Regarding the northwest IP coast, *WP* values are also similar to those obtained in previous investigations, with higher values around 50 kWm^{-1} in the western part of the Bay of Biscay [160–162], and lower values (30-40 kWm^{-1}) in the central and east sections of the Bay of Biscay [139,163,164], and along the west IP coast (20-35 kWm^{-1}) [165,166].

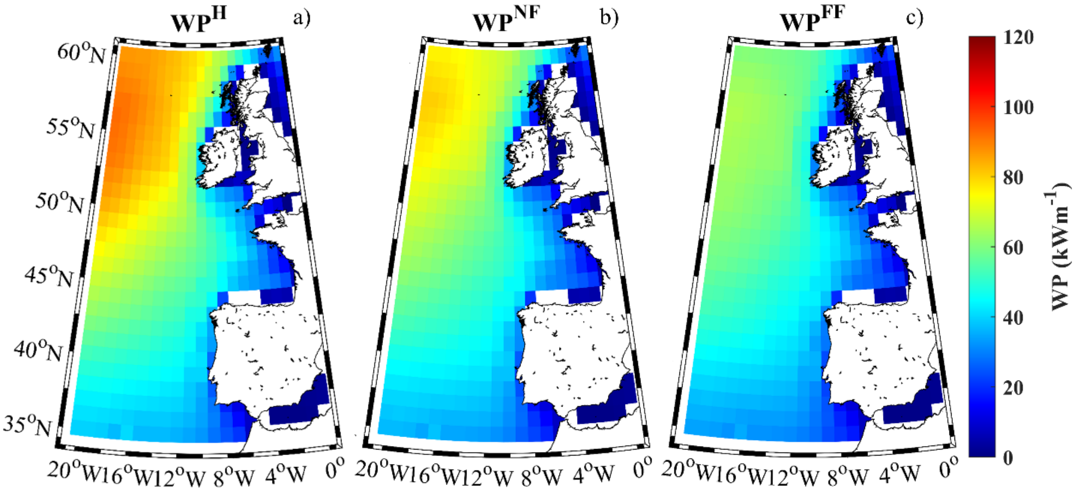

Figure 3.1 - Multi-model mean of the wave power (kWm^{-1}) in the Atlantic Arc calculated by means of WWIII simulations forced with MIROC5 and MRI-CGCM3 GCMs for (a) the historical period (1979- 2005), (b) near future (2026- 2045) and (c) far future (2081- 2100).

The *WP* in this region diminishes for the future periods, remaining confined to ocean locations north of 47.5ºN. Similarly, *WP* values ranging from 40 to 60 kWm^{-1} reach 35ºN for the historical period at ocean locations and tend to retract northward in the future. This decrease in *WP* is consistent with trends detected by [167] for the historical period (1985-2008) in the same area. Despite the interest of this analysis to detect changes in wave energy resource, the coarse resolution is not fine enough to provide good results in near coastal areas, which are precisely the areas projected for future exploitation due to lower installation and maintenance costs and proximity to the ports under analysis in this thesis.

3.3 DYNAMICAL DOWNSCALING

The implementation of a model aiming to assess the wave energy resource should follow the recommendations of the International Electrotechnical Commission (IEC). The IEC lists a series of recommendations to develop a standard methodology for assessing energy resources of ocean waves, the technical specification IEC-TS 62600-101 [126]. These assessments are classified into three different stages: Reconnaissance (stage 1), Feasibility (stage 2) and Design (stage 3). All stages have the corresponding model setup requirements, depending on the physical process, boundary types and spatial and temporal resolutions (Table 3.1). However, all stages must cover a minimum of ten years of sea state, with a minimum of three-hour output.

Table 3.1 - Description of the IEC-TS 62600-101 model setup recommendations. Mandatory (•), Recommended (∗), Acceptable (○), Not permitted (-). Adapted from [168].

	Component	**Reconnaissance**	**Feasibility**	**Design**
Type of assessment	Uncertainty	High	Medium	Low
	Longshore extent (km)	>300	20-500	<25
Physical processes	Wind-wave growth	•	•	•
	White capping	•	•	•
	Quadruplet interactions	•	•	•
	Wave breaking	○	•	•
	Bottom friction	○	•	•
	Triad interactions	•	•	•
	Diffraction	•	•	•
	Refraction	•	•	•
	Wave reflections	•	•	•
	Wave-current interactions	•	•	•
Numerics	Parametric wave model	○		
	2nd generation spectral wave model	○	○	
	3rd generation spectral wave model	∗	∗	∗
	Mild-slope wave model	○	○	○
	Spherical coordinates	•	○	○
	Non-stationary solution	○	○	○
	Min. spatial resolution (m)	5000	500	50
	Min. temporal resolution (h)	3	3	1
	Min. numerical wave frequencies	25	25	25
	Min. numerical azimuthal direction	24	24	24
Boundary conditions	Parametric boundary	○	-	-
	Hybrid boundary	○	○	○
	Spectral boundary	∗	∗	∗

Considering the above characteristics, the wave model developed for this study is limited by the spatial and temporal resolution and by the inputs of the GCM database available online. The available data described in Chapter 2 restrain the wave model to a Stage 1 model. Thus, Delft3D-WAVE module [121], which uses the third-generation spectral wave model SWAN [122], was used to develop a Stage 1 model to assess the wave energy resource.

The model developed comprised a set of three nested domains (Figure 3.2b). The first domain (L1) extended from 35.5°N and 12.5°W to 49.5°N and 0.5°W, the second domain from 36.5°N and 10.8°W to 47.8°N and 0.5°W and the third domain was confined to a fringe with a mean width of 100 km to the coast. The horizontal resolution of the grids of the different domains was 1/3°×1/3°, 1/9°×1/9° and 1/27°×1/27°, respectively. The bathymetry was generated from the General Bathymetry Chart of the Oceans.

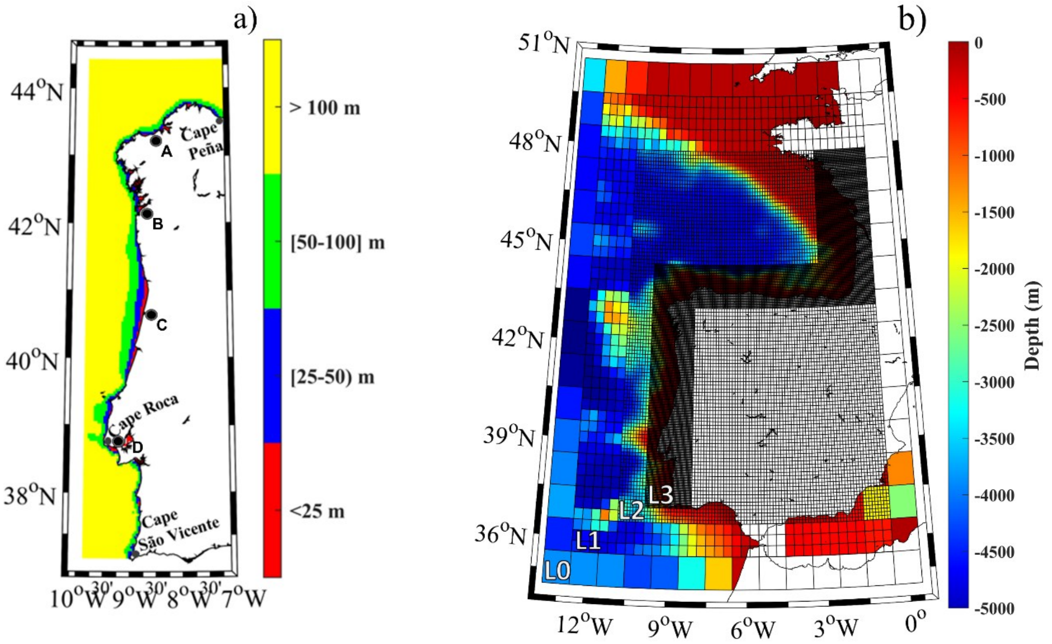

Figure 3.2 - Study area with the depth arranged in four bins and the selected ports: **A** A Coruña Outer Port, **B** Vigo Port, **C** Aveiro and **D** Lisbon Port (a). Numerical domains (b) used in the SWAN model. Nested approach from CSIRO GCMs (L0) using three domains (L1, L2 and L3) covering different areas and different resolutions (0.3°×0.3°, 0.1°×0.1° and 0.037°×0.037°, respectively).

The wave spectrum was discretised to 25 frequencies (0.0418-1 Hz) and 36 directional bands. Time and space varying wave boundary conditions were prescribed (as TPAR files [121]) containing non-stationary wave parameters, such as H_s, T_p and Directional spreading (S_m), with a temporal resolution of 6 hours. These boundaries were obtained from the MIROC5 and MRI-CGCM3 GCMs, which showed the greatest OP for H_s, T_p and *WP*, and were forced along the boundary at each grid node intersection between domain L0 and L1.

Local wave generation was also driven by the 6-hourly wind input (10 m above sea level) with a spatial resolution of 12.5 km for the MIROC5-CCLM4-8-17 RCM (Regional Climate Model) and MRI-CGCM3 GCM. Wave growth by the wind was computed with the Komen exponential term [169,170]. Physical parameters such as triads, bottom friction, depth-induced breaking and quadruplets were included. SWAN simulations were run with hourly data output covering the historical (1979-2005), the near future (2026-2045) and the far future (2081-2100) periods.

3.4 MODEL VALIDATION

The SWAN model's accuracy was also statistically analysed for each one of the selected climate models. It was considered the historical period and evaluated the OP between *in-situ* and modelled buoys and numerical PDFs for H_s, T_p and *WP*. The latter is not a SWAN output, and therefore, *WP* will be determined beforehand.

As mentioned before, the dynamical downscaling along the northwest Iberian Peninsula coast was performed using the SWAN model fed with the WWIII simulations driven with wind from the MIROC5-CCLM4-8-17 RCM and MRI-CGCM3 GCM (see the sketch in Figure 2.1). The accuracy of the SWAN model near the coast was analysed for the historical period using the OP functions between *in-situ* and modelled buoys (Figure 3.3), and numerical PDFs for H_s, T_p and *WP*.

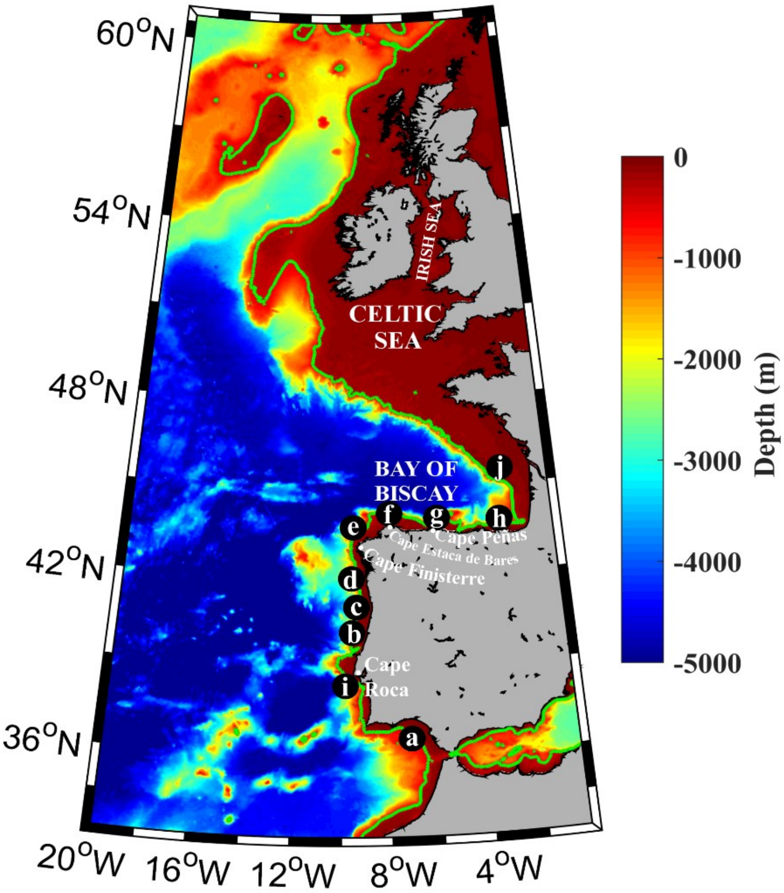

Figure 3.3 - Bathymetry of the Atlantic Arc area. The green line represents the 1000 m isobath. Location of the *in-situ* and modelled buoys for a) Cádiz, b) Figueira da Foz, c) Leixões, d) Cape Silleiro, e) Villano Sisargas, f) Estaca de Bares, g) Cape Peñas, h) Bilbao-Vizcaya, i) SIMAR 1042054 and, j) SIMAR 1068084.

The OP is greater than 74% for all buoys and variables (Table 3.2) for both MIROC5-CCLM4-8-17 RCM and MRI-CGCM3 GCM (Table 3.3), except for Cádiz, Leixões and Figueira da Foz buoys, where the OP is around 62% for T_p. The geographic location of these coastal buoys, close to the shore (Figueira da Foz and Leixões) and close the boundary of the nested domain, slightly decreases the SWAN accuracy due to the grid resolution in these areas. The averaged OP for all buoys is 80±4% for H_s, 75±8% for T_p and, 83±5% for *WP,* forcing the SWAN model with wind from the MIROC5 CCLM4-8-17 RCM. In the same way, the average OP for all buoys is 84±4% for H_s, 73±8% for T_p and, 85±5% for *WP,* forcing the SWAN model with wind from MRI MRI-CGCM3 GCM. Previous research in the same area [52] calculated the OP between winds at all coastal buoys moored around the Iberian Peninsula and winds determined by numerical models at the same locations, obtaining a mean OP of 69±10% for GCMs and 83±3% for RCMs.

Table 3.2 - Overlap percentage between *in-situ* buoy data and historical numerical PDFs considering the MIROC5 CCLM4-8-17 RCM climate model for H_S, T_p and *WP* for the Atlantic Arc. D represents the distance between the nearest gridpoint of the SWAN grid to the buoy location.

Buoy name	D (km)	OP H_S (%)	OP T_p (%)	OP *WP* (%)
Cádiz	3.9	88	64	80
Figueira da Foz	1.6	83	57	96
Leixões	0.5	75	74	82
Cape Silleiro	1.6	80	76	81
Villano Sisargas	0.5	78	74	76
Estaca de Bares	2.1	83	84	84
Cape Peñas	1.8	80	84	84
Bilbao-Vizcaya	2.0	79	80	83
SIMAR 1042054	0.7	74	77	75
SIMAR 1068084	1.8	78	75	85

Table 3.3 - Overlap percentage between *in-situ* buoy data and historical numerical PDFs considering the MRI-CGCM3 GCM climate model for H_S, T_p and *WP* for the Atlantic Arc. D represents the distance between the nearest gridpoint of the SWAN grid to the buoy location.

Buoy name	D (km)	OP H_S (%)	OP T_p (%)	OP *WP* (%)
Cádiz	3.9	91	62	88
Figueira da Foz	1.6	93	62	96
Leixões	0.5	81	63	84
Cabo Silleiro	1.6	83	78	83
Villano Sisargas	0.5	80	74	77
Estaca de Bares	2.1	82	85	83
Cape Peñas	1.8	84	79	84
Bilbao-Vizcaya	2.0	84	79	85
SIMAR 1042054	0.7	84	74	84
SIMAR 1068084	1.8	80	76	82

3.5 DELPHI: A METHOD TO CLASSIFY THE WAVE ENERGY RESOURCE

The following Delphi method relies on the use of a multi-model ensemble using the SWAN model forced with boundary conditions from WAVEWATCH III simulations driven by historical and future winds from MIROC5 and MRI-CGCM3 GCMs under the RCP8.5 scenario, focusing on the exploitation of wave energy resources in the present (1979-2005), the near future (2026- 2045), and the far future (2081- 2100).

The evolution of each normalised Index of the Delphi was analysed by comparing the near and far future with historical values. The water depth (*WD*) and the distance to coast (*DC*) indices were not considered because they only depend on topographic constraints and, hence, they will remain constant in the future.

The wave power index for the historical period (WP^H, Figure 3.4a) shows the highest values (0.6 - 0.7) at ocean locations around Cape Finisterre and Estaca de Bares, between 42.5ºN and 44.5ºN. In general, lower *WP* values are detected along coastal areas, and, in particular, the lowest *WP* values (below 0.2) are detected along the Bay of Biscay coast (southeast corner of the Bay of Biscay) and along the Portuguese coast south Lisbon. The wave power index for the near future (WP^{NF}, Figure 3.4b) is similar to that obtained for the historical period, although slightly decreasing in the whole area. When observing the far future (WP^{FF}, Figure 3.4c), the general decrease is more noticeable than from the historical to the near future, showing a maximum index around 0.6. The decrease is especially evident for the southeast corner of the Bay of Biscay. That decrease is consistent with that observed for nearshore locations in Figure 3.4, although the coarse resolution of that figure makes it difficult to analyse the projected changes for coastal locations.

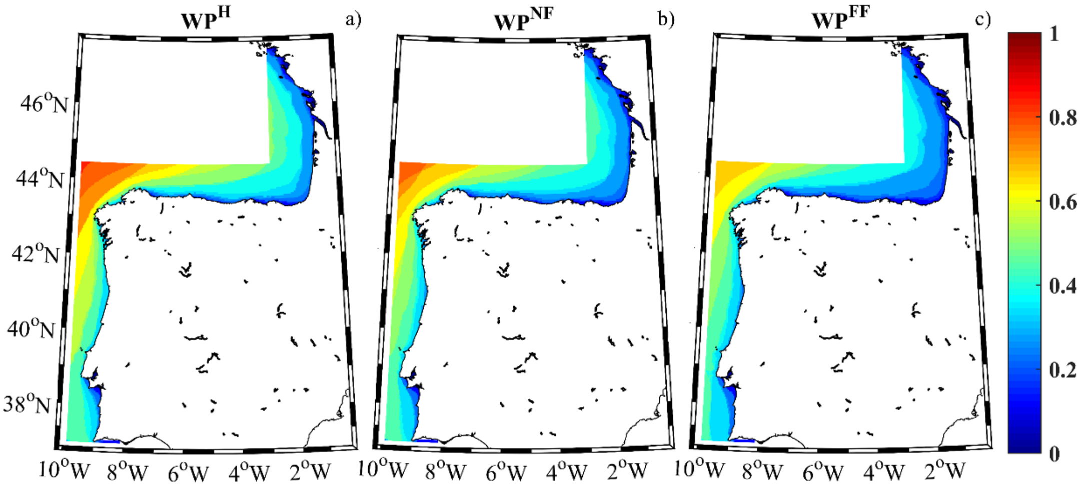

Figure 3.4 - Wave power index along the northwest Iberian Peninsula coast and the Atlantic French coast for (a) the historical period (1979–2005), (b) near future (2026–2045) and (c) far future (2081–2100).

Future changes in the indices that account for stability in the wave power resource, C_v and M_V, are represented in Figure 3.5 and Figure 3.6, respectively. C_v index shows values ranging from 0.35 to 0.45 for the historical period (Figure 3.5a). Future C_v shows a decrease of ~ 0.05 in the variability index for the near future at ocean locations with values around 0.35 northern 41ºN and around 0.45 southern 41ºN (Figure 3.5b). This decrease is higher for the far-future, ~0.1 when compared with the historical values. Only a narrow fringe along the south bay of the Biscay coast shows a slight decrease in the future.

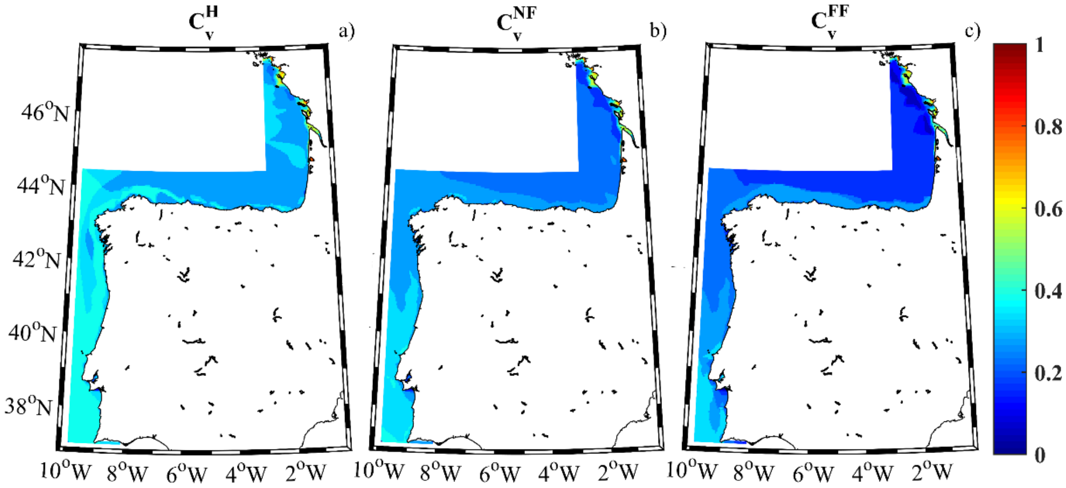

Figure 3.5 - C_v index along the northwest Iberian Peninsula coast and the Atlantic French coast for (a) the historical period (1979- 2005), (b) near future (2026- 2045) and (c) far future (2081- 2100).

The M_v index, which accounts for monthly variability, shows historical values around 0.55 for the whole region except for ocean locations in the northwest corner of the area under study, where values around 0.45 were detected (Figure 3.6a). M_v index shows historical values slightly higher than those obtained for the C_v index, which suggests that the primary source of variability is the presence of short events, possibly linked to the passage of fronts during winter. M_v index for the near future shows no significant changes, increasing in some specific locations such as in the south coast of the Bay of Biscay and the west coast of the Iberian Peninsula (Figure 3.6b). In contrast, the far-future monthly variability index decreases for the whole region (Figure 3.6c). In summary, both variability indices show a common decreasing pattern for the future in most regions, which implies worse future conditions for wave energy harvesting, except a nearshore area along the south coast of the Bay of Biscay.

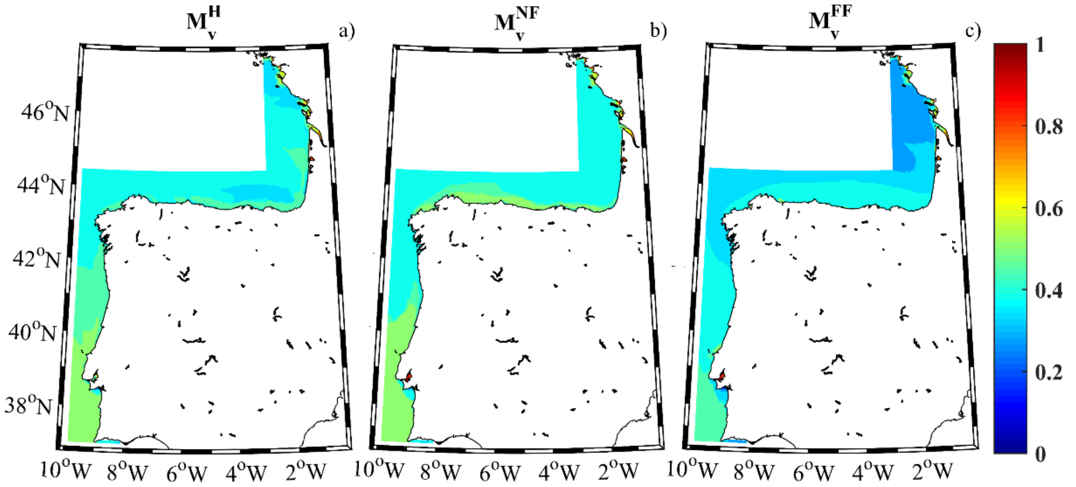

Figure 3.6 - M_v index along the northwest Iberian Peninsula coast and the Atlantic French coast for (a) the historical period (1979- 2005), (b) near future (2026- 2045) and (c) far future (2081- 2100).

The *Downtime* index's behaviour, which indicates a measure of the time in which a WEC is working efficiently, is represented in Figure 3.7. Note that the *Downtime* index has been normalised so that favourable conditions correspond to values close to 1. Overall, wave conditions are optimal in most regions, with downtime values close to 1 for the historical period, which indicates that most of the time H_s is between 1 m and 8 m, allowing WECs to work efficiently and adequately (Figure 3.7a). Conditions are slightly worse at nearshore locations, especially at the southeast corner of the Bay of Biscay, where the lower limit (H_s < 1 m) is reached more frequently. This region becomes wider under near future conditions (Figure 3.7b) and progressively increases to a higher area under far future conditions (Figure 3.7c), with a projected *Downtime* index between 0.8 and 0.9. No changes were detected for the rest of the northwest Iberian Peninsula coast.

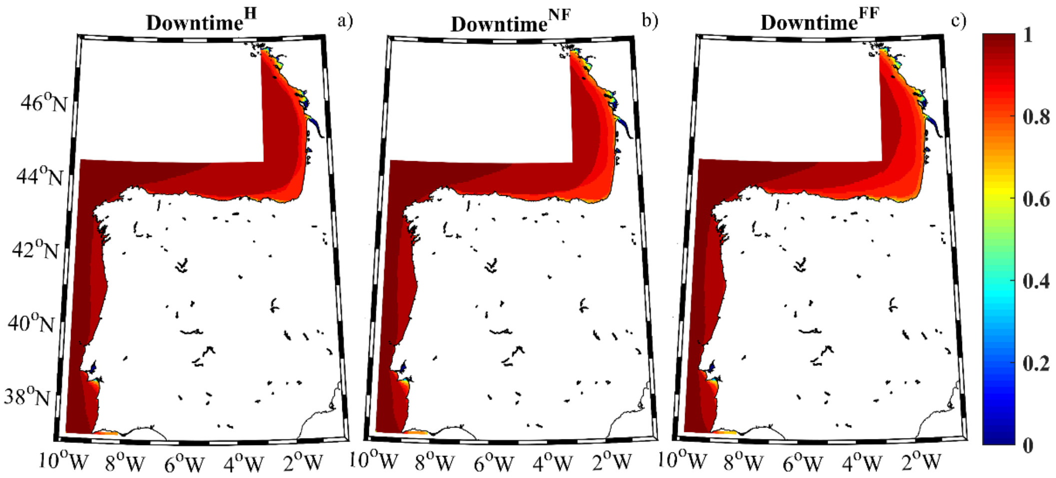

Figure 3.7 - *Downtime* index along the northwest Iberian Peninsula coast and the Atlantic French coast for (a) the historical period (1979- 2005), (b) near future (2026- 2045) and (c) far future (2081- 2100).

The *Risk* index, which considers extreme waves that can affect ocean engineering safety, is represented in Figure 3.8. The *Risk* Index for the historical period shows high values (0.7) in oceanic water in the northwest corner of the domain, increasing towards the shore reaching the maximum value of 1 along the whole Atlantic coast (Figure 3.8a). The *Risk* index projected for the near future retracts along the Atlantic coast, with values ~0.5 in the northwest corner of the domain (Figure 3.8b). This trend is more noticeable for the far future (Figure 3.8c), with lower values (0.3) in the northwest corner of the domain and the continuous retraction of the area with a higher index. Note that the regions with the lowest values (the worst risk conditions) correspond to the zones where the best conditions in terms of the *WP* index are achieved. Comparing historical and future periods, the places with the highest decrease in extreme conditions measured by the *Risk* index (see, for example, the area around 10ºW and 44ºN) coincide with regions with an increase in mean values measured by the *WP* Index. Some regions previously studied [167,171] showed that the changes in extreme wave values do not necessarily match the changes observed for mean values.

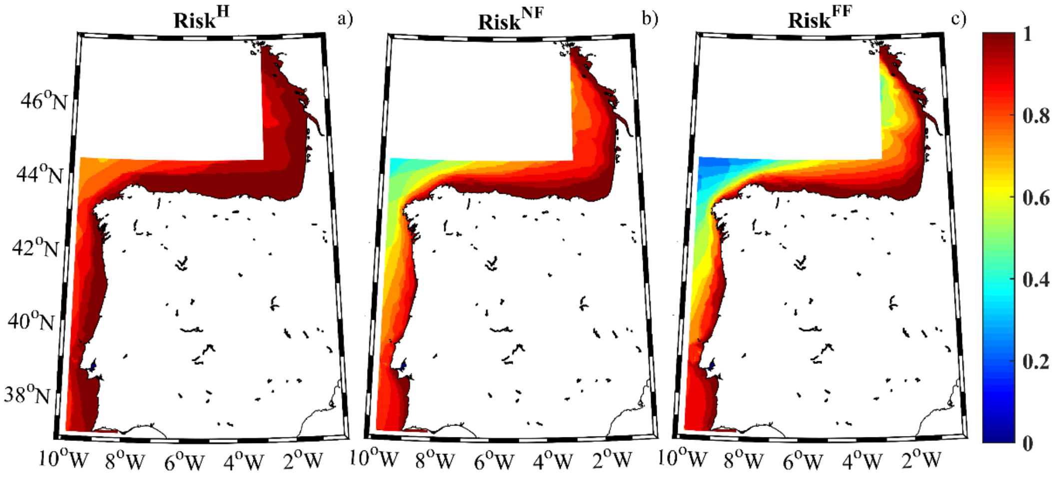

Figure 3.8 - *Risk* index along the northwest Iberian Peninsula coast and the Atlantic French for (a) the historical period (1979- 2005), (b) near future (2026- 2045) and (c) far future (2081- 2100).

As mentioned before, the distance to coast (*DC*) (Figure 3.9a) and water depth (*WD*) (Figure 3.9b) do not vary in time since they only depend on topographic constraints.

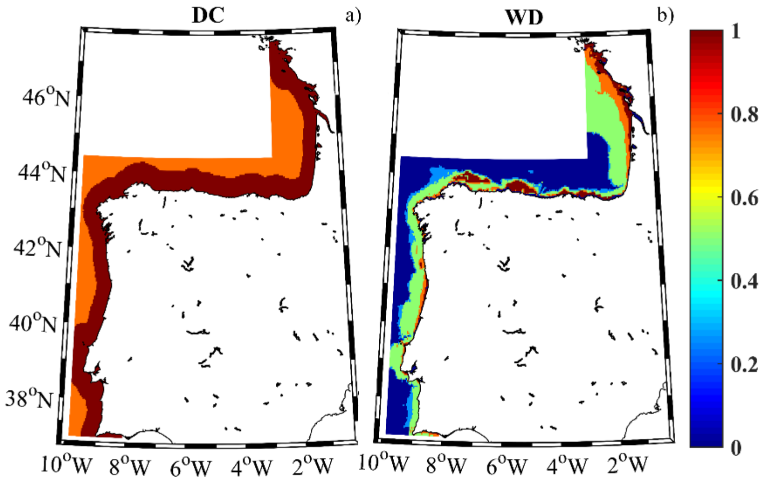

Figure 3.9 - Distance to coast (*DC*) and water depth (*WD*) for the northwest Iberian Peninsula coast and the Atlantic French coast.

The mean classification index obtained solving Equation (9) is shown in Figure 3.10. The mean Index for the historical period (Figure 3.10a) shows the highest values (>0.65) at ocean locations around Cape Finisterre and Estaca de Bares, between 42.5ºN and 44.5ºN, similarly to the *WP* index. The west coast of the Iberian Peninsula also shows values greater than 0.6 north of Cape Roca and 0.5 for the rest of the domain. The near future (Figure 3.10b) shows the same pattern for the index in most of the domain, however, the regions with higher values decreased significantly by 0.15 at the ocean location with the highest index, whereas the area between this location and Cape Roca retracted to a small fringe (~0.6). For the far future (Figure 3.10c), an identical decreasing pattern is found for the same locations, with the highest index (0.6) restrained to a fringe between Cape Roca and Cape Peñas.

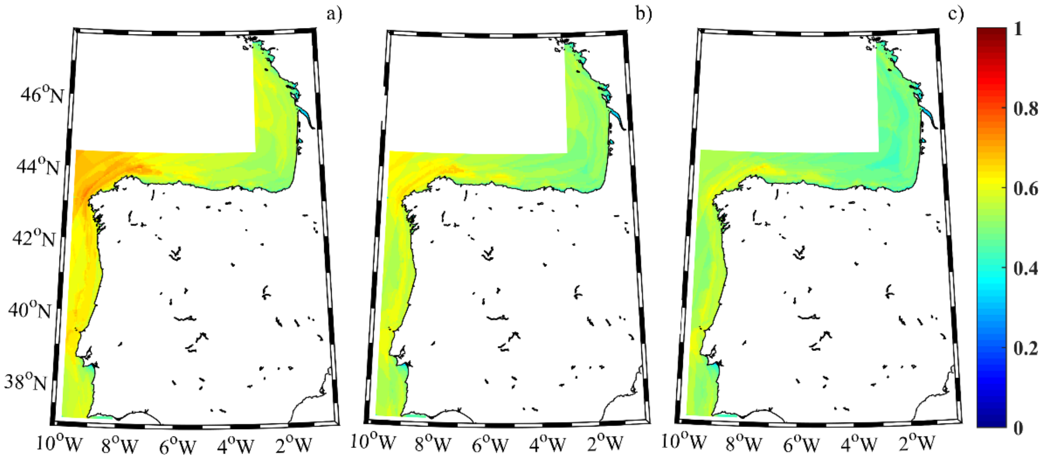

Figure 3.10 - Mean classification index along the northwest Iberian Peninsula coast and the Atlantic French for (a) the historical period (1979- 2005), (b) near future (2026- 2045) and (c) far future (2081-2100).

3.5.1 Sensitivity analysis

The final index's dependence to classify wave resources on the variability of the weight coefficients applied to the normalised indices is shown in Figure 3.11. This figure shows the $RMSE^k$ calculated for each pixel k following Equation (16). Overall, its scale is at least one order of magnitude lesser than observed for the mean classification index (Figure 3.10). In particular, the low $RMSE^k$ observed in a continuous fringe covering the coast between Cape Roca and Cape Peña, which contrasts with the high values of the mean classification index observed for the same area. This result is also verified in the histogram of the $RMSE_j$, calculated for all cases following Equation (17) (Figure 3.12). The $RMSE_j$ histogram presents values below 0.07, the most probable $RMSE_j$ around 0.03, again one order of magnitude smaller than the mean classification index. The sensitive analysis shows that the final index's dependence on the weight coefficients selected is not decisive.

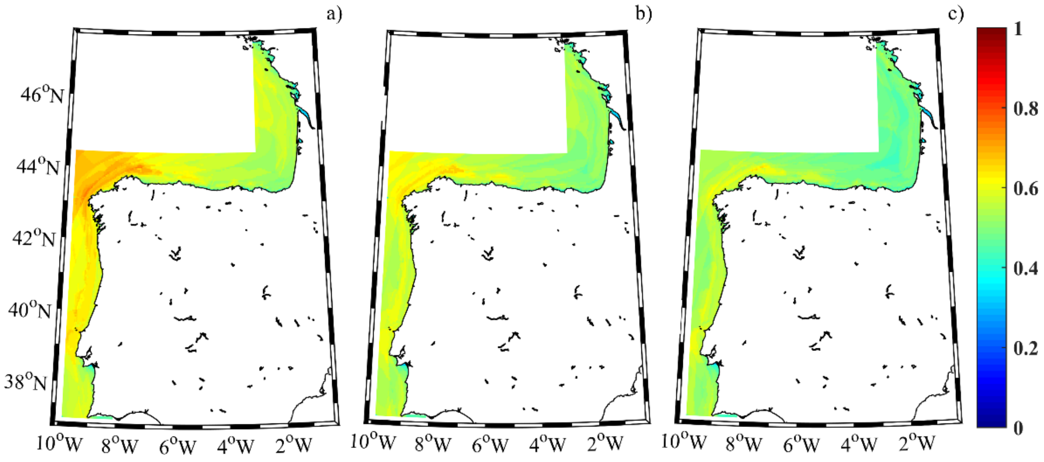

Figure 3.11 - Sensitivity analysis for wave energy. Map of the $RMSE^k$ for the historical period (1979-2005), (b) near future (2026- 2045) and (c) far future (2081- 2100).

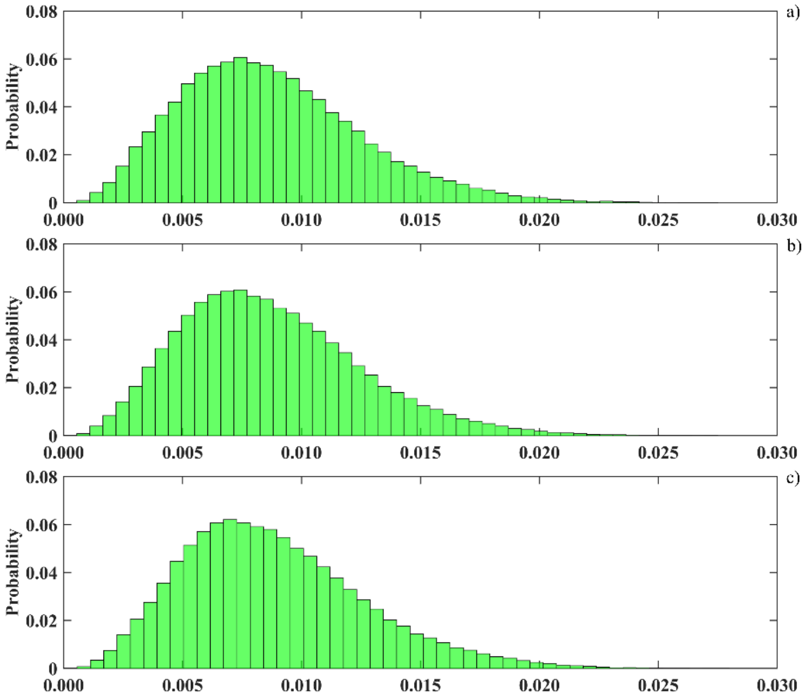

Figure 3.12 - Sensitivity analysis for wave energy: $RMSE_j$ histogram for (a) the historical period (1979-2005), (b) near future (2026- 2045) and (c) far future (2081- 2100).

3.5.2 Resource classification

As a result of the application of the Delphi method, the wave energy resource along the northwest coast of the Iberian Peninsula coast was classified for the historical (Figure 3.13a), near future (Figure 3.13b) and far future (Figure 3.13c), according to the criteria specified in Table 2.15. For the historical period, only a small fringe of oceanic water from Cape Finisterre to Cape Estaca de Bares reached superb (7), while the west coast of the Iberian Peninsula, especially from Cape Roca to Cape Peñas, reached the score of outstanding (6). Finally, the excellent (5) score was reached along the east part of the Bay of Biscay coast and at several regions along the Atlantic coast south of Cape Roca. Almost no region attained values equal to or smaller than 4. The pattern obtained for the near future (Figure 3.13b) is, in general, similar to that obtained for the historical one but with lower scores. The small fringe of oceanic water from Cape Finisterre to Cape Estaca de Bares will reach outstanding (6). According to previous studies, this area close to the Iberian Peninsula's northwest corner will be one of the few areas where wind energy is projected to increase during this century [52]. Thus, this area will constitute a strong possibility for the deployment of hybrid wind and wave converters [61]. Finally, most of the Atlantic coast of the Iberian Peninsula will reach a score of excellent (5) and the southeast corner of the Bay of Biscay a score of good (4). At the end of the century (Fig 14c), the general score decreased even more, with the outstanding (6) score found only in isolated spots in the Cape Finisterre and Cape Estaca de Bares. Most of the west coast of the Iberian Peninsula shows the score of excellent (5) with some locations near Cape Roca and most of the Bay of Biscay coast with the score of good (4).

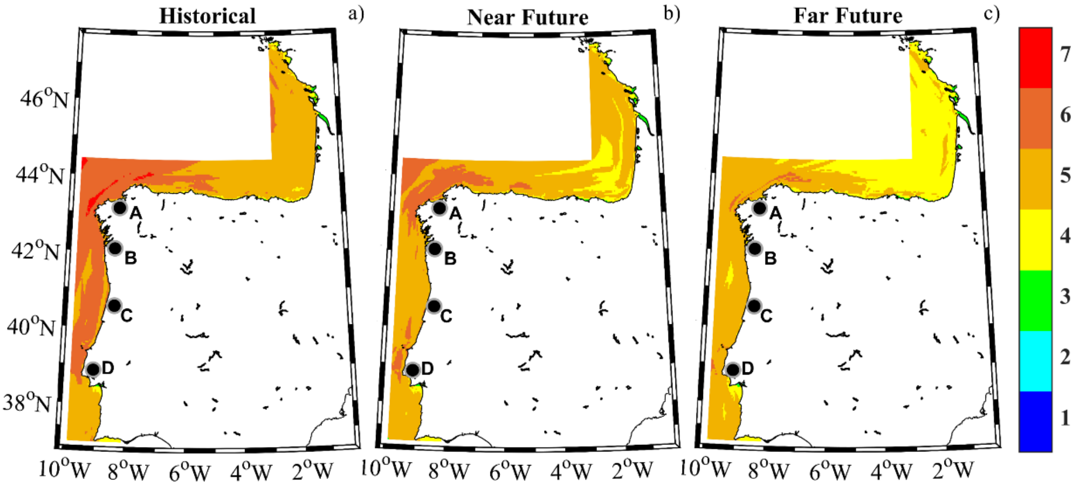

Figure 3.13 - Classification of the wave energy resource according to Table 2.15, for the northwest Iberian Peninsula coast and the Atlantic French coast for (a) the historical period (1979- 2005), (b) near future (2026- 2045) and (c) far future (2081- 2100). Locations of the **A** A Coruña Outer Port, **B** Vigo Port, **C** Aveiro Port and **D** Lisbon Port.

The historical period classification shows that the regions surrounding the ports located in the uppermost part of the NWIC benefit from the highest score in the coastal region, with a score of outstanding (6), and a small fringe with a score of superb (7) in the vicinity of the A Coruña Outer port and Vigo Port. The Ports of Aveiro and Lisbon lies in areas with excellent (5) scores but relatively close to outstanding (6) locations. For the near future period is found that the port surroundings are classified as excellent (5), but close to ocean areas with a classification of outstanding (6), except for Aveiro Port. The general classification score in the port's surroundings diminishes for the far future period, where the ports areas show a score of excellent (5), whereas A Coruña Outer Port benefits from a small fringe of the ocean with an outstanding classification (6).

3.6 HYBRID ENERGY RESOURCE PARAMETERS ASSESSMENT

As mentioned before, the assessment of the hybrid wave-wind energy resource was performed through the classification of the available resource in the study area, following a procedure similar to the one used in section 3.5. The following hybrid wind-wave classification relies on the use of a multi-model ensemble approach for 8 wind RCMs (section 2.3.4) and results from the SWAN model downscale of MIROC5 GCM under the RCP8.5 scenario, focusing on the exploitation of hybrid wind-wave energy resource for the near future (2026- 2045).

The assessment of the potential energy resource for a hybrid wind-wave farm was carried out along the northwest Iberian Peninsula coast for the near future as mentioned before. From the methodology followed resulted in spatial maps of all the wind and wave indices that make up the calculation of categories of resource richness, variability, risk and cost.

The richness category accounts for the available resource in terms of W_{ann}, *RLO* and *DWNT* for the wind resource (Figure 3.14) and *WP* and *DWNT* for the wave resource (Figure 3.15). W_{ann} index (Figure 3.14a) shows the maximum value of 1 in the ocean and decreases to less than half near land. This is consistent with the *WPD* values shown for this region in [172]. The *RLO* index pattern is similar to the that found for W_{ann}, with the lowest values (around 0.1) being detected along the coast and the maximum values, of around 0.7, on the northwest region. The *DWNT* index shows a smaller difference (0.2) between the ocean and the coastal region.

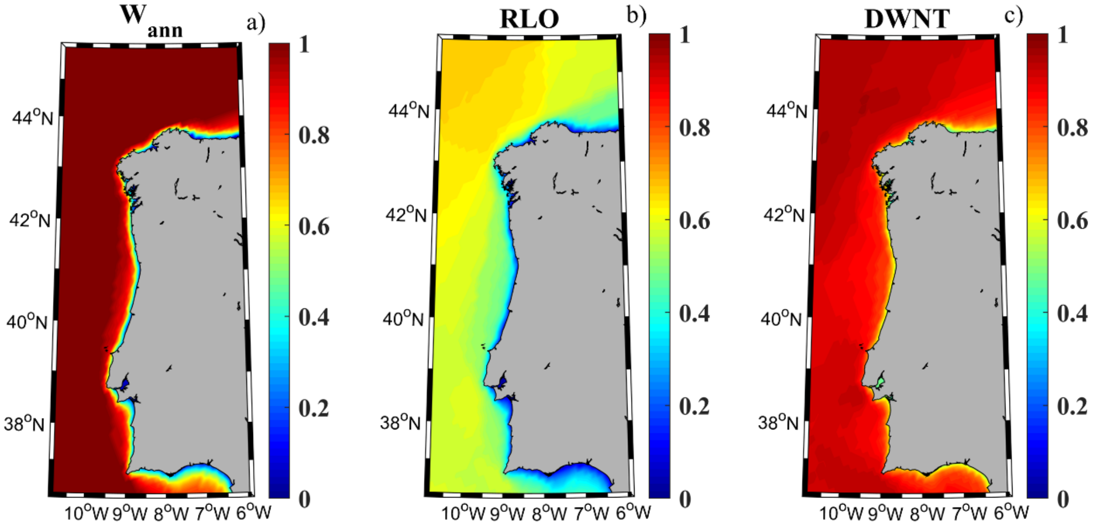

Figure 3.14 - Richness indices for wind energy resource. Annual average wind speed (a), rich level occurrence (b), and downtime (c) in the NW Iberian Peninsula for the near future (2026–2045).

Wave richness resource shows some similarities to that of the wind, mostly due to the waves being generated as a result of the wind forcing on the water surface. *WP* index (Figure 3.15a) shows its maximum (0.7) on the northwest region, as the *RLO* index. The lowest *WP* values are found near the coast, in particular in the Gulf of Cadiz (< 0.2). Regarding wave *DWNT* index (Figure 3.15b), it should be noted that it reaches the maximum value of 1 in most of the study area, except in the Gulf of Cadiz.

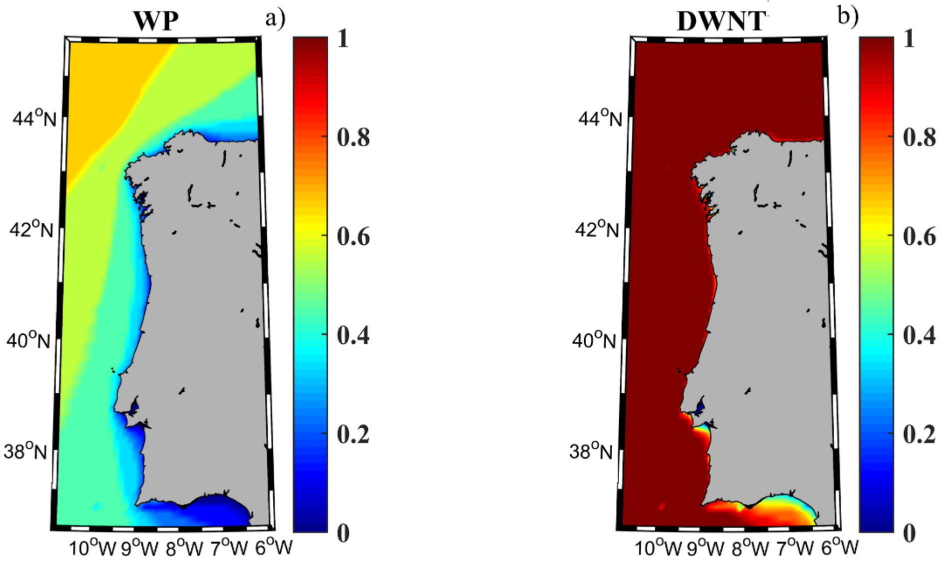

Figure 3.15 - Richness indices for wave energy resource. Wave power (a) and downtime (b) in the NW Iberian Peninsula for the near future (2026–2045).

The indices that account for the wind power resource variability, C_v and M_v, are represented in Figure 3.16a and Figure 3.16b, respectively. In general, the highest C_v values of 0.5 are in the ocean region south of Cape Finisterre, which is not optimal for energy production. However, the M_v index is very good (> 0.8) for the same region. These M_v and C_v indices suggest the presence of short events linked to seasonal fronts.

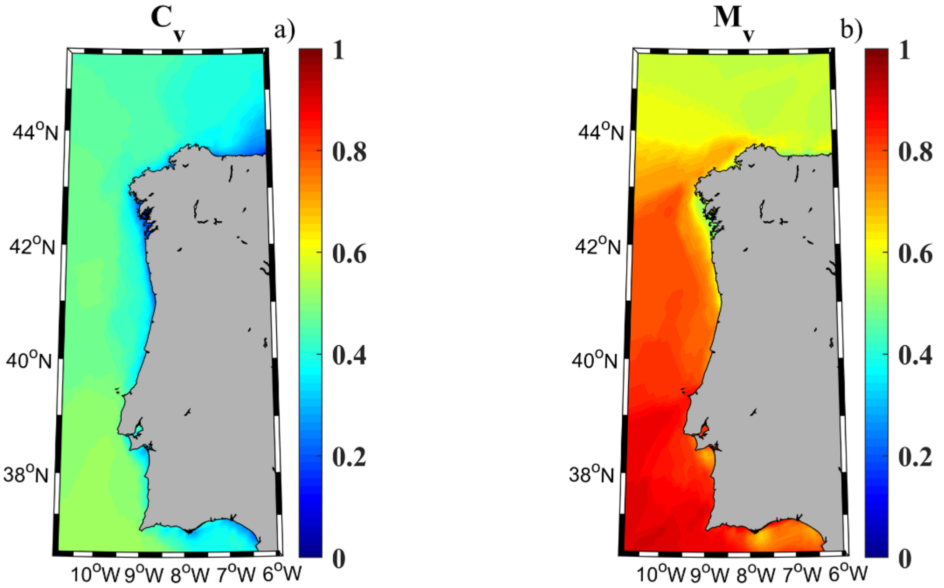

Figure 3.16 - Variability indices for wind energy resource. Variation coefficient (a) and monthly variability (b) in the NW Iberian Peninsula for the near future (2026–2045).

The wave power resource variability behaviour shows a high resemblance with the that found for the wind. A C_v index (Figure 3.17a) of around 0.4 is obtained for the northern part of the area, with higher values (~0.5) in the southern part. M_v (Figure 3.17b) shows values higher than 0.6 in the southwest region of the study area and in a small fringe along the north coast of Spain. For the rest of the area under study, *Mv* shows values of 0.5. Once again, the lowest values of C_v and M_v indices are located in the Gulf of Cadiz.

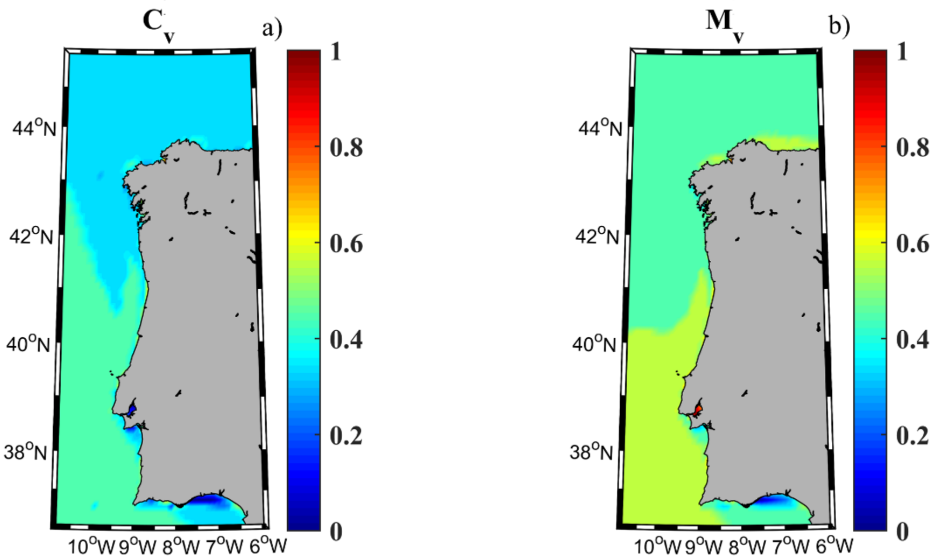

Figure 3.17 - Variability indices for wind energy resource. Variation coefficient (a) and monthly variability (b) in the NW Iberian Peninsula for the near future (2026–2045).

Figure 3.18 represents the risk category that considers the *EWS* and *EWH* indices, which affect the safety related to the manoeuvrability of energy devices. The wind *Risk* index (Figure 3.18a) shows high values (> 0.8) along a narrow fringe in the coastal region, moderate values in the southwest region (0.6), and low values (< 0.3) in the northwest region. The wave *Risk* index (Figure 3.18b) is close to 1 in most of the area, apart from the northwest region, where values of 0.5 are shown. It is noticeable that the lowest risk values (the worst risk conditions) in both wind and wave energy resources occur in the same region, the northwest section of the study area. This is precisely the region with the highest values of W_{ann}, *RLO* and *WP* indices.

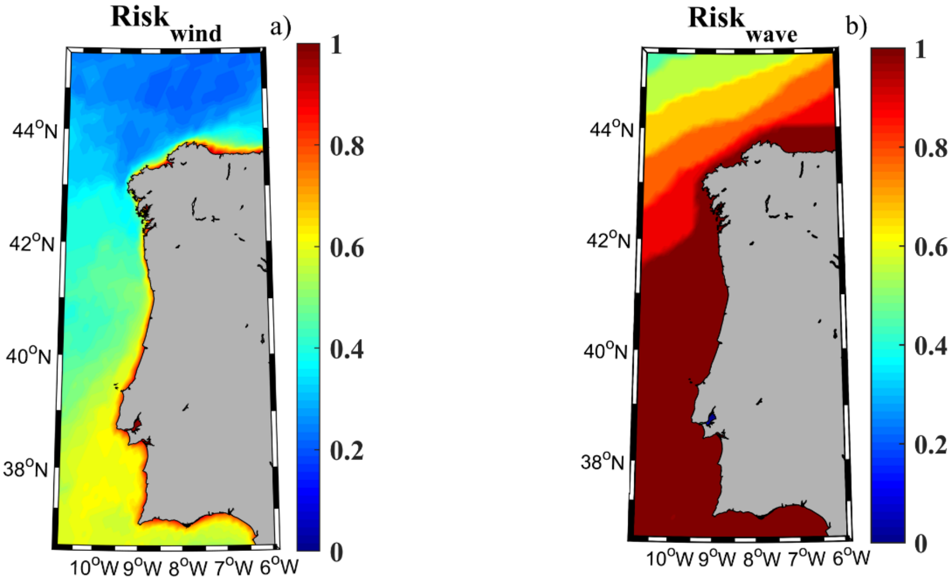

Figure 3.18 - Risk indices for wind (a) and wave (b) energy resources in the NW Iberian Peninsula for the near future (2026–2045).

The cost category, represented by *DC* (Figure 3.19a) and *WD* (Figure 3.19b) is the same for both wind and wave resources, since they only depend on topographic constraints.

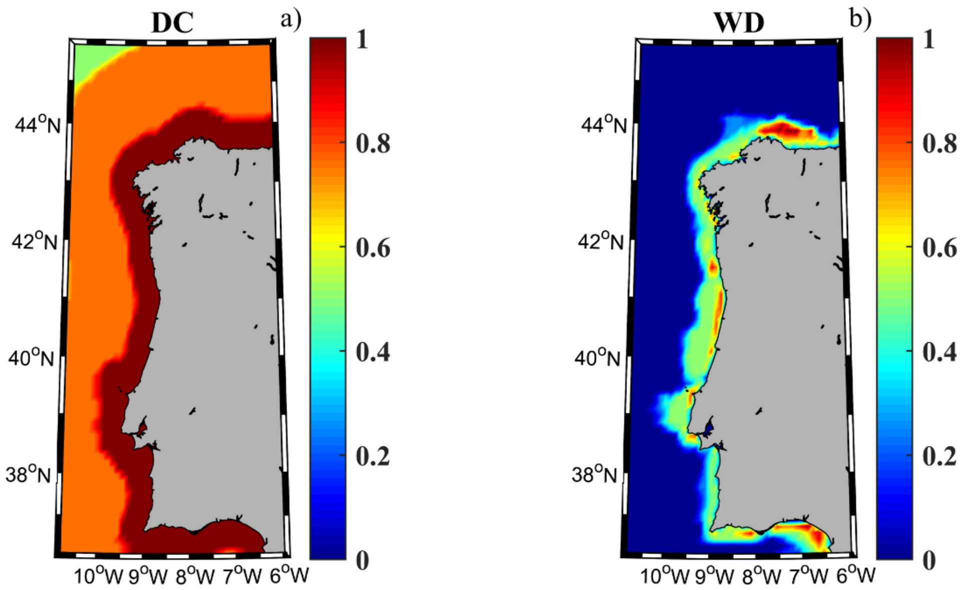

Figure 3.19 - Cost indices: (a) distance to coast (*DC*), and (b) water depth (*WD*) for wind and wave energy resources in the NW Iberian Peninsula for the near future (2026–2045).

The classification indices calculated following Equation (9) for wave and Equation (10) for wind resources index are shown in Figure 3.20. The Wind index (I_{wind}, panel a) shows high values (> 0.6 in most of the area). Only a very narrow fringe along the cost shows values lower than 0.5. High values can be observed in a wider fringe (~50 km wide) along the coast, the highest being observed from Cape São Vicente to Cape Roca (around 0.7). The wave classification index (I_{wave}, panel b) shows a pattern like that observed for the wind index, but with lower values (between 0.4 and 0.7) in the whole region. In this case, the coastal fringe with the highest values goes from Cape Roca to approximately Cape Peña.

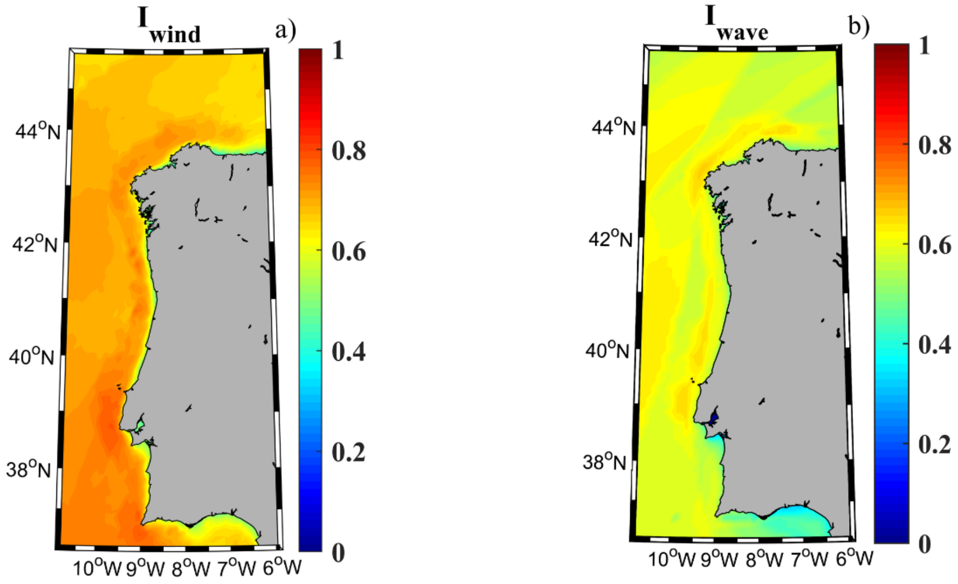

Figure 3.20 - Classification of the wind (a) and wave (b) energy resources in the NW Iberian Peninsula for the near future (2026–2045).

3.6.1 Sensitivity analysis

The patterns observed in Figure 3.20 are similar to those depicted in Figure 3.21 and Figure 3.22 obtained through the sensitivity analysis described in Section 2.3.10. In particular, Figure 3.21a and Figure 3.22a calculated with Equation (18) are similar to Figure 3.20a and Figure 3.20b, respectively. The *RMSE* values (Figure 3.21b and Figure 3.22b) obtained from Equation (16) are at least one order of magnitude lower than the average classification indices. This fact is corroborated by the distribution of the $RMSE_j$ calculated from Equation (17) (Figure 3.21c and Figure 3.22c).

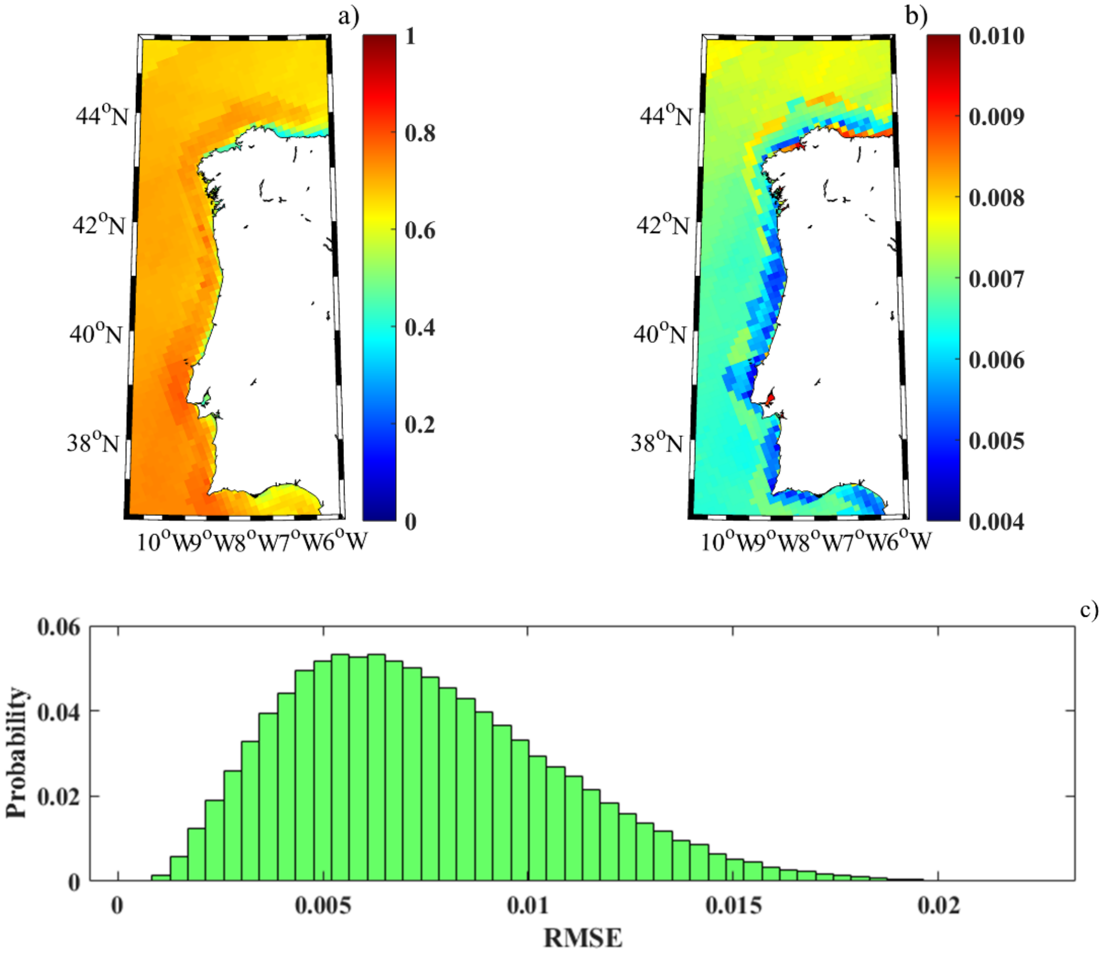

Figure 3.21 – Sensitivity analysis for wind energy. (a) Map of the mean classification index, $\langle \boldsymbol{I_j^k} \rangle$ calculated from Equation (18); (b) Map of the $RMSE^k$ calculated from Equation (16); and (c) $RMSE_j$ histogram calculated from Equation (17).

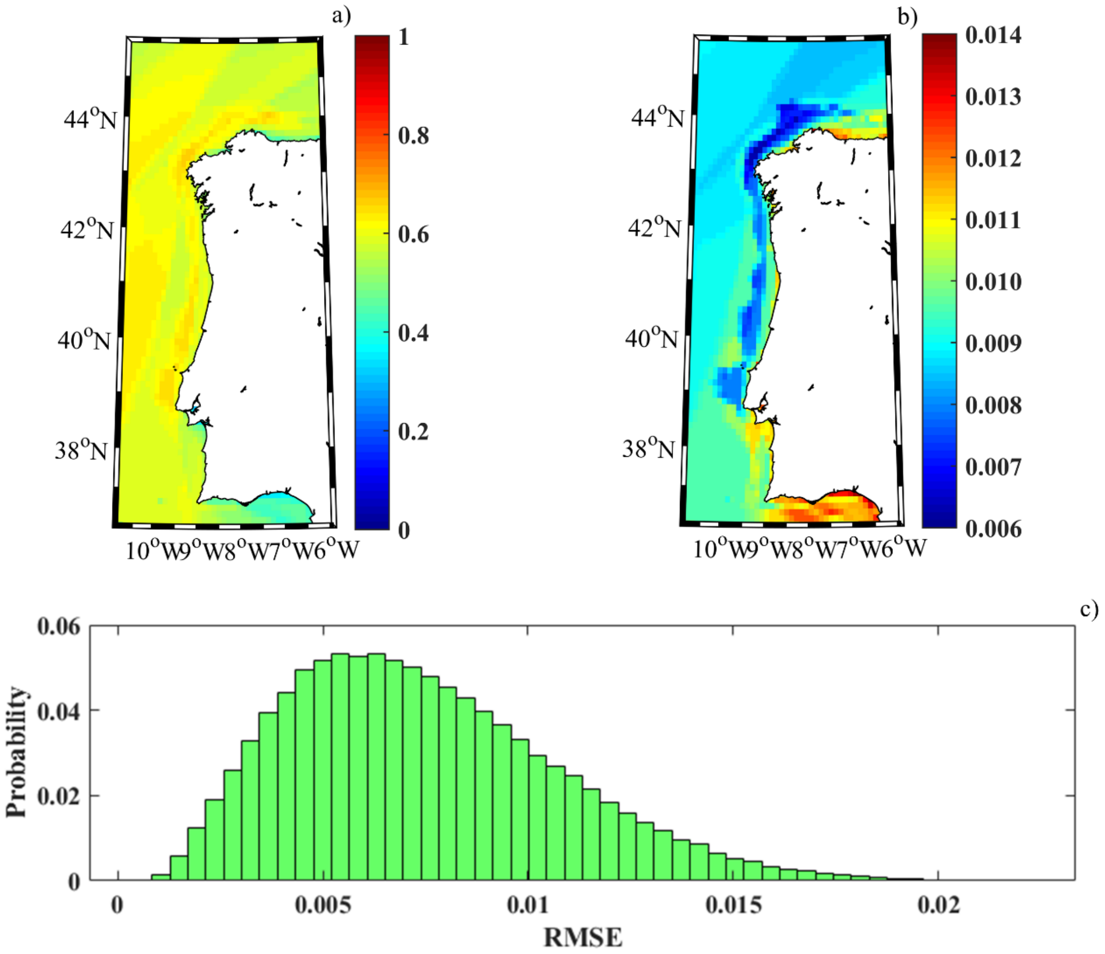

Figure 3.22 – Sensitivity analysis for wave energy. (a) Map of the mean classification index, $\langle C_j^k \rangle$ calculated from Equation (18); (b) Map of the $RMSE^k$ calculated from Equation (16); and (c) $RMSE_j$ histogram calculated from Equation (17).

3.6.2 Resource Classification

The combined index (*CI*) to classify the hybrid wind-wave energy resource (Figure 3.23) shows strong similarities to the patterns observed in Figure 3.13b. In general, the *CI* is lower than I_{wind} (Figure 3.20a) and higher than I_{wave} (Figure 3.20b). The narrow coastal fringe with low values, and the wider coastal fringe with high values (from Cape Peñas to Cape São Vicente) can also be observed in this case. Once again, the lowest values, around 0.5, are observed in the Gulf of Cadiz.

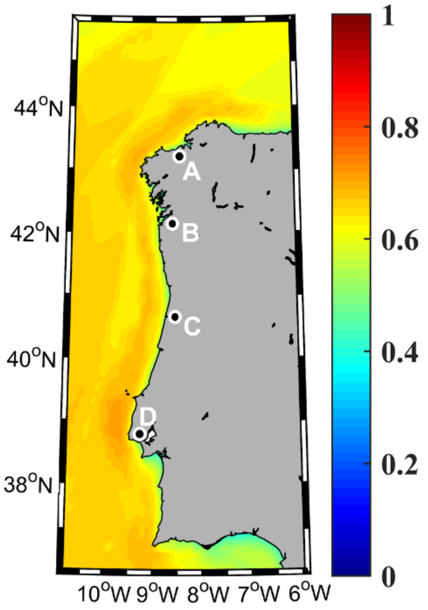

Figure 3.23 – Classification of the combined wind-wave energy resource in the NW Iberian Peninsula for the near future (2026–2045), with the location of the **A** A Coruña Outer Port, **B** Vigo Port, **C** Aveiro Port and **D** Lisbon Port.

The near future period classification for the hybrid wave-wind resource shows a pattern similar to that observed in Figure 3.13b, where the surroundings of the port shared roughly the same classification close to the shore, and small fringes with higher resource classification in the nearest ocean regions. These fringes are observed in Figure 3.23, where an evident fringe along the NWIC with a *CI* around 0.65 shows a high resource potential, with particular emphasis for the A Coruña Outer Port and Lisbon Port. In oceanic regions near these ports is found the maximum CI of 0.7 for the whole region under study, namely in the vicinity of the Cape Finisterre at the north and Cape Roca at the south.

3.7 WAVE ENERGY CONVERTERS EFFICIENCY

The WECs efficiency and cost of energy over their life-cycle was also evaluated, taking into account the results from the SWAN model downscaling of MIROC5 GCM under the RCP8.5 scenario, focusing on the efficiency of WECs in transforming wave energy into electricity, which is evaluated using two parameters, the load factor and the capture width [72,113,115,130].

The lifetime cost energy of the WECs can be estimated by the sum of the capital, operational, and maintenance costs. Other aspects, such as the size of the device or the design of the wave farm, were not considered in the present study due to the unavailability of open-source information. These parameters are calculated from the wave power resource and the wave power of each wave device. The wave power of each WEC is calculated, considering the historical and future percentages of sea states (structured into bins of H_s and T_p) and the power matrix and nominal power provided by the manufacturer.

The NWIC where the selected ports are located is the target area of this analysis, being one of the regions in the world with the highest wave power resource, as observed before. In this region, the current and future wave energy resources were analysed, and different evaluations of several WECs were performed to determine which technology is the most suitable for commercial exploitation in this area [113–115,130]. The area is affected by important bathymetric constraints (Figure 3.2a), since 80% is deeper than 50 m and only 5.2% has a depth between 25 and 50 m, which limits the type of WECs that can be used. Thence, the efficiency of the WECs will be analysed for two types of devices whose technical specificities allow their operation in intermediate water depths: a point absorber (Aqua Buoy) and an attenuator (Pelamis). A picture of both devices can be found in Figure 3.24 and their power matrix in [114].

Figure 3.24 – The two WECs considered in this assessment: Pelamis (left) and Aqua Buoy (right). Image copyright from [173].

The wave power energy was used to identify the wave power resource available along the NWIC coast both for the historical period (1979–2005) and the near future (2026–2045), and also the assessment of the projected changes in terms of mean wave power was made by computing the difference ΔP in the wave power resource between both periods (Figure 3.25). For the historical period, P increases northward, with the highest value (> 65 $\mathrm{kWm^{-1}}$) observed at the northwestern corner of the NWIC (Figure 3.25a). In general, P gradually decreases landward. The pattern is similar to that previously obtained by other authors [165]. A similar trend is shown for the near future, although the maximum values do not exceed 60 $\mathrm{kWm^{-1}}$ (Figure 3.25b). ΔP is negative for the entire region, suggesting that P will decrease for the near future, although at different rates (Figure 3.25c). In general, $|\Delta P|$ increases with the distance to the coast and from south to north. This pattern will affect mostly the potential for wave energy harvest located close to A Coruña Outer Port, whereas Lisbon Port shows the lower decrease in $|\Delta P|$. However, the ports in the uppermost section of the study area still show the highest potential for wave resource harvest, benefiting the A Coruña Outer Port and Vigo Port compared with Aveiro and Lisbon Ports. The decrease in P for the near future is consistent with previous research by [167], who found that despite the overall increase for the Atlantic basin since 1948, P has decreased over recent years for the Northeast Atlantic.

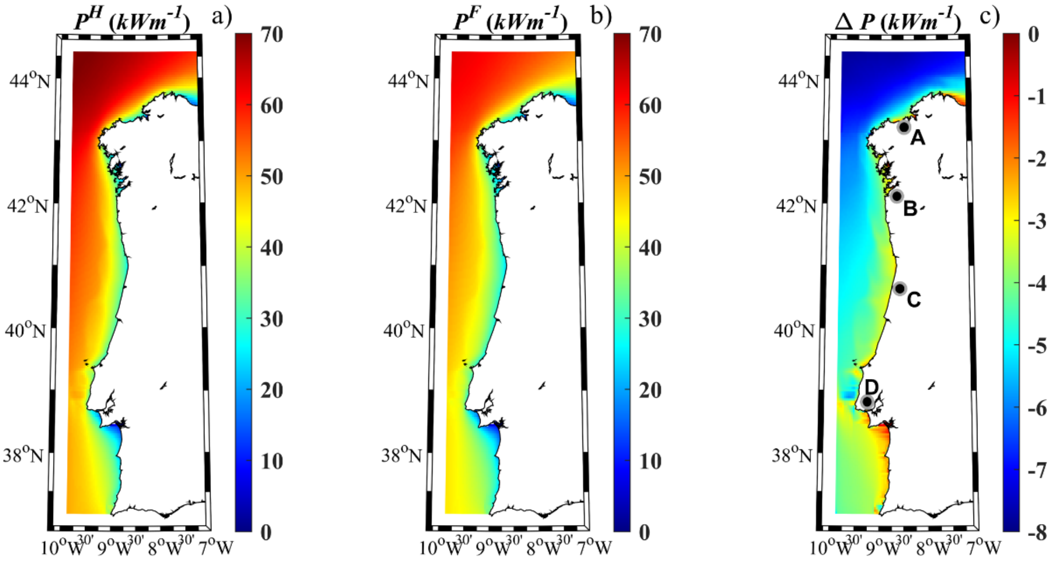

Figure 3.25 - Wave power resource. Mean wave power energy in the NW Iberian Peninsula for (a) the historical period (1979–2005) and (b) near future (2026–2045), and (c) the difference between both periods (Future - Historical), with the locations of the **A** A Coruña Outer Port, **B** Vigo Port, **C** Aveiro Port and **D** Lisbon Port.

The P decrease can compromise the overall WECs efficiency and consequently lower the total wave power harvested in a wave farm located or planned for these locations. In addition, the average lifespan of WECs is assumed to be around 25 years [118,174] with the current technology, leading to a weighted investment due to the constraints for an optimized wave energy harvest. However, despite the P decrease obtained for the near future, the potential of this region for the wave harvest is still viable due to WEC technical specificities such as P_{max}, which represents the maximum electric power that can be harvested from different sea states. Several authors have assessed the efficiency of WEC prototypes for commercial purposes in different coastal environments along the NWIC [115,116,165]. Some of the WECs assessed by those authors are Pelamis and Aqua Buoy, due to technical specificities that allow them to operate between intermediate water depths (50–70 m) [115], and the available information of the power matrix [114] and the corresponding P_{max} are 750 kW for Pelamis and 250 kW for Aqua Buoy [115].

Thus, the Pelamis and Aqua Buoy electric power capacity (P_E) was calculated based on their power matrix and the sea states previously obtained from the SWAN simulations for the historical and near-future periods (Figure 3.26 and Figure 3.27). Both figures show the historical values, the near-future projections, and the change in P_E between both periods for Pelamis and Aqua Buoy, respectively. The results show that the P_E patterns for Pelamis and Aqua Buoy are similar to those previously found for P. In addition, the decreasing pattern previously observed for ΔP is also detected for ΔP_E. Pelamis shows a maximum ΔP_E reduction (> 10 kW in absolute value) at ocean locations in the northern part of the study area (Figure 3.26c). The ΔP_E values are almost negligible from Roca Cape to 43°N. Only a narrow fringe north of 43.5°N shows a decrease higher than 4 kW in absolute value. Aqua Buoy shows a maximum ΔP_E reduction (~ -7 kW) also in the northern part (Figure 3.27c). ΔP_E will decrease between -2.5 and -4 kW south of 43.5°N, reaching the lowest differences close to the shore between Roca Cape and São Vicente Cape. Overall, both devices show a different ΔP_E pattern south of 43.5°N, with a similar pattern north of 43.5°N. These patterns mostly affect the regions near the A Coruña Outer Port, while the ports located at the southern section of the study area show the lower ΔP_E reductions. These patterns are explained by the differences in the power matrices of the WECs, whose diagrams of scattered T_p-H_s joint distributions have different ranges, between 1–5.5 s and 5–17 m for Aqua Buoy and 0.5–8 s and 5–13 m for Pelamis [114]. These varieties of ranges confer each device a diverse variety of sea states under which they can operate, retrieving the maximum electric power energy.

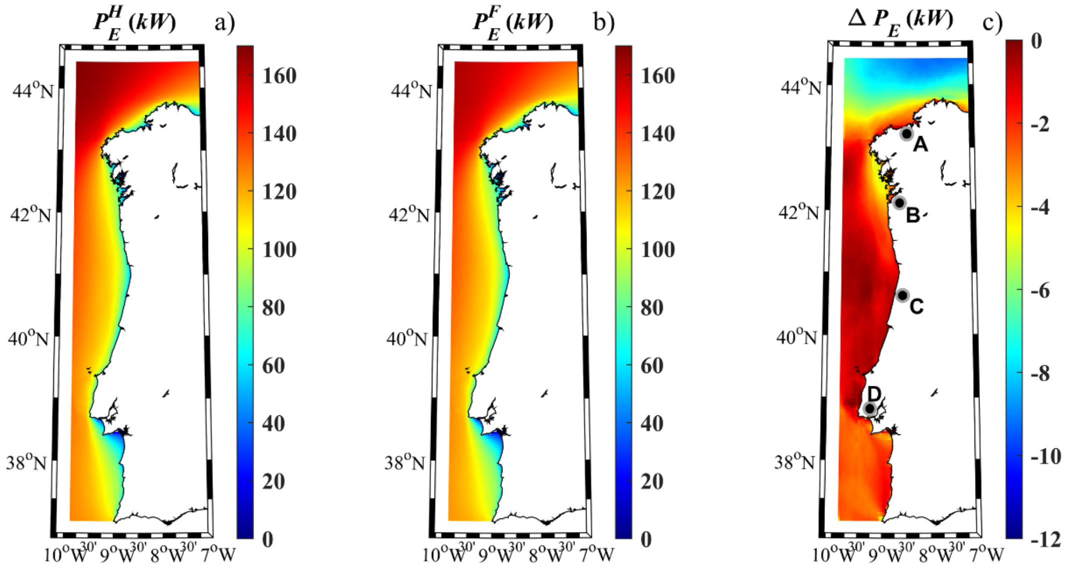

Figure 3.26 - Pelamis electric power capacity along the northwest Iberian Peninsula coast for (a) the historical period (1979–2005) and (b) the near future (2026–2045), and (c) the difference between both periods (Future - Historical), with the locations of the **A** A Coruña Outer Port, **B** Vigo Port, **C** Aveiro Port and **D** Lisbon Port.

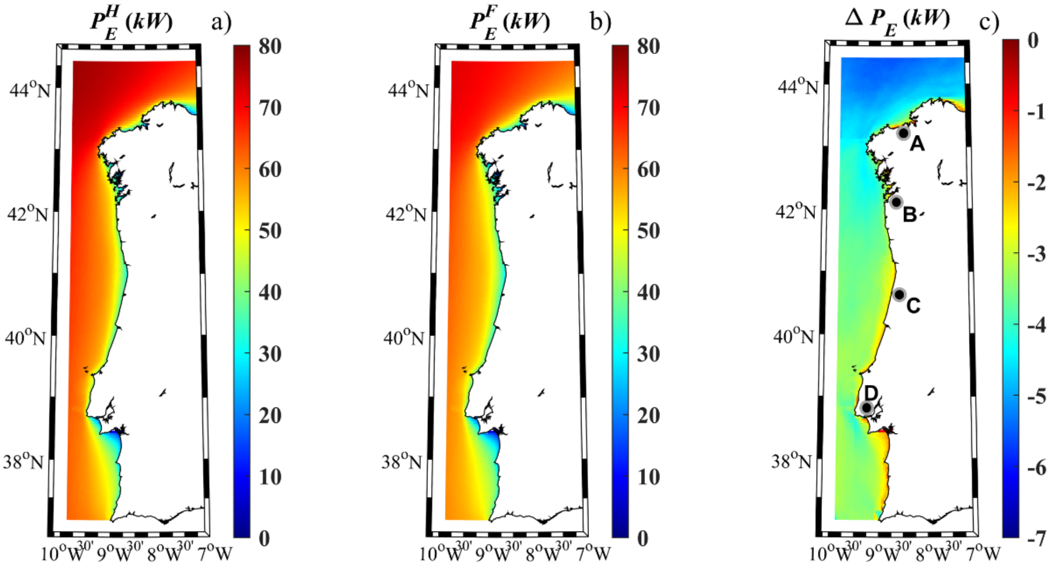

Figure 3.27 - Aqua Buoy electric power capacity along the northwest Iberian Peninsula coast for (a) the historical period (1979–2005) and (b) the near future (2026–2045), and (c) the difference between both periods (Future - Historical), with the locations of the **A** A Coruña Outer Port, **B** Vigo Port, **C** Aveiro Port and **D** Lisbon Port.

The performance of WECs may vary depending on the topographic constraints and sea states, in such a way that just a portion of the total energy is converted into electric power. The power load factor (ε) was calculated for both devices to assess the total energy (in %) harvested under the different sea states. Figure 3.28 and Figure 3.29 show the power load factor for Pelamis and Aqua Buoy for the historical period (a) and the near future (b), and (c) the difference between both periods ($\Delta\varepsilon$). The power load factor for Pelamis and Aqua Buoy presents maximum values (25% and 30%, respectively) at ocean locations north of 43.5 °N and lower values nearshore both for historical and near-future periods (Figure 3.28a,b and Figure 3.29a,b). Although the ε pattern is similar for both periods, differences can be highlighted in terms of the $\Delta\varepsilon$ parameter (Figure 3.28c and Figure 3.29c). The Pelamis power load factor will remain practically unchanged (< 0.5% in absolute value) (Figure 3.28c), except for the region north of 43.5 °N, where reductions between −1% and −1.5% are expected. The Aqua Buoy power load factor will decrease between −1% and −2% across the region, as shown in Figure 3.28c.

These patterns show that Pelamis $\Delta\varepsilon$ almost has no changes in the regions in the vicinity of the Vigo, Aveiro and Lisbon ports and some reductions north of the A Coruña Outer port region. In contrast, Aqua Buoy $\Delta\varepsilon$ reduction impacts all port regions, whereas the coastal waters contiguous to the ports show the lower reduction (-1%), increasing towards the ocean where the highest wave power resource is located.

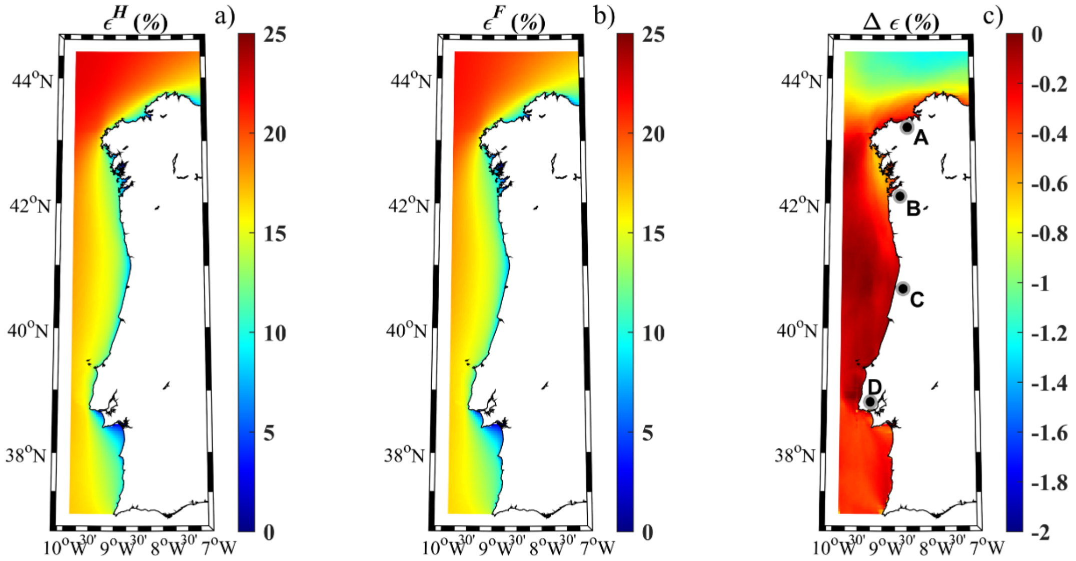

Figure 3.28 - Power load factor for Pelamis along the northwest Iberian Peninsula coast for (a) the historical period (1979−2005) and (b) the near future (2026−2045), and (c) the difference between both periods (Future - Historical), with the locations of the **A** A Coruña Outer Port, **B** Vigo Port, **C** Aveiro Port and **D** Lisbon Port.

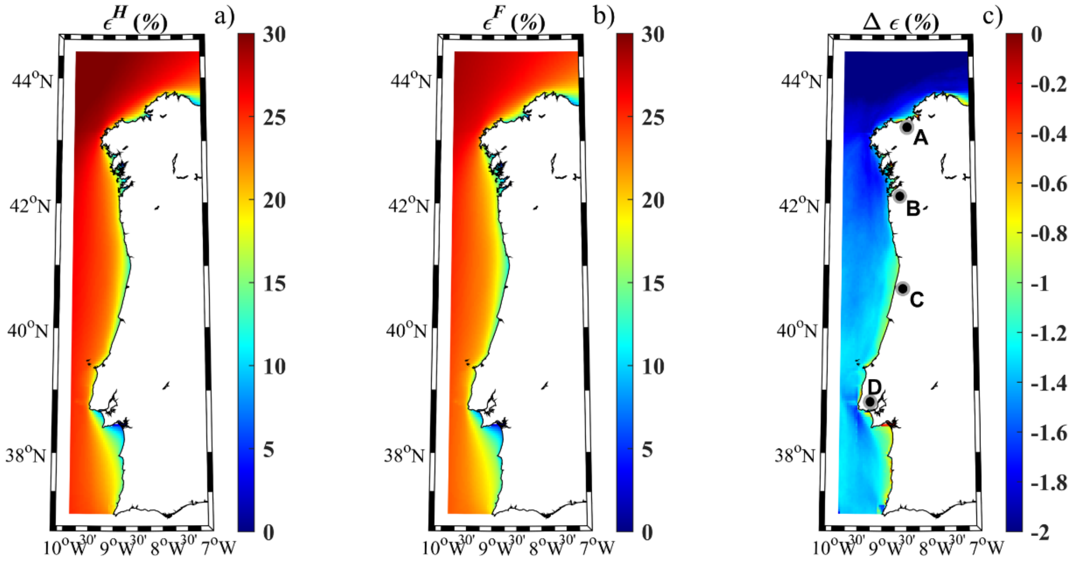

Figure 3.29 - Power load factor for Aqua Buoy along the northwest Iberian Peninsula coast for (a) the historical period (1979−2005) and (b) the near future (2026−2045), and (c) the difference between both periods (Future - Historical), with the locations of the **A** A Coruña Outer Port, **B** Vigo Port, **C** Aveiro Port and **D** Lisbon Port.

The second indicator of the efficiency of a WEC is the capture width (C_w), which represents the width of the wave front where the energy is extracted by the WEC [115,116]. Lower values correspond to reduced efficiency in transforming the wave energy into electricity. The C_w for both wave devices shows higher values near the coast than at ocean locations, both for the historical and future time periods. In addition, it also tends to increase southward. C_w values between 2.4 and 2.8 m were obtained for Pelamis (Figure 3.30a) and between 1.2 and 1.4 m for Aqua buoy (Figure 3.31a) during the historical period. The highest C_w values, 3 m for Pelamis and 1.5 m for

Aqua Buoy, were obtained for a small region located on the north coast of Spain. Overall, the capture width will increase for the near future (Figure 3.30b and Figure 3.31b), showing a pattern similar to that observed for the historical period, but with higher C_w values, especially near the shore. The ΔC_w ranges from 0.2 to 0.25 m between Roca Cape and Peña Cape for Pelamis (Figure 3.30c). The highest ΔC_w is detected in Roca Cape, with values higher than 0.3 m. Aqua Buoy shows the same ΔCw pattern as Pelamis, although with a more modest increment (between 0.04 and 0.06 m). Aqua Buoy also shows a maximum ΔC_w (~ 0.07 m) near Cape Roca (Figure 3.31c). Both WECs show an increase in ΔC_w in the regions surrounding all the ports, where A Coruña Outer port, Aveiro and Lisbon ports show higher values, with the maximum found on the latter.

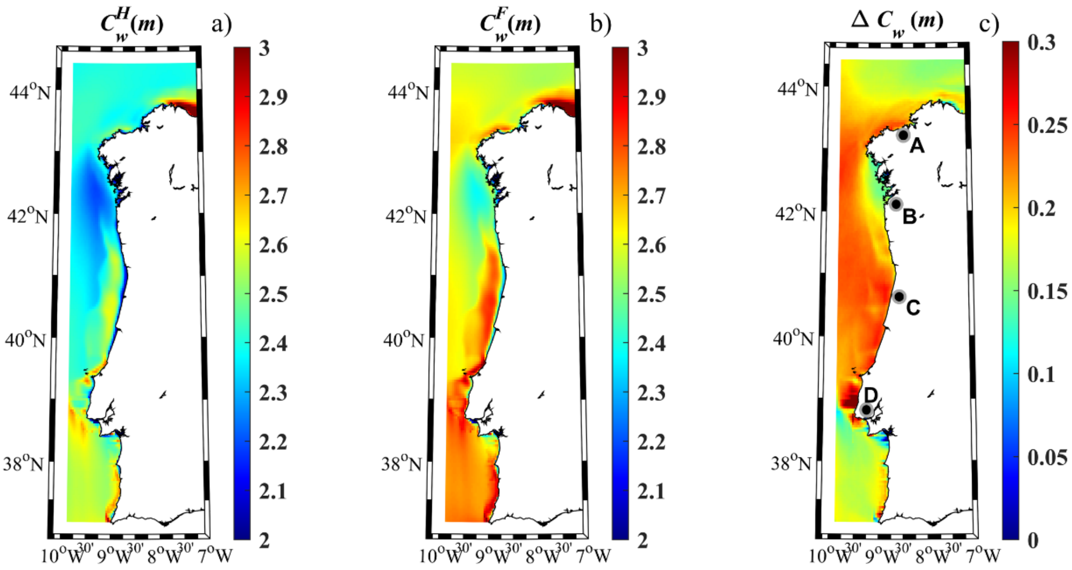

Figure 3.30 – Capture width for Pelamis along the northwest Iberian Peninsula coast for (a) the historical period (1979−2005) and (b) the near future (2026−2045), and (c) the difference between both periods (Future - Historical), with the locations of the **A** A Coruña Outer Port, **B** Vigo Port, **C** Aveiro Port and **D** Lisbon Port.

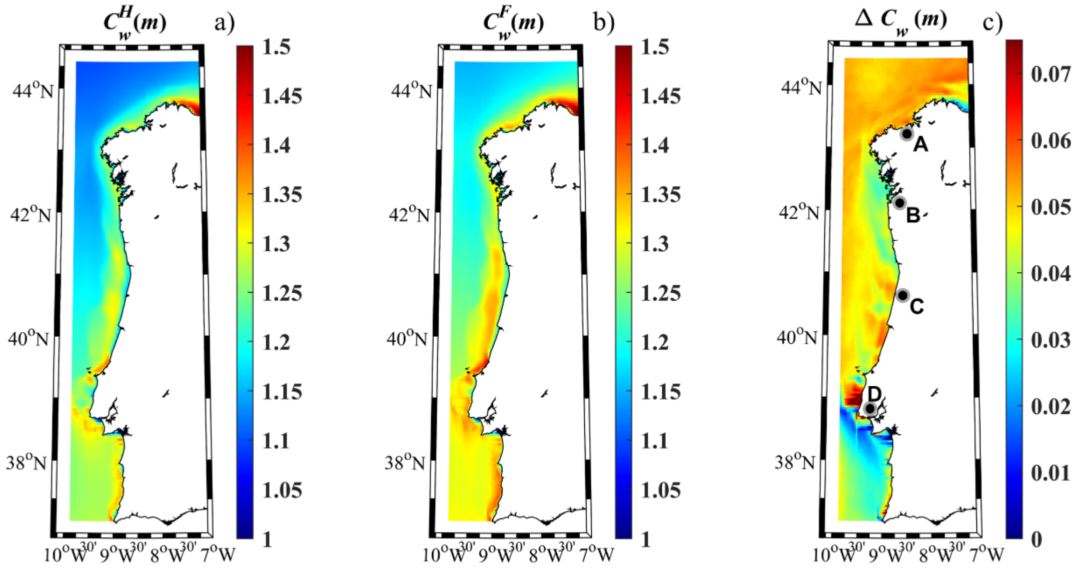

Figure 3.31 - Capture width for Aqua Buoy along the northwest Iberian Peninsula coast for (a) the historical period (1979−2005) and (b) the near future (2026−2045), and (c) the difference between both periods (Future - Historical), with the locations of the **A** A Coruña Outer Port, **B** Vigo Port, **C** Aveiro Port and **D** Lisbon Port.

The lack of knowledge about the energy cost of WECs in future climate conditions is very high. Here, the cost of energy for the near future is calculated by considering the current capital (C_A), operation, and maintenance (C_{OM}) costs and the generated energy during a life-cycle of 25 years, as described before (Equations (22) and (23)). Figure 3.32 and Figure 3.33 show the estimated cost of energy (C_E) for Pelamis and Aqua Buoy, respectively. Costs are calculated for the historical period (a) and the near future (b). In addition, the cost increase between both periods is depicted in the frame (c). The C_E patterns are similar for both WECs, with higher values confined to the coast and lower values offshore. In general, the C_E is higher for Pelamis (400−1000 EUR/MWh) than for Aqua Buoy (120−300 EUR/MWh) due to the lower production, operation, and maintenance costs. Pelamis shows a maximum ΔC_E increase (>20 EUR/MWh) south of Cape Roca, between 42°N and Cape Finisterre, and in the northeast area (Figure 3.32c). Only in the ocean section between 39°N and 43°N the cost of energy is the same as at present. The Aqua Buoy ΔC_E also increases in the same areas, with the exception of the northeast region. Both WECs show a ΔC_E increase, namely in the regions surrounding Vigo and Lisbon ports, whereas regions near the Aveiro and A Coruña Outer ports show lower ΔC_E magnitudes.

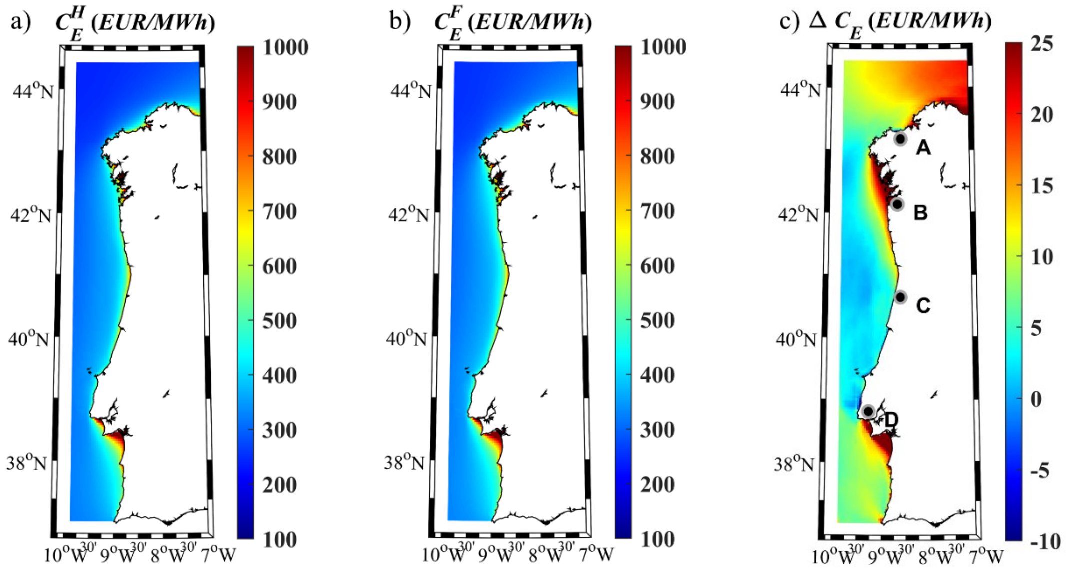

Figure 3.32 - Cost of energy for Pelamis along the northwest Iberian Peninsula coast for (a) the historical period (1979−2005) and (b) the near future (2026−2045). Frame (c) represents the increase in cost between both periods (Future - Historical), with the locations of the **A** A Coruña Outer Port, **B** Vigo Port, **C** Aveiro Port and **D** Lisbon Port.

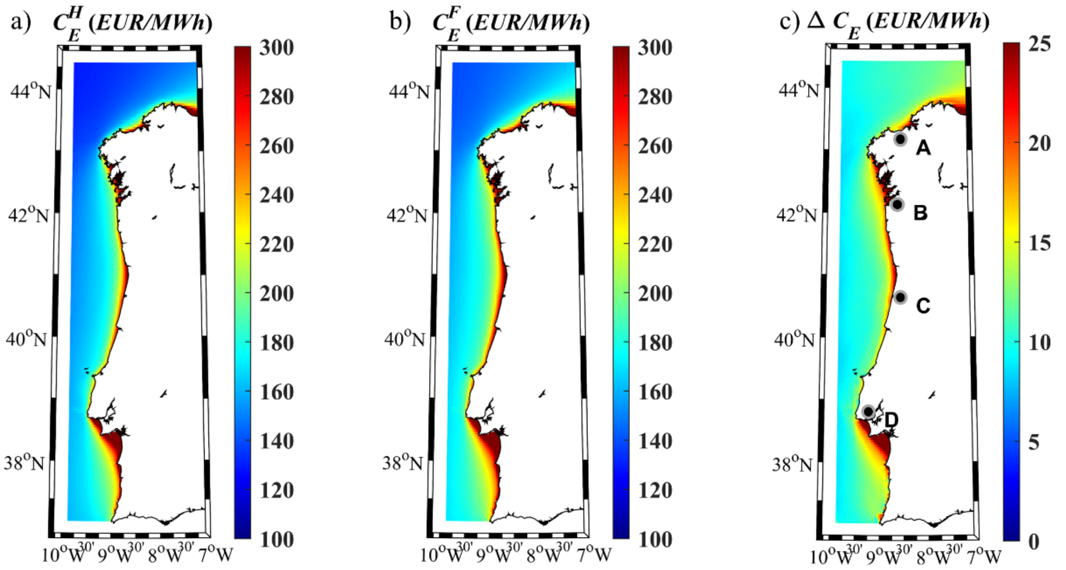

Figure 3.33 - Cost of energy for Aqua Buoy along the northwest Iberian Peninsula coast for (a) the historical period (1979−2005) and (b) the near future (2026−2045). Frame (c) represents the increase in cost between both periods (Future - Historical), with the locations of the **A** A Coruña Outer Port, **B** Vigo Port, **C** Aveiro Port and **D** Lisbon Port.

3.7 CONCLUSIONS

This chapter aimed to classify the present and future energy resources along the northwest Iberian Peninsula coast by means of a dynamical downscaling (~0.037°×0.037°) of the significant wave height (H_s) and peak period (T_p) considering different Global Climate Models (GCMs) and

RCMs for wind data. Wave propagation models were driven by historical and future wind data under the RCP8.5 greenhouse gas emission scenario.

A classification based on a Delphi method was performed with different factors related to the physical characteristics of the wave resource, stability, risk and installation and maintenance costs. A comparative analysis using a multi-model mean between historical (1979-2005), near future (2026-2045) and far future (2081-2100) projections was performed.

Following this strategy, the viability of exploiting the energy to be produced in hybrid wind-wave farms in the NWIC and in the vicinity of the selected ports for the near future was investigated using a Delphi method to classify wind and wave energy resources by considering different indices that represent the resource richness, variability, risk, and cost of the energy resources. In addition, the electric power capacity, the efficiency, and the cost of energy of two WECs (Pelamis and Aqua Buoy) were calculated both for the present and near future.

The classification of the wave resource based on the Delphi method shows that historically, most of the Iberian Peninsula's Atlantic coast can be classified as outstanding, being excellent along the coast of the Bay of Biscay. In contrast, the score will decrease in most of the region in the future, especially in the far future, when the Iberian Peninsula's west coast will be classified as excellent and only good along the Bay of Biscay coast. These reductions of the conditions for the future exploitation of wave energy are mainly due to the decrease in wave energy and the increase in the variability for most of the region in the future. Even the risk conditions can slightly increase in the future, a decrease in the mean wave field does not imply a decrease in extreme values. In fact, more severe and energetic storms are projected for the future despite lower average energetic conditions will occur.

Only a few small areas will present an outstanding score in the future, being of particular relevance the northwest corner of the Iberian Peninsula, since this area will also experience a future improvement in the conditions for offshore wind energy exploitation [26]. Thus, this area will be a suitable location for installing hybrid wind and wave converters, as observed by [61]. The general classification score in the regions surrounding the port's under analysis in this study diminishes for future periods, although most of the port areas show a score of excellent, whereas A Coruña Outer Port benefits from small oceanic areas with a classification of outstanding.

Additionally, it is observed that the hybrid assessment for the near future shows some similarities with the wave resource assessment, which is explained by the dependence of the wave regime on the wind conditions. Thus, the richness category is expected to show the same patterns for both energy resources, with the highest values in the NW corner of the study area. The variability of the resource also shows a similar pattern for both wind and waves, with the highest values located south of Cape Finisterre. Both resource and variability factors are higher (better) for wind than for wave resource, on the other hand, the downtime factor shows the best values for waves.

The best risk conditions occur along the coastal region, both for wind and waves. In the oceanic part, the conditions improve from north to south. In general, the risk index is worst for wind than for waves.

Finally, a macroscopic evaluation of the hybrid wind-wave resource shows that most of the NW Iberian Peninsula presents good conditions (*CI* > 0.6) for harvesting energy from wind and wave resources simultaneously. In particular, there are some optimal areas (*CI* > 0.7), such as the region near Cape Roca and the Galician coast, which had already been highlighted in previous studies on wind [176] and wave [72] resources. These regions can be used by the A Coruña Outer Port and Vigo Port for future exploitation of the energy resources. In contrast, the Aveiro and Lisbon ports are located in less energetic regions, however, they can maximize the energy resource harvest in the nearby oceanic regions where higher energy resource is observed.

An additional assessment to further identify the most suitable locations to moor a particular device both at present and in the near future, resulting in around 7000 points that constitute possible locations to install WEC farms [61].

The electric power capacity follows the same spatial pattern as the wave power resource across the region both for the Pelamis and Aqua Buoy devices. The maximum decrease in electric power for the near future was detected at ocean locations in the northern part of the study area, close to Vigo and A Coruña Outer ports, both for Pelamis (decrease > 10kW) and Aqua Buoy (decrease ~7 kW). South of 43°N, Pelamis shows a negligible decrease, while Aqua Buoy shows a decrease ranging from 2.4 kW to 4.5 kW, which is the lowest decrease observed at southern locations where Aveiro and Lisbon ports are located.

The power load factor for Pelamis will remain practically unchanged (< 0.5% in absolute value) throughout the area, except for the region north of 43.5°N, where reductions between 1% and 1.5% are expected. The power load factor for the Aqua Buoy will decrease between 1% and 2% across the region. These results indicate that the power load will decrease slightly for both devices for most of the ports surrounding areas.

The capture width will increase from 0.2 to 0.25 m between Cape Roca and Cape Peña for Pelamis, near Lisbon and A Coruña Outer ports, respectively. The greatest increase is detected in Cape Roca, with values greater than 0.3 m. Aqua Buoy shows the same spatial distribution for the capture width as Pelamis, although with a more modest increase (between 0.04 and 0.06 m). Aqua Buoy also will show a maximum increase (~ 0.07 m) near Cape Roca, in the Lisbon Port area.

The cost of energy was projected to increase in the near future for the entire region for both devices mainly due to the decrease in the electric power (P_E). A maximum increase nearshore south of Cape Roca and Cape Finisterre was projected for both devices, close to Vigo and Lisbon port regions. In addition, a noticeable future increase in C_E is also observed in the northeast area for Pelamis.

The WEC assessment has shown that the efficiency of the different devices depends not only on the wave resource at a certain study area, but also on the relationship between the sea states and the power matrix of the WECs that can operate in that area. The projected changes in wave parameters that affect wave resources can be magnified or reduced depending on the particular features of the device.

The approach presented in this chapter provides useful insights and an assessment of the applicability of future wave and hybrid wind-wave resource harvest potential, and WEC efficiency. These analyses can be applied for global and local scale studies by predicting future marine resources for researchers and decision-makers that can use the marine energies to tackle climate change through the implementation of renewable energy sources at the ports under the EU and UN climate change policies. It gives them a holistic view - a near future assessment that can provide a set of decision support tools that effectively identifies the best wave collection locations, considering a wide range of parameters that contribute to management, adaptation, and resilience. Additionally, this analysis provides a far future assessment that evaluates the farm's long-term reliability.

The assessment analyses should be interpreted with caution, as wave converters capture only a fraction of the available wave energy. Furthermore, this energy resource classification should be considered as a first step, as it considers the resource only from a physical perspective. Further analyses to determine the feasibility of exploiting wave energy should also focus on the capacity of the different devices [175] to extract energy and some factors related to *WP*, downtime, and risk should be defined explicitly for each wave energy converter. In addition, the estimation of energy cost in the future for different devices will constitute an added value for the study, allowing the assessment of the economic viability of wave farms under future climate conditions.

The practical implications of the application of the energy resource assessment essentially presents a reconnaissance perspective, since there is a significant uncertainty in the wave parameters estimation. This is explained by limitations in the SWAN mesh resolution and restrictions in boundary conditions. This level of accuracy is reliable and accurate to identify potential sites in a larger region, as the one analysed in this study. For further analysis, an increase in the reliability and accuracy of the results must be addressed by detailed modelling, through numerical mesh refinement, 500 m for the feasibility stage, and 50 m for the design stage, followed by updates in bathymetric, wind, current and tidal data throughout the specific study area.

The energy evaluation performed in this study can be improved if legal aspects such as environmental laws, uses of the sea and shipping lines are considered and if the technical features of the different WECs and the costs associated with the WEC deployment and the connection to the electricity grid are also made available in detail and counted on in the study. However, these parameters are difficult to establish as they can vary in a short time due to: adaptation to local and international legislation; the broad type of WECs and their technology readiness level; and the energy price volatility that depends on the aggregators of renewable energy sources.

Chapter 4

FLOOD ASSESSMENT

This chapter presents an assessment of the resilience of the port infrastructures to climate change drivers by addressing the flooding conditions of the A Coruña Outer Port, Vigo, Aveiro and Lisbon ports under climate change drivers for 10-, 25- and 100-year return periods. The results make it possible to identify the areas of the ports that are most vulnerable to flooding through the analysis of flood maps.

4.1 INTRODUCTION

Due to marine transportation's operational characteristics, maritime ports are usually located in protected areas with access to navigable waterways. Port's primary function is to supply services to freight and ships and cover a wide range of functions that involve port operability. For instance, cargo oriented infrastructures have been developed and expanded to new inland areas contiguous to the port to facilitate land and maritime transport systems in order to sustain the planned longevity of the infrastructural assets to about 40-50 years [3]. These characteristics turn the ports susceptible to complex dynamics of the multi-dimensional environment [177,178] on which they are located, from the ocean (sea levels, storm surges and sea weather) to rivers that can annihilate the ability to maintain the port activities efficiently.

Unprecedented climate change is occurring changing meteocean patterns around the globe [95,167,179,180], and recent studies show no signs of deceleration with sea-level rise exceeding 2 m globally [38,181] under higher emission scenarios, surpassing the IPCC AR5 [13] and the recent AR6 projections, with the potential to increase the vulnerability of coastal regions to floods. Wind and wave regimes are expected to be affected [11] by climate change, along with weather events becoming more extreme [14,15,19,20].

Given the ports' location and role in the globalised trading system, the ports adaptation and building their resilience to climate change is an urgent problem to be countered. Studies focusing on the European ports [18,182] showed that high warming scenarios (Representative Concentration Pathway - RCP8.5) indicate that Europe's ports will be exposed to higher risk, where most of the ports exposed to extreme sea levels (ESL) higher than 4.5 m in 2100 are located in the Iberian Peninsula (IP) [18]. Direct consequences on the number of trading goods may occur, with an estimated cargo reduction of 25%. Broader impacts are expected since most

IP ports operations are performed in low-lying areas contiguous to the ports. Thus, acknowledge the flood extent under climate change is critical to flood resilience enhancing once ports are exposed to the risk of climate change impacts.

Due to the NWIC port's location and characteristics, the infrastructures of these ports are prone to floods [21], which may be aggravated in the future due to climate change, which may threaten the port's performance and compromise the port's importance to Portugal and Spain's national economies [36]. However, floods are not necessary to occur with the same magnitude and impacts in these ports, instead, these are most likely to be both temporally and spatially variable due to differences in climate change drivers (depicted characteristics are listed in the corresponding port section).

Thus, the present chapter aims to assess the flooding conditions in these ports in response to climate change drivers through a detailed modelling approach that quantifies the flooded area in a reference scenario that represents the present conditions and in climate change scenarios for the 10-, 25- and 100-year return period events (from now on referred to as Tr^{10}, Tr^{25} and Tr^{100}, respectively). The flood assessment will be determined by the simulation of the ESL (mean sea level + astronomical tide + storm surge) simultaneously with wave regime as the ocean drivers, and including also the riverine flows.

4.2 REGIONAL WAVE MODEL

The BCC-CSM1.1 GCM (section 2.3.2) represents the best climate model to reproduce the IP west coast's extreme wave climate showing the best *RMSE* and *Bias* (Table 2.7) among the different GCMs analysed for the NWIC. The coarse resolution of the BCC-CSM1.1 GCM is not suitable for being used at a regional scale, which makes it necessary to perform a dynamical downscaling to propagate the wave to finer resolution at the port entrance. The third-generation spectral wave model SWAN [122] was used through the Delft3D-WAVE module in an implementation similar to that developed by [61,72], following the recommendations of the International Electrotechnical Commission (IEC) for a stage 1 (reconnaissance) model [126]. The downscaling was accomplished by making a two-step approach, the first step is to downscale the selected GCM, and the latter is to simulate the scenarios by coupling WAVE with FLOW modules.

The downscaling was conducted by implementing the model in a nested approach, comprising 3 sets of domains with different resolutions (Figure 4.1). The larger domain (L1) extends from 34.54°N and 14.54°W to 45.54°N and 5.54°W, followed by the second domain (L2) from 37.54°N and 12.54°W to 44.54°N and 6.88°W, and the third set of domains (Punta Langosteira (L3), Vigo (L4), Aveiro (L5) and Tagus (L6)) which correspond to local ports domains. The resolution applied to each domain was the ratio of 1/3 from the previous domain, creating a resolution of 1/3°, 1/9° and 1/27° for domain L1, L2 and L3-L6, respectively. The numerical bathymetry was built based on the GEBCO database.

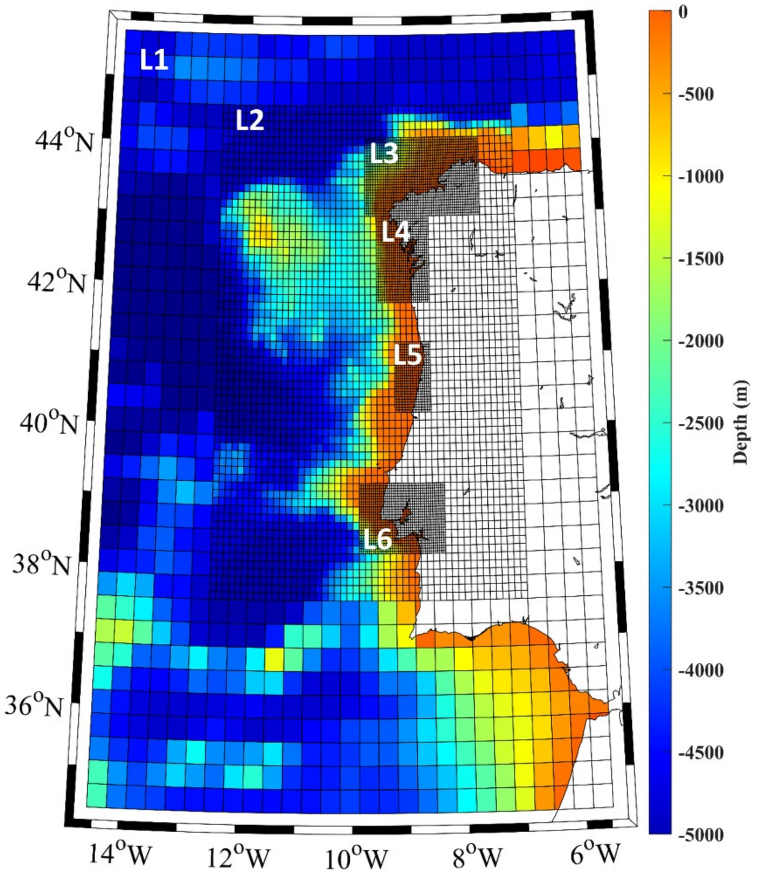

Figure 4.1 - Study area with the extents of the numerical domains and bathymetry used for SWAN implementations, the downscale of the BCC-CSM1.1 GCM using a nested approach for the domains: Punta Langosteira (L3), Vigo (L4), Aveiro (L5) and Tagus (L6).

Similarly to [61,72], the BCC-CSM1.1 GCM wave field was imposed as a time and space varying boundary, with a temporal resolution of 6 hours. A wave spectrum of 25 frequencies (0.0418-1 Hz) and 36 directional bands were applied. The model was also forced with 3-hourly winds from the BCC-CSM1.1 GCM r1i1p1 (rip refers to realisation, initialisation method and physics version used). The use of a GCM instead of an RCM is explained by the lack of an RCM using this GCM for this particular region. This GCM is characterised by a horizontal resolution of 1.125°×1.125° with a 3-hourly temporal resolution. The physical parameters included a stage 1 IEC model and triads, bottom friction, depth-induced breaking and quadruplets [61,72,126] (Table 3.1). The simulations were run for the climate periods between 1979-2005, 2026-2045 and 2081-2099, corresponding to the historical, near future and far future periods.

The results from these simulations will be used to feed the local FLOW and WAVE simulations for each port, in order to simulate the scenarios under different climate and return periods.

4.3 AVEIRO PORT

The Aveiro port is located in Ria de Aveiro, an inland lagoon, on the IP west coast facing the Atlantic Ocean (Figure 4.2). The lagoon is comprised of four main channels (Mira, Ílhavo, Espinheiro and S. Jacinto) and a single artificial channel connecting the lagoon to the Atlantic Ocean [93]. The elongated lagoon up to 45 km in length lies behind sandy barriers and extends up to 10 km onshore, covering an area of 89.2 km^2 at spring tide, which is reduced to 64.9 km^2 at neap tide [183]. An average depth of 1 m characterises the lagoon due to the predominance of small channels, large areas of mudflats and salt marshes, and up to 15 m at the entrance and port area [53]. The lagoon region is characterised by low topography, which increases the potential to be flooded during certain conditions.

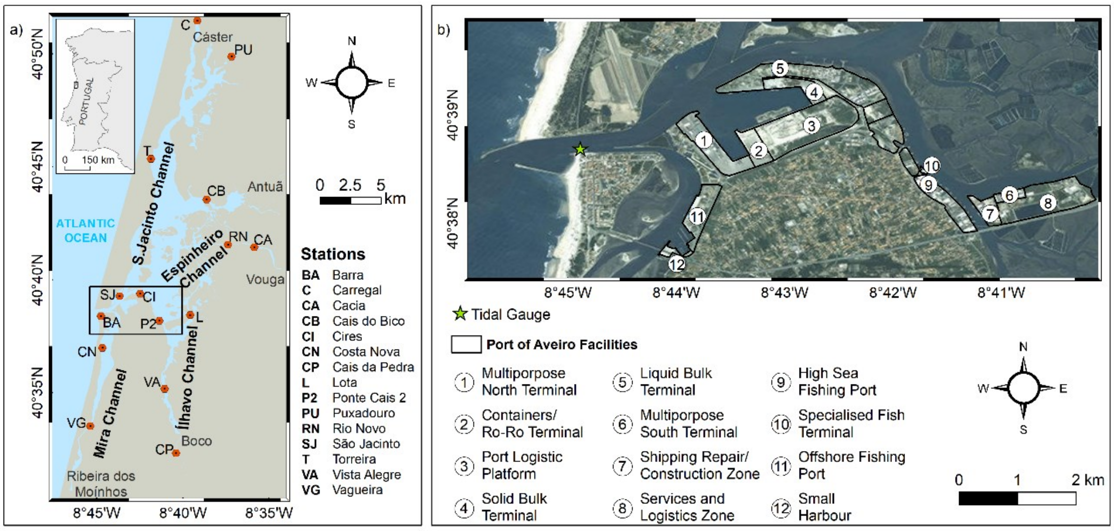

Figure 4.2 - Study area with the *in-situ* stations (a) used to validate the hydrodynamic model (Table 2.4). Location of the Aveiro port and the business areas in the port administration jurisdiction (b).

The tide is the most important among the lagoon dynamic drivers, characterised by a semidiurnal regime with a small diurnal pattern, reaching average tidal amplitudes of 0.46 m at the neap tide and 3.52 m at spring tide. Several rivers also contribute to local hydrodynamics, with five major sources (Vouga, Antuã, Ribeira dos Moínhos, Cáster and Boco rivers), where the Vouga river is the main contributor reaching a mean discharge of 80 m^{3}s^{-1} [184]. These characteristics make the lagoon vertically homogeneous, except during high inflows of fresh water in the channel's upper part, where some vertical stratification is found [185,186].

With a northwest regime, the coastal waves are characterised by a mean significant wave height of 2 m and a mean wave period of 12 s, increasing significantly in winter, reaching 8 m during 5-day storm events [187]. Despite these high wave heights, studies showed that breakwaters along the lagoon mouth diminish the influence of the waves at the entrance, slightly affecting the currents and sea level at the port operation areas [94,188]. In addition, storm surges can occur during adverse weather conditions, leading to an over-elevation ranging from 0.3 to 1.1 m [93,189,190].

The changes occurring in meteocean drivers contribute to the increase in the lagoon's flood risk, which has been assessed for the historical period [53,189,191,192] to understand and predict future developments [91,93,94,183] of the flooded area and the implications on the surroundings. The Aveiro lagoon has been historically shaped by human activities, harbouring urban structures of small to medium-sized cities and related activities, and increasing industrialisation prompted by the Aveiro port [193], and consequently boosting the Aveiro port activities and dimension.

The Aveiro port's strategic location (40° 39' N, 8° 45' W) and its favourable maritime and land accessibilities allow this infrastructure to serve a vast economic hinterland in Portugal and central Spain. This port is the most recent national infrastructure, showing a well-ordered and integrated area, benefiting from the natural protection from the coastal hazards bestowed by the sandy barriers. In fact, the port structure lies inside Ria de Aveiro, and the connection between the port and the ocean is carried out by a single navigation channel protected by the construction of two breakwaters. These engineering works extend seaward north with an extension of 1200 m and south with 700 m, securing a 500 m wide entrance and narrowing to a 300 m wide channel to the port facilities.

Following [91,94,188], waves are expected to play a significant role in the lagoon inlet's sea surface height, affecting currents and sea level near the entrance channel. Moreover, the breakwaters orientation is the most crucial coastal defence structure of the port, protecting the navigation channel from wave actions even during storms with extreme waves [188]. The inlet features allow achieving the channel's required depth and stability even during rough winters, being a good shelter during these periods. However, low amplitude waves have been observed visually in the entrance channel between both breakwaters.

Such features attract large ships with a length up to 200 m and an average draft up to 9.75 m through the port entrance, located 2.4 km from the north sector (North Terminal; Container and Roll-on/Roll-off Terminal; Solid Bulk Cargo and Liquid Bulk Cargo Terminal) and 7.2 km from the south sector (South Terminal, High Sea Fishing Port and Specialised Fisheries Terminal) (Figure 4.2b) (portodeaveiro.pt).

4.3.1 Model setup

Delft3D model is used to simulate the flooding conditions in Aveiro port through FLOW and WAVE modules (Section 2.4), allowing flow and wave simulations in coastal, river and estuarine areas. A model simulation's fate is mainly determined by the inputs, reflecting the model's accuracy to specific physical processes. These processes must be evaluated and determined, focusing on assessing the Aveiro port's flood rate, which strongly depends on high sea levels and riverine flows.

4.3.1.1 Downscaling approach

The coarse resolution of the regional model is insufficient to conduct the wave propagation on the port region and simulate the scenarios under different climate and return periods. Thus, a new model is required to undergo the scenarios with finer resolutions to FLOW and WAVE simultaneously. This local model was developed using a nested approach with 2 domains, one covering the coastal region close to the port entrance (I – Figure 4.3), extended from 40.3°N to 41.0°N and a fringe of 30 km distance to coast, and a horizontal resolution of 1 km. The second domain (II – Figure 4.3) used the same numerical grid and bathymetry in the FLOW module, which is an irregular grid with space varying resolution (up to 25 m). SWAN can perform computations on a curvilinear grid, allowing the same grid as FLOW and SWAN, which permits the perfect coupling between the modules.

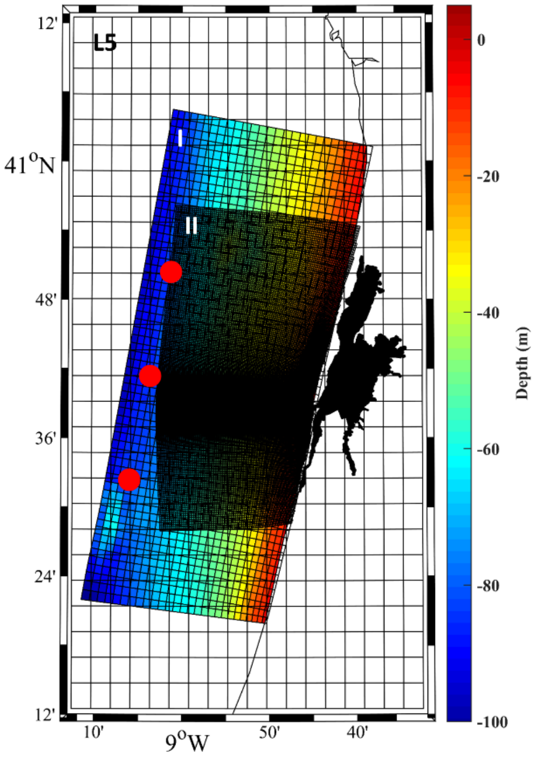

Figure 4.3 – Study area with the extents of the numerical domains and bathymetry used for the SWAN (I and II) and hydrodynamic (II) model in the study area. The red dots indicate the grid nodes assessed in terms of wave parameters to determine the return periods.

The model physics was similar to those used for the GCM downscaling purpose, including triads, bottom friction, depth-induced breaking, and whitecapping computed with Komen exponential term [169]. The diffraction and reflections are also available. The wave spectrum was discretised to 25 frequencies (0.0418-1 Hz) and 36 directional bands.

4.3.1.2 Characterisation of H_s, T_p and Dm

Studying extreme waves on a coastal location was based on analysing the wave parameters H_s, T_p and *Dm* (mean wave direction). These parameters are often used to study the extreme waves, including runup, erosion, wave-driven longshore transport, which can change the coastal processes during these events [83,194]. Also, coastal flooding highly depends on H_s and T_p combined with high tides and storm surges [195].

For this purpose, starting from the downscaled results of the BCC-CSM1.1 GCM, three grid nodes located in front of the port entrance and parallel to the shore were selected as control points (Figure 4.3) to calculate the return periods for the wave parameters. The hourly values obtained over 1979–2005 were used to determine the maximum H_s and T_p and fitted to statistical distributions, similar to the approach described in section 2.2.7 for the river discharge and used to estimate *Hs* and *Tp* for Tr^{10}, Tr^{25}, and Tr^{100}.

The *Dm* is depicted in Figure 4.4, showing wave arrival predominantly from northwest and north-northwest directions for the historical climate during winter, in agreement with previous studies [166,196] for the historic period. Following these results and taking into account [197], the mean wave direction will be the mean of the predominant wave directions. The wave parameters are presented in Table 4.1.

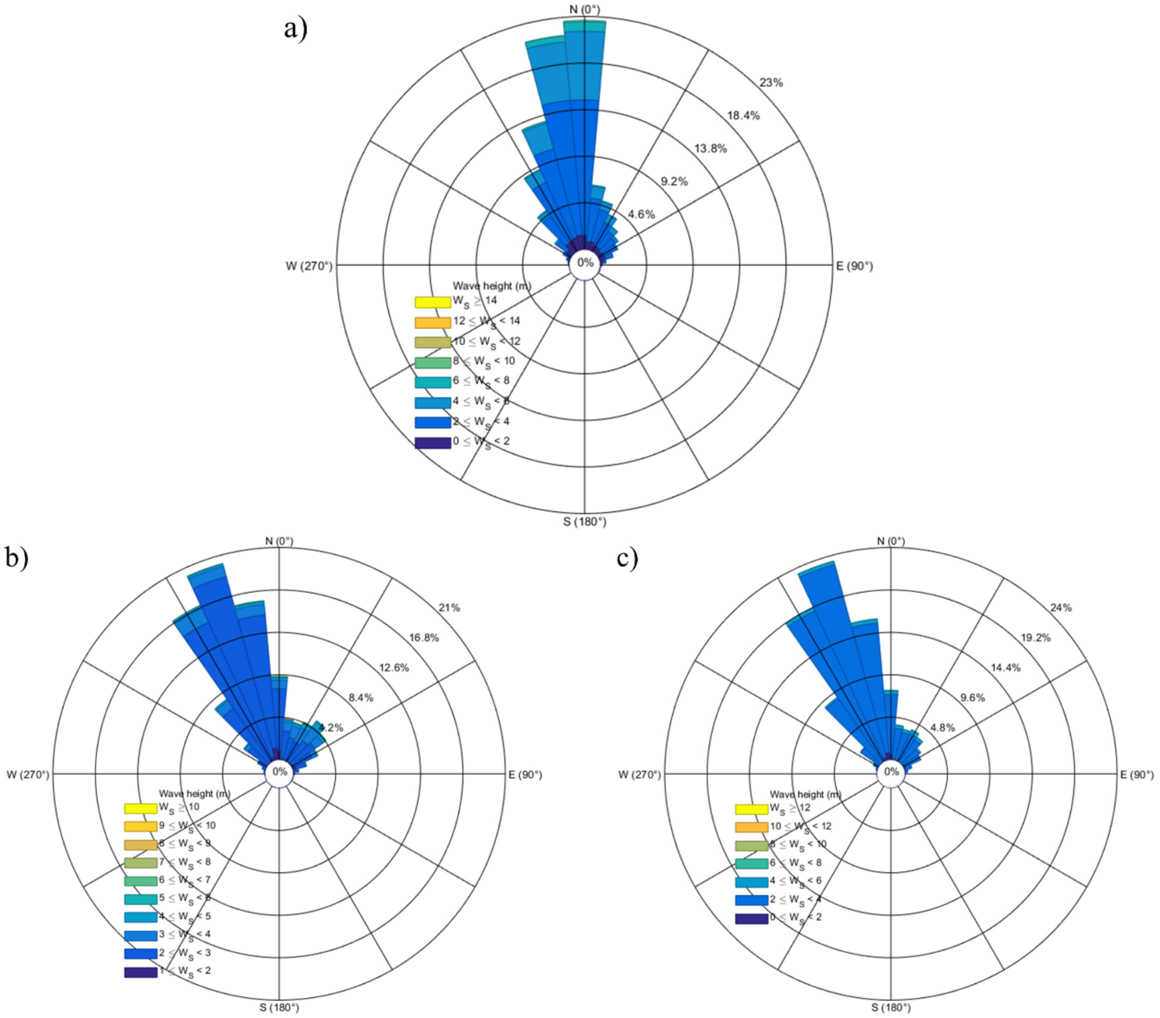

Figure 4.4 – Mean wave direction for the control points (Figure 4.3) for (a) the historical (1979-2005), (b) near future (2026-2045), and (c) far future (2081-2100) periods.

Table 4.1 - Wave height (H_s), peak period (T_p), and mean wave direction (*Dm*) for each climate period and return period.

	H_s (m)			**T_p (s)**			**Dm (°)**
	Tr^{10}	**Tr^{25}**	**Tr^{100}**	**Tr^{10}**	**Tr^{25}**	**Tr^{100}**	**-**
Historical	9.4	10.5	12.1	20.3	21.3	22.7	355
Near Future	8.6	9.5	10.6	20.7	21.9	23.6	345
Far Future	9.4	10.3	11.6	20.7	21.8	23.3	345

4.3.1.3 Hydrodynamic model

Delft3D suite was used to simulate the hydrodynamics of the study area due to the available features comprising tide and wind-driven flows, river flow, and wave-driven currents. The hydrodynamic conditions are modelled in the Delft3D-FLOW module [123], and are used in the WAVE module [121], which are executed in a combination between the modules allowing a two-way wave-current interaction.

The Delft3D-FLOW module was used to simulate the flood extent in Aveiro port. Flow module simulates the two-dimensional (2D) unsteady flow resulting from oceanic, fluvial and atmospheric drivers. An overview of the model physics can be found in [123]. A 2D model was setup with 577×421 cells curvilinear irregular grid with space varying resolution (II - Figure 4.3), where higher resolution is found in the port jurisdiction area (25 m) (Figure 4.2b). The bathymetry (Figure 4.5) was constructed based on several sources. In the coastal region was used the GEBCO database, and for the port's region was used multibeam bathymetry data collected in March of 2020 [198]. Detailed topographic data was obtained from the Aveiro Port Administration for the marginal areas under the port jurisdiction. Concerning the lagoon channels, bathymetry data from surveys performed between 1987 and 2012 [53] were used, while the topography for the lagoon was obtained from LIDAR topographic data in 2011, provided by the Portuguese General Direction of the Territory. The modelling time step was 60 seconds, and the bottom roughness was estimated with a standard coefficient of friction [199]. Background horizontal viscosity and diffusivity was set to 10 m^2s^{-1}. The model provided outputs with a temporal resolution of 5 minutes.

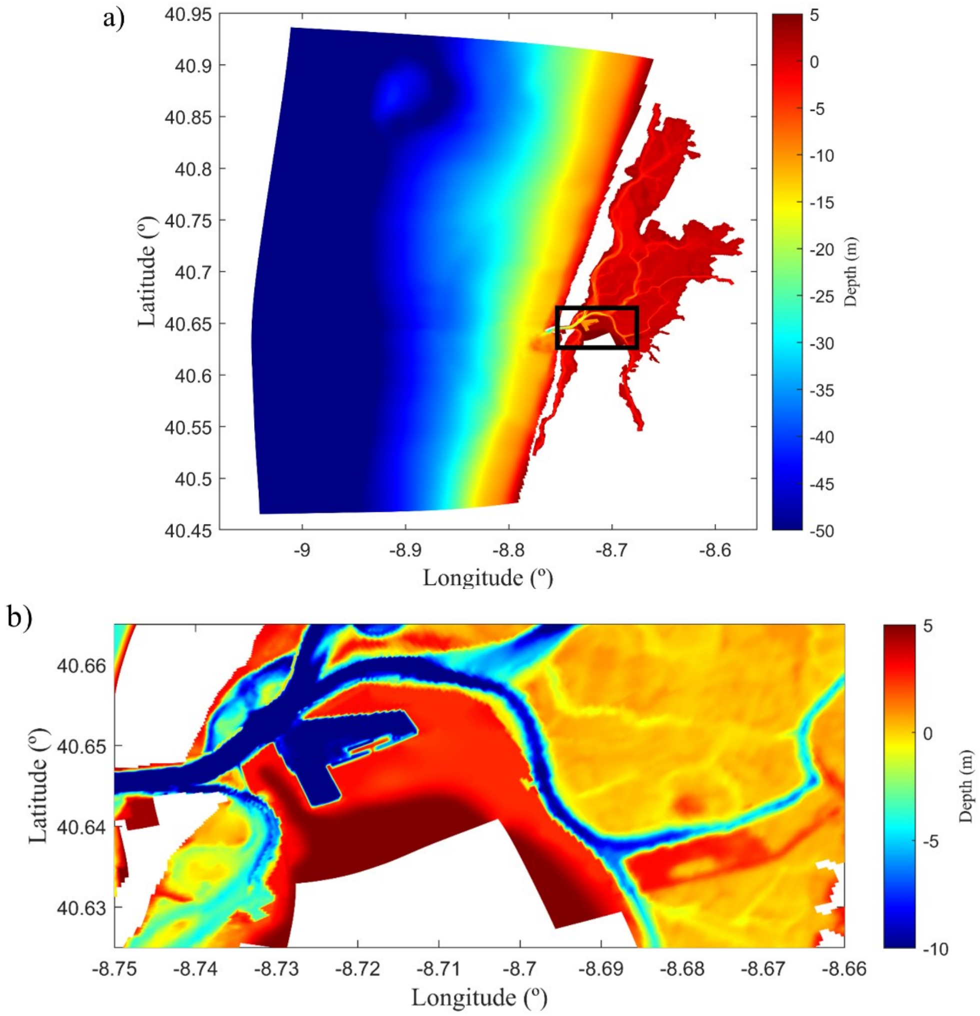

Figure 4.5 – Detailed numerical bathymetry used in the hydrodynamic model application for the (a) domain II and (b) Aveiro Port.

The model calibration and validation using the model setup described above was performed for two distinct periods and different open boundaries, aiming at different purposes: the tide propagation (i) and the storm surge propagation (ii).

The model was calibrated and validated for tidal propagation (i) considering the surveys conducted in July of 2019 and between 2002 and 2003 for the stations shown in Figure 4.2a. The model calibration setup was forced at the open boundaries with the astronomic constituents (Section 2.2.5). The calibration simulation was run for July of 2019, with one month as spin-up. The calibration process was performed by determining the *RMSE* and *Skill* [191] between measured and model results time series of the sea surface elevation at the stations with data available (Table 4.2). A *RMSE* close to zero and a *Skill* higher than 0.95 represents an excellent agreement between the model results and observed sea surface elevation [200].

Table 4.2 - Tidal model performance resulting from the calibration.

Tidal station		*RMSE* (m)	*Skill*
BA	Barra	0.0868	0.9967
C	Carregal	0.3658	0.8383
CA	Cacia	0.1701	0.9806
CB	Cais do Bico	0.1198	0.9900
CI	Cires	0.1373	0.9919
CN	Costa Nova	0.087	0.9963
CP	Cais da Pedra	0.2073	0.9610
L	Lota	0.1041	0.9950
P2	Ponte Cais	0.0752	0.9975
PU	Puxadouro	0.2868	0.9102
RN	Rio Novo	0.1172	0.9917
SJ	São Jacinto	0.1115	0.9937
T	Torreira	0.0875	0.9938
VA	Vista Alegre	0.1937	0.9685
VG	Vagueira	0.1380	0.9889

Overall, the model's ability to predict the spring-neap cycle in the port region (stations BA, SJ, CI, P2) is excellent. The highest disagreements were found in the inner stations, which show higher *RMSE* and lower *Skill*. These results are in agreement with previous studies [183,191,201], where the best results were found near the lagoon mouth, in the port jurisdiction surroundings, showing *RMSE*s ranging from 0.06 to 0.08 m in BA, 0.06 to 0.11 m in JS, 0.13 to 0.15 m in CI, and around 0.08 in P2.

The model validation for storm surge propagation (ii) was done for an event identified by [191] that occurred between 19th and 20th January 2013, which was monitored in seven stations located inside the lagoon.

The model setup was forced at the open boundaries using the same approach followed in [191], by prescribing a sea level at the open ocean boundary retrieved from the NEMO-v3.6 model, which comprises a spatial resolution of 0.028° and hourly outputs and is forced by the atmospheric pressure component (http://marine.copernicus.eu). The use of this database relies on the numerical domain limitation in space, as for an excellent reproduction of the surge propagation a large domain is required. In addition, the model setup was forced with mean sea level pressure and wind components at 10 m retrieved from Meteogalicia (http://mandeo.meteogalicia.es), with a spatial resolution of 12 km and hourly outputs. A spin-up of one month was used similarly to the calibration procedure described in (i).

The validation process was performed comparing the peak values in the residual levels for model results and observations (Figure 4.6) and determining the *RMSE* between these time series (Table 4.3). The model underestimates the observed surge peak, and the *RMSE* increases towards the inner lagoon stations, namely for the RN station, where an *RMSE* of 0.27 m is observed due to the proximity of the mouth of the largest river discharging in the lagoon and the observed riverine data shortage. The remaining stations show an *RMSE* under 0.12 m, similar to those found in [191], and therefore the model is considered validated for storm surge propagation.

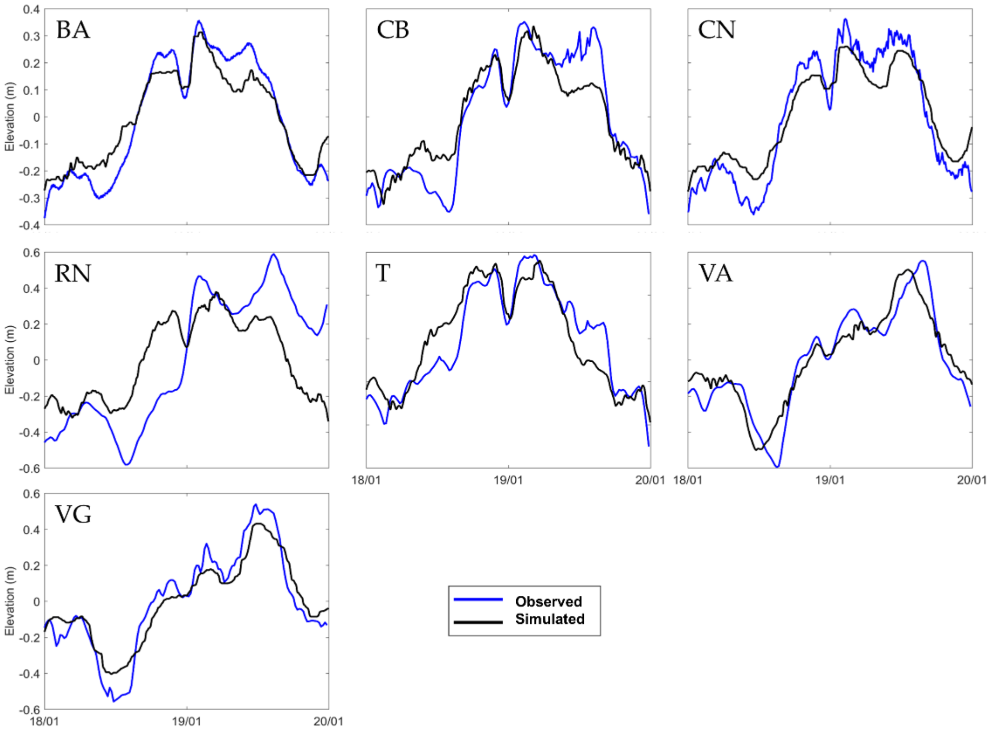

Figure 4.6 – Storm surge heights for observations (blue line) and model results (black line) under the storm surge event in January 2013.

Table 4.3 - Model performance under storm surge propagation resulting from the validation procedure.

Tidal Station	***RMSE* (m)**	**Peak**	
		Observed	**Simulated**
BA	0.07	0.36	0.31
CB	0.12	0.44	0.41
CN	0.08	0.36	0.25
RN	0.27	0.59	0.38
T	0.11	0.39	0.36
VA	0.09	0.54	0.43
VG	0.10	0.55	0.50

4.3.1.4 Scenarios design

The scenarios were modelled using the coupling between WAVE and FLOW modules. The hydrodynamic model was run using the ESL, taking into account the mean sea level, storm surge height and astronomic tide (Section 2.3.5), the riverine discharges (Section 2.3.6) and the wave parameters depicted in Table 4.1. The hydrodynamic implementation simulated the historical, near and far future periods for the Tr^{10}, Tr^{25} and Tr^{100}. A reference scenario representing the present climate extreme level was also determined, considering the inputs in Table 2.10 and Table 2.11. Table 4.4 shows an overview of the scenarios determined to assess the flood at Aveiro port.

Table 4.4 - Scenario definition. Extreme sea levels (ESL, m) and riverine discharge for Vouga (rd, $m^3 s^{-1}$) for the 10-, 25- and 100-year return periods for the reference scenario (referred to present climate), and the historical (1979-2005), near (2026-2045) and far future (2081-2099).

	Tr^{10}		Tr^{25}		Tr^{100}		**Reference**	
	ESL	rd	ESL	rd	ESL	rd	ESL	rd
Historical	4.23	1302	4.37	1559	4.56	1943	3.30	136.16
Near Future	4.42	1159	4.56	1388	4.75	1756		
Far Future	4.91	1029	5.05	1232	5.24	1535		

For each scenario, time series of sea levels and river discharges were constructed to impose at the oceanic and land boundaries, respectively. Figure 4.7 shows these time series for the historical period under the Tr^{100} as an example, highlighting the moment when the peak of the ESL was obtained. Regarding the oceanic boundary, a similar approach to [93] was conducted, taking into account the sea level evolution and a storm surge event coincident with high tide. For this purpose, the tidal constants of 2019 obtained from the tidal gauge located at the lagoon entrance (Figure 4.2b) were used to reconstruct the tidal signal in order to determine the tidal range and the level of mean high water springs (for a detailed methodology the reader is referred to [53,93]). The storm surge height was generated synthetically by using a sine function and assuming that storm surge persists during 3 days. The tidal and storm signals were then added, matching the storm surge to the level of mean high water springs (see the orange dashed line in Figure 4.7). Regarding river discharges, a constant value (annual average) was used in the first 9 days of simulation, rising to the peak value in the last 2 days (see the blue dashed line in Figure 4.7).

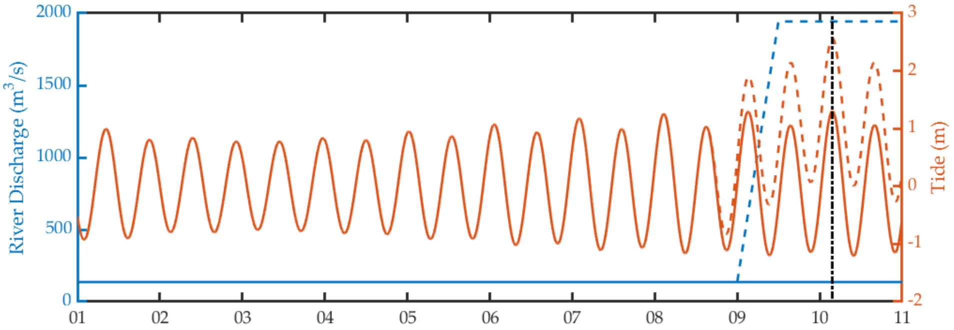

Figure 4.7 – The historical period under the 100-year return period scenario setup. Continuous lines represent the reference conditions, while the dashed line considers the 100-year return period conditions for riverine discharge and extreme sea level.

The identification of the driver that contributes most to the Aveiro port's inundation was also assessed by a set of simulations considering the far future scenario and Tr^{100} of ESL, storm surges, waves and riverine discharges. To fulfil this task, each simulation considered only a single driver independently (e.g. MSLR, without other oceanic drivers during the simulation. See Table 2.5) and were subsequently compared to the Reference scenario.

4.3.2 Flood assessment

The flood assessment for Aveiro Port was carried out for the historical, near and far future periods, considering the flood drivers for Tr^{10}, Tr^{25}, and Tr^{100}. Flood extent maps and flooded areas of the Aveiro Port’s terminals and zones under its jurisdiction for the historical, near, and far future scenarios and for each return period were determined. The flood assessment is conducted considering the reference level as a starting point, where no flood is present for the entire port jurisdiction area. This scenario considers the tide with the historical MSL and average riverine discharges. A comparison between the reference and the Tr^{10}, Tr^{25}, and Tr^{100} of ESL, storm surges, waves, and riverine discharge scenarios is conducted, indicating the port terminals susceptible to floods and the corresponding flooded area (Table 4.5).

Table 4.5 - Flooded areas of the terminals (Figure 4.2) at the Aveiro Port shown in percentage (%) relative to the total area of each terminal for the historical (H), near (NF), and far future (FF) periods and for the 10-, 25-, and 100-year return periods. Terminal 10 is not shown due to being designed as a single berthing dock.

		Tr^{10}			Tr^{25}			Tr^{100}		
Terminal	**Total (m^2)**	**H**	**NF**	**FF**	**H**	**NF**	**FF**	**H**	**NF**	**FF**
1	350334.1	26.1	26.1	26.1	26.1	26.1	26.8	27	29.1	33.1
2	158764.4	13.6	13.6	13.6	13.6	13.6	14.5	15.4	17.2	22.8
3	1570748.7	3.2	3.3	3.7	3.3	3.7	5.6	6.2	28.1	45.3
4	335462.1	5.6	5.6	5.8	5.6	5.6	6	6	19	38.4
5	654002	29	29.7	30.5	29.9	30.3	31.4	31.4	76.6	86.4
6	63166.5	100	100	100	100	100	100	100	100	100
7	120637.1	68.1	69.4	70.8	69.4	70.8	72.2	72.2	76.5	83.6
8	562141.5	49.3	51.2	63.5	52	60.4	71.2	71.2	77.1	84.6
9	483702.1	28.4	29.4	29.4	29.4	29.4	30.3	30.3	98.1	99.2
11	255672.6	38.1	45.1	45.1	45.1	45.1	45.2	45.2	45.4	46.8
12	37822.7	61.8	86.4	95.9	86.4	95.9	98.3	98.3	98.3	100

Concerning the historical period (1979–2005) (Figure 4.8a), the flooded areas are located primarily on the central lagoon region for a Tr^{10} and increase with the return period. Although this region is in the port’s jurisdiction, it is not relevant since it is not used for port activities. However, some floods can occur in the Shipping Repair/Construction Zone (7), Services, Logistics Zone (8) (Figure 4.8b), and in the Small Harbour (12), showing an increase of around 68.1, 49.3, and 61.8% of the flooded area for Tr^{10}, respectively, and leading partially to complete inundation under the Tr^{100} (76.5, 77.1 and 98.3%, respectively). Also, even under Tr^{10}, some marginal areas are inundated for most of the terminals, which are slightly expanded for higher return periods, including most of the terminals and zones covered by the port’s jurisdiction, namely the Liquid Bulk terminal (5), High Sea Fishing (9) and the Offshore Fishing (11) ports, with over 30% of the areas flooded. However, the Multipurpose South Terminal (6) shows a complete inundation under all climate scenarios for the Tr^{10}, Tr^{25}, and Tr^{100}. The flood extent shown under the historical period shows that Aveiro Port's resilience to floods is high under Tr^{10} and Tr^{25}, showing some vulnerable areas under the Tr^{100} scenario.

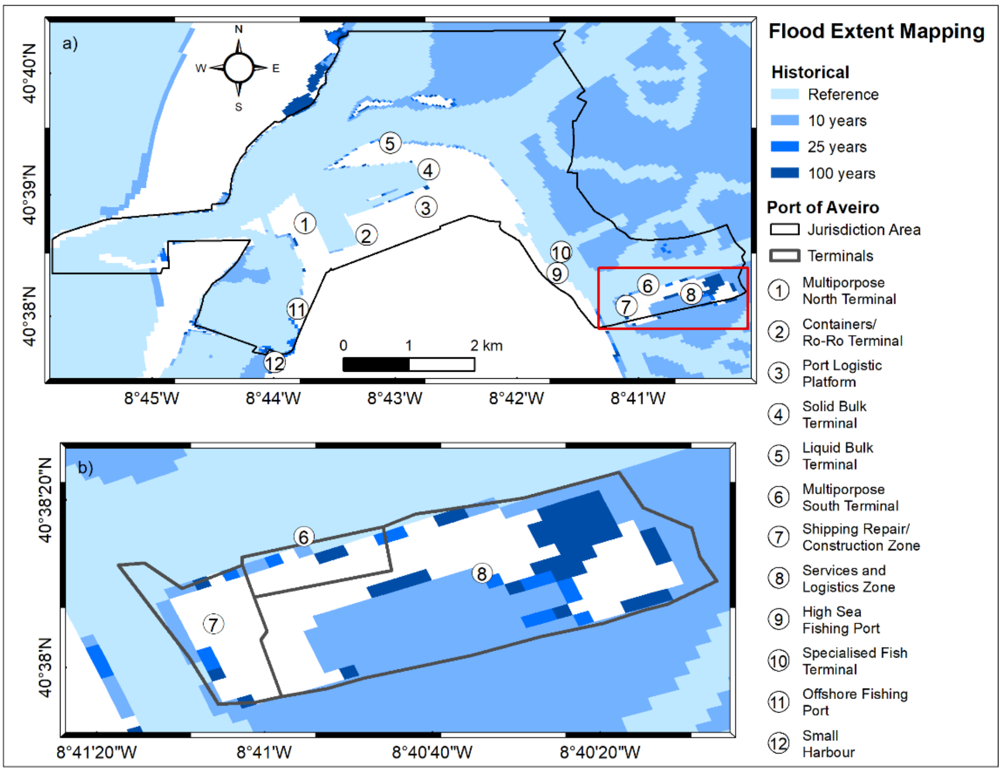

Figure 4.8 – Flood extent mapping of the Aveiro Port's terminals and zones (numbers 1–12) under its jurisdiction (a) (black line) and zoom of the most flooded area (b) (red line). Reference scenario under present climate and 10-, 25-, and 100-year return periods are determined for the historical (1979–2005) climate period.

In contrast to the historical period, the upcoming climate represented by the near-future period (2026–2045) (Figure 4.9a) shows a significant flood extent. The port's terminal area affected by flood increased under Tr^{10}, being more prominent in the Offshore Fishing (11) and Small Harbour (12) (a rise of 7 and 24.6% from the historical period, respectively). The Small Harbour (12) is almost totally flooded under the depicted scenarios and will keep this trend for the far future period scenarios. The flood rate is more evident under Tr^{25} and Tr^{100}, where most zones 5, 9, and 12 are nearly completely flooded in contrast with the previous climate scenario. Most of the terminals and zones show marginal flood, where the Port Logistic Platform (3) shows a sizeable marginal flood under Tr^{100}. Under the historical period (Figure 4.9b), the most vulnerable port areas increased their flood risk under this climate scenario, where over three-quarters of these terminals are flooded.

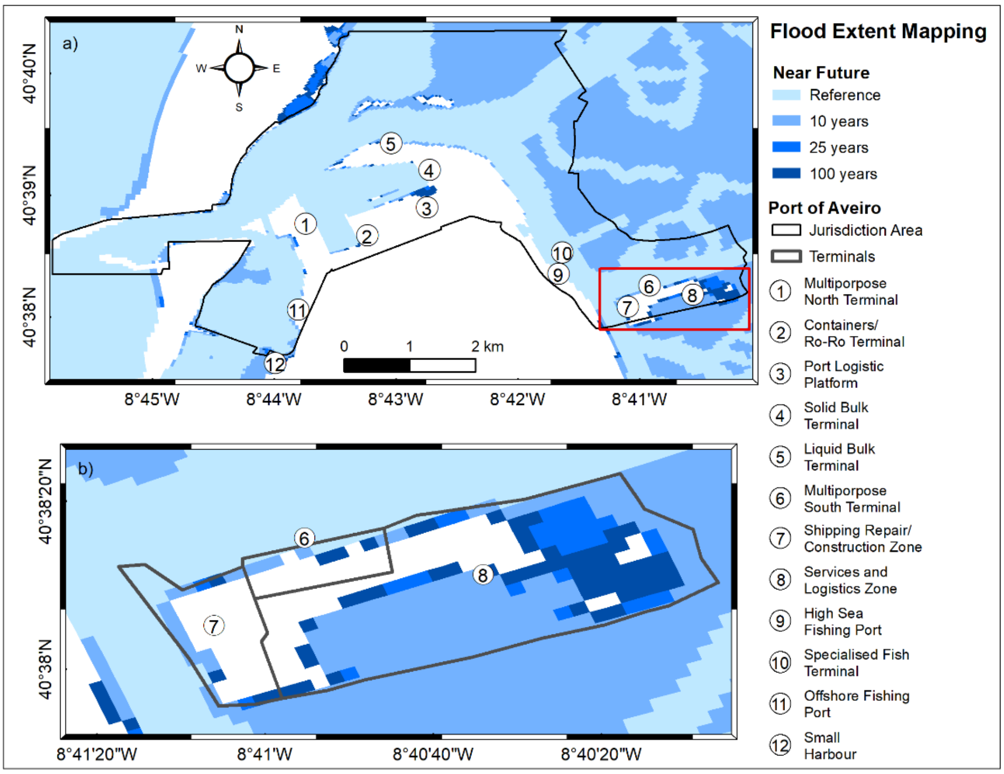

Figure 4.9 – Flood extent mapping of the Aveiro Port's terminals and zones (numbers 1–12) under its jurisdiction (a) (black line) and zoom of the most flooded area (b) (red line). Reference scenario under present climate and 10-, 25-, and 100-year return periods are determined for the near future (2026–2045) climate period.

Previous works demonstrated that climate change is expected to increase Ria de Aveiro's flood risk [93] due to increased oceanic and fluvial drivers, posing higher impacts at the end of the century [18]. In this context, and analysing the flood extent maps under far future climate drivers (Figure 4.10a), the marginal areas of most significant risk for Tr^{10} are all terminals and zones under Aveiro Port's jurisdiction as well as the Services and Logistics Zone (8), where the highest flood area increase was observed (12.3%) from the previous climate scenario. For the Tr^{25} the inundation extent increases, and Shipping Repair/Construction (7) and Services and Logistics (8) Zones are at risk of being completely flooded. The Containers/Ro-Ro Terminal (2) and Port Logistic Platform (3) will be subject to significant inundation, being both considerably affected by the far future meteocean drivers.

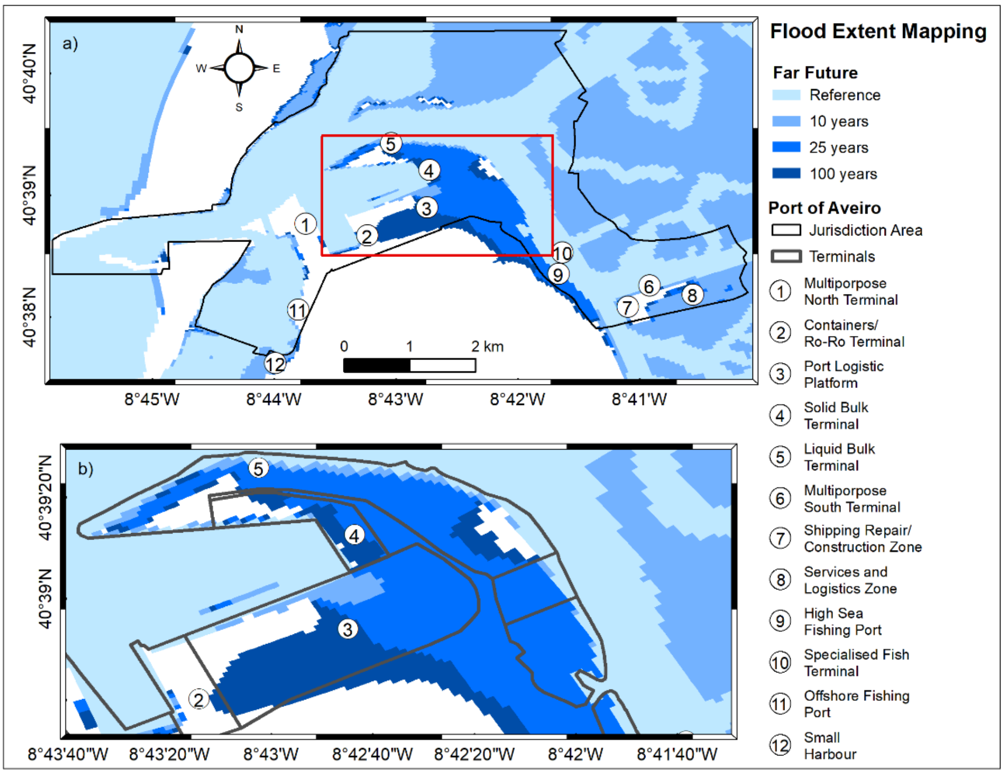

Figure 4.10 – Flood extent mapping of the Aveiro Port's terminals and zones (numbers 1–12) under its jurisdiction (a) (black line) and zoom of the most flooded area (b) (red line). Reference scenario under present climate and 10-, 25-, and 100-year return periods are determined for the far future (2081–2099) climate period.

Regarding the Tr^{100}, the flood extent increases significantly at most terminals, covering higher areas than for the Tr^{25}. The Services and Logistics Zone (8) is almost completely flooded, similarly to the High Sea Fishing Port (9) and Liquid Bulk Terminal (5), where most of the areas will be inundated. With the mean sea-level rise under this scenario, the flooded area now comprises a large section of the Port Logistic Platform (3) and the Offshore Fishing Port (11), and marginal flooding of the Solid Bulk Terminal (4). Analysing the entire port jurisdiction area, only the Multipurpose North Terminal (1) and the Containers/Ro-Ro Terminal (2) suffer a minor marginal inundation, indicating a low risk of flooding.

4.3.2.1 Climate driver contribution to flood

When evaluating the general evolution of the flood extent during the different climatic scenarios studied, it is verified that the severity of the flood extent is noticeable over the port's jurisdiction area, although some areas are more vulnerable to climate change than others. These areas could be impacted differently by each climate change driver taken into consideration in this study. Therefore, the contribution that these make to flood extent in Aveiro Port requires further investigation. Thus, a set of simulations was run considering the far future scenario and Tr^{100} of ESL, storm surges, waves, and riverine discharges to identify which driver contributes most to the Aveiro Port's inundation (Figure 4.11).

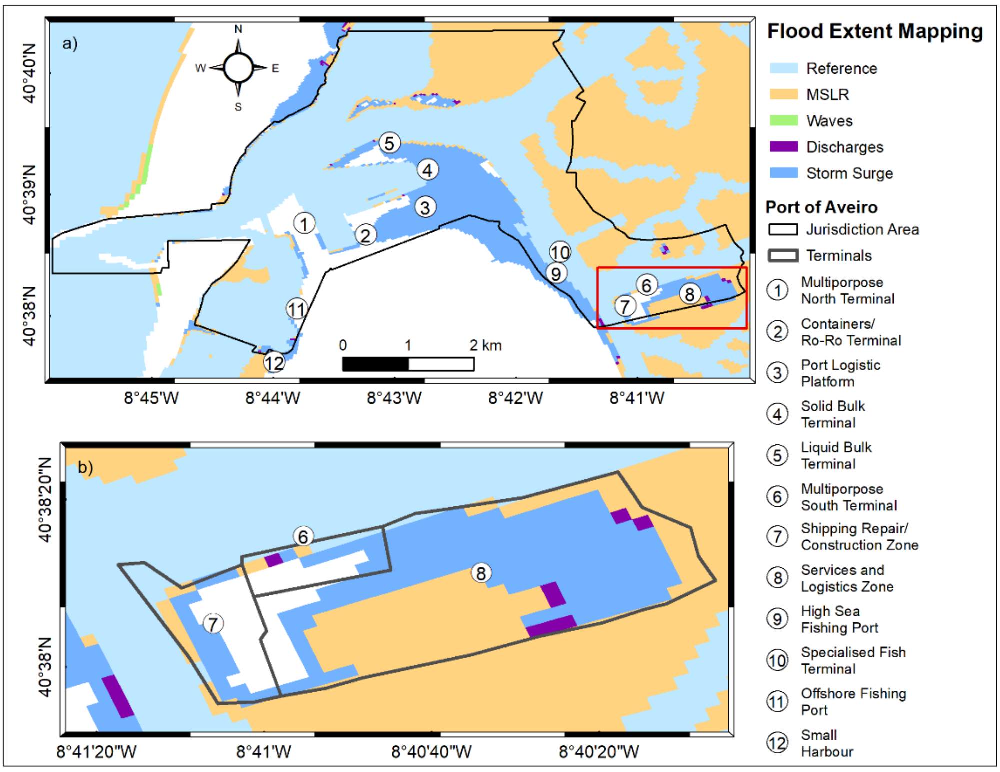

Figure 4.11 – Flood extent mapping of the Aveiro Port's terminals and zones (numbers 1–12) under its jurisdiction (a) (black line) and zoom of the most flooded area (b) (red line). Reference scenario and 100-year return period drivers for the far future (2081–2099) climate period, considering the climate drivers individually.

The MSLR is an important driver primarily due to its contribution to the total water level, a situation that can settle under the influence of other oceanic drivers. In a scenario where the MSLR is the only driver, the Aveiro Port's area affected by the flood comprises its jurisdiction area's central region, mainly affecting the marginal region of all the terminals and zones. An exception is observed at the Services and Logistics Zone (8), where the inundation occurs in most areas (Figure 4.11b). This inundation area increases when high riverine discharges occur, mainly in the Services and Logistics Zone (8) due to its proximity to the Vouga river, the most important contributor in terms of flow to the lagoon. On the other hand, the impact of the driver waves is residual, as expected due to the lagoon geometry and natural protection from the sea waves. The most prevalent oceanic driver is the storm surge events, which flooded most of the area of the majority of the terminals, and whose flood extent is highly correlated to that shown in Figure 4.10.

Moreover, there is a geographic scale mismatch between the Aveiro Lagoon and the Aveiro Port jurisdiction. While Aveiro Port can act on its jurisdiction area, some planning could occur outside of this area, involving third-party private or business stakeholders.

4.3.3 Conclusions

The assessment of the flood extent in the Aveiro Port in a climate change context under the RCP8.5 scenario was performed by providing an overview of the key areas impacted. Towards this objective, spatial flood extent maps were generated for the Aveiro Port jurisdiction area to assess and quantify the impact of climate change drivers for 10-, 25-, and 100-year return period scenarios, identifying the port terminals susceptible to flood under each scenario. Each of the climate drivers was also individually assessed in order to identify the most prevalent in the generation of floods in the Aveiro Port.

Aveiro Port, the most recent port in Portugal, is located in a low-lying lagoon, and the planned longevity of the infrastructure assets and port is inherently exposed to climate change drivers, such as rising MSL and ESL and riverine floods. As a result of these risks, Aveiro Port faces floods in the current climate, that may increase drastically at the end of the century if climate change drivers continue to accelerate as predicted, leading to large floods.

The results of this study also highlighted the impact of each driver on the flood extent under climate change scenarios, which is quite pronounced for all the return period scenarios at the end of the century on most of the terminals and zones of the port. Some of the port areas will be profoundly affected, namely within the innermost jurisdiction area where the riverine discharges and storm surges, along with MLSR, contribute the most to the inundation pattern found, which may lead to possible disruptions in operations and damages on property, resulting in serious economic repercussions due to Aveiro Port value to the region. Similar impacts of extensive floods due to the future climate drivers are expected in most of the ports located on the Atlantic coast of Europe [18,182].

Aveiro Port's vulnerability to rising sea levels will require planning adaptation measures to increase the port's resilience to climate change. Such measures to deal with long-term prospects of high flood extents must be assessed by forecasting the flood areas and identifying vulnerable locations since most of the infrastructures lie in areas threatened by the relative sea-level rise.

One should keep in mind that this flood assessment must be considered a support toolkit to identify the port's weakness in order to assist in the definition of adaptation, management, and resilience measures for future challenges.

4.4 LISBON PORT

The Lisbon port is located in Tagus estuary, on the IP west coast facing the Atlantic Ocean (Figure 4.12a). The Tagus estuary is one of the largest estuaries of the west coast of Europe and the largest of the Iberian Peninsula, having an East-West direction, with a total area of 320 km^2 [202]. A deep, narrow inlet channel and a shallow inner bay compose the estuary. The inlet channel is 15 km long, 2 km wide and reaches depths of 40 m in some places, constituting the deepest part of the estuary [203]. The inner bay is about 25 km long and 15 km wide, being the shallowest part of the estuary and has complex bottom topography with narrow channels, tidal flat areas and small islands on the innermost part of the estuary [204,205].

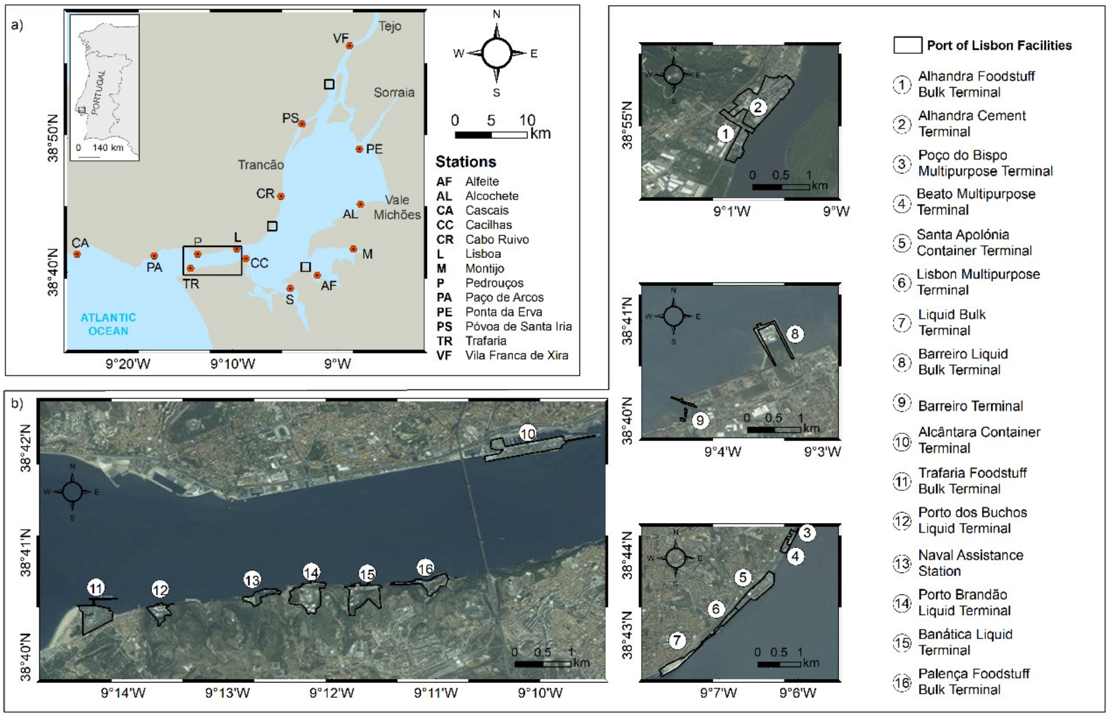

Figure 4.12 –Study area with the *in-situ* stations (a) used to validate the hydrodynamic model (Table 2.4). Location of the Lisbon port and the business areas in the port administration jurisdiction (b).

The estuary hydrography is mainly controlled by the tidal propagation and fluvial discharge [206], which can show a seasonal variability due to the influence of the river discharges [207,208], with particular emphasis during storms, where wind, atmospheric pressure and surface waves may influence the circulation [209]. The tides are semi-diurnal, and the M_2 harmonic constituent is dominant with amplitudes of 1 m [204], with tidal ranges varying from 0.75 m in neap tides in Cascais to 4.3 m in spring tides in the upper estuary [203,210]. The amplitudes of astronomic constituents grow rapidly in the lower estuary and more steady in the upper estuary and then decrease up to Vila Franca de Xira [204]. The tidal amplitude is larger than offshore as a result of a small resonance effect [211,212].

The hydrography of the estuary is modulated by the tidal propagation and fluvial discharge from the major rivers, Tagus, Sorraia, Trancão and Vale Michões tributaries. The Tagus River is the primary source of freshwater of the estuary, showing a pronounced dry/wet season signal and a large inter-annual variation [202]. Tagus river has an annual average discharge of 350 m^3s^{-1}, but varies significantly from summer to winter between approximately 30 m^3s^{-1} in a dry summer to 2000 m^3s^{-1} in a wet winter [207], where instantaneous records can reach flows of about 15000 m^3s^{-1} [206]. The other tributaries display a lower average annual discharge, Sorraia showing a mean flow of about 39.5 m^3s^{-1}, Trancão with 2.5 m^3s^{-1} [204] and Vale Michões is highly dependent on the rainfall and can reach up from 8 to 83 m^3s^{-1} in moderate and high discharges [213], respectively, during winter.

The dominant wind patterns display a seasonal signal, where summer shows a North-Northeast and West-Southwest directions, whereas winter shows East-Northeast and West-Southwest directions [214]. The presence of extreme wind speeds (> 8 ms^{-1}) are linked to West-Southwest directions [214]. The circulation at the estuary's mouth is also affected by the wave regime, being often exposed to the predominant swells from various incident directions. However, strong winds can induce local waves. These generated waves are enhanced by the tidal currents at the estuary entrance [215]. Ebb currents generate higher wave heights along the entrance channel, where the enhancements reach up to 60% in the navigation channel. However, in the central part of the estuary, significant wave heights are mostly related to the local wind-generated waves [214,215].

Historically, these hydrodynamic drivers and morphological settings promote the flooding of estuarine margins [204,216–218]. In fact, the conjugation of the extreme astronomic tidal levels and storm surge conditions led to flood events in the past [209,219] that especially impacted the flood-prone areas, affecting several residential and economic activities. The anthropogenic pressure over the estuary has been increasing in the margins, with Lisbon being the most populated city in Portugal. The inundation risk of this region is expected to increase in severity due to climate change effects [220], as identified in sections 2.2.6 and 2.2.7, with sea-level rise and an increase in extreme discharges.

As observed nowadays, Lisbon port location and structure was established during the first decades of the 20th century, boosted by the local industry and maritime traffic. Since then, the expansion of the port towards inner regions of the estuary took place, with the settlement of new terminals (www.portodelisboa.pt/). Its location turned Lisbon port an essential link between the Mediterranean and Northern Europe and a hub for international trade between Europe, America, and Africa. The port activities range from handling of containerised cargo, Roll-on/Roll-off, break-bulk cargo (located on the North Bank of the port) and liquid and solid bulk cargo (South Bank of the port) (Figure 4.12b). These allowed Lisbon Port to maintain its national leadership in the market of agri-bulk.

4.4.1 Model setup

Delft3D was proved to be a tool suitable for simulating flooding conditions during extreme events as previously observed for Aveiro port. Thus, the FLOW and WAVE modules are used to simulate the flooding assessment in Lisbon Port.

4.4.1.1 Downscaling approach

Following a similar approach to that used for Aveiro Port, a dynamical downscaling was required to address the lack of resolution in the regional model. FLOW and WAVE were used to design a model to propagate wave parameters across the region (Figure 4.13) and simultaneously simulate the hydrodynamic conditions for each climate and return period.

This local model was developed considering 3 nested domains using the WAVE module, one covering the coastal region close to the Tagus estuary entrance (I – Figure 4.13), extended from 38.2°N to 39.0°N and 9.87°W to the shore, with a horizontal resolution of 1 km. The second domain comprises the section contiguous to the estuary mouth, from 38.4°N to 38.8°N and including the shore between 8.67°W and the upper estuary, showing a resolution of 330 m. The third domain (III – Figure 4.13) is shared between WAVE and FLOW modules, using the same numerical grid and bathymetry, with higher resolution in the areas close to the terminals, permitting the perfect coupling between the modules.

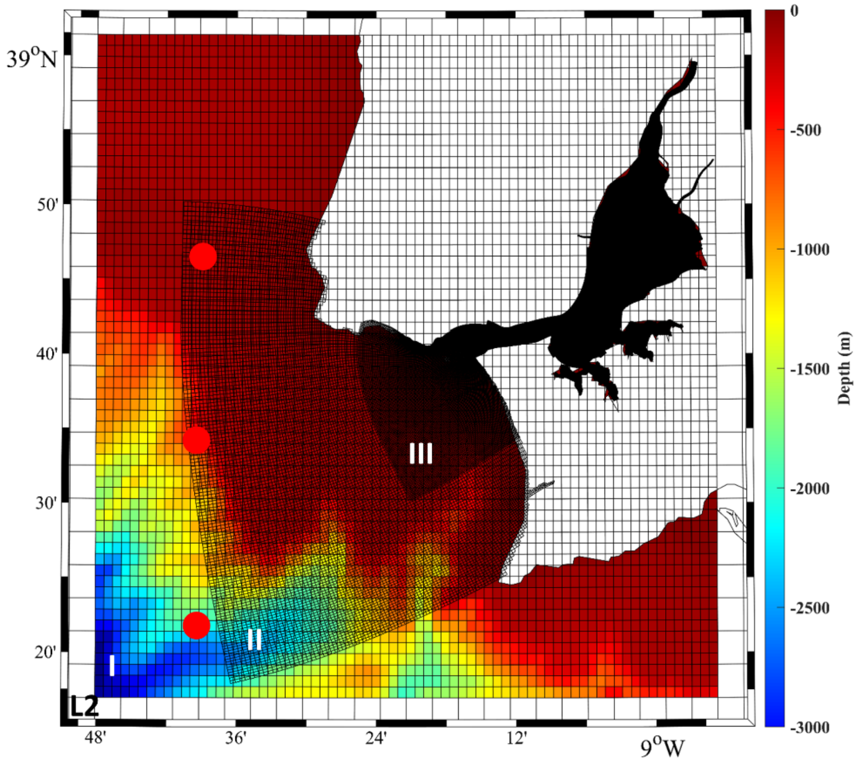

Figure 4.13 – Study area with the extents of the numerical domains and bathymetry used for the SWAN implementations and the wave propagation in the hydrodynamic model in the study area (I, II and III). The red dots indicate the grid nodes assessed in terms of wave parameters to determine the return periods.

The SWAN model physics was similar to that used for the Aveiro Port case. Triads, bottom friction, depth-induced breaking, and whitecapping computed with Komen exponential term [169] were considered by determining diffraction and reflections. The wave spectrum was discretised to 25 frequencies (0.0418-1 Hz) and 36 directional bands.

4.4.1.2 Characterisation of H_s, T_p and Dm

The wave parameters H_s, T_p and *Dm* were determined to study the extreme waves. Through the downscaled results of the BCC-CSM1.1 GCM, three grid nodes near the Tagus estuary mouth and parallel to the shore were selected as control points (Figure 4.13) to calculate the return periods for the wave parameters. As for the approach used to determine these parameters for Aveiro Port, hourly values obtained over 1979–2005 were used to determine the maximum H_s and T_p and fitted to statistical distributions to estimate H_s and T_p for Tr^{10}, Tr^{25}, and Tr^{100}.

The *Dm* is depicted in Figure 4.14, showing wave arrival predominant from north-northwest direction for all climate periods during winter. Following these results and considering [197], the mean wave direction will be the mean of the predominant wave directions. The wave parameters can be seen in Table 4.6.

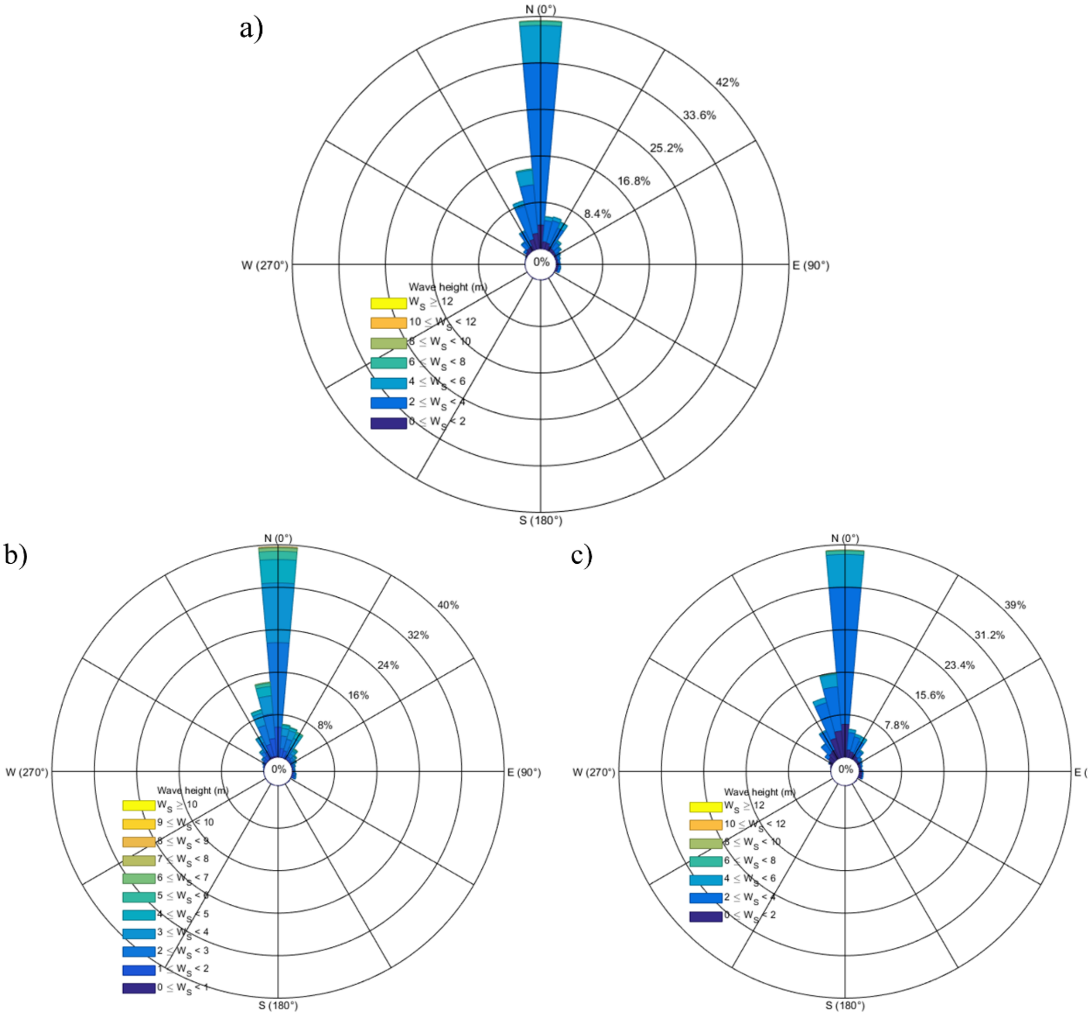

Figure 4.14 – Mean wave direction for the control points (Figure 4.13) for (a) the historical (1979-2005), (b) near future (2026-2045), and (c) far future (2081-2100) periods.

Table 4.6 - Wave height (H_s), peak period (T_p), and mean wave direction (Dm) for each climate period and return period.

	H_s (m)			T_p (s)			Dm (°)
	Tr^{10}	Tr^{25}	Tr^{100}	Tr^{10}	Tr^{25}	Tr^{100}	-
Historical	8.5	9.6	11.2	20.1	20.9	22.3	355
Near Future	8.7	9.7	11.3	20.5	21.5	22.9	355
Far Future	8.05	8.8	9.8	20.2	21.1	22.4	355

4.4.1.3 Hydrodynamic model

Delft3D FLOW was used to simulate the flood extent in Lisbon port. A 2D model was set up with 1101×342 cells curvilinear irregular grid with varying space resolution (III -Figure 4.13), where higher resolution is found in the terminals (20 m) (Figure 4.12b,c,d,e). The bathymetry (Figure 4.15) was constructed based on several sources. In the coastal region, the GEBCO database was used, and for the port's region, a compilation of data surveys performed between 1964 and 2009 was used. Detailed topographic data was obtained from LIDAR surveys performed in 2011, provided by the Portuguese General Direction of the Territory. The modelling time step was 60 seconds, and the bottom roughness was estimated with a standard coefficient of friction [199].

Background horizontal viscosity and diffusivity was set to 10 m^{2}s^{-1}. The model provided outputs with a temporal resolution of 5 minutes.

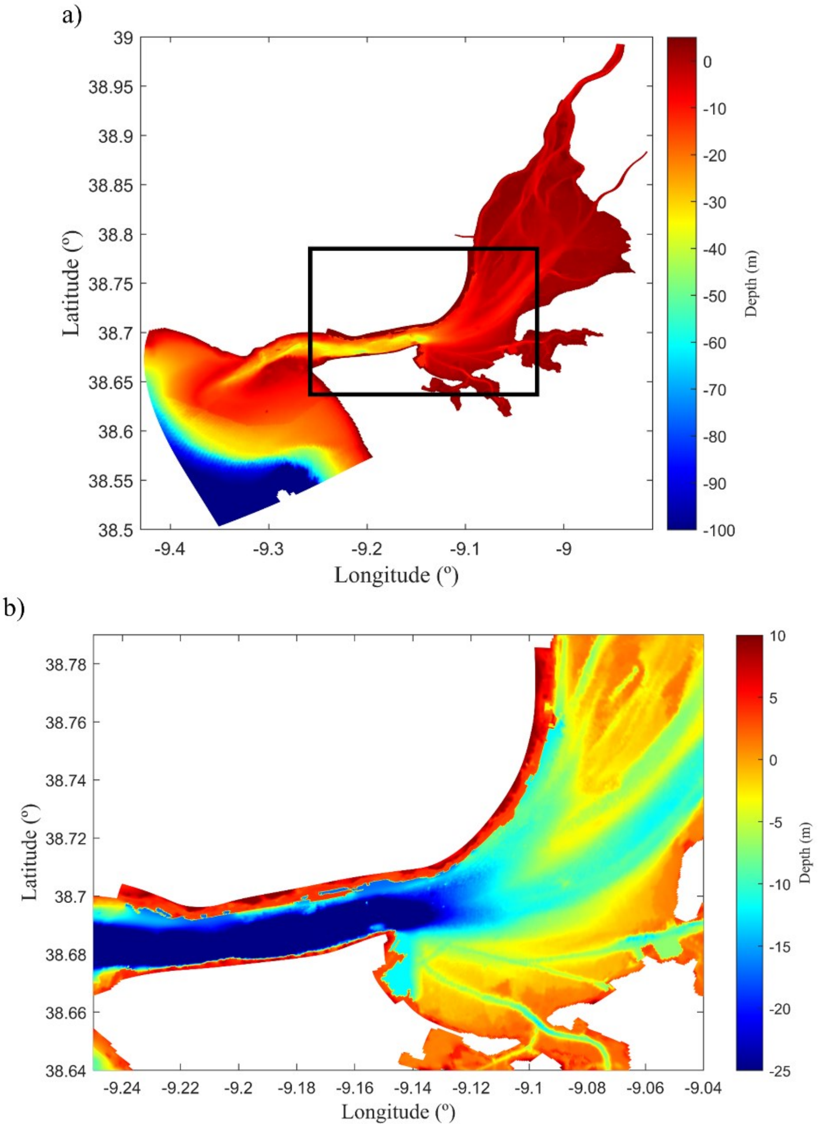

Figure 4.15 – Detailed numerical bathymetry used in the hydrodynamic model application for the (a) domain III and (b) Lisbon Port.

The model calibration was determined for different periods (Table 2.4), considering the surveys conducted in 1971, 1972 and 1981 for the stations shown in Figure 4.12a. The model calibration setup was forced at the open boundaries with the astronomic constituents (Section 2.2.5). The calibration simulations were performed for the years 1971, 1972 and 1981, with one month as spin-up. The *RMSE* and *Skill* [191] were assessed between measurements and model results time series of the sea surface elevation at the stations with available data (Table 4.7).

Table 4.7 - Tidal model performance resulting for the calibration procedure.

Tidal station		*RMSE* (m)	*Skill*
AF	Alfeite	0.1492	0.9935
AL	Alcochete	0.1529	0.9938
CA	Cascais	0.0874	0.9967
CC	Cacilhas	0.1202	0.9953
CR	Cabo Ruivo	0.1471	0.9938
L	Lisboa	0.1190	0.9954
M	Montijo	0.1380	0.9944
P	Pedrouços	0.1064	0.9957
PA	Paço de Arcos	0.0951	0.9962
PE	Ponta da Erva	0.1775	0.9919
PS	Póvoa de Santa Iria	0.1874	0.9913
S	Seixal	0.1345	0.9944
TR	Trafaria	0.1064	0.9957
VF	Vila Franca de Xira	0.3284	0.9732

The best model results were obtained for the stations closer to the estuary's mouth (*RMSE* of 9 and 11 cm and *Skill* of 0.99 for CA and L, respectively), and the lowest was found for station VF with *RMSE* around 0.33 m (error of about 8 %) of tidal range and *Skill* of 0.97. The high *RMSE* may be explained by the time lag between the bathymetry and the tidal observational data, as well as considering the high dynamism of the study area. These results are in agreement with previous studies [212,213], where the best results were found near the estuary mouth. The model's accuracy in predicting the spring-neap cycle for the inner stations is slightly smaller than for the stations near the mouth, where most of the terminals are located, indicated by the smaller *Skill* and higher *RMSE*.

The storm surge validation in the Tagus estuary was not considered because its morphology is characterised by a wide and deep channel that connects the ocean to the inner bay. Under these characteristics, the storm surge signal propagates almost unchanged along most of the estuary [209].

4.4.1.4 Scenarios design

The approach defined to Lisbon Port was similar to the presented for Aveiro Port case, by forcing the hydrodynamic model with ESL, taking into account the mean sea level, storm surge and astronomic tide (Section 2.3.5), the riverine discharges (Section 2.3.6) and the wave parameters (Table 4.6). The simulations targeted the historical, near and far future periods for the Tr^{10}, Tr^{25} and Tr^{100} with a reference scenario representing the present climate extreme level. An overview of the scenarios is presented in Table 4.8.

Table 4.8 - Scenario definition. Extreme sea levels (ESL, m) and riverine discharge for Tagus (rd, $m^3 s^{-1}$) for the 10-, 25- and 100-year return periods for the reference scenario (referred to present climate), and the historical (1979-2005), near (2026-2045) and far future (2081-2099).

	Tr^{10}		Tr^{25}		Tr^{100}		**Reference**	
	ESL	rd	ESL	rd	ESL	rd	ESL	rd
Historical	4.22	5318	4.32	6906	4.45	9256	3.30	994
Near Future	4.41	4892	4.51	6354	4.64	8515		
Far Future	4.90	4095	5.00	5318	5.13	7127		

Each scenario was forced at the open boundaries with time series of ESL and river discharge. The initial 9 days were used as a spin-up with a tide and discharge considering the reference values. The river discharge was increased in the following 2 days, reaching its peak simultaneously with the storm surge and the tide representing the ESL for each climate period and return period (Figure 4.16). Figure 4.16 shows the simulation setup for the historical period under the *Tr*^{100}, highlighting the moment when the peak of the ESL was obtained.

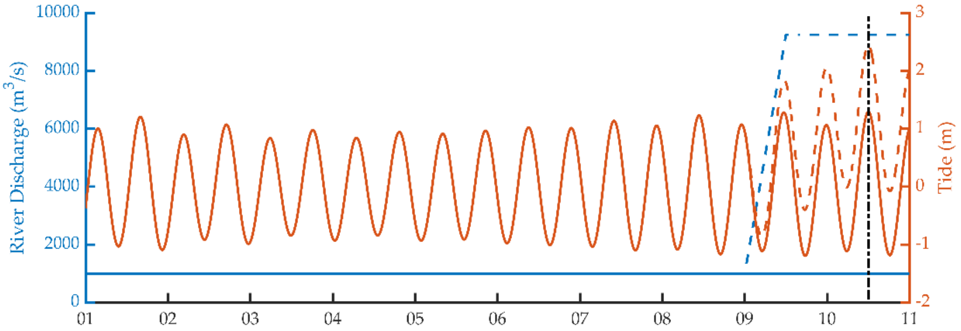

Figure 4.16 – The historical period under the 100-year return period scenario setup. Continuous lines represent the reference conditions, while the dashed line considers the 100-year return period conditions for riverine discharge and extreme sea level.

4.4.2 Flood assessment

The flood assessment for Lisbon Port was performed for the historical, near and far future periods, considering the flood drivers for *Tr*^{10}, *Tr*^{25}, and *Tr*^{100} return periods. Flood extent maps and flooded areas of the Lisbon Port's terminals were determined. The flood assessment is conducted considering the reference level as a starting point, where no flood occurs in the terminals. This scenario considers the tide with the historical MSL and average riverine discharges. A comparison between the reference and the *Tr*^{10}, *Tr*^{25}, and *Tr*^{100} of ESL, storm surges, waves, and riverine discharge scenarios is performed, indicating the port terminals susceptible to floods and the corresponding flooded area (Table 4.9).

Table 4.9 - Flooded areas of the terminals (Figure 4.12) at the Lisbon Port shown in percentage (%) relative to the total area of each terminal for the historical (H), near (NF), and far future (FF) periods and for the 10-, 25-, and 100-year return periods.

			Tr^{10}			Tr^{25}			Tr^{100}		
		Total (m^2)	**H**	**NF**	**FF**	**H**	**NF**	**FF**	**H**	**NF**	**FF**
Terminals	1	160846.4	41.2	41.2	42.0	41.2	42.0	42.0	42.0	42.0	42.0
	2	400043.0	17.3	25.6	36.8	26.1	32.3	37.7	32.3	32.3	38.0
	3	34567.2	43.6	44.0	74.6	44.0	48.4	81.5	48.4	65.4	100.0
	4	32285.9	7.6	25.9	42.9	11.5	25.9	56.1	25.9	25.9	92.1
	5	197486.8	14.0	18.4	69.2	17.1	25.7	82.0	21.4	28.7	88.9
	6	48411.4	9.4	25.4	39.8	9.4	35.6	39.8	32.9	38.8	63.8
	7	110555.5	59.0	59.8	70.8	59.8	62.1	74.3	62.1	63.2	95.3
	8	67794.8	55.2	65.8	74.7	57.8	67.5	77.7	65.8	67.5	78.2
	9	17255.4	83.9	83.9	83.9	83.9	83.9	83.9	83.9	83.9	92.3
	10	238170.3	18.8	19.6	25.8	18.8	20.3	27.8	20.3	21.5	31.8
	11	164927.1	14.5	14.5	16.4	14.5	14.5	19.3	14.5	16.4	22.8
	12	66565.0	16.9	16.9	16.9	16.9	16.9	16.9	16.9	16.9	16.9
	13	65145.8	35.3	38.8	42.3	38.8	38.8	42.3	38.8	38.8	45.7
	14	178806.6	9.2	9.2	9.5	9.2	9.2	9.5	9.2	9.2	9.5
	15	169354.6	8.0	8.0	8.0	8.0	8.0	11.5	8.0	8.0	11.5
	16	96200.1	28.8	28.8	35.1	28.8	28.8	35.1	28.8	33.0	35.1

The Lisbon port is scattered along the Tagus estuary margins under different morphological characteristics that could affect the terminals flood extent. This variability is shown for the historical period (1979–2005) (Figure 4.17), where the most flooded terminals are located primarily on the inner region, whereas the terminals (10-16) located in the main entrance channel (Figure 4.17b) are only exposed marginally, with particular emphasis on the Naval Assistance Station (13) and Palença Foodstuff Bulk Terminal (16). These terminals show over a quarter of their area flooded under the Tr^{10} scenario due to low lying margins, which slightly increases for higher return periods.

The terminals in the inner estuary exposed to intense floods are the Alhandra Foodstuff Bulk Terminal (1), Poço do Bispo Multipurpose Terminal (3), Liquid Bulk Terminal (7), Barreiro Liquid Bulk Terminal (8) and Barreiro Terminal (9). For a Tr^{10} scenario, the flood extent for these terminals is over 40% of its area, reaching 84% in the Barreiro Terminal (9). The flood extent intensifies with higher return periods, being more notorious under the Tr^{100}, where most of the terminals, including Alhandra Cement Terminal (2), Beato and Lisbon Multipurpose Terminal (4 and 6, respectively) and Santa Apolónia Container Terminal (5) faces over 20% of its area flooded.

The flood extent for the historical period shows that Lisbon Port's resilience to floods is high for the terminals located at the entrance channel (10-16), while the terminals located inside the estuary are highly vulnerable to floods under the Tr^{100} scenario.

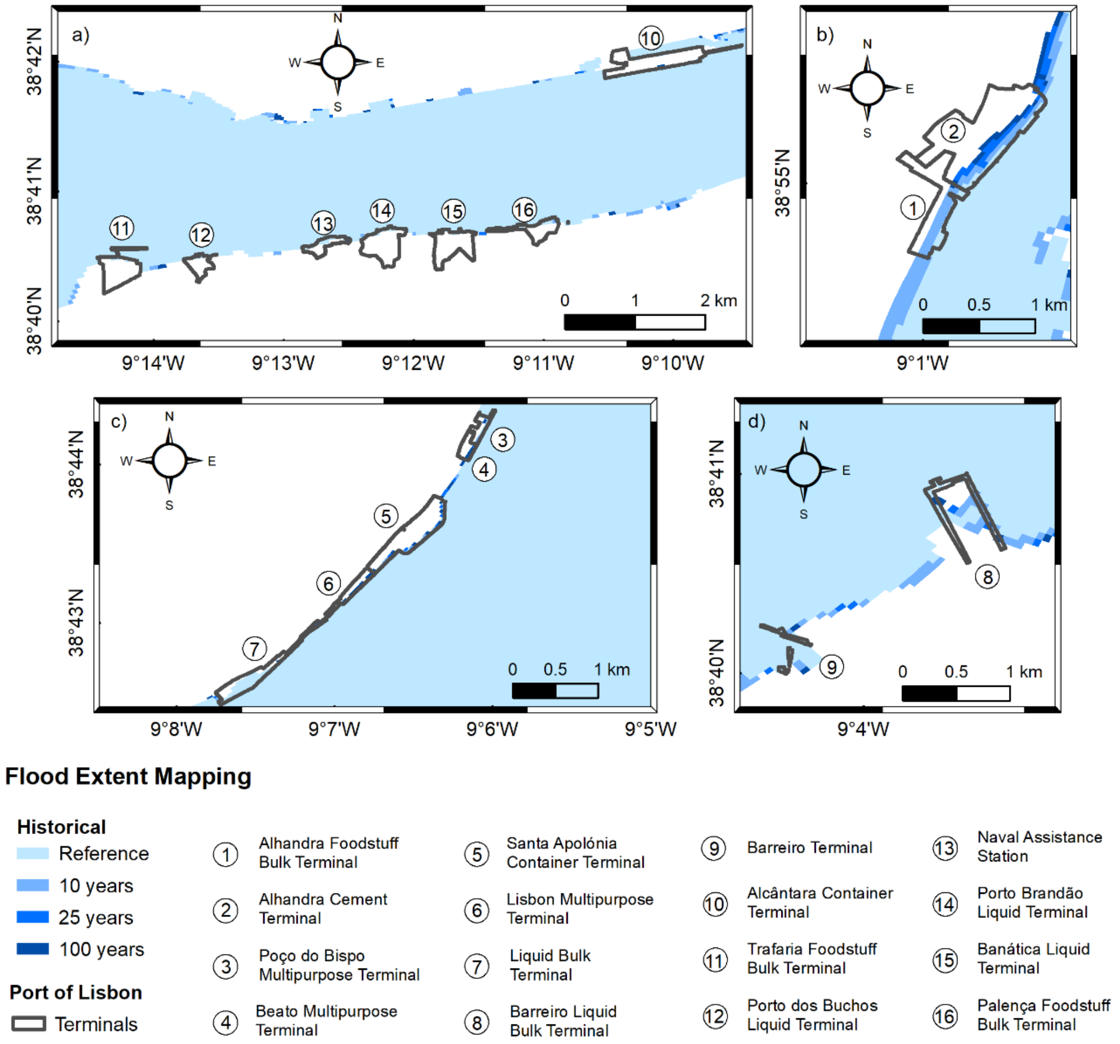

Figure 4.17 – Flood extent mapping of the Lisbon Port's terminals (numbers 1–16) located along the estuary margins (a,b,c,d). Reference scenario under present climate and 10-, 25-, and 100-year return periods are determined for the historical (1979–2005) climate period.

Looking at the near future period (2026-2045) (Figure 4.18), the flood risk increases for most of the terminals, except for those located at the main channel. The flood extent pattern is similar for all return periods in the historical period, where marginal floods occur on the terminals 10-16, and the Naval Assistance Stations (13) slightly increased its flooded area. The terminals located on the south margin of the estuary remained with severe floods, where Barreiro Liquid Bulk Terminal (8) increased the flooded area by 10% compared with the historical period. However, the flooded area was similar to that observed in the historical period, for all return periods.

The terminals located on the northern margin present a higher flooded area for the Tr^{10}, showing most of the marginal areas flooded for terminals 1 to 7. However, the Poço do Bispo Multipurpose (3) and the Liquid Bulk Terminals (7) significantly increased more than 60% of their flooded area.

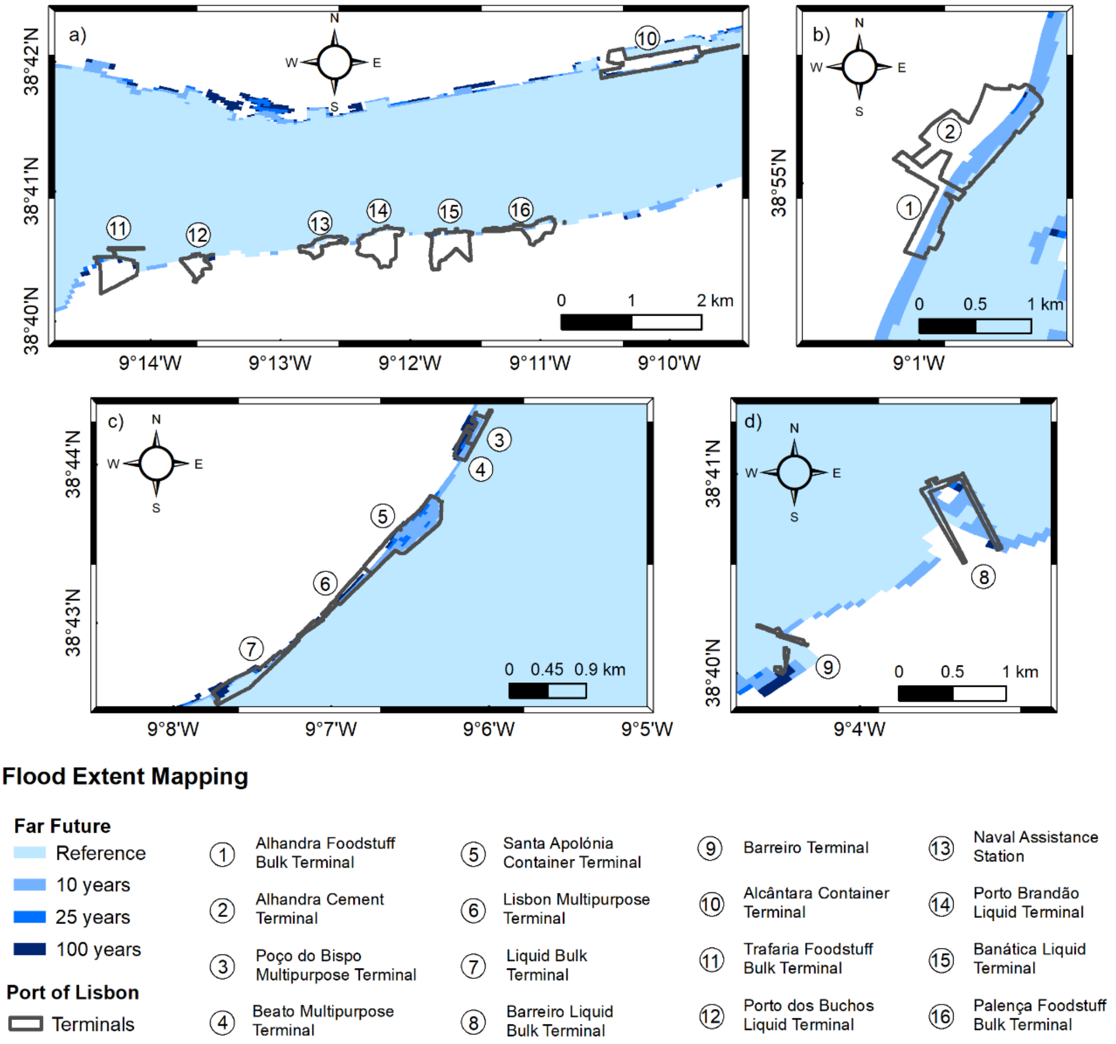

Figure 4.18 – Flood extent mapping of the Lisbon Port's terminals (numbers 1–16) located along the estuary margins (a,b,c,d). Reference scenario under present climate and 10-, 25-, and 100-year return periods are determined for the near future (2026–2045) climate period.

Regarding the far future period (2081-2100) (Figure 4.19), the flood extent increases significantly at most terminals, covering higher areas than for the previous climate periods, except for the terminals located at the main channel. *Tr*^{10} scenario shows severe floods in the terminals located in the estuary margins, some partially floods are observed in the Poço do Bispo and Beato Multipurpose Terminal (3 and 4, with 74.6 and 42.9% respectively), Santa Apolónia Container (5) and Lisbon Multipurpose (6) Terminals (69.2 and 39.8%, respectively).

The *Tr*^{25} scenario shows an expansion of the flooded area in all terminals listed above, reaching its peak in the *Tr*^{100} scenario, where the terminals are completely flooded in the northern and southern margins of the estuary. The floods are notorious on the Poço do Bispo (3) and Beato (4) Multipurpose Terminals, Santa Apolónia Container (5) and Liquid Bulk (7) Terminals and Barreiro Terminal (9), where over 90% of their area will be inundated.

Considering the the mean sea-level rise under this scenario, the resulting flooded area indicates a high risk to floods for the Lisbon Port.

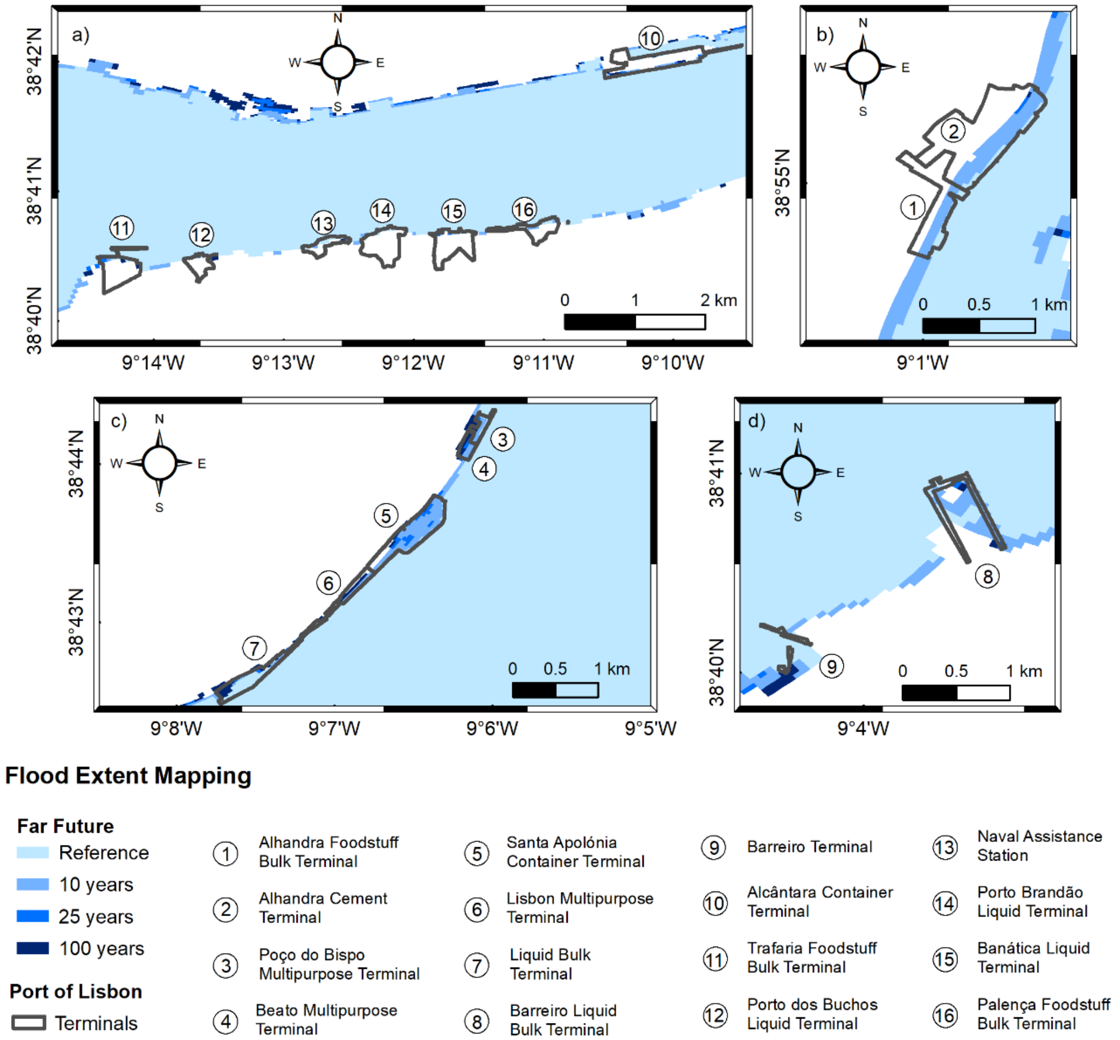

Figure 4.19 – Flood extent mapping of the Lisbon Port's terminals (numbers 1–16) located along the estuary margins (a,b,c,d). Reference scenario under present climate and 10-, 25-, and 100-year return periods are determined for the far future (2081–2099) climate period.

4.4.3 Conclusions

The assessment of the flood extent on Lisbon Port in a climate change context under the RCP8.5 scenario was performed by providing an overview of the key areas impacted by the floods under different return periods. Flood extent maps were generated to assess and quantify the impact of climate change drivers for 10-, 25-, and 100-year return period scenarios, identifying the port terminals susceptible to flood under each scenario.

Lisbon Port benefits from a natural shelter, where its entrance orientation protects the Port from the most north-northwest energetic waves during winter. However, the low-lying margins of the estuary compromise the port resilience to rising sea levels caused by the climate drivers MSL, ESL and riverine discharges. As a result of these drivers, most of the Lisbon Port terminals are threatened by floods, with emphasis on the terminals located in the inner estuary for the historical period, as previously observed by [218]. The flood hazard increases for higher return periods with the increase of ESL, whereas for future periods, the climate drivers such as the MSL promote large floods along the estuary margins[220]. The terminals located in the entrance channel of the estuary faces marginal inundations under Tr^{10} scenario, which increases significantly under Tr^{25} and Tr^{100} scenarios.

Lisbon Port's risk to floods is high with the present climate drivers under Tr^{10}, Tr^{25} and Tr^{100} scenarios. These floods are observed today under dangerous meteorological conditions, and it is expected that the increase in MSL will enhance its extent and impact. Thus, the risk will increase significantly in some terminals under climate change scenarios, where large sections of the port may be flooded. These results highlight the risk of flooding at Lisbon Port, which requires adaptation measures to increase the port's resilience to climate change to counteract projected flood patterns.

4.5 VIGO PORT

Vigo port is located in Ria de Vigo, the widest of the four V-shaped valleys with SSE-NNW orientation in the Rias Baixas, between 42°N and 43°N (Figure 4.20). According to the hydrodynamic characteristics, Rias de Vigo is divided into inner, middle and outer sectors. In Ria de Vigo, the outer section is protected by the Cíes Islands, endowing a natural harbour with around 14.000 hectares of sheltered water from the direct influence of the ocean. The middle sector is the central part of the Ria, where the Port is located. The inner sector covers the shallow head of the Ria, where the Oitavén-Verdugo river flows. Ria de Vigo supports the most significant population hub in the region, with an important touristic and industrial activity [221], being a major shipyard centre and Europe’s principal landing point for fishing [222]. The Vigo Port jurisdiction area comprises the whole Ria de Vigo region (Figure 4.20a), limited in the south by the Punta Lameda, and at the north by Cape Home, and at the west by the Cíes Islands [223]. These features allow the port to operate 365 days a year. Most of the infrastructures (Figure 4.20b) in Vigo Port are for freight, passenger and fishing, which are located in the southern margin of the Ria de Vigo, in Vigo municipality. A detailed concession map of the terminals can be obtained on the Vigo Port’s official website (https://www.apvigo.es/en/paginas/descargas_de_planos). However, there are other port facilities placed in the service area of the port, on the northern margin and in the inner section of the Ria de Vigo, but are under a private domain.

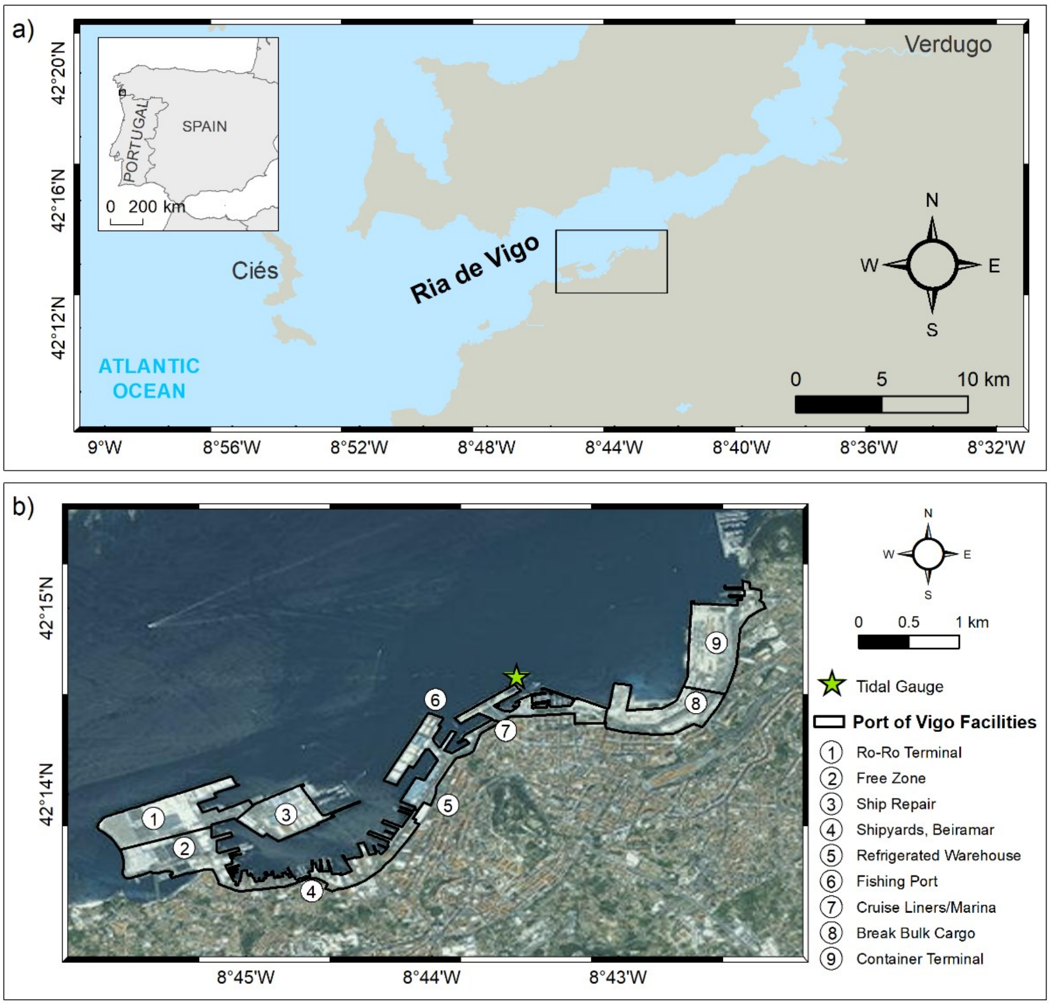

Figure 4.20 – Study area and location of the Vigo Port (a) with the business areas and the *in-situ* station used to validate the hydrodynamic model (Table 2.4) (b).

The Oitavén-Verdugo river is the main tributary of the Ria, with a mean annual discharge of 13 m^3s^{-1} characterized by high seasonal variability, ranging from 120 m^3s^{-1} to 1 m^3s^{-1}, in winter and summer, respectively [224]. The mesotidal tide [225] also contributes to the Ria circulation, characterised by a semidiurnal pattern.

The Azores anticyclone characterises the weather and climate observed in the Rias Baixas region, where the winds are predominant from NNE in the winter, and from northeast to the northwest in the summer [225,226]. This seasonal pattern is also observed in the wave regime, with great inter-annual variability, where the swell component is predominant during most of the year [227]. In the winter, the significant wave height usually ranges between 1-3 m, reaching up to 10 m during storms, and northwest is the dominant wave direction [228].

The Ria de Vigo shelters a large aquaculture industry close to the Vigo Port, which coexists with the urban and industrial activities in the inner part of the Ria [229]. The fishing industry has been the mainstay of Vigo Port activities for centuries, being the base of the port's economy. Nowadays, the Port activity has expanded to more industrial sectors, which has reinforced the importance of Vigo Port for the regional economy. Thus, the need to adapt the Vigo Port strategic plan [223], focusing on climate change resilience, is of paramount importance to ensure its future activities.

4.5.1 Model setup

FLOW and WAVE were used to simulate the hydrodynamic conditions during extreme events, following a similar approach to that used for Aveiro and Lisbon Ports.

4.5.1.1 Downscaling approach

As in previous case studies, the downscaling of the wave parameters is required to increase the H_s and T_p accuracy, which requires finer grid resolution to simulate the wave propagation. WAVE module was implemented using 3 nested domains, from coarser horizontal resolution (~1 km) covering the region limited by 41.85°N to 42.85°N and 9.23°W to the shore (Figure 4.21 - I), and a second domain from 41.98°N to 42.52°N, limited between 9.09°W and the coast (Figure 4.21 - II) with a mean resolution of 300 m. The third domain (Figure 4.21 - III), which is shared by WAVE and FLOW modules, is restricted to Ria de Vigo, covering roughly the jurisdiction area of Vigo Port, with a mean resolution of 30 m on the navigation channel and up to 10 m in the port terminals.

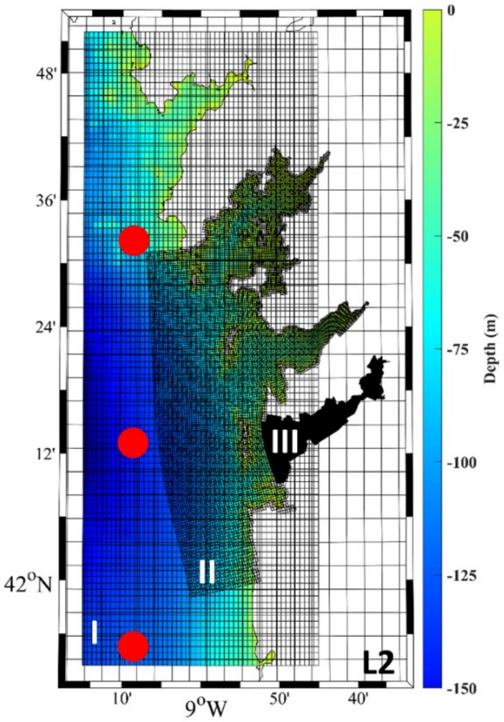

Figure 4.21 – Study area with the numerical domains extension and bathymetry used for the SWAN implementations and the wave propagation in the hydrodynamic model in the study area (I, II and III). The red dots indicate the grid nodes assessed in terms of wave parameters to determine the return periods.

The SWAN model physics is similar to that used to simulate wave propagation for the previous case studies, having also been applied a wave spectrum discretised for 25 frequencies (0.0418-1 Hz) and 36 directional bands.

4.5.1.2 Characterisation of H_s, T_p and Dm

The wave parameters obtained through the downscaling of the BCC-CSM1.1 GCM was analysed, considering three control points (Figure 4.21) located in the vicinity of the Rias Baixas entrance, characterizing the wave climate in the region. The Tr^{10}, Tr^{25}, and Tr^{100} return periods for the wave parameters were determined by means of statistical distributions of hourly values considering the maximum H_s and T_p. Figure 4.22 shows the predominant wave direction (*Dm*), divided into 36 bins, for the climate periods. The historical period (Figure 4.22a) shows that most of the wave exhibits a north direction, which will remain unchanged for future periods (Figure 4.22b,c). The historical (1979-2005), near- (2026-2045) and far-future (2081-2100) return periods of *Dm*, H_s and T_p can be observed in Table 4.10.

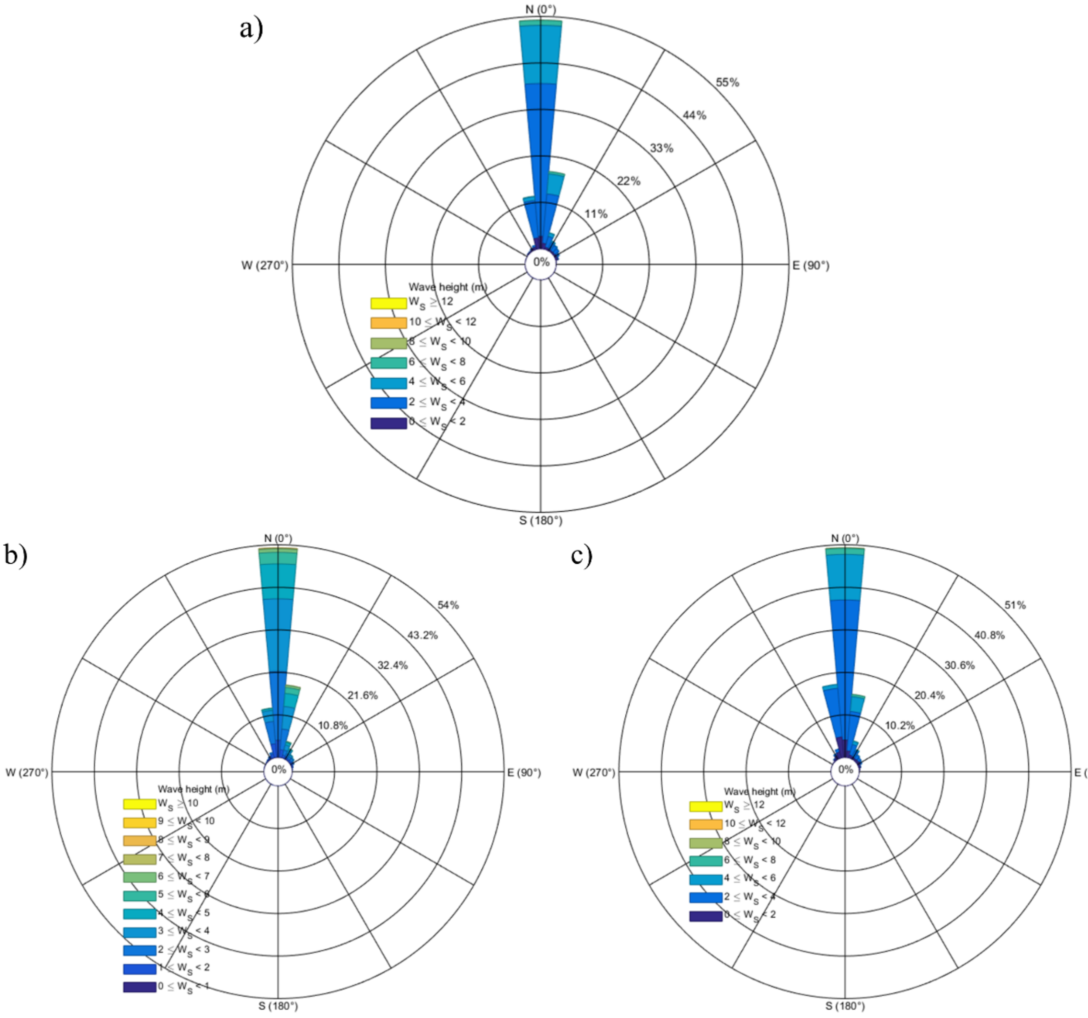

Figure 4.22 – Mean wave direction for the control points (Figure 4.21) for (a) the historical (1979-2005), (b) near future (2026-2045), and (c) far future (2081-2100) periods.

Table 4.10 - Wave height (H_s), peak period (T_p), and mean wave direction (*Dm*) for each climate period and return period.

	H_s (m)			**T_p (s)**			***Dm* (°)**
	Tr^{10}	**Tr^{25}**	**Tr^{100}**	**Tr^{10}**	**Tr^{25}**	**Tr^{100}**	**-**
Historical	9.2	10.0	11.2	20.5	21.6	23.3	355
Near Future	8.9	9.7	10.8	20.7	21.8	23.5	355
Far Future	9.4	10.1	11.2	20.6	21.5	22.9	355

4.5.1.3 Hydrodynamic model

FLOW and WAVE modules were run simultaneously in a two-way wave-current interaction to simulate the flood extent in Vigo Port. A 2D model using FLOW was set up with 1434×429 cells in a curvilinear irregular grid with varying space resolution (Figure 4.23 - III). Multibeam-sourced bathymetries provided by the General Fishing Secretary with a resolution of 5 m were used to build the numerical bathymetry. The topography was obtained from the LIDAR topographic data obtained in 2009, which can be found in an online database (http://mapas.xunta.gal/centro-de-descargas). As for the previous model implementations developed for each port, a modelling time step of 60 seconds was used and a bottom roughness was estimated with a standard coefficient of friction [199]. Background horizontal viscosity and diffusivity was set to 10 m^2s^{-1}. The model provided outputs with a temporal resolution of 5 minutes.

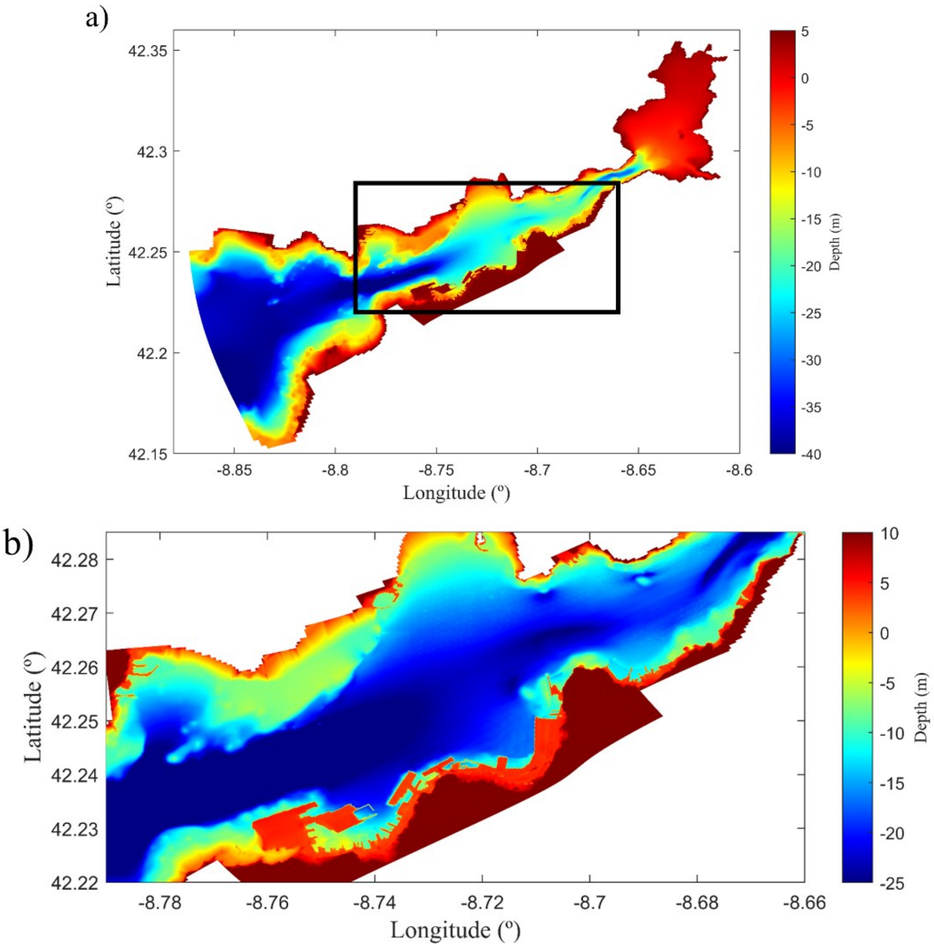

Figure 4.23 – Numerical bathymetry for FLOW domain (Figure 4.21- III) (a) and detailed bathymetry for the Vigo Port (b). ESL analysis was performed at the tide gauge closest to the harbour entrance (white dot (b)).

The calibration simulation was performed for the year of 2009 by using the astronomic constituents at the open boundaries (section 2.2.5), with one month as spin-up. The *RMSE* and *Skill* between model results and observed time series of the sea surface elevation at the station (Table 4.11) were assessed.

Table 4.11 - Tidal model performance for the calibration in the validation periods.

	Tidal station	***RMSE* (m)**	***Skill***
V	Vigo*	0.0714	0.9957

A high agreement between model results and observed time series was found, which is supported by the *RMSE* of 0.07 and *Skill* of 0.99. This result is in agreement with previous studies [230,231], which found similar *RMSE* and *Skill*. Validation for storm surge was not considered due to Ria de Vigo morphology, with a V-shaped valley and deep channels on the centre, as the storm surge signal is considered to propagate unchanged along the estuary [232].

4.5.1.4 Scenarios design

As for the flooding analysis carried out for the previous studied ports, the hydrodynamic model was forced with ESL, considering the sea level, storm surge and astronomic tide (Section 2.3.5), the riverine discharges (Section 2.3.6) and the wave parameters (Table 4.10). The simulations aimed the historical, near and far future periods for the Tr^{10}, Tr^{25} and Tr^{100} with a reference scenario representing the present climate extreme level. An overview of the scenarios can be viewed in Table 4.12.

Table 4.12 - Scenario definition. Extreme sea levels (ESL, m) and riverine discharge for Oitavén-Verdugo (rd, m^3 s^{-1}) for the 10-, 25- and 100-year return periods for the reference scenario (referred to present climate), and the historical (1979-2005), near (2026-2045) and far future (2081-2099).

	Tr^{10}		Tr^{25}		Tr^{100}		**Reference**	
	ESL	rd	ESL	rd	ESL	rd	ESL	rd
Historical	4.47	1302	4.57	1559	4.67	1943	3.79	136.16
Near Future	4.66	1159	4.76	1388	4.86	1756		
Far Future	5.15	1029	5.25	1232	5.35	1535		

For each scenario, the model was forced with time series of ESL and river discharge. The initial 9 days were used as a spin-up with a tide and discharge considering the reference values. The river discharge was increased in the following 2 days, reaching its peak simultaneously with the storm surge and tide representing the ESL for each climate period and return period (Figure 4.24). Figure 4.24 shows the simulation setup for the historical period under the Tr^{100}, highlighting the moment when the peak of the ESL was obtained.

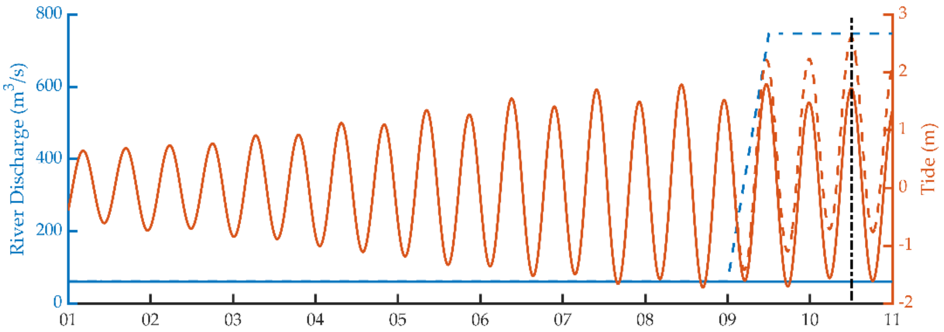

Figure 4.24 – The historical period under the 100-year return period scenario setup. Continuous lines represent the reference conditions, while the dashed line considers the 100-year return period conditions for riverine discharge and extreme sea level.

4.5.2 Flood assessment

The flood assessment for Vigo port was carried out for the historical, near and far future periods, considering the flood drivers for Tr^{10}, Tr^{25}, and Tr^{100}. Flood extent maps and flooded areas for the Vigo Port's terminals were determined for the historical, near, and far future scenarios and for each return period. The starting point, a reference scenario, assume no flood for the entire port. This scenario considers the tide with the historical MSL and average riverine discharges (Table 4.12). A comparison between the reference and the Tr^{10}, Tr^{25}, and Tr^{100} of ESL, storm surges, waves, and riverine discharge scenarios is conducted, indicating the port terminals susceptible to floods and the corresponding flooded area (Table 4.13).

Table 4.13 – Flooded areas of the terminals (Figure 4.20) at the Vigo Port shown in percentage (%) relative to the total area of each terminal for the historical (H), near (NF), and far future (FF) periods and for the 10-, 25-, and 100-year return periods.

			Tr^{10}			**Tr^{25}**			**Tr^{100}**		
		Total (m^2)	**H**	**NF**	**FF**	**H**	**NF**	**FF**	**H**	**NF**	**FF**
Terminal	1	357485.0	6.2	7.0	8.1	6.6	7.3	8.2	7.0	7.5	8.7
	2	293007.4	9.2	10.0	13.7	9.6	10.3	14.6	10.0	11.0	17.4
	3	209488.1	6.8	7.1	9.7	6.9	7.1	10.2	7.1	7.3	10.8
	4	226881.9	25.0	27.0	36.8	26.1	27.9	40.8	27.1	29.5	54.7
	5	141594.4	17.5	19.8	38.3	18.0	21.0	56.1	19.9	23.3	68.7
	6	99849.3	18.2	18.9	22.5	18.4	19.5	24.1	18.9	19.7	32.7
	7	164697.2	13.2	13.8	16.7	13.7	14.3	17.2	13.8	14.6	19.0
	8	264178.3	2.1	2.1	2.1	2.1	2.1	2.1	2.1	2.1	2.1
	9	357706.9	4.8	4.8	5.4	4.8	5.0	5.5	4.8	5.0	5.7

The historical and near future periods (Figure 4.25 and Figure 4.26) are characterized by marginal flooding on most of the terminals (<15%), with particular emphasis on the Shipyards, Beiramar terminals (4), Refrigerated warehouse (5) and fishing port (6), with residual flooding for the Tr^{10}, and gradually expanding for the Tr^{100} scenario. The terminal most affected by flooding is located in the shipyard sector (4), where up to 30% of the sector is flooded under Tr^{100} scenario. These floods occur on the margins of the terminals, where the slipways are located, which will not restrain the activities.

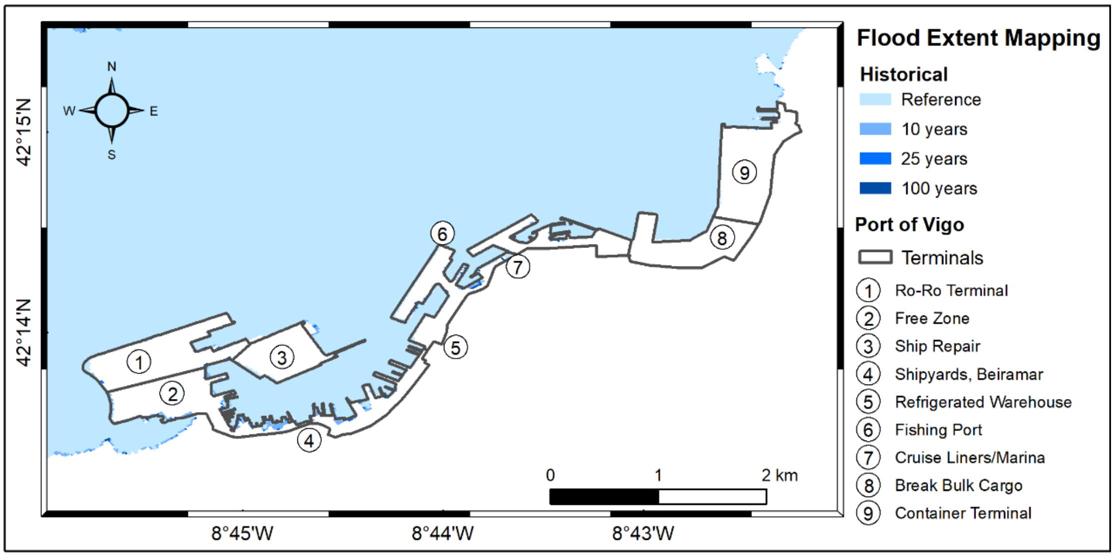

Figure 4.25 – Flood extent mapping of the Vigo Port's terminals (numbers 1–9). Reference scenario under present climate and 10-, 25-, and 100-year return periods are determined for the historical (1979–2005) climate period.

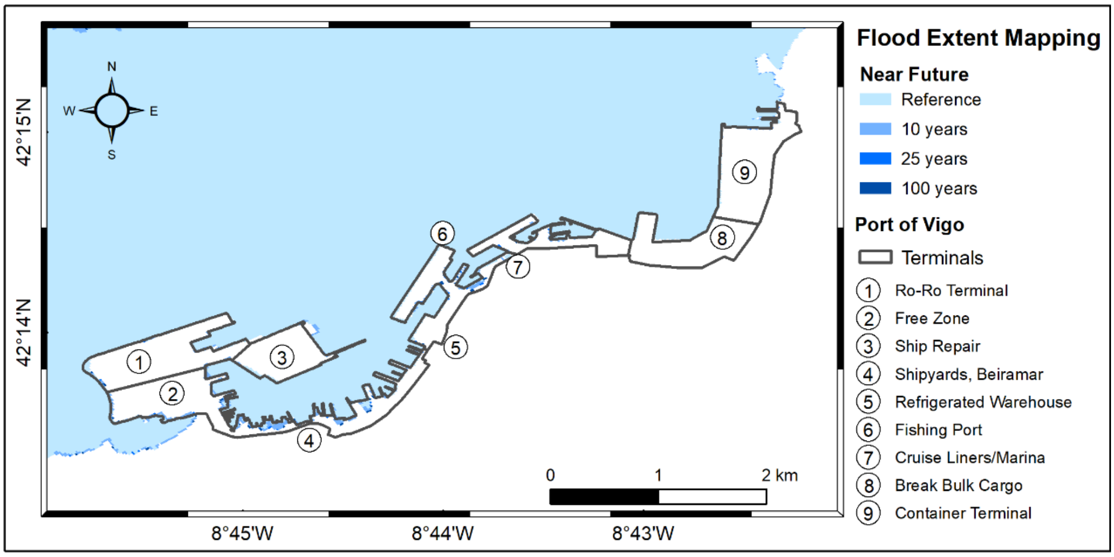

Figure 4.26 – Flood extent mapping of the Vigo Port's terminals (numbers 1–9). Reference scenario under present climate and 10-, 25-, and 100-year return periods are determined for the near future (2026–2045) climate period.

Regarding the far-future period (2081-2100) (Figure 4.27), the flooded areas occur mainly in the terminals identified (4, 5 and 6) in the previous climate periods, located in the central part of the port, with flooded areas significant for the Tr^{10} scenario, which increase for higher return periods. Larger flood extent is found in other terminals, such as the Free zone (2) and the cruise liners/Marina (7), where the flooded region increases up to 19%. However, these terminals are characterized by slipways and low-level docks that can be locally adapted for rising sea levels. In contrast to the historical and near future periods, the flood extent covers over 50% of the terminal dedicated to Shipyard, Beiramar (4), located in the inland part of the left sector and therefore affecting the dry docks for the Tr^{100}. In this case, the flood is extended to repair zone of fishing vessels, docks and cold storage located on the Fishing terminal (6), where significant flooding

(>25%) under *Tr*^{25} and *Tr*^{100} occurs in the refrigeration facilities, potentially endangering the port activities as well as the safe storage of goods in this sector. The terminal dedicated to the Refrigerated warehouse (5) is also significantly affected by flooding under the *Tr*^{10} scenario, increasing the flooded area for longer return periods of 25 and 100 years. In this case, the flooded area can reach two-thirds of the total, compromising the security and operability of this terminal.

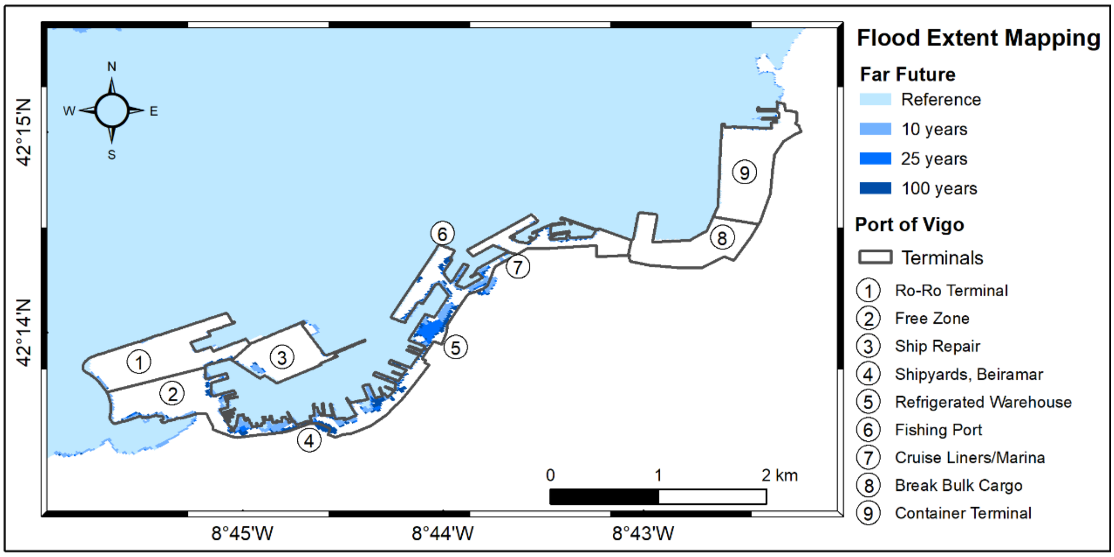

Figure 4.27 – Flood extent mapping of the Vigo Port's terminals (numbers 1–9). Reference scenario under present climate and 10-, 25-, and 100-year return periods are determined for the far future (2081–2099) climate period.

Vigo Port will be affected by climate drivers in the far-future period, namely the MSL rise, which is the main flooding driver, as the Cíes Islands protects Ria de Vigo from external drivers (waves), and the only freshwater source in the inner sector of the Ria shows low discharge. When the high tide coincides with a storm surge, the flooding risk highly increase, leading to a greater flood extent.

4.5.3 Conclusions

The flooding extent in the Vigo Port was evaluated in a climate change context under the RCP8.5 scenario by providing an overview of the key flood areas. Flood extent maps were drawn considering the impact of climate change drivers for 10-, 25-, and 100-year return period scenarios and identifying the port terminals that are susceptible to flood during this period.

This study highlighted that Vigo Port has high resilience to the climate drivers in the historical period, as only some marginal areas of the port terminals are inundated. The ports resilience is also observed for the near future climate drivers, where the flood extent impact slightly increase comparing to the historical period. The flooded area is considerably expanded for the far-future climate drivers, representing some challenges regarding long-term climate change readiness. During this period, the flooding of some port areas is quite significant, compromising the port activities in these sectors, particularly the central section of the Port, the Shipyards, Beiramar, the Refrigerated warehouse and the Fishing Port. These flood patterns suggest that the climatic drivers considered in this study are quite relevant for determining future flooding at this port, which could result in damage and interruptions to terminals in the distant future [18,182].

The Port Authority of Vigo is already focusing on the flood risk under future climate through the implementation of several mitigation measures, such as reducing Port's carbon footprint and increasing the resilience under climate change drivers, namely the rising sea levels. These measures are aligned with the port's challenges in resolving threats and weaknesses by the sustainable expansion of the port infrastructures.

4.6 A CORUÑA OUTER PORT

The Port Authority of A Coruña manages and controls the correct operation of two port zones: the inner port, located in the Ria da Coruña (43.37°N, 8.39°W), in the city of A Coruña, and the new facilities corresponding to the outer port (43.35°N, 8.51°W). Both ports have a privileged geographical situation located on the main international maritime routes between the north of Europe, the Mediterranean and Africa, and Western Europe and the Americas.

The significant shortage of port space and the conflict of interests between the port and the city due to the Port's hazardous nature and environment [233] have promoted the expansion of the port facilities outside the city. This need was accelerated by the Prestige oil spill in November 2002 [234], and the construction work on the new facilities in Punta Langosteira (outer port) have started in March 2005 (Figure 4.28).

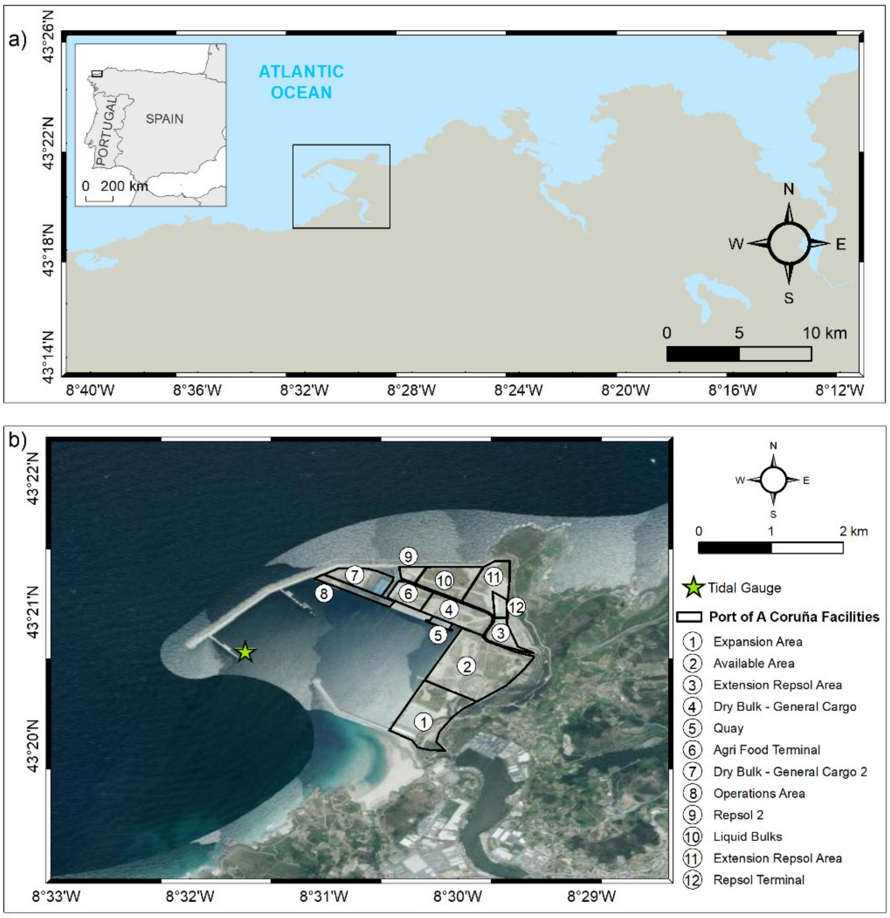

Figure 4.28 – Study area and location of the A Coruña outer Port (a) with the business areas and the *in-situ* station used to validate the hydrodynamic model (Table 2.4) (b).

The Outer Port, the most recent port in the Iberian Peninsula [235,236], is located in a marine environment near A Coruña city, facing hazardous weather and waves arriving from the Atlantic Ocean.

Wave climate is a key factor for new ports built-in marine environments, such as the Outer Port. The conditions tend to be severe, exhibiting higher wave heights, currents and winds. These effects are especially evident in the NW Galician coast, where long periods and energetic waves [162,237,238] are difficult to dissipate and can be boosted by the tide.

The Outer port is still in development by merging the energy operations from the inner port to the new location. The port facilities involved the construction of a 3360 m long breakwater with three alignments and the creation of a dock basin with 230 ha of sheltered waters, with a capacity for nine berths for oil tankers up to 300 m and 200000 tons. It also contains a 900 m long quay with depths ranging from 16 to 22 m, creating 143 ha of esplanade land (Figure 4.28). The port aims to handle breakbulk, dry bulk and liquid bulk cargoes (http://www.puertocoruna.com/en/autoridad-portuaria).

The main task of the Outer Port is to handle the energy resources, such as hydrocarbons and other petrol-based energy products. However, the Port Authority of A Coruña is committed to become a decarbonisation hub and a reference point for the supply of green energy in the region. This plan was followed by several partners, namely the Repsol and Elecnor groups, proposing to empower the outer port as a green energy hub by building assets dedicated to renewable energies. The proposal aims to use the port facility to operate a green hydrogen production plant and use it as a filling station for ships, heavy-duty vehicles, port machinery and industrial processes.

As mentioned above, the port was designed to consider the climate change impacts predicted at the time of its assessment, but it should be considered that climate predictions accuracy is still improving by considering new insights on the climate dynamics. Thus, the following study focuses on the flood assessment considering updated oceanic drivers, such as wave climate and sea-level rise, to provide an updated overview of the port resilience to floods.

4.6.1 Model setup

The FLOW and WAVE modules were used following a similar approach to that used for the remaining ports analysed. However, the Port is more exposed to the wave climate due to the oceanic location, as previously referred. As identified before, the WAVE module uses the SWAN model in the background, which computes random, short-crested wind-generated waves. These features confer some limitations, such as the computation of overtopping on structures, and for this reason and considering the purpose of this study, different approaches must be considered. Thus, the present model set-up will only consider the flooding by the integrated flow determined by the wave-current interaction, and the overtopping analysis will be performed in the next section.

4.6.1.1 Downscaling approach

The wave parameters require finer resolutions for correct wave propagation at a local scale. Thus, by employing the WAVE module, two nested domains were adopted, with different resolutions. One covers the coastal region, parallel to the shore (Figure 4.29 - I), extending from 9°W to 8.17°W and around 20 km offshore. The second domain (Figure 4.29 - II) is intended for the WAVE and FLOW modules, with a curvilinear grid and variable resolution, increasing towards the Port, extending from 8.83°W to 8.32°W. This configuration allows the wave propagation with higher accuracy and improves numerical convergence [239], once this region is characterized by highly extreme waves [233].

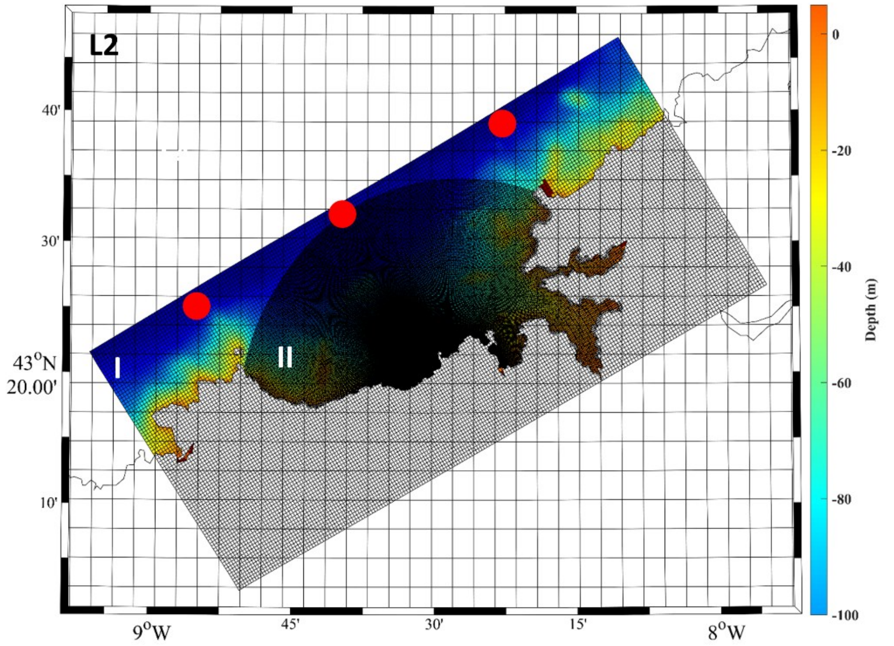

Figure 4.29 – Study area with the extents of the numerical domains and bathymetry used for the SWAN implementations and the wave propagation in the hydrodynamic model in the study area (I and II). The red dots indicate the grid nodes assessed in terms of wave parameters to determine the return periods.

SWAN model physics was kept equal to those used on the previous cases, including triads, bottom friction, depth-induced breaking, white capping, diffraction, and reflections. The wave spectrum was discretised to 25 frequencies (0.0418-1 Hz) and 36 directional bands.

4.6.1.2 Characterisation of H_s, T_p and Dm

The wave climate is the primary driver that can contribute to the potential flood of the Port. Thus, the wave parameters analysis is essential for a good flood assessment. The wave parameters from the downscaled results of the BCC-CSM1.1 GCM were analysed at the three control points (Figure 4.30) equally distributed along the shore to capture the wave climate in this coastal region and determine the return periods. Hourly values over 1979-2005 were used to calculate the H_s and T_p and fitted to statistical distributions and used to estimate H_s and T_p for Tr^{10}, Tr^{25}, and Tr^{100}.

The *Dm* was also assessed (Figure 4.30), observing a wave arrival predominant from northwest and north-northwest direction for the historical climate during winter, in agreement with previous studies [238,240] for the historic period. Following these results and taking into account [197], the mean wave direction will be the mean of the predominant wave directions. The wave parameters are depicted in Table 4.14.

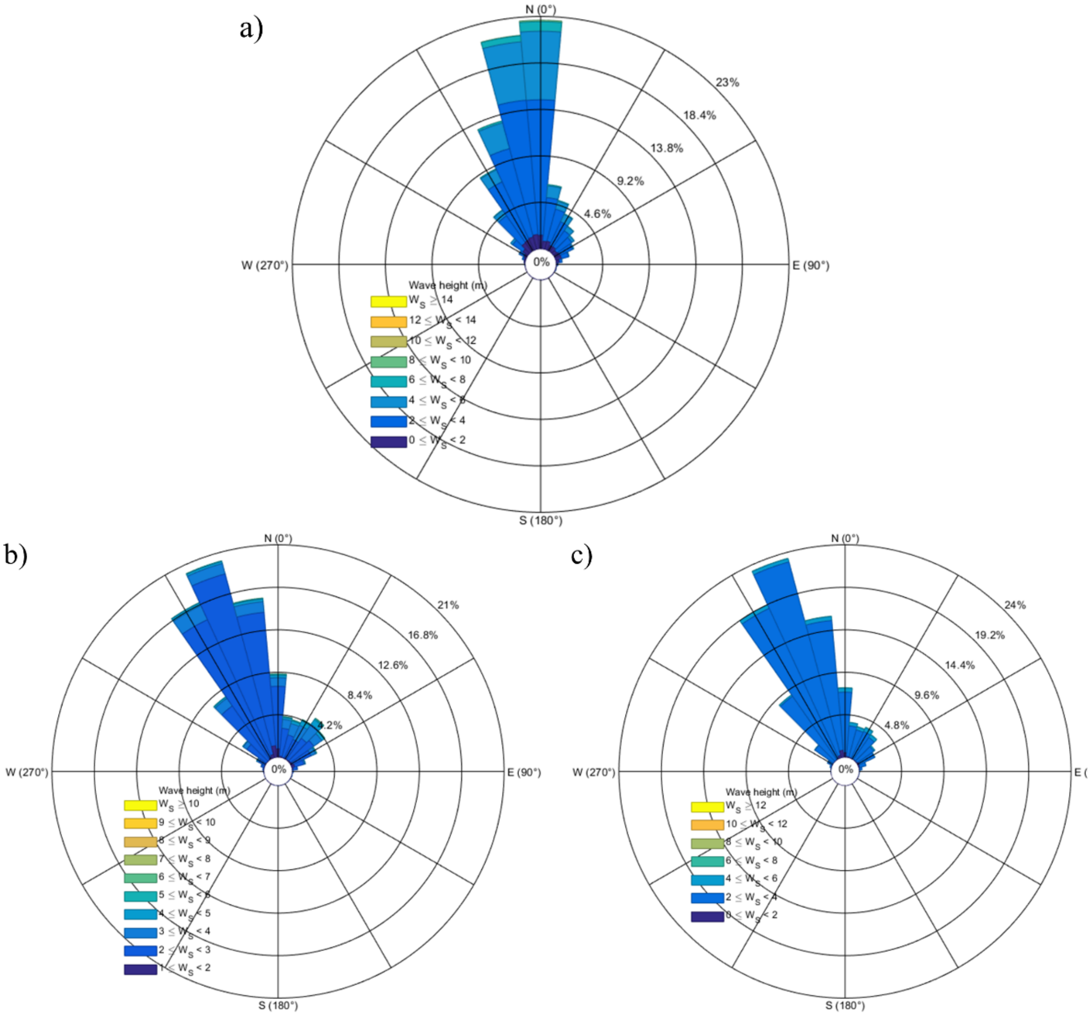

Figure 4.30 – Mean wave direction for the control points (Figure 4.29) for (a) the historical (1979-2005), (b) near future (2026-2045), and (c) far future (2081-2100) periods.

Table 4.14 – Wave height (H_s), peak period (T_p), and mean wave direction (Dm) for each climate period and return period.

	H_s (m)			T_p (s)			Dm (°)
	Tr^{10}	Tr^{25}	Tr^{100}	Tr^{10}	Tr^{25}	Tr^{100}	-
Historical	11.5	12.8	14.8	19.9	20.8	22.2	345
Near Future	10.1	11.0	12.2	20.0	20.9	22.3	335
Far Future	10.5	11.4	12.8	20.6	21.6	23.1	335

4.6.1.3 Hydrodynamic model

The local hydrodynamic was modelled by the FLOW and WAVE, allowing the correct simulation of wave-current interaction at the port entrance. The flow module was set up with a curvilinear irregular grid with 216×155 cells with varying space resolution (Figure 4.29 - II). The bathymetry (Figure 4.31) was constructed based on several sources. For the coastal region was used the GEBCO database, for the port's region (Figure 4.31b) multibeam bathymetric data collected in 2017 and detailed topographic data based on LIDAR surveys collected in 2019 obtained from the A Coruña Port Authority. The modelling time step was 60 seconds, and the bottom roughness was estimated with a standard coefficient of friction. Background horizontal viscosity and diffusivity was set to 10 m^2s^{-1}. The model provided outputs with a temporal resolution of 5 minutes.

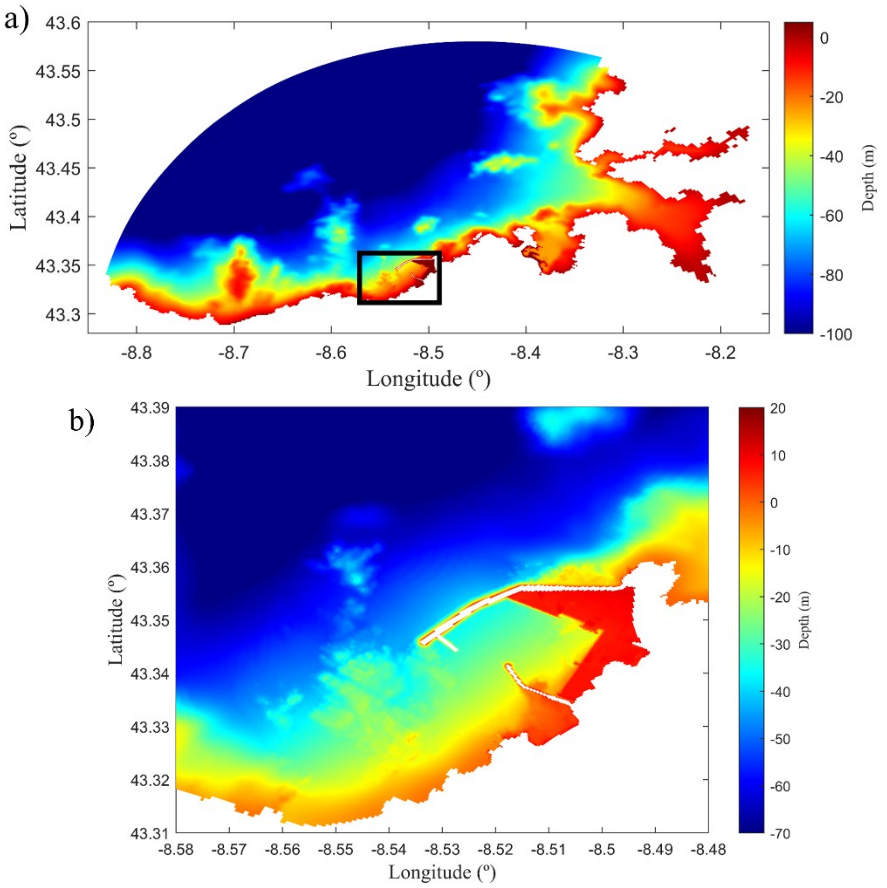

Figure 4.31 – Detailed numerical bathymetry used in the hydrodynamic model application for the (a) domain II and (b) for the A Coruña Outer Port (b).

The model calibration was performed considering the year 2019 for the Punta Langosteira station shown in Figure 4.28, located on the inner side of the breakwater. The model was forced at the open boundaries with the astronomic constituents (Section 2.2.5), with one month of simulation for spin-up. The *RMSE* and *Skill* between model results and observed time series of the sea surface elevation at this station (Table 4.15) were determined.

Table 4.15 – Tidal model performance for the calibration in the validation periods.

Tidal station		***RMSE* (m)**	***Skill***
PL	Punta Langosteira*	0.1222	0.9957

A high agreement between model results and observed time series is supported by the *RMSE* of 0.12 and *Skill* of 0.99. The Port's high depths and location make it unnecessary to validate storm surge, since this signal propagates unchanged under these features [232].

4.6.1.4 Scenarios design

The flood assessment was performed considering the ESL (combination of sea level, storm surge and tide (Section 2.3.5) and the wave parameters (Table 4.14). The hydrodynamic simulations covered the historical, near and far future periods for the Tr^{10}, Tr^{25} and Tr^{100} with a reference scenario representing the present climate extreme level (Table 4.16).

Table 4.16 – Scenario definition. Extreme sea levels (ESL, m) for the 10-, 25- and 100-year return periods for the reference scenario (referred to present climate), and the historical (1979-2005), near (2026-2045) and far future (2081-2099).

	Tr^{10}	Tr^{25}	Tr^{100}	**Reference**
	ESL	ESL	ESL	ESL
Historical	5.21	5.30	5.38	4.49
Near Future	5.40	5.49	5.57	
Far Future	5.89	5.98	6.06	

The different scenarios were forced at the open ocean boundary with time series of ESL with 9 days as initial spin-up, and with a tide considering the reference value. After, for the following 2 days is considered the storm surge and the tide, with the matching between their peaks representing the ESL for each climate period and return period (Figure 4.32). Figure 4.32 shows the simulation setup for the historical period under the Tr^{100}, highlighting the moment when the peak of the ESL was obtained.

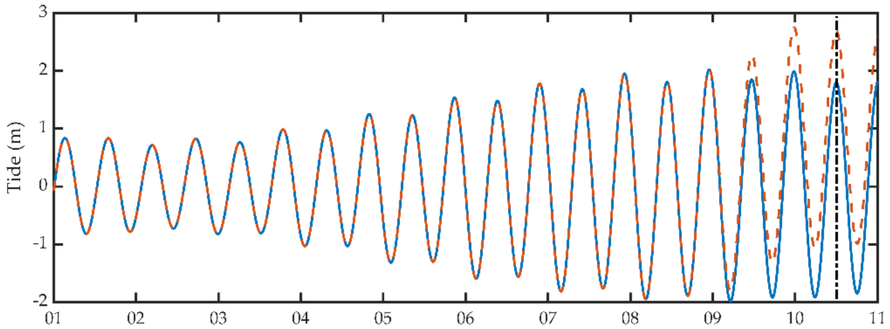

Figure 4.32 – The historical period under the 100-year return period scenario setup. Continuous lines represent the reference conditions, while the dashed line considers the 100-year return period conditions for extreme sea level.

4.6.2 Flood assessment

A Coruña Outer Port flood assessment was performed by drawing flood extent maps for the historical, near and far future periods, considering the flood drivers for Tr^{10}, Tr^{25}, and Tr^{100}. The assessment was conducted by assuming the reference level as a no flood condition for the entire port area. In contrast with the previous case studies analysed, the Outer port is located in a marine system influenced only by the oceanic drivers. In addition, the port is relatively recent, and therefore climate change impacts were considered during its design and recent adaptations. Based on this, it is expected that climate drivers do not contribute to the flooding of the port terminals, as shown in Figure 4.33. Note that terminal 1, an expansion terminal, is not in use and is intended to be flooded during high tides at the date of this study. Thus, the port shows high resilience to flooding, even under Tr^{100} of ESL. This resilience is also observed for future periods (Figure 4.34 and Figure 4.35), where no flood is observed on the port terminals.

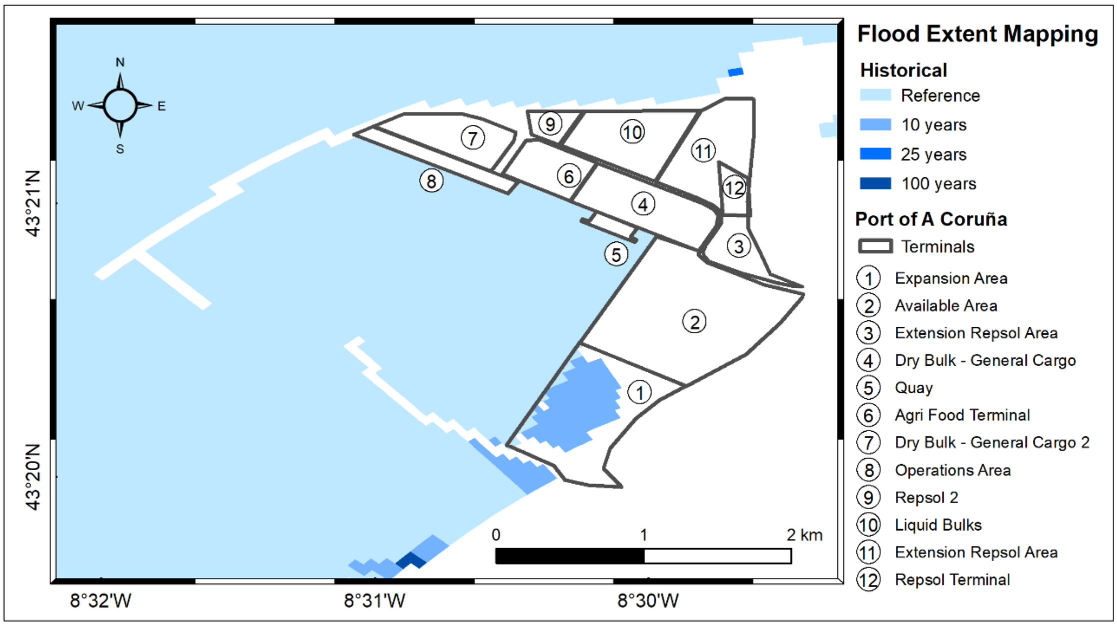

Figure 4.33 – Flood extent mapping of the Coruña Outer Port's terminals (numbers 1–12). Reference scenario under present climate and 10-, 25-, and 100-year return periods are determined for the historical (1979–2005) climate period.

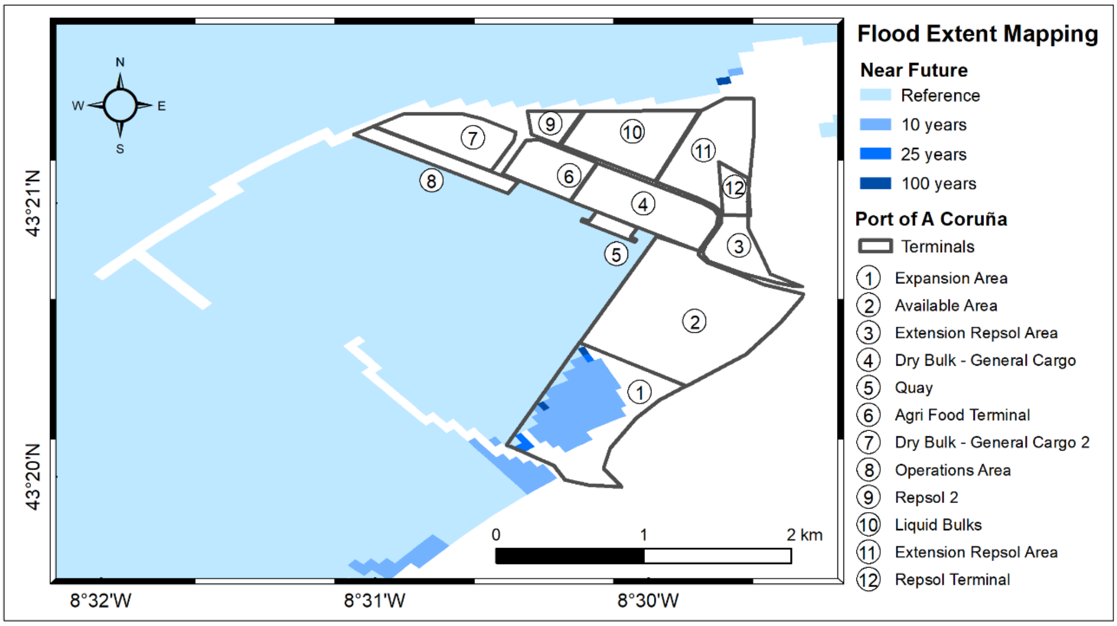

Figure 4.34 – Flood extent mapping of the Coruña Outer Port's terminals (numbers 1–12). Reference scenario under present climate and 10-, 25-, and 100-year return periods are determined for the near future (2026–2045) climate period.

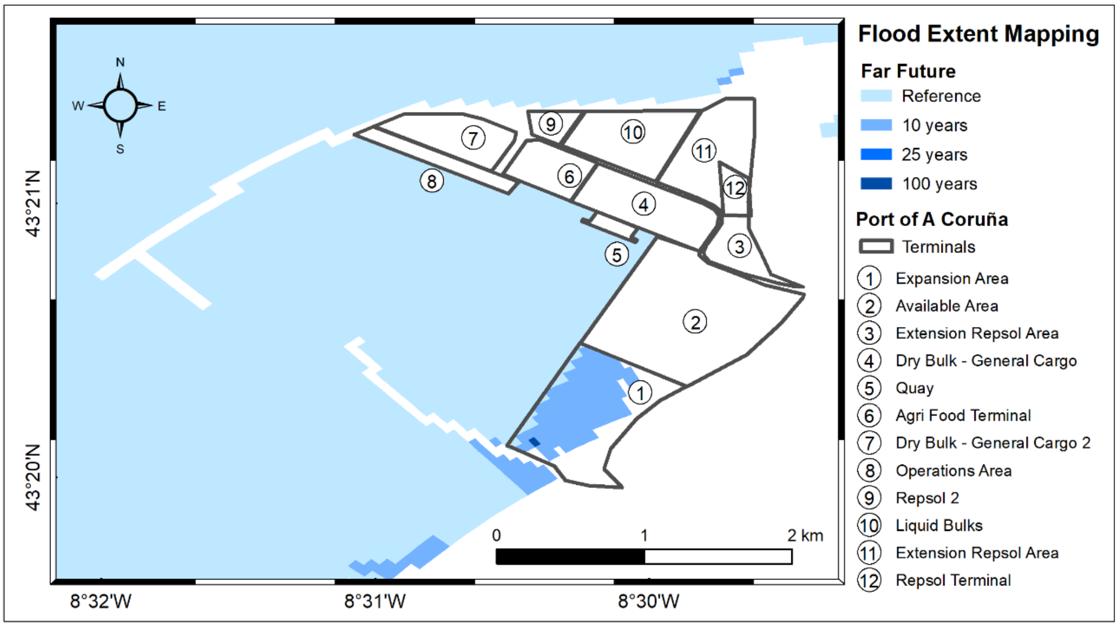

Figure 4.35 – Flood extent mapping of the Coruña Outer Port's terminals (numbers 1–12). Reference scenario under present climate and 10-, 25-, and 100-year return periods are determined for the far future (2081–2099) climate period.

Evaluating the overall flood extent under different climatic scenarios shows the port's resilience to floods. However, some of the port areas may be impacted differently by analysing the north breakwater's overtopping, but this requires a different approach due to the limitations of the numerical model used to assess the flood extent. Therefore, a comprehensive analysis is performed considering the overtopping of the north breakwater in Chapter 5 of this thesis.

4.6.3 Conclusions

The flood assessment of A Coruña Outer Port in a climate change context under the RCP8.5 scenario was performed through spatial flood extent maps, designed to identify and quantify the impact of climate change drivers for 10-, 25-, and 100-year return period scenarios.

The Outer Port, the most recent Port in the Iberian Peninsula, is located in a marine environment exposed to oceanic drivers and built to endure extreme weather conditions, such as high waves and sea-level rise. As a result of these measures, the flood risk from vertical movements is expected to be minimal, leading to high safety standards. The results of this study highlighted the resilience to flooding of this port, which is pronounced even under the most extreme scenario, under a 100-year return period for the historical and future scenarios.

However, it is important to note that coastal ports are susceptible to other climatic threats, which are not included in this assessment due to numerical model limitations and the proposed aims of this dissertation. Some processes were not included, such as the breakwater overtopping, which can occur under storms with extreme waves and boosted by intense winds, and port oscillations due to reflection and diffraction inside the port. Regarding the Port's vulnerability to rising sea levels, no additional planning adaptation measures are required to increase the port's resilience to climate change. One should remember that the present flood assessment must be considered a support toolkit to sustain the port's resilience to sea level rise under updated climate drivers.

4.7 SUMMARY

Climate change is expected to profoundly affect the ports exposed to sea-level rise and extreme weather events. The impacts can vary according to the geographic location and the surrounding pressure, from anthropogenic sources to the morphological features, which can be identified as the significant interventions on construction, operation and maintenance that can result from the vulnerability to the various stresses along their life span. This issue is particularly important considering the exposition of some ports to the climate drivers, whereas natural harbours shelter some ports, others rely on artificial structures that provide protection against high waves and strong currents.

This Chapter assessed climate change impacts on four Iberian Peninsula ports with different characteristics, which included sea-level rise, storm surges and waves, under extreme weather events during the winter season, by considering the 10-, 25- and 100-year return period for the historical, near, and far future scenarios. A reference scenario was also considered, representing the present conditions. Climate drivers were statistically analysed to determine the return periods for each variable based on historical values, whereas wave regime was determined based on the best GCM to describe the wave climate for this region, the BCC-CSM1.1 GCM.

Each Port was independently assessed in terms of flood extent by imposing the climate drivers on the numerical model DELFT3D by simulating the wave-current interaction in the jurisdiction port areas. The flood assessment assumed the reference level as a no-flood condition and considers the tide with the historical MSL and average riverine discharges. The reference and the Tr^{10}, Tr^{25}, and Tr^{100} of ESL, storm surges, waves, and riverine discharge scenarios are compared, identifying the port terminals susceptible to floods and the corresponding flooded area.

Following the identification of the significant threats to each port, it was possible to assess the flood risk due to the climate drivers, which can be summarized as:

- Aveiro Port, located in an inland lagoon system with a single connection to the ocean, serves as a natural shelter from hazardous weather and waves. This environment is characterized by low and flat topography making it susceptible to floods when sea levels or river discharges are high. The combination of these drivers increases the flood hazard drastically, which was observed in Aveiro Port under the Tr^{100} scenarios with several terminals subject to significant inundation. The flood extent increases significantly at most of the terminals under future drivers, highlighting the flood risk resulting from the mean sea level rise and storm surges, which can be enhanced by coincident river discharges.
- Lisbon Port is located in the Tagus estuary. The hydrodynamic drivers are directly influenced by the geomorphology of the estuary with a deep inlet channel and a broad and shallow inner domain. These characteristics constrain ocean waves' propagation and limit the influence of the river discharges in the estuary.

However, the estuary geomorphology, hydrodynamic conditions, and territory occupation promote large floods observed under the Tr^{100} scenarios for all climate periods. The flood risk in these scenarios is higher in the inner domain, where several terminals may be completely flooded for the end of century climate drivers, highlighting the need to increase the Ports resilience to future ESL.

- Vigo Port is situated in the Ria de Vigo. The Ria is characterized by a wide mouth and a funnel shape, and it is sheltered by the Cíes Islands, which grants protection from extreme waves. The Port terminals face partial inundations under far future scenarios, with increased flood risk for the Tr^{100} case for some terminals. The flood patterns show that Vigo Port is susceptible to flooding for the combination of sea-level rise and storm surges under climate change drivers.
- A Coruña Outer Port is different from the other ports, being the most recent and located in a coastal environment, which is exposed to the Atlantic storms. This port relies on an artificial shelter from hazardous weather provided by the breakwaters. The Port's high resilience to climate change protects the Port from floods driven by the ESL and storm surges.

The definition of adaptation or mitigation countermeasures against flooding is not straightforward due to the high uncertainty of projections related to climate change’s multiple spatial and time scales. Climate projections rely on probabilities of occurring specific processes, and ports tend to focus on the observed general conditions and act accordingly by adapting or building new structures to reduce the impacts. The port's planning horizons are also around 5 to 10 years [241] and are subject to the volatility of the changing business circumstances. These time scales are much shorter than existing infrastructures and typical climate change time scales, which are on the scale of thirty to hundreds of years, making it challenging to implement efficient long-term measures.

Drawing on the above, planning responses must be applied on the resilience of the infrastructures and operational measures, like relocating the terminals and zones according to the commercial value of the services and goods. However, continuous observation and flood assessment must be uninterrupted performed, due to the development of new climate models, which will result in more reliable and accurate climate change predictions.

In summary, this study provides a valuable methodology to analyse the projected flood extent on ports under extreme climate change scenarios and, therefore, can be replicated and applied to other ports at risk due to climate change. Thus, the flood assessment must be considered a support toolkit to identify the port’s weakness to assist in the definition of adaptation, management, and resilience measures for future challenges.

Chapter 5

OVERTOPPING – A CORUÑA OUTER PORT CASE

This chapter is dedicated to assess the overtopping occurring in A Coruña Outer Port. The study was developed in collaboration with A Coruña Port Authority, Environmental Physics Laboratory (Ephyslab, University of Vigo), Estuarine and Coastal Modelling Division (NMEC – University of Aveiro), Water and Environmental Engineering Group (GEAMA – University of A Coruña) and Meteogalicia. This partnership has a twofold objective, assessing the overtopping under climate change for the project MarRISK, Interreg POCTEP, and developing a tool to increase the port's safety and predict the breakwater overtopping based on an operational model that can simulate and process the data in the shortest time possible, granting in time accurate results.

5.1 INTRODUCTION

The A Coruña Outer Port is located on the northwest coast of the Iberian Peninsula, being one of the most significant constructions projects in Galicia. The Port location is exposed to the waves and storms of the North Atlantic. For this reason, robust breakwaters were designed by the Port Authority of A Coruña to withstand the hazardous weather and serve as an artificial harbour for large ships. A detailed analysis of the harbour design can be found in [233,235,236].

During the design process, an extensive assessment was performed to characterize the wave climate, with a particular interest in the winter conditions, at the particular site planed for the facilities: Punta Langosteira [233]. Huge waves in the area were characterized by high periods and heights, which may eventually result in overtopping. Tests using physical models were performed in WL Delft Hydraulics to assess wave propagation under 74 storm conditions [233]. Extreme waves were scaled, considering the significant wave height for storm conditions. It was concluded that the design of the main breakwater could withstand a significant wave height with a return period of 140 years, guaranteeing accessibility and operability [233].

The main breakwater, which was designed to allow wave overtopping during normal operation, shelters a total of 143.5 Ha of land and 230.5 ha of water surface, with an extension of 3354 m. Its foundations go up to 40 m deep, and it is divided into several sections with different characteristics and designs in order to dissipate the energetic waves and allow the overtopping (http://www.puertocoruna.com/en/puerto-exterior/puerto).

During the recent winter storms, intense overtopping was observed in some sections of the main breakwater due to high energetic waves that occurred during winter storms. As an illustrative example, refer to the Evi storm, that occurred in 17th January of 2018, and generated waves with a maximum significant wave height of about 10 m (https://www.lavozdegalicia.es/noticia/galicia/2018/01/19/ola-solitaria-punta-langosteira/0003_201801H19P51991.htm) over a period of 24 hours. During this storm, the maximum wave height observed at the Langosteira Buoy was 19.2 m, about 1.68 higher than the significant wave height at the moment.

Overtopping has been continuously observed through real-time monitoring carried out by the Port Authority, being frequent under extreme wave conditions and boosted by winds. The overtopping events are not limited to local storms, where hazardous weather on the north Atlantic can generate extreme waves and be propagated through swell to the breakwater, as observed in Figure 5.1.

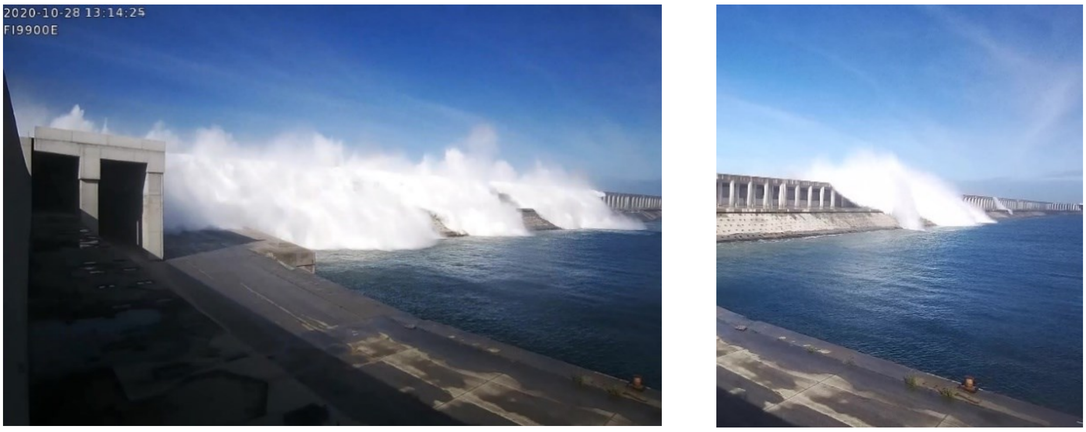

Figure 5.1 – Photos of an overtopping occurring at the main breakwater of the A Coruña Outer Port, in 28 of October of 2020. Source: Water and Environmental Engineering group and A Coruña Port Authority.

Risk maps can boost the operability and safety of harbours, with an emphasis on the protected water surface adjacent to the breakwater. Based on this, an operational model tool to predict overtopping was designed and implemented aiming to provide overtopping risk maps in real-time.

5.2 DATA AND METHODS

Various empirical, analytical and numerical models have been developed in the past to simulate overtopping on structures. These numerical models show advantages and challenges: from time-demanding and requiring specialized equipment but simulating all the wave processes; to be cost-efficient and achieve results in a short period of time but lack wave processes. An example of the latter was the model used in the previous chapters, SWAN, which can simulate the wave propagation in a short time, but compromise the accuracy, especially concerning short waves. An operational model must provide accurate results and be simultaneously fast in delivering its outputs. This section intends to present the required data and the numerical model used to simulate the overtopping in the main breakwater of the A Coruña Outer Port.

5.2.1 Bathymetry and structures design

The definition of the main breakwater was set up by taking into account bathymetry based on multibeam data (Figure 5.2a) collected in 2017 and detailed topographic data based on LIDAR surveys (Figure 5.2b) collected in 2019, as well as a detailed floor plan of the port and buildings. These data were obtained from the A Coruña Port Authority.

The breakwater is divided into 13 sections (Figure 5.2c) defined by the A Coruña Port Authority based on the design, orientation, and the bathymetry contiguous to the breakwater. These sections serve as a reference to register the overtopping events by assigning the probability of overtopping between January 2016 and June 2021 (Figure 5.2d). Note that the section 13 is not considered due to the limitation of the CCTV system.

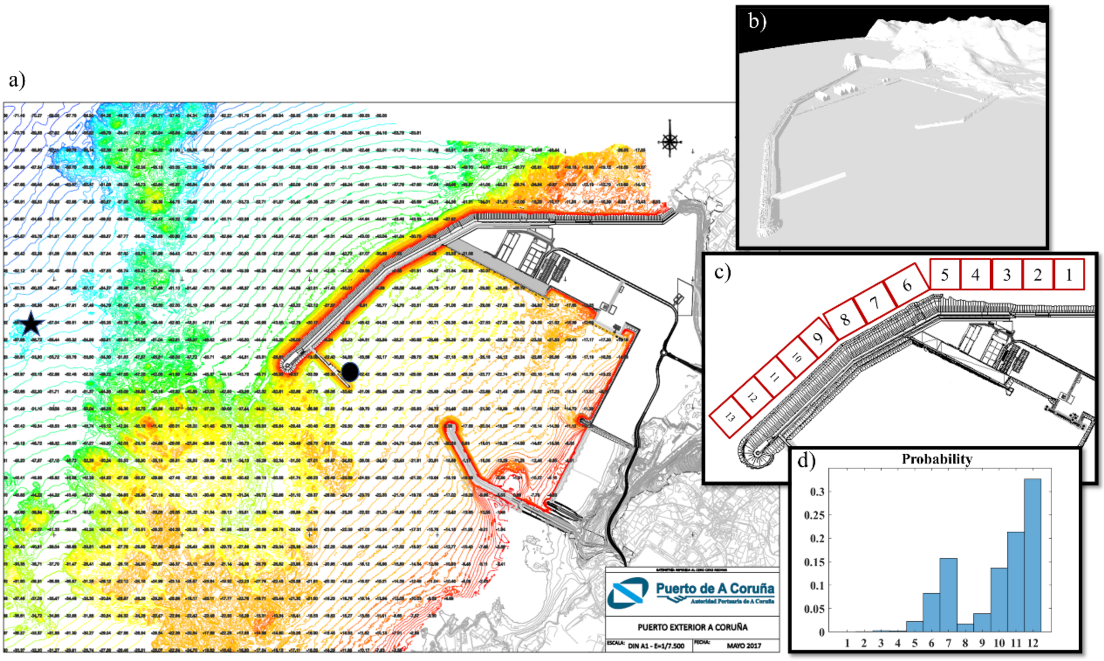

Figure 5.2 – Example of the bathymetry chart used for the A Coruña Outer Port (a) showing the neighbouring submerged reef systems and topography (b) with the main structures (c) and the probability of overtopping occurrence (d). Star and circle indicate the location of the wave directional buoy and the overtopping CCTV system, respectively. Source: GEAMA and A Coruña Port Authority.

The orientation of sections 10, 11 and 12 of the breakwater receives the direct action of the NW Atlantic storms, corresponding to the most energetic waves. Thus, these sections show the highest number of overtopping events, counting around 70% of all.

Detailed information was also obtained for the main breakwater, for each sector and dike layout, which can be observed in [235]. The main breakwater is composed by five different sizes of blocks (https://www.cubipod.com/en/references/langosteira-i-north-and-south-breakwaters-port-of-a-corunna/) characterized by a porosity between 0.6 and 0.62, with a density of 2.35 g cm^{-3}.

5.2.2 *In-situ* data

Wave and tide time series are available in the online database (http://www.puertos.es/en-us/oceanografia/Pages/portus.aspx) managed by the Spanish Port Authority, with an hourly output of real-time data for waves and sea level.

The recording method of the wave data is crucial to assess the resilience of the breakwater. The Langosteira II Buoy (Figure 5.2a - star) is a directional buoy that records data during the first 15 minutes of every hour's and determines the wave parameters for the hour based on that record length.

The overtopping occurrence is identified by a dedicated CCTV system (Figure 5.2a) positioned to cover the inner side of the main breakwater. However, several limitations are linked to this method: the system only works during the daytime; and the wave parameters that generated the overtopping are given by the Langosteira II Buoy, which is located around 1.7 km apart from the main breakwater. Thus, a cautious approach must be considered due to the directional buoy limitations and the distance between the buoy and the breakwater.

5.2.3 Forecasted data

Meteogalicia, has an online database (https://www.meteogalicia.gal/web/modelos/threddsIndex.action) with historical and daily wave forecasts. Depending on the chosen model results (WAVEWATCH III and SWAN), the wave parameters (H_s, T_p and Dm) are available and forecast up to 24 hours. A high-resolution unstructured SWAN domain covers the Galician coast, with higher resolution towards the shore, and provides daily forecasts of the wave parameters.

5.2.4 XBeach non-hydrostatic model

XBeach is a two-dimensional numerical model of near shore processes during time-varying storm and hurricane conditions, consisting of formulations for short wave envelope propagation and non-stationary shallow water equations. It is a public-domain model that has been developed with major funding from the US Army Corps of Engineers, Rijkswaterstaat and the EU, supported by a consortium of UNESCO-IHE, Deltares (formerly WL|Delft Hydraulics), Delft University of Technology and the University of Miami.

Boussinesq models were designed for wave propagation and proved to be efficient [242–246], by solving the wave behaviour in shallow water, while in deep water is solved by the linear wave theory. However, these formulations are not valid to describe the waves at transitional water depth due to the ratio between depth and amplitude, where the vertical and horizontal water motions should be considered (https://oss.deltares.nl/web/xbeach/home).

Ports, characterized by complex geometries and in these transitional waters, require depth-averaged models that consider the vertical flow. Thus, the XBeach non-hydrostatic model is suitable for the task of simulation waves at intermediary waters. Governing equations are the three-dimensional nonlinear shallow water and momentum in the vertical direction. The term non-hydrostatic refers to the non-hydrostatic pressure term in the horizontal momentum equation, considering the flow's vertical hydrodynamic properties and the frequency dispersion. This allows the discretisation of the hydrodynamic properties in the vertical direction rather than depth-averaged (wave-resolving type). The vertical resolution is a function of the dimensionless water depth *kd-value* [246], where the vertical movements are integrated with the solution. In addition, the wave breaking is included considering the mass and momentum conservation.

The features listed above make the XBeach non-hydrostatic model suitable for assessing areas before and after wave breaking.

5.2.5 Model implementation

The XBeach non-hydrostatic model is used to simulate the Outer port overtopping. The model developed includes a stationary mode for refraction based on the mean direction with different boundary conditions prescribed in wave generator boundary (front), lateral boundaries and the back boundary (https://xbeach.readthedocs.io/). The front boundary is set to a non-hydrostatic option (will be detailed later), the back boundary is an absorbing (weakly-reflective) boundary, which allows the waves to propagate with minimal reflection. Regarding the lateral boundaries, an intermediate form of Neumann and wall boundary is chosen, where the velocity at the boundary will be calculated from the Non-linear Shallow Water Equations, which only includes the advective terms. The wave-spectrum boundary condition at the front is prescribed as a single parametric spectrum (JONSWAP) (https://xbeach.readthedocs.io/).

The sea level is set to a constant value corresponding to a return period of 100 years of extreme sea level under the historical period (5.38 m). This constant sea level value was chosen to represent the most pessimistic scenario. A constant manning roughness of 0.02 is defined, which is equivalent to the porosity of the breakwater. The model time step is dynamic, adjusting according to a constant Courant–Friedrichs–Lewy (CFL) of 0.2. The model output is in NetCDF format, with a time step of 1 second.

The numerical grid comprises the sections 10-12 of the main breakwater, where most of the overtopping occur, with higher resolution in the wave incident side (left to right) of the breakwater (Figure 5.3). The numerical grid was built considering the main breakwater dimensions and design with a scale of 1:1.

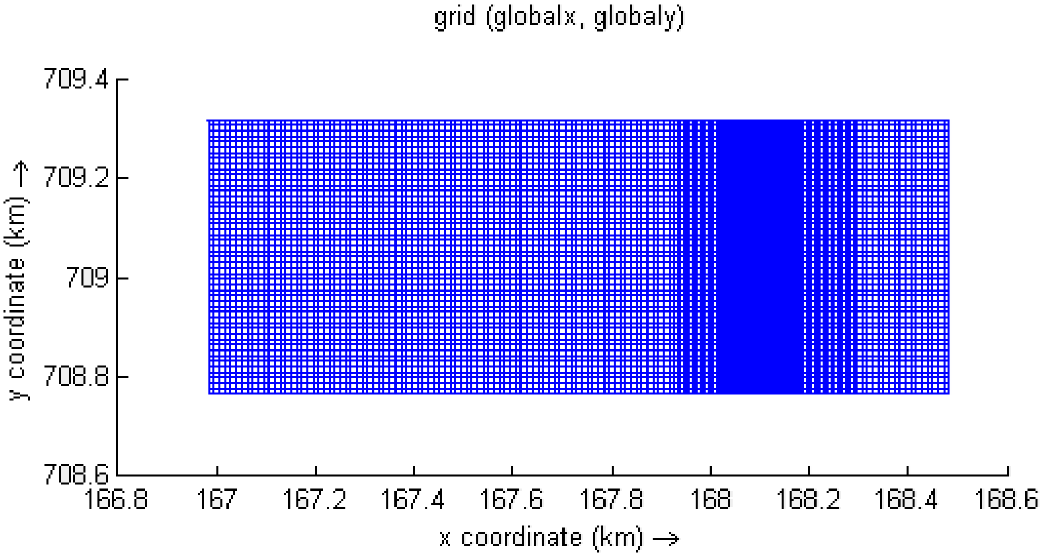

Figure 5.3 – Numerical grid representing sections 10-12 of the main breakwater.

5.2.6 Model boundaries

The model allows two different options for wave boundary conditions. Spectral conditions and non-spectral conditions, such as stationary wave conditions or time-series. The type of data available limits the choice of the boundary. Therefore, the inexistence of wave spectra time-series constraint the selection of this boundary type.

The spectral conditions are the most used boundary condition in XBeach due to the variety of possibilities that can be defined. Thus, a wave spectrum determined from JONSWAP parameters regardless of water depth restriction and sea state conditions is used. This method has disadvantages, such as the low accuracy of parameterisation, which can lead to a weak correlation between the modelled wave parameters and the measured data: the shape of the modelled spectra will not accurately fit the *in-situ* spectra.

The generation of the JONSWAP spectra is determined by the SWAN outputs available in the online database provided by Meteogalicia. The outputs used to generate spectra are H_s, T_p (converted to frequency) and wave direction.

A calibration was performed, where the gamma coefficient, a peak-enhancement factor, is set to a constant value of 1 [247], and the highest frequency is used to create the spectrum of 0.4. The directional spreading is set to 10.

5.2.7 Model validation

The model developed considered the boundaries and the physical parameters indicated above, and the model validation was done for three winter storm events characterized by different magnitudes of wave power (Table 5.1). The model was used to run a total of 5 simulations per instant by considering a different wave spectrum for each simulation, considering the wave parameters and the tide level for each instant, followed by the averaged modelled overtopping. The hydrodynamic features and the number of overtopping events are listed in Table 5.1.

Table 5.1 – Observed wave properties in the Langosteira II buoy and overtopping during energetic storms and the corresponding tidal level recorded at the tidal gauge.

						Overtopping events	
Date (instant)	**H_s (m)**	**T_p (s)**	***Dm* (°)**	**Tide (m)**	***WP* (Kwm^{-1})**	**Observed**	**Modelled**
08/02/2016 15:00	8.00	22.0	324	3.85	1408	6	9
08/02/2016 16:00	9.60	22.0	321	3.53	2028	17	16.4
08/02/2016 17:00	9.40	22.0	321	2.93	1944	21	13.8
08/02/2016 18:00	9.60	20.0	318	2.10	1843	9	12.4
08/02/2016 15:00	8.00	22.0	324	3.85	1408	6	9
08/02/2016 16:00	9.60	22.0	321	3.53	2028	17	16.4
17/01/2018 8:00	8.20	17.6	331	1.26	1183	2	2.6
17/01/2018 9:00	9.27	19.0	329	0.87	1633	4	4.8
17/01/2018 10:00	8.91	18.0	330	0.84	1429	8	4.2
17/01/2018 11:00	10.40	18.3	331	1.17	1979	5	10.1
17/01/2018 12:00	9.97	19.2	330	1.72	1908	3	11
17/01/2018 13:00	10.78	19.2	329	2.34	2231	7	18.1
17/01/2018 14:00	9.69	20.0	327	2.94	1878	13	12.6
17/01/2018 15:00	10.65	18.9	327	3.35	2144	8	14.6
17/01/2018 16:00	10.78	19.7	327	3.43	2289	7	11.6
17/01/2018 17:00	11.45	19.6	329	3.18	2570	7	26.6
01/02/2019 07:00	6.55	15.4	317	1.77	661	3	0.8
01/02/2019 08:00	6.59	15.4	316	1.86	669	9	0.8
01/02/2019 09:00	6.97	15.4	317	2.23	748	3	1.4
01/02/2019 10:00	6.69	13.3	315	2.68	595	6	0
01/02/2019 11:00	6.93	18.2	316	3.11	874	4	3.2
01/02/2019 12:00	6.69	16.7	315	3.46	747	2	2.6
01/02/2019 13:00	6.85	15.4	315	3.56	723	4	3.8
01/02/2019 14:00	6.58	16.7	314	3.42	723	1	2.8
01/02/2019 15:00	6.57	14.3	316	3.04	617	3	0.8
01/02/2019 16:00	6.46	18.2	315	2.53	760	0	0.6
01/02/2019 17:00	6.86	16.7	317	1.99	786	1	2
01/02/2019 18:00	6.48	15.4	318	1.60	647	2	0.6

Overall, the model's ability to reproduce the overtopping in the breakwater is high. The highest disagreements were found when the *WP* is low, which corresponds to lower values of H_s and T_p. However, the model simulated the overtopping events in most of the instants under low *WP*. The instant corresponding to 17/01/2018 at 17:00 shows the highest difference between model results and observations, which is explained by the observation method's limitations that rely on a CCTV system that only works during daytime. Although the model tends to overestimate the number of overtopping events during high *WP*, this is not relevant since the main objective is to indicate the occurrence of overtopping.

5.3 BREAKWATER RESILIENCE UNDER CLIMATE CHANGE

The climate change assessment was performed by applying the methodology used in the previous chapter to determine the flood extent for A Coruña Outer Port. Therefore, the overtopping assessment was carried out for the near and far future periods, considering the climate drivers for Tr^{10}, Tr^{25}, and Tr^{100}.

5.3.1 Scenarios design

The overtopping assessment was developed by considering the Evi storm event in January 2018 characterized by 24 hours with maximum significant wave height higher than 8 m. The wave properties observed during this event were recorded at the Langosteira II buoy, in the vicinity of the Outer Port, and the tide was synthetized through the harmonic constituents and therefore not considered the meteorological input. The data for this event can be observed in Table 5.2.

Table 5.2 –Observed wave properties in the Langosteira II buoy during an energetic storm in January of 2018 and the corresponding tidal level.

Date (instant)	**H_s (m)**	**H_{max} (m)**	**T_p (s)**	**Dm (°)**	**Tide (m)**
17/01/2018 8:00	8.20	13.16	17.6	331	1.26
17/01/2018 9:00	9.27	13.66	19.0	329	0.87
17/01/2018 10:00	8.91	13.44	18.0	330	0.84
17/01/2018 11:00	10.40	15.36	18.3	331	1.17
17/01/2018 12:00	9.97	13.64	19.2	330	1.72
17/01/2018 13:00	10.78	14.80	19.2	329	2.34
17/01/2018 14:00	9.69	13.81	20.0	327	2.94
17/01/2018 15:00	10.65	14.86	18.9	327	3.35
17/01/2018 16:00	10.78	13.98	19.7	327	3.43
17/01/2018 17:00	11.45	19.23	19.6	329	3.18

The overtopping assessment for the near and far future periods, considering the climate drivers for Tr^{10}, Tr^{25}, and Tr^{100} was performed by using the observed hourly wave parameters in Table 5.2, and the tide level was updated with the predicted storm surge and MSL (Table 5.3) expected for the RCP8.5 using the same methodology followed in Chapter 4.

Table 5.3 –Scenario's definition. Mean sea levels (MSL, m) and Storm-surge (SS, m) for the 10-, 25- and 100-year return periods for the near (2026-2045) and far future (2081-2099).

	Tr^{10}	**Tr^{25}**	**Tr^{100}**	
	SS	SS	SS	MSL
Near Future	0.72	0.81	0.89	0.19
Far Future				0.68

A spectral boundary was defined through a spectre constructed by the wave parameters for each hourly wave state. As mentioned before, the spectral boundary assigns a random time series based on the wave parameters used to construct the spectrum. Thus, a total of 5 simulations for each hour were performed, and the number of overtopping events was averaged for each hour.

5.3.2 Overtopping assessment

The climate change assessment was carried out for the near and far future periods, considering the climate drivers for Tr^{10}, Tr^{25}, and Tr^{100}. Evi storm was used as a starting point (reference scenario), and a set of simulations totalling 5 per sea state were performed. A comparison between the reference and the Tr^{10}, Tr^{25}, and Tr^{100} of MSL and storm surges scenarios are conducted, indicating the main breakwater susceptibility to overtopping under climate change.

Table 5.4 lists the number of overtopping events during the Evi storm in sections 10-12 of the breakwater and the increment in the events under sea-level rise due to climate change. Concerning the near future period and a Tr^{10} scenario, a sea-level rise of 0.91 m increases the number of events at most times, which grows even more under higher return periods where the events can double.

Table 5.4 –Observed and increment in the number of events that occurred in January 2018 storm (as a reference scenario) and under climate change drivers, for the near (NF) and far future (FF) periods and for the 10-, 25-, and 100-year return periods.

		Increment (%)					
		Tr^{10}		Tr^{25}		Tr^{100}	
Date (instant)	**Observed**	**NF**	**FF**	**NF**	**FF**	**NF**	**FF**
17/01/2018 8:00	2	50	67	50	50	67	83
17/01/2018 9:00	4	0	0	0	0	0	10
17/01/2018 10:00	8	67	67	100	100	83	133
17/01/2018 11:00	5	27	27	34	67	40	47
17/01/2018 12:00	3	25	42	25	42	50	50
17/01/2018 13:00	7	8	10	8	10	14	14
17/01/2018 14:00	13	26	26	13	20	33	33
17/01/2018 15:00	8	30	26	26	30	44	44
17/01/2018 16:00	7	15	20	20	20	32	36
17/01/2018 17:00	7	15	20	20	35	27	27

Regarding the far future period, with an expected sea-level rise ranging between 1.40 and 1.57 m, the number of overtopping events increases significantly for all instants, reaching up to 133% for the sea state observed at 10 hours.

5.4 OVERTOPPING OPERATIONAL MODEL

An operational model requires a balance between accuracy and time efficiency. The achievement of this objective is only possible by performing a correct assessment of the wave conditions that generate overtopping to limit the number of numerical calculations to the minimum without compromising the results. This model will provide real-time predictions which can help the decision tree of the port.

5.4.1 Wave data analysis

Numerical models provide results based on numerical approximations that may lead to underestimating the wave parameters, even using a high-resolution unstructured grid followed by calibration of physical parameters that better suit the wave climate in this coastal region. The underestimation can be more pronounced under storm events. The underestimation of the total energy transferred into the wave action equations, especially in the lower frequency bands with higher spectral energy, resulted from the wave growth conditions along the coast in winter storms.

Furthermore, a statistical analysis must be carried to identify the variation between the observed (Langosteira II Buoy) and simulated (SWAN high-resolution) wave parameters for the instants identified by the surveillance overtopping system. The nearest point of the unstructured SWAN grid to the Langosteira II Buoy was chosen to perform this analysis. This analysis is of the utmost importance, hence an operational model aiming to forecast the overtopping risk under storm conditions must contain inputs close to that observed. Thus, the observed and simulated wave parameters H_s and T_p are analysed in Figure 5.4.

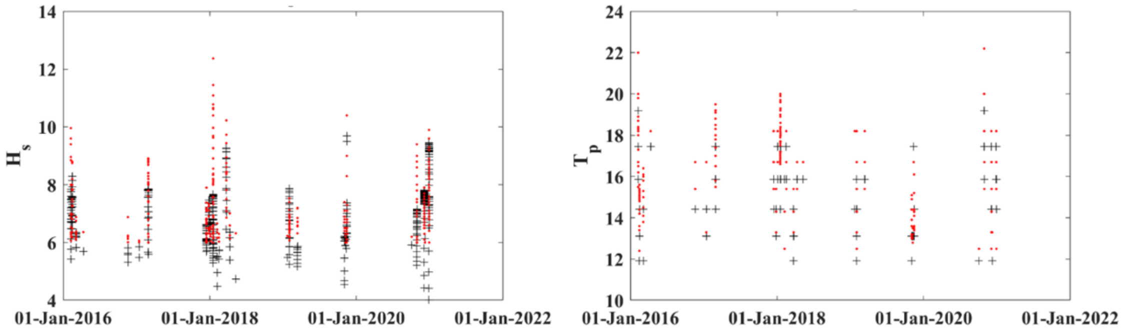

Figure 5.4 – Comparison between the high-resolution SWAN model results (black) and the observed (red) wave parameters during winter storms where overtopping occurred on the main breakwater.

An underestimation of both wave parameters was found, showing that the numerical model is not reproducing the high energetic waves during winter storms, evidencing a limitation of the SWAN operational model developed by the Meteogalicia. A correction must be applied on the wave parameters to be used as input for the XBeach model. Further, another limitation is related to the waves that generate the overtopping. The higher energetic waves are responsible for these events linked to the H_{max} parameter rather than H_s, which is related to the highest waves in contrast to the one-third of higher waves that occurred in a time interval. The difference between the H_s and H_{max} and the quantification (Figure 5.5a) of the difference (Figure 5.5b) was performed.

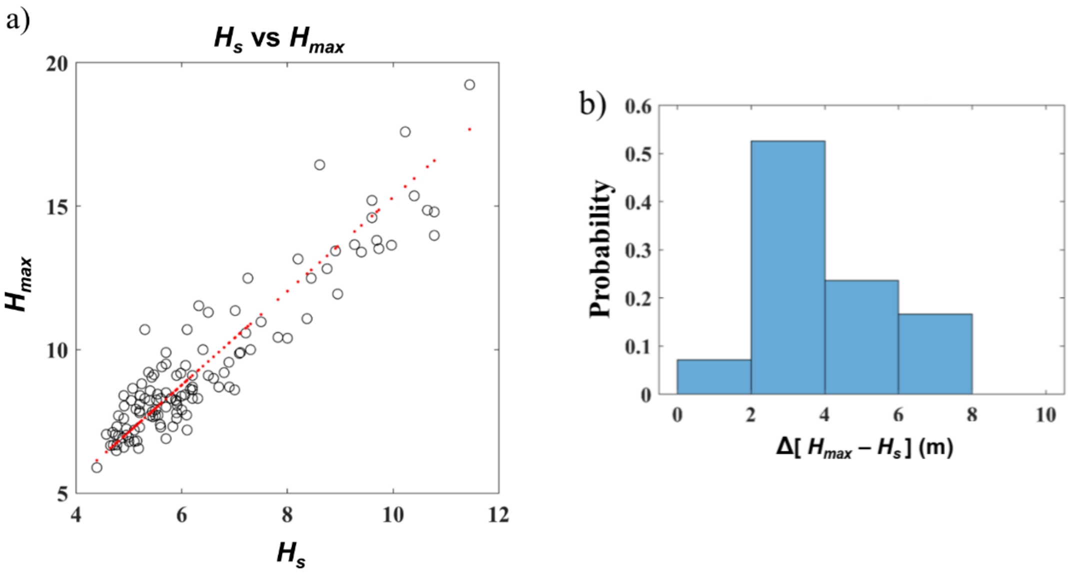

Figure 5.5 – Comparison (a) and difference (b) between observed H_s and H_{max} at the Langosteira II Buoy under the winter storms.

The dispersion is high under higher waves, around 1.5 times between the observed and simulated, where over 50% of the waves show a difference between 2-4 meters, 40% between 4-8 meters, and some events showed H_s and H_{max} differences up to 9 meters.

5.4.2 Model implementation

The operational model developed was set up to be time-efficient, and for this purpose, a protocol was assigned to the different tools, that can be listed as follows:

- Python subroutines access the Meteogalicia server and automatically download the wave parameters predictions;
- Meteogalicia predictions go up to 84 hours, however, only the predictions for the next 24 h are considered due to higher reliability;
- H_s and T_p are retrieved from a node point at a distance of about 1 km from the breakwater. These parameters are increased by 1.5 as a correction factor in order to approximate the predictions to the observed wave conditions;
- Python subroutines determine the wave power (Equation (1)) and, based on the threshold value of 640 kWm^{-1} evaluate the need to simulate the overtopping. If the wave power surpasses the threshold, XBeach will generate wave spectra based on the corrected wave parameters and the ESL under Tr^{100} and launch the simulation;
- The simulation is run with a dynamic time-step to increase the results reliability and minimize the numerical errors on the wave breaking zone due to the high velocities that occur in these sections of the structure;
- The results are post-processed using Python subroutines that determine the extension of the overtopping at the top of the breakwater.

An overview of the operational model is depicted in Figure 5.6.

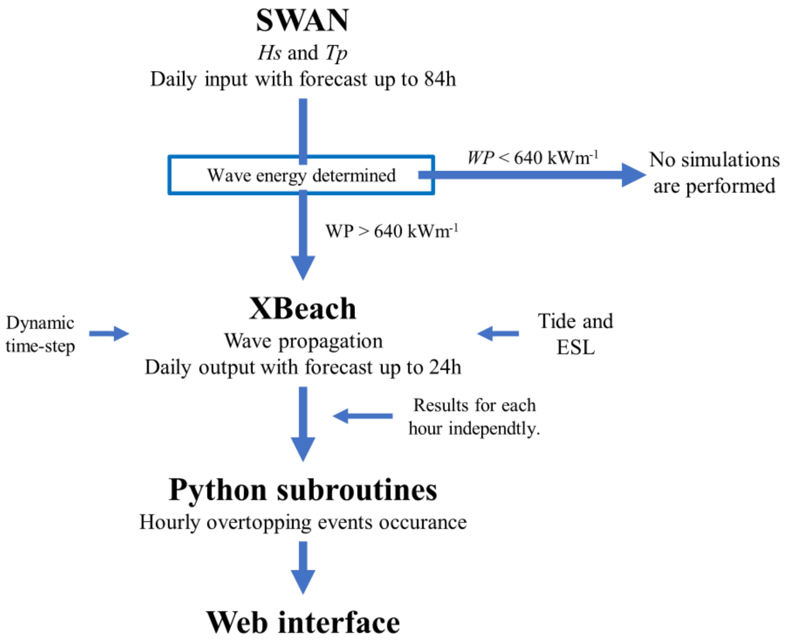

Figure 5.6 – Operational model sketch.

5.4.3 Tool interface

The operational overtopping model performs the overtopping assessment to increase the port's safety and predict the breakwater overtopping based on an operational model (Figure 5.6) that can simulate and process the data in the shortest time possible, granting accurate results.

Considering that risk is the possibility of something bad or undesired happening, a set of three colours designs the overtopping risk system: green, yellow and red, representing no risk ($WP <$ 640 kWm^{-1}), moderate and high risk, respectively. The moderate is characterized when up to two overtopping events are identified, and high when more than two events are simulated.

The tool interface can be found in https://overtopping.ephyslab.uvigo.es/, and the layout is presented in Figure 5.7.

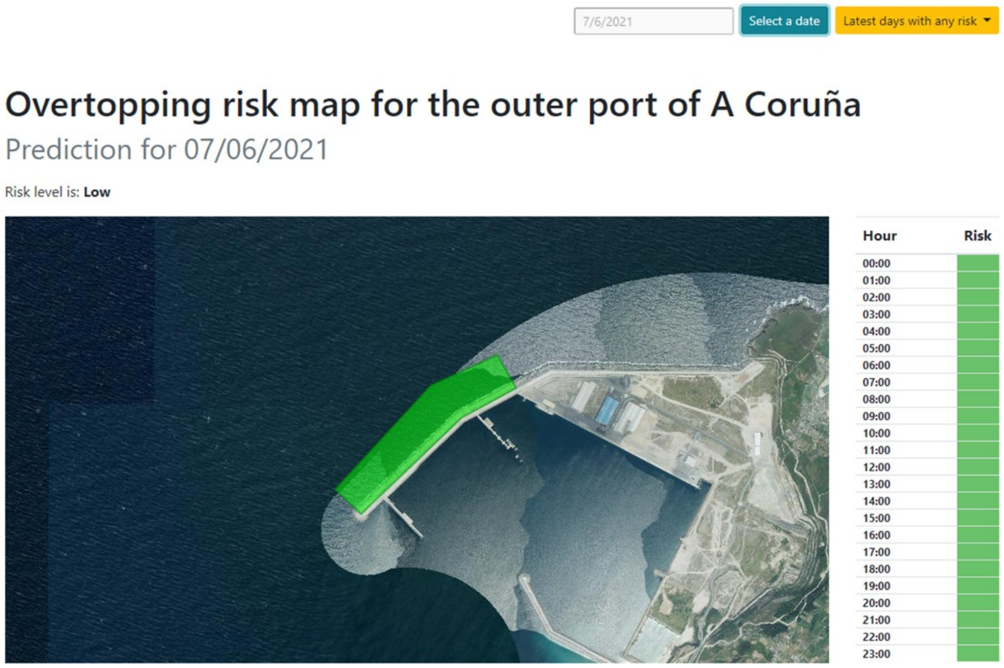

7/6/2021

Overtopping risk map for the outer port of A Coruña

Prediction for 07/06/2021

Risk level is: **Low**

Hour	Risk
00:00	🟩
01:00	🟩
02:00	🟩
03:00	🟩
04:00	🟩
05:00	🟩
06:00	🟩
07:00	🟩
08:00	🟩
09:00	🟩
10:00	🟩
11:00	🟩
12:00	🟩
13:00	🟩
14:00	🟩
15:00	🟩
16:00	🟩
17:00	🟩
18:00	🟩
19:00	🟩
20:00	🟩
21:00	🟩
22:00	🟩
23:00	🟩

Figure 5.7 – Alert system layout, showing no overtopping hazard.

The tool developed allows to represent the risk of overtopping by a colour system and select a historical date and the last events where overtopping was found.

This tool is of utmost importance due to the capability of predicting the overtopping with time efficiency and identifying the risk even under circumstances where direct observation is not possible, such as during the night and under hazardous weather conditions. An example of the alert system under these conditions is represented in Figure 5.8.

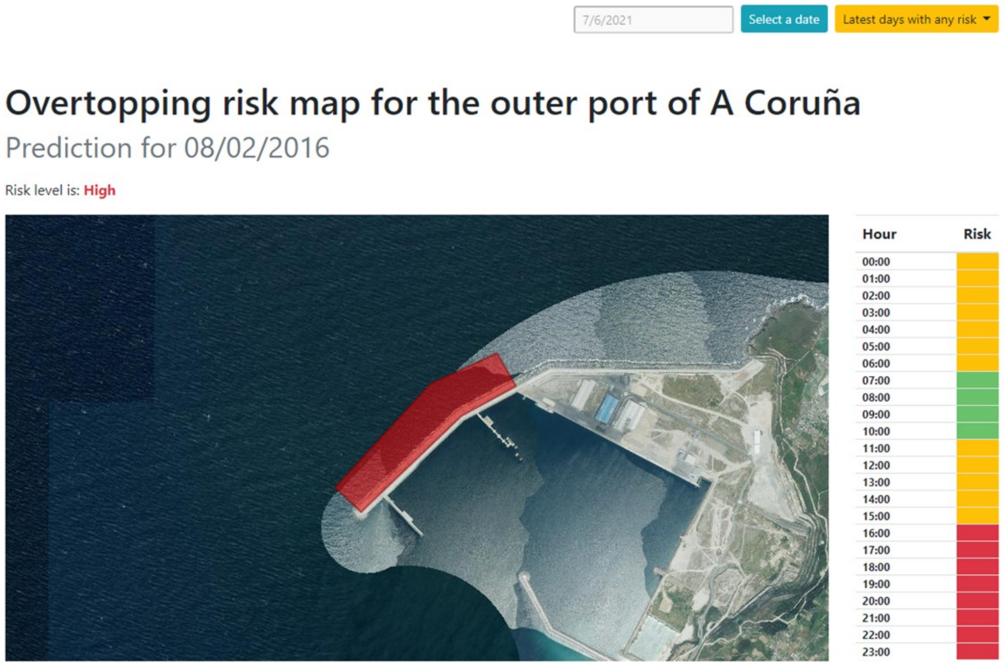

7/6/2021

Overtopping risk map for the outer port of A Coruña

Prediction for 08/02/2016

Risk level is: **High**

Hour	Risk
00:00	🟨
01:00	🟨
02:00	🟨
03:00	🟨
04:00	🟨
05:00	🟨
06:00	🟨
07:00	🟩
08:00	🟩
09:00	🟩
10:00	🟩
11:00	🟨
12:00	🟨
13:00	🟨
14:00	🟨
15:00	🟨
16:00	🟥
17:00	🟥
18:00	🟥
19:00	🟥
20:00	🟥
21:00	🟥
22:00	🟥
23:00	🟥

Figure 5.8 – Alert system indicating a high overtopping risk.

5.5 SUMMARY

A real-time overtopping prediction system can provide valuable information for planning operations by identifying the risk of overtopping on the main breakwater of A Coruña Outer Port. The system described in this chapter addresses the operational model protocol and features in acquiring the desired winter storm overtopping events.

In this study was developed an XBeach non-hydrostatic model implementation using high-resolution bathymetry and the breakwater layout for the sections covering sectors 10-12. Two analyses were performed: assessing the breakwater resilience under climate change for near and far future considering the ESL for Tr^{10}, Tr^{25}, and Tr^{100}; and the development of an operational model capable of forecasting up to 24 hours the overtopping of the main breakwater.

The main breakwater faces punctual overtopping under hazardous weather, which can increase significantly in the near future, with greater impact under far future climate drivers. Under the far future climate, overtopping events can increase up to 133% when the most energetic waves are observed during the analysed storm.

The operational model developed to forecast the overtopping events uses hourly inputs from the Meteogalicia high-resolution SWAN model, which generates a spectral boundary considering the correction of the predicted wave parameters to represent the observed sea state during that specific time hour. This process is replicated for the remaining hourly inputs, and the model is executed by simulating simultaneously the 24 hours that comprise the day and providing the forecast of wave propagation towards the breakwater.

The model simulations are only performed when the wave energy surpasses a threshold of 640 kWm^{-1}, indicating the possibility of occurring overtopping. The XBeach model uses a dynamic time step in a high-resolution grid. The model results are post-processed and displayed on a web interface, indicating the overtopping risk through a set of three colours: green, yellow and red, for the low, moderate and high possibility of overtopping occurrence.

The practical capabilities of this tool allow to predict the overtopping with time efficiency and identify the overtopping risk even under circumstances where direct observation is not possible. This tool can be improved by further optimizing the XBeach model and incorporating a new numerical model capable of determining the overwash flow such as DualPhysics, a Smoothed Particle Hydrodynamics (https://dual.sphysics.org/). This model is time-consuming but can be used as a supportive assessment for the more extreme events identified with the XBeach model, increasing the accuracy significantly.

Chapter 6

FINAL CONCLUSIONS AND FUTURE WORK

Climate change is a long-term shift in climate patterns that varies from place to place. Climate change leads to warmer temperatures, which contribute to the partial melt of glaciers and ice sheets, increasing sea levels boosted by the ocean water expansion as the atmosphere warms. The rise in the sea level is likely to be faster and greater than previously thought. In a worst-case emissions scenario, a sea-level rise between 0.61 m and 1.1 m is now likely by 2100 due to a better understanding of how the Antarctic ice sheet is melting [7]. The rise could be substantially higher, reaching up to 2 m in some locations [8]. The risk of a disastrous 2-metre sea-level rise can still be avoided if emissions are cut quickly by every player. In addition to sea levels rising, weather can become more extreme through more intense storms.

The general objective of this thesis was to assess the climate change impact on NWIC port structures resilience and the feasibility of using new energy resources to reduce the ports carbon footprint. This study is based on the conceptual analysis of historical, present and future climate with the challenge of linking the ports enhancement towards a sustainable and resilient future by anticipating and limiting damage to people and property and reducing economic losses towards the use of green energies and carbon emissions.

Drawing on the above, the A Coruña Outer Port, Vigo, Aveiro and Lisbon ports were selected considering their geographical locations: coastal, Rias, lagoon and estuary environments, which may face different challenges under climate change. Thus, the NWIC and these ports were analysed in terms of new insights on tackling climate change through renewable energies and future flood risk. The following conclusions are made:

1. A Delphi method was developed based on physical point of view indices aiming to facilitate the classification of the viability of energy exploitation, and was applied to assess both the wave energy and the hybrid wind-wave energy resources along with the NWIC. This Delphi is a valuable tool to assess the surrounding areas of ports by identifying the potential of renewable energy sources that can improve the port in terms of energy generation or energy consumption towards achieving a self-sufficient port model, improving energy efficiency and sustainability in port environments, and adopting innovative energy technologies such as wave energy converters.

   The resource classification showed that the NWIC has high viability for wave and hybrid wind-wave energy farms in the historical period, with particular emphasis on a narrow fringe along the coast of the study area and on the NWIC northern extreme, where the Vigo and A Coruña Outer Port are located. Globally, the available resource decreases towards the south of the NWIC, limiting the available resource in the Aveiro and Lisbon Ports vicinity. This high resource potential will decline slightly in the near future and more significantly in the far future. The resource potential can be maximized by exploiting the hybrid wind-wave farms in the optimal areas identified through the Delphi application. In addition, the ports can use WECs to exploit wave energy close to their facilities, even when the available resource is low. The exploitation in these conditions relies on the power matrix and type of the WEC. Thus, Pelamis and Aqua Buoy were evaluated for the historical and near future and showed that Pelamis is most suitable for wave farms in most NWIC, since the projected changes in wave parameters that affect wave resources can be magnified using this WEC. However, Aqua Buy can also be considered a good solution since its dimensions are considerably lower than the Pelamis.

2. The flood risk of the ports was assessed under the historical and future climates. This assessment was conducted under extreme weather events during the winter season by considering climate change scenarios for the 10-, 25- and 100-year return periods. This study showed that the flood risk varies significantly according to the location of the ports, where some environments are more exposed to particular climate drivers than others, threatening the port's performance. The ports of Aveiro and Lisbon are located in low and flat topography areas and protected by natural shelters from hazardous weather and waves, making them prone to the ESL with particular emphasis on higher return period scenarios. This risk will increase under future climate, where sea level rise is expected to impact these environments significantly and lead to severe floods in some sections of these ports.

The flood risk is lower for Vigo Port. The port is located in the Ria de Vigo and is sheltered by the Cíes Islands, which protect the port facilities from hazardous weather and waves. This environment with a funnel-shaped valley is characterised by an irregular topography, making this environment more resilient to the sea level rise. The Vigo Port resilience to floods is high for the historical period, however, the flood risk will increase under future periods leading to floods in some sectors prone to the ESL. Regarding A Coruña Outer Port, which is located on the coast and is the most recent of the ports analysed, it is exposed to the Atlantic storms. This port was designed to be resilient to floods, even with high return periods under climate change, which was observed in this study where no floods occurred.

3. The main breakwater of the A Coruña Outer Port protects the port from the Atlantic hazardous weather and waves. Recent storms highlight the overtopping risk, which could disrupt port operations. Thus, the XBeach non-hydrostatic model was applied to evaluate the overtopping under extreme weather events during the winter season by considering climate change scenarios. This study highlighted that overtopping risk could increase in the future under the most energetic waves during hazardous weather. The

model was also used to design an operational model as a hazard tool, focusing on the forecast of the wave regime under high energetic waves and predicting the overtopping to prevent and overcome losses of property and human safety.

From a holistic conclusion, Port's flood risk under future climate will increase significantly under winter storms if climate change drivers accelerate as predicted. Port infrastructure needs to be strengthened to protect from sea-level rise, which brings local problems in terms of application and planning. There can be no single general solution at a port or national scale because the infrastructure and risk vary in space. The combination of MSL and storm surges are the main threats to floods, but the effects of river discharge and waves cannot be excluded, as they can contribute significantly to the ESL in the lagoons and coastal environments, respectively. The waves mainly affect the ports located outside of natural harbours, which can cause flood overtopping in these locations. In addition, sea level rise is projected to double the frequency of coastal flooding at most locations [20,21], enhancing the overtopping by energetic waves during hazardous weather. These inundations may lead to possible disruptions in operations and damages on property, resulting in serious economic repercussions due to ports value to the economies.

Effective mitigation strategies must be implemented to counter these threats [38]. These measures can lie on the use of WEC since they can provide coastal protection [150–152] by extracting a considerable portion of wave energy, diminishing, therefore, the amount of energy in the surf zone, which attenuates the intensity of coastal processes, and can act preventively on the attenuation of the wave overtopping risk. In addition, investment in energy efficiency, decarbonization and renewables provides a valuable approach for climate change mitigation and adaptation. This can be achieved by exploiting the energy resource in the vicinity of the ports. The ports on the NWIC can also serve as technical and logistic green hubs for energy farm, since the NWIC is one of the regions with the highest ocean energy, with high potential due to its favourable climatic conditions for wind and wave energy devices [113].

This thesis provided valuable methodologies to analyse the renewable energy potential and the projected flooding extent on ports under climate change scenarios, focusing on the need for action on climate change adaptation and resilience-building for ports, which includes on the Global Climate Action Pathways for Transport and Resilience of the United Nations Conference on Trade and Development. However, the energy resource assessment should be interpreted with caution, as wave converters capture only a fraction of the available wave energy. The developed energy resource classification should be considered the first step in this process, as it considers the resource only from a physical point of view. The flood assessment must be considered a support toolkit to assist in the definition of adaptation, management, and resilience measures for future challenges.

As future work, and beyond that already mentioned throughout this study, the impact of climate change on precipitation and consequently on the rivers discharge should be deeply considered because it will cause changes in the water density and current patterns, which would make shipping more difficult, since lower density water force the ships to carry less cargo and hamper the ship navigation through narrow channels.

REFERENCES

---

1. IMO IMO’s contribution to sustainable maritime development. Capacity-building for safe, secure and efficient shipping on clean oceans through the Integrated Technical Co-operation Programme. International Maritime Organization - United Nations. **1999**, 12.
2. Wright, P. *Marine Climate Change Impact Partnership Annual Report Card 2007-2008 Review: Shipping. London.*; 2007;
3. Rodrigue, J.-P.; Comtois, C.; Slack, B. *The Geography of Transport Systems*; 4th Editio.; Routledge: London, 2016; ISBN 9781315618159.
4. Strauss, B.H.; Orton, P.M.; Bittermann, K.; Buchanan, M.K.; Gilford, D.M.; Kopp, R.E.; Kulp, S.; Massey, C.; Moel, H. de; Vinogradov, S. Economic damages from Hurricane Sandy attributable to sea level rise caused by anthropogenic climate change. *Nat. Commun.* **2021**, *12*, 2720, doi:10.1038/s41467-021-22838-1.
5. Almar, R.; Ranasinghe, R.; Bergsma, E.W.J.; Diaz, H.; Melet, A.; Papa, F.; Vousdoukas, M.; Athanasiou, P.; Dada, O.; Almeida, L.P.; et al. A global analysis of extreme coastal water levels with implications for potential coastal overtopping. *Nat. Commun.* **2021**, *12*, 3775, doi:10.1038/s41467-021-24008-9.
6. Dangendorf, S.; Hay, C.; Calafat, F.M.; Marcos, M.; Piecuch, C.G.; Berk, K.; Jensen, J. Persistent acceleration in global sea-level rise since the 1960s. *Nat. Clim. Chang.* **2019**, *9*, 705–710, doi:10.1038/s41558-019-0531-8.
7. Grinsted, A.; Christensen, J.H. The transient sensitivity of sea level rise. *Ocean Sci.* **2021**, *17*, 181–186, doi:10.5194/os-17-181-2021.
8. Bamber, J.L.; Oppenheimer, M.; Kopp, R.E.; Aspinall, W.P.; Cooke, R.M. Ice sheet contributions to future sea-level rise from structured expert judgment. *Proc. Natl. Acad. Sci.* **2019**, *116*, 11195–11200, doi:10.1073/pnas.1817205116.
9. USCCSP Impacts of Climate Change and Variability on Transportation Systems and Infrastructure: Gulf Coast Study, Phase I. A Report by the U.S. Climate Change Science Program and the Subcommittee on Global Change Research. Washington DC. *Systematics* **2008**, 445 pp.
10. Grenzeback, L.R.; Lukmann, A.T. Case Study of the Transportation Sector ’ s Response to and Recovery from Hurricanes Katrina and Rita. Cambridge Systematics, Inc. *Heal. (San Fr.* **2007**, 1–44.
11. Harrison, G.P.; Wallace, A.R. Sensitivity of Wave Energy to Climate Change. *IEEE Trans. Energy Convers.* **2005**, *20*, 870–877, doi:10.1109/TEC.2005.853753.
12. Coumou, D.; Di Capua, G.; Vavrus, S.; Wang, L.; Wang, S. The influence of Arctic amplification on mid-latitude summer circulation. *Nat. Commun.* **2018**, *9*, 2959, doi:10.1038/s41467-018-05256-8.
13. IPCC *Climate Change 2014: Synthesis Report. Contribution of Working Groups I, II and III to the Fifth Assessment Report of the Intergovernmental Panel on Climate Change. [Core Writing Team, R.K. Pachauri and L.A. Meyer (eds.)]*; 2014; ISBN 9789291691432.
14. Swain, D.L.; Singh, D.; Touma, D.; Diffenbaugh, N.S. Attributing Extreme Events to Climate Change: A New Frontier in a Warming World. *One Earth* **2020**, *2*, 522–527, doi:10.1016/j.oneear.2020.05.011.
15. Diffenbaugh, N.S.; Singh, D.; Mankin, J.S.; Horton, D.E.; Swain, D.L.; Touma, D.; Charland, A.; Liu, Y.; Haugen, M.; Tsiang, M.; et al. Quantifying the influence of global warming on unprecedented extreme climate events. *Proc. Natl. Acad. Sci.* **2017**, *114*, 4881–4886, doi:10.1073/pnas.1618082114.
16. Wunderling, N.; Donges, J.F.; Kurths, J.; Winkelmann, R. Interacting tipping elements increase risk

of climate domino effects under global warming. *Earth Syst. Dyn.* **2021**, *12*, 601–619, doi:10.5194/esd-12-601-2021.

17. Bruneau, N.; Fortunato, A.B.; Dodet, G.; Freire, P.; Oliveira, A.; Bertin, X. Future evolution of a tidal inlet due to changes in wave climate, Sea level and lagoon morphology (Óbidos lagoon, Portugal). *Cont. Shelf Res.* **2011**, *31*, 1915–1930, doi:10.1016/j.csr.2011.09.001.

18. Christodoulou, A.; Christidis, P.; Demirel, H. Sea-level rise in ports: a wider focus on impacts. *Marit. Econ. Logist.* **2019**, *21*, 482–496, doi:10.1057/s41278-018-0114-z.

19. Vitousek, S.; Barnard, P.L.; Fletcher, C.H.; Frazer, N.; Erikson, L.; Storlazzi, C.D. Doubling of coastal flooding frequency within decades due to sea-level rise. *Sci. Rep.* **2017**, *7*, 1399, doi:10.1038/s41598-017-01362-7.

20. Vousdoukas, M.I.; Mentaschi, L.; Voukouvalas, E.; Verlaan, M.; Jevrejeva, S.; Jackson, L.P.; Feyen, L. Global probabilistic projections of extreme sea levels show intensification of coastal flood hazard. *Nat. Commun.* **2018**, *9*, 2360, doi:10.1038/s41467-018-04692-w.

21. Lambert, E.; Rohmer, J.; Le Cozannet, G.; van de Wal, R.S.W. Adaptation time to magnified flood hazards underestimated when derived from tide gauge records. *Environ. Res. Lett.* **2020**, *15*, 074015, doi:10.1088/1748-9326/ab8336.

22. Gaythwaite, J.W. *Design of Marine Facilities for the Berthing, Mooring, and Repair of Vessels*; American Society of Civil Engineers: Reston, VA, 2004; ISBN 978-0-7844-0726-4.

23. Stenek, V.; Amado, J.; Connell, R.; Palin, O.; Wright, S.; Pope, B.; Hunter, J.; Mcgregor, J.; Morgan, W.; Stanley, B.; et al. Climate Risks and Business Ports: Terminal Marítimo Muelles el Bosque (Cartagena, Colombia). International Finance Corporation. **2011**, 190.

24. Nicholls, R.J.; Hanson, S.; Herweijer, C.; Patmore, N.; Hallegatte, S.; Corfee-Morlot, J.; Château; Muir-Wood, R. Ranking Port Cities With High Exposure and Vulnerability to Climate Extremes: Exposure Estimates. Organisation for Economic Co-operation and Development. Environment Working Papers No. 1. Paris. **2008**, 61 pp.

25. Hennessy, K.; Bathols, C.P.J.; Mcinnes, K.; Pittock, B.; Suppiah, R.; Walsh, K.; Hennessy, K. Climate Change in the Northern Territory Climate Change in the Northern Territory. Climate Impact Group, CSIRO (Commomwealth Scientific and Industrial Research Organisation) Atmospheric Research. Consultancy report for the Northern Territory Department of. *Atmos. Res.* **2004**, 1–64.

26. GEF-UNDP-IMO GloMEEP Project; IAPH *Port Emissions Toolkit, Guide No.2, Development of port emissions reduction strategies*; 2018;

27. ETIPOCEAN *Strategic Research and Innovation Agenda for Ocean Energy*; 2020;

28. SET Plan Temporary Working Group Ocean Energy *SET Plan Ocean Energy Implementation Plan*; 2018;

29. European Commission COM(2020) 80 final *Proposal for a REGULATION OF THE EUROPEAN PARLIAMENT AND OF THE COUNCIL establishing the framework for achieving climate neutrality and amending Regulation (EU) 2018/1999 (European Climate Law)*; Brussels, 2020;

30. Wan, Z.; Zhu, M.; Chen, S.; Sperling, D. Pollution: Three steps to a green shipping industry. *Nature* **2016**, *530*, 275–277, doi:10.1038/530275a.

31. Ocean Energy Systems *Annual Report: An overview of Ocean Energy Activities in 2019*; 2020;

32. UNCLOS United Nations Convention on the Law of the Sea Act 1996. *Int. J. Mar. Coast. Law* **1997**, *12*, 202 pp, doi:10.1163/15718089720491594.

33. MSP-Portugal Country Report: Portugal. European Commision study on the economic effects of Maritime Spatial Planning (MSP) in Portugal. *Reproduction* **2010**, 1–51.

34. MSP-Spain Country Report: Spain. European Commision study on the economic effects of Maritime Spatial Planning (MSP) in Spain. **2011**, 18 pp.

35. Otero, P.; Ruiz-Villarreal, M.; Allen-Perkins, S.; Vila, B.; Cabanas, J.M. Coastal exposure to oil spill impacts from the Finisterre Traffic Separation Scheme. *Mar. Pollut. Bull.* **2014**, *85*, 67–77, doi:10.1016/j.marpolbul.2014.06.020.

36. da Cruz, M.R.P.; de Matos Ferreira, J.J. Evaluating Iberian seaport competitiveness using an alternative DEA approach. *Eur. Transp. Res. Rev.* **2016**, *8*, 1, doi:10.1007/s12544-015-0187-z.

37. Castro-Santos, L.; DeCastro, M.; Costoya, X.; Filgueira-Vizoso, A.; Lamas-Galdo, I.; Ribeiro, A.; Dias, J.M.; Gómez-Gesteira, M. Economic Feasibility of Floating Offshore Wind Farms Considering Near Future Wind Resources: Case Study of Iberian Coast and Bay of Biscay. *Int. J. Environ. Res. Public Health* **2021**, *18*, 2553, doi:10.3390/ijerph18052553.

38. Kulp, S.A.; Strauss, B.H. New elevation data triple estimates of global vulnerability to sea-level rise and coastal flooding. *Nat. Commun.* **2019**, *10*, 4844, doi:10.1038/s41467-019-12808-z.

39. Jackson, R.B.; Le Quéré, C.; Andrew, R.M.; Canadell, J.G.; Korsbakken, J.I.; Liu, Z.; Peters, G.P.; Zheng, B. Global energy growth is outpacing decarbonization. *Environ. Res. Lett.* **2018**, *13*, 120401, doi:10.1088/1748-9326/aaf303.

40. Le Quéré, C.; Andrew, R.M.; Friedlingstein, P.; Sitch, S.; Hauck, J.; Pongratz, J.; Pickers, P.A.; Korsbakken, J.I.; Peters, G.P.; Canadell, J.G.; et al. Global Carbon Budget 2018. *Earth Syst. Sci. Data* **2018**, *10*, 2141–2194, doi:10.5194/essd-10-2141-2018.

41. Christensen, P.; Gillingham, K.; Nordhaus, W. Uncertainty in forecasts of long-run economic growth. *Proc. Natl. Acad. Sci.* **2018**, *115*, 5409–5414, doi:10.1073/pnas.1713628115.

42. Moss, R.H.; Edmonds, J.A.; Hibbard, K.A.; Manning, M.R.; Rose, S.K.; van Vuuren, D.P.; Carter, T.R.; Emori, S.; Kainuma, M.; Kram, T.; et al. The next generation of scenarios for climate change research and assessment. *Nature* **2010**, *463*, 747–756, doi:10.1038/nature08823.

43. van Vuuren, D.P.; Edmonds, J.; Kainuma, M.; Riahi, K.; Thomson, A.; Hibbard, K.; Hurtt, G.C.; Kram, T.; Krey, V.; Lamarque, J.-F.; et al. The representative concentration pathways: an overview. *Clim. Change* **2011**, *109*, 5–31, doi:10.1007/s10584-011-0148-z.

44. Mateus, M.; Riflet, G.; Chambel, P.; Fernandes, L.; Fernandes, R.; Juliano, M.; Campuzano, F.; de Pablo, H.; Neves, R. An operational model for the West Iberian coast: products and services. *Ocean Sci.* **2012**, *8*, 713–732, doi:10.5194/os-8-713-2012.

45. Serri, L.; Sempreviva, A.-D.; Pontes, T.; Murphy, J.; Lynch, K.; Airoldi, D. *Resource data and GIS tool. For offshore renewable energy projects in Europe. EU FP7 co-ordinated action project “offshore renewable energy conversion—ORECA”;* 2012;

46. Loukogeorgaki, E.; Vagiona, D.; Vasileiou, M. Site Selection of Hybrid Offshore Wind and Wave Energy Systems in Greece Incorporating Environmental Impact Assessment. *Energies* **2018**, *11*, 2095, doi:10.3390/en11082095.

47. Rusu, L. Evaluation of the near future wave energy resources in the Black Sea under two climate scenarios. *Renew. Energy* **2019**, doi:10.1016/j.renene.2019.04.092.

48. Fortunato, A.B.; Li, K.; Bertin, X.; Rodrigues, M.; Miguez, B.M. Determination of extreme sea levels along the Iberian Atlantic coast. *Ocean Eng.* **2016**, *111*, 471–482, doi:10.1016/j.oceaneng.2015.11.031.

49. Gómez-Gesteira, M.; Gimeno, L.; DeCastro, M.; Lorenzo, M.; Alvarez, I.; Nieto, R.; Taboada, J.; Crespo, A.; Ramos, A.; Iglesias, I.; et al. The state of climate in NW Iberia. *Clim. Res.* **2011**, *48*, 109–144, doi:10.3354/cr00967.

50. Gimeno, L.; Trigo, R.; Gómez-Gesteira, M. Regional climate change in the NW Iberian Peninsula. *Clim. Res.* **2011**, *48*, 105–108, doi:10.3354/cr01017.

51. Costoya, X.; Rocha, A.; Carvalho, D. Using bias-correction to improve future projections of offshore wind energy resource: A case study on the Iberian Peninsula. *Appl. Energy* **2020**, *262*, 114562, doi:10.1016/j.apenergy.2020.114562.

52. Santos, F.; Gómez-Gesteira, M.; DeCastro, M.; Añel, J.A.; Carvalho, D.; Costoya, X.; Dias, J.M. On the accuracy of CORDEX RCMs to project future winds over the Iberian Peninsula and surrounding ocean. *Appl. Energy* **2018**, *228*, 289–300, doi:10.1016/j.apenergy.2018.06.086.

53. Lopes, C.L.; Dias, J.M. Assessment of flood hazard during extreme sea levels in a tidally dominated lagoon. *Nat. Hazards* **2015**, *77*, 1345–1364, doi:10.1007/s11069-015-1659-0.

54. Dias, J.M.; Lopes, C.L.; Coelho, C.; Pereira, C.; Alves, F.L.; Sousa, L.P.; Antunes, I.C.; Fernandes, M. da L.; Phillips, M.R. Influence of climate change on the Ria de Aveiro littoral: adaptation strategies for flooding events and shoreline retreat. *J. Coast. Res.* **2014**, *70*, 320–325, doi:10.2112/SI70-054.1.

55. Valentim, J.M.; Vaz, N.; Silva, H.; Duarte, B.; Caçador, I.; Dias, J.M. Tagus estuary and Ria de Aveiro salt marsh dynamics and the impact of sea level rise. *Estuar. Coast. Shelf Sci.* **2013**, *130*,

138–151, doi:10.1016/j.ecss.2013.04.005.

56. Hemer, M.; Trenham, C.; Durrant, T.; Greenslade, D. CAWCR Global wind-wave 21st century climate projections. v2. CSIRO. Service Collection. 2015.

57. Tolman, H.L.; Group, W.D. User manual and system documentation of WAVEWATCH III version 4.18. *NOAA / NWS / NCEP / MMAB Tech. Note* **2014**.

58. Durrant, T.; Hemer, M.; Smith, G.; Trenham, C.; Greenslade, D. CAWCR Wave Hindcast - Aggregated Collection. v5. CSIRO. Service Collection. **2019**, doi:10.4225/08/523168703DCC5.

59. Hemer, M.A.; Katzfey, J.; Trenham, C.E. Global dynamical projections of surface ocean wave climate for a future high greenhouse gas emission scenario. *Ocean Model.* **2013**, doi:10.1016/j.ocemod.2012.09.008.

60. EURO-CORDEX - Coordinated Downscaling Experiment - European Domain Available online: https://www.euro-cordex.net/ (accessed on Jun 23, 2020).

61. Ribeiro, A.; Costoya, X.; de Castro, M.; Carvalho, D.; Dias, J.M.; Rocha, A.; Gomez-Gesteira, M. Assessment of Hybrid Wind-Wave Energy Resource for the NW Coast of Iberian Peninsula in a Climate Change Context. *Appl. Sci.* **2020**, *10*, 7395, doi:10.3390/app10217395.

62. Sotillo, M.G.; Cailleau, S.; Lorente, P.; Levier, B.; Aznar, R.; Reffray, G.; Amo-Baladrón, A.; Chanut, J.; Benkiran, M.; Alvarez-Fanjul, E. The MyOcean IBI Ocean Forecast and Reanalysis Systems: operational products and roadmap to the future Copernicus Service. *J. Oper. Oceanogr.* **2015**, *8*, 63–79, doi:10.1080/1755876X.2015.1014663.

63. Egbert, G.D.; Erofeeva, S.Y. Efficient Inverse Modeling of Barotropic Ocean Tides. *J. Atmos. Ocean. Technol.* **2002**, *19*, 183–204, doi:10.1175/1520-0426(2002)019<0183:EIMOBO>2.0.CO;2.

64. Arnold, J.G.; Allen, P.M.; Bernhardt, G. A comprehensive surface-groundwater flow model. *J. Hydrol.* **1993**, *142*, 47–69, doi:10.1016/0022-1694(93)90004-S.

65. Dias, J.M.; Alves, F.L.; Coelho, C.; Rocha, A.; Fortunato, A.B.; Lopes, C.L.; Sousa, L.; Pereira, C.; Rodrigues, N.T.R.; Silva, P.A.; et al. *ADAPTARia: Modelação das Alterações Climáticas no Litoral da Ria de Aveiro - Estratégias de Adaptação para Cheias Costeiras e Fluviais.*; Aveiro, Portugal, 2013;

66. Donnelly, C.; Andersson, J.C.M.; Arheimer, B. Using flow signatures and catchment similarities to evaluate the E-HYPE multi-basin model across Europe. *Hydrol. Sci. J.* **2016**, *61*, 255–273, doi:10.1080/02626667.2015.1027710.

67. GEBCO Compilation Group (2021) GEBCO 2021 Grid., doi:10.5285/c6612cbe-50b3-0cff-e053-6c86abc09f8f.

68. National Center for Atmospheric Research Staff (Eds) Last modified 08 Nov 2017. “The Climate Data Guide: Climate Forecast System Reanalysis (CFSR).” Retrieved from https://climatedataguide.ucar.edu/climate-data/climate-forecast-system-reanalysis-cfsr.

69. Multon, B. *Marine Renewable Energy Handbook*; Wiley, 2012; ISBN 978-1-848-21332-6.

70. Sierra, J.P.; Casas-Prat, M.; Campins, E. Impact of climate change on wave energy resource: The case of Menorca (Spain). *Renew. Energy* **2017**, doi:10.1016/j.renene.2016.08.060.

71. Astariz, S.; Iglesias, G. The collocation feasibility index – A method for selecting sites for co-located wave and wind farms. *Renew. Energy* **2017**, doi:10.1016/j.renene.2016.11.014.

72. Ribeiro, A.S.; DeCastro, M.; Rusu, L.; Bernardino, M.; Dias, J.M.; Gomez-Gesteira, M. Evaluating the Future Efficiency of Wave Energy Converters along the NW Coast of the Iberian Peninsula. *Energies* **2020**, *13*, 3563, doi:10.3390/en13143563.

73. Ribeiro, A.S.; DeCastro, M.; Costoya, X.; Rusu, L.; Dias, J.M.; Gomez-Gesteira, M. A Delphi method to classify wave energy resource for the 21st century: Application to the NW Iberian Peninsula. *Energy* **2021**, *235*, 121396, doi:10.1016/j.energy.2021.121396.

74. Fu, G.; Liu, Z.; Charles, S.P.; Xu, Z.; Yao, Z. A score-based method for assessing the performance of GCMs: A case study of southeastern Australia. *J. Geophys. Res. Atmos.* **2013**, *118*, 4154–4167, doi:10.1002/jgrd.50269.

75. Perkins, S.E.; Pitman, A.J.; Holbrook, N.J.; McAneney, J. Evaluation of the AR4 climate models’ simulated daily maximum temperature, minimum temperature, and precipitation over Australia using probability density functions. *J. Clim.* **2007**, doi:10.1175/JCLI4253.1.

76. Perkins, S.E.; Pitman, A.J.; Sisson, S.A. Smaller projected increases in 20-year temperature returns over Australia in skill-selected climate models. *Geophys. Res. Lett.* **2009**, *36*, L06710, doi:10.1029/2009GL037293.

77. Perkins, S.E.; Pitman, A.J.; Sisson, S.A. Systematic differences in future 20 year temperature extremes in AR4 model projections over Australia as a function of model skill. *Int. J. Climatol.* **2013**, *33*, 1153–1167, doi:10.1002/joc.3500.

78. Sun, Q.; Miao, C.; Duan, Q. Comparative analysis of CMIP3 and CMIP5 global climate models for simulating the daily mean, maximum, and minimum temperatures and daily precipitation over China. *J. Geophys. Res. Atmos.* **2015**, *120*, 4806–4824, doi:10.1002/2014JD022994.

79. Maxino, C.C.; McAvaney, B.J.; Pitman, A.J.; Perkins, S.E. Ranking the AR4 climate models over the Murray-Darling Basin using simulated maximum temperature, minimum temperature and precipitation. *Int. J. Climatol.* **2008**, *28*, 1097–1112, doi:10.1002/joc.1612.

80. Errasti, I.; Ezcurra, A.; Sáenz, J.; Ibarra-Berastegi, G. Validation of IPCC AR4 models over the Iberian Peninsula. *Theor. Appl. Climatol.* **2011**, *103*, 61–79, doi:10.1007/s00704-010-0282-y.

81. Krishnan, A.; Bhaskaran, P.K. Skill assessment of global climate model wind speed from CMIP5 and CMIP6 and evaluation of projections for the Bay of Bengal. *Clim. Dyn.* **2020**, *55*, 2667–2687, doi:10.1007/s00382-020-05406-z.

82. Hemer, M.A.; Trenham, C.E. Evaluation of a CMIP5 derived dynamical global wind wave climate model ensemble. *Ocean Model.* **2016**, *103*, 190–203, doi:10.1016/j.ocemod.2015.10.009.

83. Erikson, L.H.; Hegermiller, C.A.; Barnard, P.L.; Ruggiero, P.; van Ormondt, M. Projected wave conditions in the Eastern North Pacific under the influence of two CMIP5 climate scenarios. *Ocean Model.* **2015**, *96*, 171–185, doi:10.1016/j.ocemod.2015.07.004.

84. Camus, P.; Losada, I.J.; Izaguirre, C.; Espejo, A.; Menéndez, M.; Pérez, J. Statistical wave climate projections for coastal impact assessments. *Earth's Futur.* **2017**, *5*, 918–933, doi:10.1002/2017EF000609.

85. Shimura, T.; Mori, N.; Hemer, M.A. Variability and future decreases in winter wave heights in the Western North Pacific. *Geophys. Res. Lett.* **2016**, *43*, 2716–2722, doi:10.1002/2016GL067924.

86. Costoya, X.; DeCastro, M.; Santos, F.; Sousa, M.C.; Gómez-Gesteira, M. Projections of wind energy resources in the Caribbean for the 21st century. *Energy* **2019**, *178*, 356–367, doi:10.1016/j.energy.2019.04.121.

87. Amidror, I. Scattered data interpolation methods for electronic imaging systems: a survey. *J. Electron. Imaging* **2002**, doi:10.1117/1.1455013.

88. Tebaldi, C.; Arblaster, J.M.; Knutti, R. Mapping model agreement on future climate projections. *Geophys. Res. Lett.* **2011**, *38*, n/a-n/a, doi:10.1029/2011GL049863.

89. Gibbons, J.D.; Chakraborti, S. *Nonparametric Statistical Inference*; Fifth edit.; Chapman & Hall/CRC Press, Taylor & Francis Group, 2011; ISBN 9781420077612.

90. Izaguirre, C.; Mendez, F.J.; Menendez, M.; Luceño, A.; Losada, I.J. Extreme wave climate variability in southern Europe using satellite data. *J. Geophys. Res.* **2010**, *115*, C04009, doi:10.1029/2009JC005802.

91. Ribeiro, A.S.; Lopes, C.L.; Sousa, M.C.; Gomez-Gesteira, M.; Dias, J.M. Flooding Conditions at Aveiro Port (Portugal) within the Framework of Projected Climate Change. *J. Mar. Sci. Eng.* **2021**, *9*, 595, doi:10.3390/jmse9060595.

92. Costoya, X.; deCastro, M.; Carvalho, D.; Gómez-Gesteira, M. On the suitability of offshore wind energy resource in the United States of America for the 21st century. *Appl. Energy* **2020**, *262*, 114537, doi:10.1016/j.apenergy.2020.114537.

93. Lopes, C.L.; Alves, F.L.; Dias, J.M. Flood risk assessment in a coastal lagoon under present and future scenarios: Ria de Aveiro case study. *Nat. Hazards* **2017**, *89*, 1307–1325, doi:10.1007/s11069-017-3025-x.

94. Lopes, C.L.; Silva, P.A.; Dias, J.M.; Rocha, A.; Picado, A.; Plecha, S.; Fortunato, A.B. Local sea level change scenarios for the end of the 21st century and potential physical impacts in the lower Ria de Aveiro (Portugal). *Cont. Shelf Res.* **2011**, *31*, 1515–1526, doi:10.1016/j.csr.2011.06.015.

95. Kirezci, E.; Young, I.R.; Ranasinghe, R.; Muis, S.; Nicholls, R.J.; Lincke, D.; Hinkel, J. Projections

of global-scale extreme sea levels and resulting episodic coastal flooding over the 21st Century. *Sci. Rep.* **2020**, *10*, 11629, doi:10.1038/s41598-020-67736-6.

96. Vousdoukas, M.I.; Mentaschi, L.; Voukouvalas, E.; Verlaan, M.; Feyen, L. Extreme sea levels on the rise along Europe's coasts. *Earth's Futur.* **2017**, *5*, 304–323, doi:10.1002/2016EF000505.

97. David Pugh *Changing Sea levels. Effects of Tides, Weather and Climate.*; Cambridge University Press, Ed.; Cambridge, 2004; ISBN 9780521532181.

98. Pugh, D.T. *Tides, Surges and Mean Sea-Level (reprinted with corrections), Chichester, UK, John Wiley & Sons Ltd. pp 486*; 1996;

99. Kaplan, E.L.; Meier, P. Nonparametric Estimation from Incomplete Observations. *J. Am. Stat. Assoc.* **1958**, *53*, 457–481, doi:10.1080/01621459.1958.10501452.

100. Woodworth, P.L. A survey of recent changes in the main components of the ocean tide. *Cont. Shelf Res.* **2010**, *30*, 1680–1691, doi:10.1016/j.csr.2010.07.002.

101. Garner, A.J.; Mann, M.E.; Emanuel, K.A.; Kopp, R.E.; Lin, N.; Alley, R.B.; Horton, B.P.; DeConto, R.M.; Donnelly, J.P.; Pollard, D. Impact of climate change on New York City's coastal flood hazard: Increasing flood heights from the preindustrial to 2300 CE. *Proc. Natl. Acad. Sci.* **2017**, *114*, 11861–11866, doi:10.1073/pnas.1703568114.

102. Rahmstorf, S. Rising hazard of storm-surge flooding. *Proc. Natl. Acad. Sci.* **2017**, *114*, 11806–11808, doi:10.1073/pnas.1715895114.

103. Sousa, M.C.; Ribeiro, A.; Des, M.; Gomez-Gesteira, M.; deCastro, M.; Dias, J.M. NW Iberian Peninsula coastal upwelling future weakening: Competition between wind intensification and surface heating. *Sci. Total Environ.* **2020**, *703*, 134808, doi:10.1016/J.SCITOTENV.2019.134808.

104. Blöschl, G.; Hall, J.; Viglione, A.; Perdigão, R.A.P.; Parajka, J.; Merz, B.; Lun, D.; Arheimer, B.; Aronica, G.T.; Bilibashi, A.; et al. Changing climate both increases and decreases European river floods. *Nature* **2019**, *573*, 108–111, doi:10.1038/s41586-019-1495-6.

105. deCastro, M.; Costoya, X.; Salvador, S.; Carvalho, D.; Gómez-Gesteira, M.; Sanz-Larruga, F.J.; Gimeno, L. An overview of offshore wind energy resources in Europe under present and future climate. *Ann. N. Y. Acad. Sci.* **2019**, *1436*, 70–97, doi:10.1111/nyas.13924.

106. Zheng, C. wei; Xiao, Z. niu; Peng, Y. hua; Li, C. yin; Du, Z. bo Rezoning global offshore wind energy resources. *Renew. Energy* **2018**, doi:10.1016/j.renene.2018.05.090.

107. Mahajan, V.; Linstone, H.A.; Turoff, M. *The Delphi Method: Techniques and Applications*; 1976; Vol. 13;.

108. Cornett, A.M. A global wave energy resource assessment. In Proceedings of the Proceedings of the International Offshore and Polar Engineering Conference; 2008.

109. Reeve, D.E.; Chen, Y.; Pan, S.; Magar, V.; Simmonds, D.J.; Zacharioudaki, A. An investigation of the impacts of climate change on wave energy generation: The Wave Hub, Cornwall, UK. *Renew. Energy* **2011**, doi:10.1016/j.renene.2011.02.020.

110. Amante, C.; Eakins, B.W. *ETOPO1 1 Arc-Minute Global Relief Model: procedures, data sources and analysis. NOAA Technical Memorandum NESDIS NGDC-24.*; Boulder, Colorado, 2009;

111. Wessel, P.; Smith, W.H.F. A global, self-consistent, hierarchical, high-resolution shoreline database. *J. Geophys. Res. Solid Earth* **1996**, *101*, 8741–8743, doi:10.1029/96JB00104.

112. National Renewable Energy Laboratory (NREL) Wind Energy Resource Atlas of the United States. DOE/CH 10093-10094, October 1986.

113. Rusu, L.; Onea, F. The performance of some state-of-the-art wave energy converters in locations with the worldwide highest wave power. *Renew. Sustain. Energy Rev.* 2017.

114. Silva, D.; Rusu, E.; Guedes Soares, C. Evaluation of Various Technologies for Wave Energy Conversion in the Portuguese Nearshore. *Energies* **2013**, *6*, 1344–1364, doi:10.3390/en6031344.

115. Rusu, E. Evaluation of the Wave Energy Conversion Efficiency in Various Coastal Environments. *Energies* **2014**, *7*, 4002–4018, doi:10.3390/en7064002.

116. Aderinto, T.; Li, H. Review on Power Performance and Efficiency of Wave Energy Converters. *Energies* **2019**, *12*, 4329, doi:10.3390/en12224329.

117. Callaghan, J.; Boud, R. *Future Marine Energy: Results of the Marine Energy Challenge: Cost competitiveness and growth of wave and tidal stream energy*; Carbon Trust, 2006;

118. Bosserelle, C.; Reddy, S.; Krüger, J. *Waves and Coasts in the Pacific - Cost Analysis of Wave Energy in the Pacific*; 2015; ISBN 978-982-00-0944-8.

119. Piscopo, V.; Benassai, G.; Della Morte, R.; Scamardella, A. Cost-Based Design and Selection of Point Absorber Devices for the Mediterranean Sea. *Energies* **2018**, *11*, 946, doi:10.3390/en11040946.

120. Energy Systems Research Unit Available online: www.esru.strath.ac.uk (accessed on Jun 26, 2020).

121. Deltares *Delft3D-WAVE. Simulation of short-crested waves with SWAN. User Manual. Version: 3.05*; 2020;

122. SWAN SWAN user manual version 41.31; Delft University of Technology, Environmental Fluid Mechanics Section: Delft, The Netherlands. **2019**, 143.

123. Deltares *Delft3D-FLOW. Simulation of multi-dimensional hydrodynamic flows and transport phenomena, including sediments. User Manual. Version: 3.15*; 2020;

124. *Offshore Renewable Energy: Ocean Waves, Tides and Offshore Wind*; Eugen, R., Vengatesan, V., Eds.; MDPI: Basel, Switzerland, 2019; ISBN 978-3-03897-593-9.

125. Zheng, C.W.; Wang, Q.; Li, C.Y. An overview of medium- to long-term predictions of global wave energy resources. *Renew. Sustain. Energy Rev.* 2017.

126. IEC TS 62600-101 *Marine energy – Wave, tidal and other water current converters – Part 100: Electricity producing wave energy converters – Power performance assessment*; 2015; ISBN 9782832227244.

127. Allahdadi, M.N.; Gunawan, B.; Lai, J.; He, R.; Neary, V.S. Development and validation of a regional-scale high-resolution unstructured model for wave energy resource characterization along the US East Coast. *Renew. Energy* **2019**, *136*, 500–511, doi:10.1016/j.renene.2019.01.020.

128. Ahn, S.; Haas, K.A.; Neary, V.S. Wave energy resource classification system for US coastal waters. *Renew. Sustain. Energy Rev.* **2019**, *104*, 54–68, doi:10.1016/j.rser.2019.01.017.

129. Yang, Z.; Neary, V.S.; Wang, T.; Gunawan, B.; Dallman, A.R.; Wu, W.-C. A wave model test bed study for wave energy resource characterization. *Renew. Energy* **2017**, *114*, 132–144, doi:10.1016/j.renene.2016.12.057.

130. Rusu, L.; Onea, F. Assessment of the performances of various wave energy converters along the European continental coasts. *Energy* **2015**, doi:10.1016/j.energy.2015.01.099.

131. Siegel, S.G. Numerical benchmarking study of a Cycloidal Wave Energy Converter. *Renew. Energy* **2019**, doi:10.1016/j.renene.2018.11.041.

132. Rosa-Santos, P.; Taveira-Pinto, F.; Rodríguez, C.A.; Ramos, V.; López, M. The CECO wave energy converter: Recent developments. *Renew. Energy* **2019**, doi:10.1016/j.renene.2019.02.081.

133. Penalba, M.; Ulazia, A.; Ibarra-Berastegui, G.; Ringwood, J.; Sáenz, J. Wave energy resource variation off the west coast of Ireland and its impact on realistic wave energy converters' power absorption. *Appl. Energy* **2018**, *224*, 205–219, doi:10.1016/j.apenergy.2018.04.121.

134. Reguero, B.G.; Losada, I.J.; Méndez, F.J. A global wave power resource and its seasonal, interannual and long-term variability. *Appl. Energy* **2015**, doi:10.1016/j.apenergy.2015.03.114.

135. Fairley, I.; Lewis, M.; Robertson, B.; Hemer, M.; Masters, I.; Horrillo-Caraballo, J.; Karunarathna, H.; Reeve, D.E. A classification system for global wave energy resources based on multivariate clustering. *Appl. Energy* **2020**, *262*, 114515, doi:10.1016/j.apenergy.2020.114515.

136. Kamranzad, B.; Etemad-Shahidi, A.; Chegini, V. Developing an optimum hotspot identifier for wave energy extracting in the northern Persian Gulf. *Renew. Energy* **2017**, *114*, 59–71, doi:10.1016/j.renene.2017.03.026.

137. Canals Silander, M.F.; García Moreno, C.G. On the spatial distribution of the wave energy resource in Puerto Rico and the United States Virgin Islands. *Renew. Energy* **2019**, doi:10.1016/j.renene.2018.12.120.

138. Silva, D.; Martinho, P.; Guedes Soares, C. Wave energy distribution along the Portuguese

continental coast based on a thirty three years hindcast. *Renew. Energy* **2018**, *127*, 1064–1075, doi:10.1016/j.renene.2018.05.037.

139. Gonçalves, M.; Martinho, P.; Guedes Soares, C. A 33-year hindcast on wave energy assessment in the western French coast. *Energy* **2018**, *165*, 790–801, doi:10.1016/j.energy.2018.10.002.

140. Ulazia, A.; Penalba, M.; Ibarra-Berastegui, G.; Ringwood, J.; Saénz, J. Wave energy trends over the Bay of Biscay and the consequences for wave energy converters. *Energy* **2017**, *141*, 624–634, doi:10.1016/j.energy.2017.09.099.

141. Carballo, R.; Arean, N.; Álvarez, M.; López, I.; Castro, A.; López, M.; Iglesias, G. Wave farm planning through high-resolution resource and performance characterization. *Renew. Energy* **2019**, *135*, 1097–1107, doi:10.1016/j.renene.2018.12.081.

142. Ramos, V.; López, M.; Taveira-Pinto, F.; Rosa-Santos, P. Influence of the wave climate seasonality on the performance of a wave energy converter: A case study. *Energy* **2017**, *135*, 303–316, doi:10.1016/j.energy.2017.06.080.

143. Guedes Soares, C.; Bento, A.R.; Gonçalves, M.; Silva, D.; Martinho, P. Numerical evaluation of the wave energy resource along the Atlantic European coast. *Comput. Geosci.* **2014**, *71*, 37–49, doi:10.1016/j.cageo.2014.03.008.

144. Nassar, W.M.; Anaya-Lara, O.; Ahmed, K.H.; Campos-Gaona, D.; Elgenedy, M. Assessment of Multi-Use Offshore Platforms: Structure Classification and Design Challenges. *Sustainability* **2020**, *12*, 1860, doi:10.3390/su12051860.

145. Pérez-Collazo, C.; Greaves, D.; Iglesias, G. A review of combined wave and offshore wind energy. *Renew. Sustain. Energy Rev.* **2015**, *42*, 141–153, doi:10.1016/j.rser.2014.09.032.

146. Veigas, M.; Iglesias, G. A Hybrid Wave-Wind Offshore Farm for an Island. *Int. J. Green Energy* **2015**, *12*, 570–576, doi:10.1080/15435075.2013.871724.

147. Rusu, E.; Onea, F. A parallel evaluation of the wind and wave energy resources along the Latin American and European coastal environments. *Renew. Energy* **2019**, *143*, 1594–1607, doi:10.1016/j.renene.2019.05.117.

148. Stoutenburg, E.D.; Jenkins, N.; Jacobson, M.Z. Power output variations of co-located offshore wind turbines and wave energy converters in California. *Renew. Energy* **2010**, *35*, 2781–2791, doi:10.1016/j.renene.2010.04.033.

149. Astariz, S.; Vazquez, A.; Iglesias, G. Evaluation and comparison of the levelized cost of tidal, wave, and offshore wind energy. *J. Renew. Sustain. Energy* **2015**, *7*, 053112, doi:10.1063/1.4932154.

150. Zanopol, A.T.; Onea, F.; Rusu, E. Evaluation of the coastal influence of a generic wave farm operating in the romanian nearshore. *J. Environ. Prot. Ecol.* **2014**, *15*, 597–605.

151. Rusu, E.; Guedes Soares, C. Coastal impact induced by a Pelamis wave farm operating in the Portuguese nearshore. *Renew. Energy* **2013**, *58*, 34–49, doi:10.1016/j.renene.2013.03.001.

152. Silva, D.; Rusu, E.; Guedes Soares, C. The Effect of a Wave Energy Farm Protecting an Aquaculture Installation. *Energies* **2018**, *11*, 2109, doi:10.3390/en11082109.

153. Snyder, B.; Kaiser, M.J. Ecological and economic cost-benefit analysis of offshore wind energy. *Renew. Energy* **2009**, *34*, 1567–1578, doi:10.1016/j.renene.2008.11.015.

154. Castro-Santos, L.; Bento, A.; Guedes Soares, C. The Economic Feasibility of Floating Offshore Wave Energy Farms in the North of Spain. *Energies* **2020**, *13*, 806, doi:10.3390/en13040806.

155. Castro-Santos, L.; Martins, E.; Guedes Soares, C. Methodology to Calculate the Costs of a Floating Offshore Renewable Energy Farm. *Energies* **2016**, *9*, 324, doi:10.3390/en9050324.

156. Chan, D.; Mo, J. Life Cycle Reliability and Maintenance Analyses of Wind Turbines. *Energy Procedia* **2017**, *110*, 328–333, doi:10.1016/j.egypro.2017.03.148.

157. IPCC 2013 *Climate Change 2013: The Physical Science Basis. Contribution of Working Group I to the Fifth Assessment Report of the Intergovernmental Panel on Climate Change*; 2013;

158. Lemos, G.; Semedo, A.; Dobrynin, M.; Behrens, A.; Staneva, J.; Bidlot, J.R.; Miranda, P.M.A. Mid-twenty-first century global wave climate projections: Results from a dynamic CMIP5 based ensemble. *Glob. Planet. Change* **2019**, doi:10.1016/j.gloplacha.2018.09.011.

159. Casas-Prat, M.; Sierra, J.P. Projected future wave climate in the NW Mediterranean Sea. *J. Geophys. Res. Ocean.* **2013**, doi:10.1002/jgrc.20233.

160. Iglesias, G.; Carballo, R. Wave energy resource in the Estaca de Bares area (Spain). *Renew. Energy* **2010**, *35*, 1574–1584, doi:10.1016/j.renene.2009.10.019.

161. Iglesias, G.; Carballo, R. Wave energy potential along the Death Coast (Spain). *Energy* **2009**, *34*, 1963–1975, doi:10.1016/j.energy.2009.08.004.

162. Iglesias, G.; López, M.; Carballo, R.; Castro, A.; Fraguela, J.A.; Frigaard, P. Wave energy potential in Galicia (NW Spain). *Renew. Energy* **2009**, *34*, 2323–2333, doi:10.1016/j.renene.2009.03.030.

163. Iglesias, G.; Carballo, R. Offshore and inshore wave energy assessment: Asturias (N Spain). *Energy* **2010**, *35*, 1964–1972, doi:10.1016/j.energy.2010.01.011.

164. Iglesias, G.; Carballo, R. Wave energy and nearshore hot spots: The case of the SE Bay of Biscay. *Renew. Energy* **2010**, *35*, 2490–2500, doi:10.1016/j.renene.2010.03.016.

165. Mota, P.; Pinto, J.P. Wave energy potential along the western Portuguese coast. *Renew. Energy* **2014**, *71*, 8–17, doi:10.1016/j.renene.2014.02.039.

166. Silva, D.; Bento, A.R.; Martinho, P.; Guedes Soares, C. High resolution local wave energy modelling in the Iberian Peninsula. *Energy* **2015**, *91*, 1099–1112, doi:10.1016/j.energy.2015.08.067.

167. Reguero, B.G.; Losada, I.J.; Méndez, F.J. A recent increase in global wave power as a consequence of oceanic warming. *Nat. Commun.* **2019**, doi:10.1038/s41467-018-08066-0.

168. Ramos, V.; Carballo, R.; Ringwood, J. V. Assessing the utility and effectiveness of the IEC standards for wave energy resource characterisation. *Prog. Renew. Energies Offshore. London, UK Taylor Fr. Gr.* **2016**, 27–36, doi:10.1201/9781315229256-5.

169. Komen, G.J.; Hasselmann, K.; Hasselmann, K. On the Existence of a Fully Developed Wind-Sea Spectrum. *J. Phys. Oceanogr.* **1984**, *14*, 1271–1285, doi:10.1175/1520-0485(1984)014<1271:OTEOAF>2.0.CO;2.

170. Belo-Pereira, M.; Muacho, S.; Carvalho, A. Implementation and evaluation of an operational ocean wave forecasting system along the coast of West Iberia. *J. Oper. Oceanogr.* **2014**, *7*, 35–44, doi:10.1080/1755876X.2014.11020157.

171. Young, I.R.; Ribal, A. Multiplatform evaluation of global trends in wind speed and wave height. *Science (80-.).* **2019**, doi:10.1126/science.aav9527.

172. Gaetani, M.; Vignati, E.; Monforti-Ferrario, F.; Huld, T.; Dosio, A.; Raes, F. *Climate modelling and renewable energy resource assessment*; 2015;

173. Farkas, A.; Degiuli, N.; Martić, I. Assessment of Offshore Wave Energy Potential in the Croatian Part of the Adriatic Sea and Comparison with Wind Energy Potential. *Energies* **2019**, *12*, 2357, doi:10.3390/en12122357.

174. Kim, C.-K.; Toft, J.E.; Papenfus, M.; Verutes, G.; Guerry, A.D.; Ruckelshaus, M.H.; Arkema, K.K.; Guannel, G.; Wood, S.A.; Bernhardt, J.R.; et al. Catching the Right Wave: Evaluating Wave Energy Resources and Potential Compatibility with Existing Marine and Coastal Uses. *PLoS One* **2012**, *7*, e47598, doi:10.1371/journal.pone.0047598.

175. Veigas, M.; López, M.; Iglesias, G. Assessing the optimal location for a shoreline wave energy converter. *Appl. Energy* **2014**, doi:10.1016/j.apenergy.2014.07.067.

176. deCastro, M.; Salvador, S.; Gómez-Gesteira, M.; Costoya, X.; Carvalho, D.; Sanz-Larruga, F.J.; Gimeno, L. Europe, China and the United States: Three different approaches to the development of offshore wind energy. *Renew. Sustain. Energy Rev.* 2019.

177. Le Carrer, N.; Ferson, S.; Green, P.L. Optimising cargo loading and ship scheduling in tidal areas. *Eur. J. Oper. Res.* **2020**, *280*, 1082–1094, doi:10.1016/j.ejor.2019.08.002.

178. Song, J.-H.; Furman, K.C. A maritime inventory routing problem: Practical approach. *Comput. Oper. Res.* **2013**, *40*, 657–665, doi:10.1016/j.cor.2010.10.031.

179. Kusunoki, S.; Ose, T.; Hosaka, M. Emergence of unprecedented climate change in projected future precipitation. *Sci. Rep.* **2020**, *10*, 4802, doi:10.1038/s41598-020-61792-8.

180. Hawkins, E.; Frame, D.; Harrington, L.; Joshi, M.; King, A.; Rojas, M.; Sutton, R. Observed

Emergence of the Climate Change Signal: From the Familiar to the Unknown. *Geophys. Res. Lett.* **2020**, *47*, doi:10.1029/2019GL086259.

181. Jackson, L.P.; Jevrejeva, S. A probabilistic approach to 21st century regional sea-level projections using RCP and High-end scenarios. *Glob. Planet. Change* **2016**, *146*, 179–189, doi:10.1016/j.gloplacha.2016.10.006.

182. Aris, C.; Hande, D. *Impacts of climate change on transport: A focus on airports, seaports and inland waterways*; Brussels, 2018;

183. Lopes, C.L.; Azevedo, A.; Dias, J.M. Flooding assessment under sea level rise scenarios: Ria de Aveiro case study. *J. Coast. Res.* **2013**, *65*, 766–771, doi:10.2112/SI65-130.1.

184. Moreira, M.H.; Queiroga, H.; Machado, M.M.; Cunha, M.R. Environmental gradients in a southern Europe estuarine system: Ria de Aveiro, Portugal implications for soft bottom macrofauna colonization. *Netherlands J. Aquat. Ecol.* **1993**, *27*, 465–482, doi:10.1007/BF02334807.

185. Dias, J.M.; Lopes, J.F.; Dekeyser, I. Tidal propagation in Ria de Aveiro Lagoon, Portugal. *Phys. Chem. Earth, Part B Hydrol. Ocean. Atmos.* **2000**, *25*, 369–374, doi:10.1016/S1464-1909(00)00028-9.

186. Vaz, N.; Miguel Dias, J.; Chambel Leitão, P. Three-dimensional modelling of a tidal channel: The Espinheiro Channel (Portugal). *Cont. Shelf Res.* **2009**, *29*, 29–41, doi:10.1016/j.csr.2007.12.005.

187. Pereira, C.; Coelho, C. Mapping erosion risk under different scenarios of climate change for Aveiro coast, Portugal. *Nat. Hazards* **2013**, *69*, 1033–1050, doi:10.1007/s11069-013-0748-1.

188. Plecha, S.; Silva, P.A.; Vaz, N.; Bertin, X.; Oliveira, A.; Fortunato, A.B.; Dias, J.M. Sensitivity analysis of a morphodynamic modelling system applied to a coastal lagoon inlet. *Ocean Dyn.* **2010**, *60*, 275–284, doi:10.1007/s10236-010-0267-5.

189. Fortunato, A.B.; Rodrigues, M.; Dias, J.M.; Lopes, C.; Oliveira, A. Generating inundation maps for a coastal lagoon: A case study in the Ria de Aveiro (Portugal). *Ocean Eng.* **2013**, *64*, 60–71, doi:10.1016/j.oceaneng.2013.02.020.

190. Picado, A.; Lopes, C.L.; Mendes, R.; Vaz, N.; Dias, J.M. Storm surge impact in the hydrodynamics of a tidal lagoon: the case of Ria de Aveiro. *J. Coast. Res.* **2013**, *65*, 796–801, doi:10.2112/SI65-135.1.

191. Pinheiro, J.P.; Lopes, C.L.; Ribeiro, A.S.; Sousa, M.C.; Dias, J.M. Tide-surge interaction in Ria de Aveiro lagoon and its influence in local inundation patterns. *Cont. Shelf Res.* **2020**, *200*, 104132, doi:10.1016/j.csr.2020.104132.

192. Lopes, C.L.; Plecha, S.; Silva, P.A.; Dias, J.M. Influence of morphological changes in a lagoon flooding extension: case study of Ria de Aveiro (Portugal). *J. Coast. Res.* **2013**, *165*, 1158–1163, doi:10.2112/SI65-196.1.

193. Fidélis, T.; Teles, F.; Roebeling, P.; Riazi, F. Governance for Sustainability of Estuarine Areas—Assessing Alternative Models Using the Case of Ria de Aveiro, Portugal. *Water* **2019**, *11*, 846, doi:10.3390/w11040846.

194. Splinter, K.D.; Davidson, M.A.; Golshani, A.; Tomlinson, R. Climate controls on longshore sediment transport. *Cont. Shelf Res.* **2012**, *48*, 146–156, doi:10.1016/j.csr.2012.07.018.

195. Bromirski, P.D.; Cayan, D.R.; Helly, J.; Wittmann, P. Wave power variability and trends across the North Pacific. *J. Geophys. Res. Ocean.* **2013**, *118*, 6329–6348, doi:10.1002/2013JC009189.

196. C.A. Oliveira, T.; Cagnin, E.; A. Silva, P. Wind-waves in the coast of mainland Portugal induced by post-tropical storms. *Ocean Eng.* **2020**, *217*, 108020, doi:10.1016/j.oceaneng.2020.108020.

197. *Guide to Wave Analysis and Forecasting*; 2018 Editi.; World Meteorological Organization (WMO): Geneve, Switzerland, 2018; ISBN 978-92-63-10702-2.

198. Cavalinhos, R.; Correia, R.; Rosa, P.; Lillebo, A.I..; Pinheiro, L.M. Processed multibeam bathymetry data collected around the Ria de Aveiro, Portugal, onboard the NEREIDE research vessel. 2020.

199. van Rijn, L.C. Unified View of Sediment Transport by Currents and Waves. I: Initiation of Motion, Bed Roughness, and Bed-Load Transport. *J. Hydraul. Eng.* **2007**, *133*, 649–667, doi:10.1061/(ASCE)0733-9429(2007)133:6(649).

200. Dias, J.M.; Sousa, M.C.; Bertin, X.; Fortunato, A.B.; Oliveira, A. Numerical modeling of the impact

of the Ancão Inlet relocation (Ria Formosa, Portugal). *Environ. Model. Softw.* **2009**, *24*, 711–725, doi:10.1016/j.envsoft.2008.10.017.

201. Vargas, C.I.C.; Vaz, N.; Dias, J.M. An evaluation of climate change effects in estuarine salinity patterns: Application to Ria de Aveiro shallow water system. *Estuar. Coast. Shelf Sci.* **2017**, *189*, 33–45, doi:10.1016/j.ecss.2017.03.001.

202. Valente, A.S.; da Silva, J.C.B. On the observability of the fortnightly cycle of the Tagus estuary turbid plume using MODIS ocean colour images. *J. Mar. Syst.* **2009**, *75*, 131–137, doi:10.1016/j.jmarsys.2008.08.008.

203. Fortunato, A.B.; Baptista, A.M.; Luettich, R.A. A three-dimensional model of tidal currents in the mouth of the Tagus estuary. *Cont. Shelf Res.* **1997**, *17*, 1689–1714, doi:10.1016/S0278-4343(97)00047-2.

204. Fortunato, A.B.; Oliveira, A.; Baptista, A.M. On the effect of tidal flats on the hydrodynamics of the Tagus estuary. *Oceanol. Acta* **1999**, *22*, 31–44, doi:10.1016/S0399-1784(99)80030-9.

205. Fortunato, A.B.; Oliveira, A. Influence of Intertidal Flats on Tidal Asymmetry. *J. Coast. Res.* 2005, *215*, 1062–1067.

206. Vaz, N.; Fernandes, L.; Leitão, P.C.; Dias, J.M.; Neves, R. The Tagus estuarine plume induced by wind and river runoff: Winter 2007 case study. *J. Coast. Res.* **2009**, *Special Is*, 1090–1094.

207. Neves, F.J. Dynamics and hydrology of the Tagus estuary: results from in situ observations. PhD Thesis, University of Lisbon, Portugal, 2010.

208. Martins, M.; Calvão, T.; Figueiredo, H. *Estudo ambiental do estuário do Tagus, Estudo de Qualidade de Água. Resultados Referentes a observações sinópticas em 1982, CAN/Tagus 30-REL 27, Ministério da Qualidade de Vida, Lisboa, Portugal.*; 1983;

209. Fortunato, A.B.; Freire, P.; Bertin, X.; Rodrigues, M.; Ferreira, J.; Liberato, M.L.R. A numerical study of the February 15, 1941 storm in the Tagus estuary. *Cont. Shelf Res.* **2017**, *144*, 50–64, doi:10.1016/j.csr.2017.06.023.

210. Portela, L.I.; Neves, R. Numerical modelling of suspended sediment transport in tidal estuaries: A comparison between the Tagus (Portugal) and the Scheldt (Belgium-the Netherlands). *Netherlands J. Aquat. Ecol.* **1994**, *28*, 329–335, doi:10.1007/BF02334201.

211. Oliveira, I.B.M. Port of Lisbon: Improvement of the access conditions through the Tagus estuary entrance. *Coast. Eng.* **1992**, 2745–2757.

212. Dias, J.M.; Valentim, J.M.; Sousa, M.C. A Numerical Study of Local Variations in Tidal Regime of Tagus Estuary, Portugal. *PLoS One* **2013**, *8*, e80450, doi:10.1371/journal.pone.0080450.

213. Ribeiro, A.S.; Sousa, M.C.; Lencart, J.D.; Dias, J.M. David and Goliath Revisited : Joint Modelling of the Tagus and Sado Estuaries. **2016**, 123–127, doi:10.2112/SI75-025.1.

214. Rusu, L.; Bernardino, M.; Soares, C.G. Influence of wind resolution on the prediction of waves generated in an estuary. *J. Coast. Res.* **2009**, *56*, 1419–1423.

215. Rusu, L.; Bernardino, M.; Guedes Soares, C. Modelling the influence of currents on wave propagation at the entrance of the Tagus estuary. *Ocean Eng.* **2011**, *38*, 1174–1183, doi:10.1016/j.oceaneng.2011.05.016.

216. Rilo, A.; Freire, P.; Guerreiro, M.; Fortunato, A.B.; Taborda, R. Estuarine margins vulnerability to floods for different sea level rise and human occupation scenarios. *J. Coast. Res.* **2013**, *65*, 820–825, doi:10.2112/SI65-139.1.

217. Guerreiro, M.; Fortunato, A.B.; Freire, P.; Rilo, A.; Taborda, R.; Freitas, M.C.; Andrade, C.; Silva, T.; Rodrigues, M.; Bertin, X.; et al. Evolution of the hydrodynamics of the Tagus estuary (Portugal) in the 21st century. *Rev. Gestão Costeira Integr.* **2015**, 65–80, doi:10.5894/rgci515.

218. Rilo, A.; Freire, P.; Santos, P.; Tavares, A.; Sá, L. Historical flood events in the Tagus estuary: Contribution to risk assessment and management tools. In *Safety and Reliability of Complex Engineered Systems*; CRC Press, 2015; pp. 4281–4286.

219. Tavares, A.O.; Santos, P.P. dos; Freire, P.; Fortunato, A.B.; Rilo, A.; Sá, L. Flooding hazard in the Tagus estuarine area: The challenge of scale in vulnerability assessments. *Environ. Sci. Policy* **2015**, *51*, 238–255, doi:10.1016/j.envsci.2015.04.010.

220. Antunes, C.; Rocha, C.; Catita, C. Coastal Flood Assessment due to Sea Level Rise and Extreme

Storm Events: A Case Study of the Atlantic Coast of Portugal’s Mainland. *Geosciences* **2019**, *9*, 239, doi:10.3390/geosciences9050239.

221. Pérez-Fernández, B.; Viñas, L.; Besada, V. Concentrations of organic and inorganic pollutants in four Iberian estuaries, North Eastern Atlantic. Study of benchmark values estimation. *Mar. Chem.* **2020**, *224*, 103828, doi:10.1016/J.MARCHEM.2020.103828.

222. Sousa, M.C.; DeCastro, M.; Gago, J.; Ribeiro, A.S.; Des, M.; Gómez-Gesteira, J.L.; Dias, J.M.; Gomez-Gesteira, M. Modelling the distribution of microplastics released by wastewater treatment plants in Ria de Vigo (NW Iberian Peninsula). *Mar. Pollut. Bull.* **2021**, *166*, 112227, doi:10.1016/j.marpolbul.2021.112227.

223. Autoridad Portuaria de Vigo *Strategic Plan, 2018-2028*; Vigo, Spain, 2019;

224. Ríos, A.F.; Pérez, F.F.; Fraga, F. Water masses in the upper and middle North Atlantic Ocean east of the Azores. *Deep Sea Res. Part A. Oceanogr. Res. Pap.* **1992**, *39*, 645–658, doi:10.1016/0198-0149(92)90093-9.

225. Alvarez, I. Inter- and intra-annual analysis of the salinity and temperature evolution in the Galician Rías Baixas–ocean boundary (northwest Spain). *J. Geophys. Res.* **2005**, *110*, C04008, doi:10.1029/2004JC002504.

226. deCastro, M.; Gómez-Gesteira, M.; Prego, R.; Taboada, J.J.; Montero, P.; Herbello, P.; Pérez-Villar, V. Wind and Tidal Influence on Water Circulation in a Galician Ria (NW Spain). *Estuar. Coast. Shelf Sci.* **2000**, *51*, 161–176, doi:10.1006/ecss.2000.0619.

227. Woolf, D.K. Variability and predictability of the North Atlantic wave climate. *J. Geophys. Res.* **2002**, *107*, 3145, doi:10.1029/2001JC001124.

228. Oberle, F.K.J.; Storlazzi, C.D.; Hanebuth, T.J.J. Wave-driven sediment mobilization on a storm-controlled continental shelf (Northwest Iberia). *J. Mar. Syst.* **2014**, *139*, 362–372, doi:10.1016/J.JMARSYS.2014.07.018.

229. Reguera, P.; Viñas, L.; Gago, J. Microplastics in wild mussels (Mytilus spp.) from the north coast of Spain. *Sci. Mar.* **2019**, *83*, 337, doi:10.3989/scimar.04927.05A.

230. Sousa, M.C.; Ribeiro, A.S.; Des, M.; Mendes, R.; Alvarez, I.; Gomez-Gesteira, M.; Dias, J.M. Integrated High-resolution Numerical Model for the NW Iberian Peninsula Coast and Main Estuarine Systems. *J. Coast. Res.* **2018**, *85*, 66–70, doi:10.2112/SI85-014.1.

231. Des, M.; DeCastro, M.; Sousa, M.C.; Dias, J.M.; Gómez-Gesteira, M. Hydrodynamics of river plume intrusion into an adjacent estuary: The Minho River and Ria de Vigo. *J. Mar. Syst.* **2019**, *189*, 87–97, doi:10.1016/j.jmarsys.2018.10.003.

232. Resio, D.T.; Westerink, J.J. Modeling the physics of storm surges. *Phys. Today* **2008**, *61*, 33–38, doi:10.1063/1.2982120.

233. Arquero, F.J.N. New port facilities at Punta Langosteira, Spain. *Proc. Inst. Civ. Eng. Marit. Eng.* **2008**, *161*, 101–106, doi:10.1680/maen.2008.161.3.101.

234. Mairal, G. The Prestige disaster: risk or danger? *J. Risk Res.* **2017**, *20*, 1568–1584, doi:10.1080/13669877.2016.1200651.

235. Santos, M.; Corredor, A.; Maciñeira, E.; Bajo, V.; Gómez-Martín, M.E.; Medina, J.R. Aspectos innovadores en el dise˜no y construcción del dique Oeste en el puerto exterior de A Coru˜na en Punta Langosteira (Espa˜na). *Ribagua* **2016**, *3*, 89–100, doi:10.1016/j.riba.2016.07.005.

236. Corredor Molguero, A.; GÃ³mez-MartÃ-n, M.E.; PeÃ±a, E.; Medina, J.R. DESIGN AND CONSTRUCTION OF THE WESTERN BREAKWATER FOR THE OUTER PORT AT PUNTA LANGOSTEIRA (A CORUÃ‘A, SPAIN). *Coast. Eng. Proc.* **2017**, 14, doi:10.9753/icce.v35.structures.14.

237. Uzaki, K.; Matsunaga, N.; Nishii, Y.; Ikehata, Y. Cause and countermeasure of long-period oscillations of moored ships and the quantification of surge and heave amplitudes. *Ocean Eng.* **2010**, *37*, 155–163, doi:10.1016/j.oceaneng.2009.12.004.

238. Lorente, P.; Sotillo, M.; Aouf, L.; Amo-Baladrón, A.; Barrera, E.; Dalphinet, A.; Toledano, C.; Rainaud, R.; De Alfonso, M.; Piedracoba, S.; et al. Extreme Wave Height Events in NW Spain: A Combined Multi-Sensor and Model Approach. *Remote Sens.* **2017**, *10*, 1, doi:10.3390/rs10010001.

239. Zijlema, M.; van der Westhuysen, A.J. On convergence behaviour and numerical accuracy in stationary SWAN simulations of nearshore wind wave spectra. *Coast. Eng.* **2005**, *52*, 237–256, doi:10.1016/j.coastaleng.2004.12.006.

240. Rueda, A.; Camus, P.; Méndez, F.J.; Tomás, A.; Luceño, A. An extreme value model for maximum wave heights based on weather types. *J. Geophys. Res. Ocean.* **2016**, *121*, 1262–1273, doi:10.1002/2015JC010952.

241. Transportation Research Board and National Research Council *Potential Impacts of Climate Change on U.S. Transportation: Special Report 290*; Transportation Research Board: Washington, D.C., 2008; ISBN 978-0-309-11306-9.

242. Roelvink, D.; McCall, R.; Mehvar, S.; Nederhoff, K.; Dastgheib, A. Improving predictions of swash dynamics in XBeach: The role of groupiness and incident-band runup. *Coast. Eng.* **2018**, *134*, 103–123, doi:10.1016/j.coastaleng.2017.07.004.

243. Phillips, B.; Brown, J.; Bidlot, J.-R.; Plater, A. Role of Beach Morphology in Wave Overtopping Hazard Assessment. *J. Mar. Sci. Eng.* **2017**, *5*, 1, doi:10.3390/jmse5010001.

244. Oliveira, J.N.C.; Oliveira, F.S.B.F.; Neves, M.G.; Clavero, M.; Trigo-Teixeira, A.A. Modeling Wave Overtopping on a Seawall with XBeach, IH2VOF, and Mase Formulas. *Water* **2020**, *12*, 2526, doi:10.3390/w12092526.

245. Gallien, T.W. Validated coastal flood modeling at Imperial Beach, California: Comparing total water level, empirical and numerical overtopping methodologies. *Coast. Eng.* **2016**, *111*, 95–104, doi:10.1016/j.coastaleng.2016.01.014.

246. Smit, P.B.; G.S.Stelling; Roelvink, D.; van Thiel deVries, J.; McCall, R.; van Dongeren C. Zwinkels, A.; Jacobs, R. *XBeach: Non-hydrostatic model - Validation, verification and model description*; Delft;

247. Rueda-Bayona, J.G.; Guzmán, A.; Silva, R. Genetic algorithms to determine JONSWAP spectra parameters. *Ocean Dyn.* **2020**, *70*, 561–571, doi:10.1007/s10236-019-01341-8.